

**PHYSICS-GUIDED SOLUTIONS TO DISPERSION IN
DENSITY-FUNCTIONAL THEORY**

by

Kyle Robert Bryenton

**Submitted in partial fulfilment of the requirements
for the degree of Doctor of Philosophy in Physics**

at

**Dalhousie University
Halifax, Nova Scotia
August, 2025**

**Dalhousie University is located in the Mi'kma'ki, the
ancestral and unceded territory of the Mi'kmaq.
We are all Treaty people.**

DEDICATION

To my family, who have gotten me this far.

...

In loving memory of:
Bob Bryenton (1959–2024)
Eleanor Smith (1953–2022)

TABLE OF CONTENTS

List of Tables	x
List of Figures	xiii
Abstract	xiv
List of Abbreviations and Symbols Used	xv
Acknowledgements	xxii
Chapter 1 Introduction	1
1.1 Dispersion in Density-Functional Theory	1
1.2 The Second-Order Perturbation Theory of Dispersion	3
1.3 Early Empirical Dispersion Corrections	6
1.4 Modern Dispersion Corrections	7
1.5 Thesis Overview	9
Chapter 2 Theory	12
2.1 Density-Functional Theory	12
2.2 Perdew’s Ladder	14
2.2.1 The Ladder’s Base: Hartree–Fock	15
2.2.2 Rung 1: The Local-Density Approximation	16
2.2.3 Rung 2: The Generalized-Gradient Approximation	16
2.2.4 Rung 3: Meta-Generalized Gradient Approximations	18
2.2.5 Rung 4: Hybrid Functionals	19
2.2.6 Rung 5: Post-Kohn–Sham Correlation Methods	20
2.2.7 Chemical Accuracy and Beyond DFT	21
2.3 DFT in Periodic Solids	25
2.3.1 The Bravais Lattice and Bloch’s Theorem	25
2.3.2 Sampling the Brillouin Zone	27

2.3.3	Atomic Pseudopotentials	28
2.3.4	The Projector-Augmented Wave Method	30
2.3.5	Numerical Atom-Centred Orbitals	32
2.3.6	Gaussian-Type Orbitals	34
2.4	Forces and Stresses	36
2.4.1	The Hellmann–Feynman Force Theorem	36
2.4.2	Stresses, Strains, and Deformations	38
2.5	Dispersion Corrections	40
2.5.1	Grimme DFT-D Series of Dispersion Corrections	40
2.5.2	The TS and MBD Dispersion Models	45
2.5.3	The Exchange-Hole Dipole Moment Model	53
2.6	Delocalization Error	60
2.6.1	Introduction	60
2.6.2	Self-Interaction Error	61
2.6.3	The Exchange-Correlation Hole Picture	63
Chapter 3	Requirements for an Accurate Dispersion-Corrected Density Functional	67
3.1	Introduction	68
3.2	Requirements for the Base Density Functional	68
3.2.1	Dispersionless	68
3.2.2	Numerically Stable	72
3.3	Requirements for the Dispersion Correction	76
3.3.1	Finite Damping	76
3.3.2	Higher-Order Dispersion Terms	79
3.3.3	Response to Atomic Environment	81
3.4	Dispersion Contributions to Stresses	83
3.5	Summary	86
Chapter 4	Many-Body Dispersion in Model Systems and the Sensitivity of Self-Consistent Screening	88
4.1	Introduction	89

4.2	Theoretical Background: MBD-Free and MBD-XDM	91
4.3	Interacting Oscillator Systems	92
4.3.1	The Isotropic Quantum Harmonic Oscillator	92
4.3.2	Interaction Hamiltonian	93
4.3.3	Wavefunctions	95
4.3.4	Variationally Optimized Energies	97
4.3.5	Dispersion Coefficients and Energies for Oscillator Systems . .	99
4.4	Results and Discussion	99
4.4.1	Dispersion Energies	99
4.4.2	Analysis of C_6 Behaviour	102
4.4.3	Effect of Oscillator Frequency	105
4.4.4	Connection with Molecular Dimers and Layered Materials . .	107
Chapter 5	Comparison of Density-Functional Theory Dispersion Corrections for the DES15K Database	114
5.1	Introduction	115
5.2	Computational Methods	116
5.2.1	DFT Calculations	116
5.2.2	Correlated-Wavefunction Calculations	117
5.3	Results and Discussion	118
5.3.1	Analysis of the Full Benchmark	118
5.3.2	Examination of Outliers	120
5.3.3	Model Cation- π Complex	123
5.4	Conclusion	126
Chapter 6	The Exchange-Correlation Dipole Moment Dispersion Method	128
6.1	Introduction	129
6.2	Theory	130
6.2.1	Inclusion of Dynamical Correlation: XCDM	130
6.2.2	Damping Functions	135
6.3	Data Sets	138

6.3.1	<i>C</i> ₆ Benchmark and Fit Set	138
6.3.2	Molecular Benchmarks	138
6.3.3	Solid-State Benchmarks	140
6.4	Computational Methods	141
6.5	Results and Discussion	144
6.5.1	Molecular Benchmarks	144
6.5.2	Solid-State Benchmarks	149
6.6	Summary	152
Chapter 7	Conclusions	154
7.1	Dissertation Summary	154
7.2	Future Work	159
7.2.1	Improvement of Dispersion Forces in XDM	159
7.2.2	Continued Development of XDM and XCDM	159
7.2.3	Expanded XDM and XCDM Implementation	160
Bibliography	162
Appendix A	Chapter 1 Supplement	207
A.1	The Dispersion Interaction for the Hydrogen Dimer	208
A.2	Approximate Hydrogen-Dimer Interaction Energy	211
A.3	Interaction Between Two Oscillating Dipoles	212
Appendix B	Chapter 2 Supplement	215
B.1	Common Unit Conversion Factors	215
B.2	The Born–Oppenheimer Approximation	215
B.3	Improving DFT Dispersion Forces & Stresses	216
B.3.1	Assessment of Stress Errors with FHI-aims	216
B.3.2	Improved XDM Forces and Stresses	219
Appendix C	Chapter 6 Supplement	223
C.1	XCDM’s Use of the First Scalar Moment	223

C.2	XCDM Dimensional Analysis	224
C.3	Damping Function Parameterization	224
C.4	Analysis of WTMAD Contributions	225
C.5	Tabulated Data	227

LIST OF TABLES

3.1	Mean absolute errors obtained with selected XDM-corrected GGA functionals for the KB49 and X23 benchmarks.	71
3.2	Mean absolute errors and mean errors for the KB49 and X23 benchmarks using the B86bPBE base functional and selected XDM dispersion terms.	80
3.3	Homoatomic dispersion coefficients for selected metals.	82
3.4	Minimum-energy lattice constants of selected materials.	85
4.1	Computed binding energies for molecular dimers and layered materials.	109
4.2	Computed homoatomic C_6 dispersion coefficients for isolated molecules and selected layered materials.	110
5.1	Error statistics for the full DES15K benchmark set and for selected subsets.	119
6.1	Results for the MolC6 benchmark of homomolecular C_6 coefficients.	136
6.2	Timing comparisons for XDM and its variants.	143
6.3	WTMAD-2 and WTMAD-4 results for the GMTKN55 benchmark with selected functionals and dispersion corrections.	148
6.4	Mean absolute errors for the X23, HalCrys4, and ICE13 lattice-energy benchmarks.	150
6.5	Mean absolute errors for the layered-material benchmarks.	151
B.1	Conversion factors between common units used in electronic structure theory.	215

B.2	Comparison of the lattice-constant and energy errors for TS and XDM using FHI-aims and Quantum ESPRESSO.	217
B.3	Comparison of selected cubic solids' heteroatomic C_6 coefficient sensitivity to cell compression for TS and XDM using FHI-aims and Quantum ESPRESSO.	218
C.1	MolC6 for XCDM for all normalization functions.	230
C.2	KB49 and XDM and XCDM damping parameters for FHI-aims, for both BJ-damping and Z-damping.	231
C.3	KB49 and XDM and XCDM damping parameters for Gaussian (via postg).	232
C.4	Contributions to WTMAD values for GMTKN55 subsets. . . .	233
C.5	GMTKN55 MADs for XDM(BJ).	234
C.6	GMTKN55 MADs for XDM(Z).	235
C.7	GMTKN55 MADs for XCDM(BJ).	236
C.8	GMTKN55 MADs for XCDM(Z).	237
C.9	GMTKN55 mean absolute deviations (MAD) for D3(BJ), TS, MBD@rsSCS, and MBD-NL.	238
C.10	Per-category breakdown of GMTKN55 WTMAD-2 for all dispersion corrections.	239
C.11	Per-category breakdown of GMTKN55 WTMAD-4 for all dispersion corrections.	240
C.12	All GMTKN55 WTMADs for each functional and dispersion correction tested.	241
C.13	X23 MAE and ME results for XDM and its variants.	242
C.14	ICE13 MAE and ME results for XDM and its variants.	243
C.15	HalCrys4 MAE and ME results for XDM and its variants. . . .	244

C.16	LM26 and LM11 MAE and ME (in meV/Å ²) results for XDM and its variants.	245
C.17	LM26 and LM11 MAE and ME (in kcal/mol/cell) results for XDM and its variants.	246

LIST OF FIGURES

2.1	Perdew’s ladder of density-functional approximations	14
2.2	Sketch of the electron density for a diatomic molecule.	17
2.3	The large reduced-density-gradient behaviour of the LSDA and popular GGA functionals.	18
2.4	Types of pseudopotentials and pseudowavefunctions.	29
2.5	Visualization of the projector-augmented wave orbital components.	30
2.6	PAW volume overlap contours as functions of radius overlap and radius ratio.	31
2.7	Visualization of the numerical atom-centred orbitals used in FHI-aims.	33
2.8	A flowchart depicting geometry optimization, as performed by most electronic-structure theory software.	37
2.9	A simple cubic lattice with labelled Cauchy stress and Green–Lagrangian strain components.	39
2.10	Deformations and their corresponding deformation gradient tensors.	40
2.11	An illustration of the Becke–Roussel exchange hole.	57
2.12	Potential energy curves for H_2^+ and He_2^+ obtained with selected methods.	63
2.13	Plots of the total electron density, hole-normalization integrand, and exchange-energy densities for the hydrogen atom obtained with BR and exact exchange.	64
3.1	Graphite exfoliation energies computed using selected base density functionals.	69

3.2	Plots of the exchange enhancement factor for the LDA and selected GGA functionals.	70
3.3	Graphite exfoliation energies computed using the SCAN meta-GGA functional with varying planewave cut-offs for the electron density expansion.	73
3.4	Values of the x function used in the SCAN and r^2 SCAN functionals along the internuclear axis in Ar_2	75
3.5	Comparison of the effect of various damping functions.	77
3.6	Comparison of SCAN-D3 and B86bPBE-XDM results for the exfoliation energy of graphite.	78
3.7	B86bPBE-XDM results for NaCl and CO_2	86
4.1	The selected geometries for systems of interacting quantum harmonic oscillators.	94
4.2	Selected free-atomic orbitals for the isotropic quantum harmonic oscillator.	96
4.3	Computed potential energy surfaces for the interacting quantum harmonic oscillator systems.	98
4.4	Computed dispersion energies for the harmonic oscillator model systems.	100
4.5	Analysis of C_6 for the quantum harmonic oscillator chains. . .	103
4.6	Variation in C_6 for argon chains.	104
4.7	Variation in C_6 for quantum-harmonic oscillator and noble-gas dimers.	106
4.8	Potential energy curves and changes in dispersion coefficients for selected molecular dimers and layered materials.	108
5.1	Histograms showing the error distributions obtained with each functional and dispersion correction.	118

5.2	Scatter plots showing the errors obtained with each functional and dispersion correction.	121
5.3	Structures of the DES15K complexes that exhibited the maximum errors.	122
5.4	Selected properties for the C_{6v} Li^+ -benzene complex as a function of the distance between the cation and the benzene ring's centre of mass.	124
6.1	Sketch of various exchange and correlation holes for a diatomic molecule.	130
6.2	An illustration of the Becke–Roussel exchange hole.	133
6.3	Plots of the exchange, opposite-spin correlation, and combined exchange-correlation holes, along with their corresponding dipole moments, for the helium atom.	135
6.4	Comparison of BJ- and Z-damping functions.	137
6.5	Minimum mean absolute errors (MAEs) obtained for each benchmark within the GMTKN55 set for each DFA considered. . . .	145
6.6	Differences in mean absolute errors, relative to XDM(BJ) results for each GMTKN55 benchmark, with the three new XDM variants.	146
6.7	A scatter plot showing the overall solid-state and molecular errors with selected functionals and dispersion corrections. . .	151
C.1	Plots comparing the computed exchange-hole dipole moment with the first scalar moment of the BR exchange hole.	228
C.2	Scatter plots illustrating the overall solid-state and GMTKN55 errors for XDM and its variants.	229

ABSTRACT

Density-functional theory (DFT) has become the workhorse of modern computational chemistry, enabling first-principles modelling of large-scale systems with remarkable accuracy and efficiency. Its success is partly due to the development of numerous corrections to model London dispersion, which is the weakest of the intermolecular van der Waals forces. One such dispersion correction is the exchange-hole dipole moment (XDM) model. XDM calculates the dispersion energy by summing the contributions from all atom pairs, prompting recent questions about its treatment of many-body effects. To investigate this, variational model systems of interacting Drude oscillators were studied from first principles. XDM’s dispersion coefficients were then compared to those computed by the many-body dispersion (MBD) model, which is known to capture these many-body effects. Explicit three-body contributions were calculated using the Axilrod–Teller–Muto (ATM) and random-phase approximation (RPA) methods, but neither contributed meaningfully to the dispersion energy. We further showed that the dominant many-body effect is electronic, reflected in the dynamic response of the dispersion coefficients to changes in the surrounding chemical environment. A subsequent study compared XDM to other leading post-SCF dispersion corrections, where it showed best-in-class performance on the DES15K benchmark, which spans almost 15,000 noncovalent interactions across compressed to expanded geometries.

Building on this solid foundation of both physical rigour and numerical accuracy, we pursue physics-guided improvements to further refine dispersion modelling and reduce empiricism. Here, we introduce two new XDM variants. The first, XCDM, supplements the exchange hole with same- and opposite-spin dynamical correlation holes when calculating multipole moments. The second, XDM(Z), implements Z-damping, a novel one-parameter damping function based on atomic numbers. This reduces the number of fitted empirical parameters in XDM from two to one. These variants were tested comprehensively across both molecular systems and the solid state. XCDM proves to be exceptionally accurate for molecular systems, and the data suggests a possible use case for crystal structure prediction. Z-damping displays impressive performance considering the reduction in empirical parameters. XDM(Z) may represent a Pauling point for the XDM methods, rarely the best but consistently reliable across the widest range of systems.

LIST OF ABBREVIATIONS AND SYMBOLS USED

Symbol Description	Symbol Description
<i>General symbols and notation</i>	<i>Used atomic orbitals</i>
a Constant (upright, non-bold)	s $1s, 2s$
a Variable (italic, non-bold)	p $2p_x, 2p_y, 2p_z, 3p_x, 3p_y, 3p_z$
\mathbf{a} Vector (italic, bold)	d $3d_{z^2}, 3d_{xz}, 3d_{yz}, 3d_{xy}, 3d_{x^2-y^2}$
\mathbf{a} Tensor (upright, bold)	f $4f_{z^3}, 4f_{xz^2}, 4f_{yz^2}, 4f_{xyz}, 4f_{z(x^2-y^2)},$ $4f_{x(x^2-3y^2)}, 4f_{y(3x^2-y^2)}$
\hat{a} Operator (italic, non-bold, hat)	
$\hat{\mathbf{a}}$ Unit vector (upright, non-bold, hat)	
a' Derivative of a	
$\frac{d}{dr}a$ Derivative of a with respect to r	
$\frac{\delta}{\delta r}a$ Functional derivative of a with respect to r	
Δa Change in a	
∇a Gradient of a	
$\nabla \cdot \mathbf{a}$ Divergence of \mathbf{a}	<i>Used indices & their typical groupings</i>
$\nabla \times \mathbf{a}$ Curl of \mathbf{a}	<ul style="list-style-type: none"> · A, B, C · a, b, c · i_1, i_2, i_3, i_4 · i, j, k · k, ℓ, m · m, n · p, q · α, β, γ · σ, σ' · μ, ν
$\nabla^2 a$ Laplacian of a	
$\nabla \otimes \mathbf{a}$ Tensor product of ∇ and \mathbf{a}	
\mathbf{a}^{-1} Matrix inverse of \mathbf{a}	
\mathbf{a}^\top Matrix transpose of \mathbf{a}	
$\text{tr}[\mathbf{a}]$ Trace of matrix \mathbf{a}	
$\langle a_i $ Row vector of a_i	
$ a_i \rangle$ Column vector of a_i	
$\langle a \rangle$ Expectation value of a (see Dirac notation)	
<i>Common or fundamental constants</i>	
$\mathbf{1}$ Ones matrix, a matrix where every element is 1	
\AA Angstrom, ($= 10^{-10}$ m)	
a_0 Bohr radius, the mean radius between an electron and the nucleus for the ground-state H atom ($= 1$ a.u.)	
e Euler's number, the base of the natural logarithm ($= 2.71828182\dots$)	
e Charge of an electron ($= 1$ a.u.)	
h Planck's constant, equal to a photon's energy divided by its frequency	
\hbar Reduced Planck's constant, ($= h/2\pi = 1$ a.u.)	
\mathbf{I} Identity matrix, a square matrix with ones on the main diagonal and zeros elsewhere	
i Imaginary number, solution to $x^2 = -1$	
ϵ_0 Permittivity of free space ($4\pi\epsilon_0 = 1$ a.u.)	
π Pi, the ratio of a circle's circumference to its diameter ($= 3.14159265\dots$)	

Abbrev.	Description	Abbrev.	Description
A_mH_n	Hydride with stoichiometric coefficients m and n	DMC	Diffusion Monte Carlo method
ACFD(T)	Adiabatic connection fluctuation-dissipation theorem	DOS	Dipole oscillator strength
ADF	Amsterdam Density Functional	DOSD	Dipole oscillator strength distribution
AMS	Amsterdam Modelling Suite	dDsC	Steinmann and Corminboeuf's density-dependent dispersion correction
AE	All-electron	d	Damping
APW	Augmented planewave method	Eq.	· Equilateral triangle · Equation
ATM	Axilrod–Teller–Muto triple-dipole dispersion energy term	Eqs.	Equations
Abs	Absolute (e.g., Ice13(Abs) absolute energy	E_h	One hartree of energy
aNZ	Augmented N -zeta Dunning basis set	eV	Electron volt
a.u.	(Hartree) atomic unit	F12	Explicit correlation method (a.k.a. R12)
B3LYP	Becke, 3-parameter, Lee–Yang–Parr hybrid density functional	FCI	Full configuration interaction
B86a	Becke's B86a GGA density functional	FFT	Fast (discrete) Fourier transform
B86b	Becke's B86b GGA density functional	FHI-aims	Fritz Haber Institute <i>ab initio</i> materials simulations
B86bPBE	Becke's B86b exchange with PBE correlation GGA density functional	FI	Fractionally ionic (e.g., MBD/FI)
B86bPBE0	Becke's B86b exchange with PBE correlation hybrid density functional	FN	Fixed-node approximation
B88	Becke's B88 GGA density functional	GGA	Generalized-gradient approximation
BHLYP	Becke and Lee–Yang–Parr “half and half” hybrid density functional	GMTKN55	General main-group thermochemistry, kinetics, and non-covalent interactions
BJ	Becke–Johnson damping function (e.g. XDM(BJ))	GTO	Gaussian-type orbitals
BO	Born–Oppenheimer approximation	HF	Hartree–Fock theory
BR	Becke–Roussel exchange hole	HF-D	Scoles' dispersion-corrected Hartree–Fock method
BSC	Basis set corrected	HI	Iterative Hirshfeld partitioning scheme (e.g. MBD/HI)
C	Correlation	HSE06	Heyd–Scuseria–Ernzerhof variable exchange hybrid functional
CBS	Complete basis set	Ha.	Hartree (unit)
CC	Coupled-cluster theory (e.g. CCSD)	HalCrys4	Halogen crystal benchmark
CCSD(T)	CC theory with singles, doubles and perturbative triple excitations	Ice13	The Ice13 ice polymorph lattice energy benchmark
CFDM	Coupled fluctuating dipole model	IBZ	Irreducible Brillouin zone
CI	Configuration interaction method	Iso.	Isomerizations
CHG	Chai and Head–Gordon damping function	KB49	Kannemann–Becke benchmark set of 49 molecular dimers
CN	Coordination number	KB65	Kannemann–Becke benchmark set of 65 molecular dimers
CP	Counterpoise	kcal	Kilocalorie
CPU	Central processing unit	KS	Kohn–Sham (e.g., KS-DFT)
CSP	Crystal structure prediction	LAPW	Linearized augmented planewave methods
ca.	circa (=about)	LDA	Local-density approximation
cc-p	Correlation-consistent and polarized (e.g. aug-cc-pVTZ)	LJ	Lennard-Jones potential
D/DC	Dispersion corrected (e.g. DFT-D or DC-DFT)	LSDA	Local spin-density approximation
DC	Dynamical correlation	Lin.	Linear
DFA	Density-functional approximation	M	Mooij (e.g., f^M damping)
DFT	Density-functional theory	MAD	Mean absolute deviation
D_n	Grimme's series of dispersion corrections (e.g., DFT- D_n , $n=1, 2, 3, 4$)	MAE	Mean absolute error
		MAPD	Mean absolute percent deviation
		MAPE	Mean absolute percent error
		MAX	Maximum absolute error

Abbrev.	Description	Abbrev.	Description
MBD	Many-body dispersion model	S22	Benchmark set of non-covalent complexes
MBDQ	Many-body dispersion model with quadrupole interactions	S66	Benchmark set of 66 gas-phase dimers
MD	Mean deviation	S66 \times 7	Benchmark set of 66 gas-phase dimers with 7 inter-fragment distances
ME	Mean error	S66 \times 8	Benchmark set of 66 gas-phase dimers with 8 inter-fragment distances
mGGA	Meta-generalized gradient approximation	SCF	Self-consistent field
MolC6	Molecular C_6 dispersion coefficient benchmark by Johnson and Becke	SCS	Self-consistent screening
MP	Monkhorst–Pack \mathbf{k} -point grid sampling scheme	SIE	Self-interaction error
MP2	Møller–Plesset second-order perturbation theory	STO	Slater-type orbital
MP2C	MP2 coupled method	TMDC	Transition-metal dichalcogenides
NAO	Numerical atom-centred orbitals	TPSS	Tao–Perdew–Staroverov–Scuseria mGGA functional
NC	Norm-conserving (e.g., pseudopotential)	TS	Tkatchenko–Scheffler dispersion model
NCI	Non-covalent interactions	TSsurf	Tkatchenko–Scheffler dispersion model for surfaces
NDC	Non-dynamical correlation	UEG	Uniform electron gas
NI	Non-interacting	US	Ultra-soft (e.g., pseudopotential)
NL	Non-local (e.g. MBD-NL)	uMBD	Universal many-body dispersion model
NLDf	Non-local density functional	V	Valence (e.g., pVTZ)
Opt.	Optimization	VSXC	Voorhis and Scuseria's τ -dependent mGGA functional
PAW	Projector-augmented wave	VV	Vydrov and van Voorhis
PBE	Perdew–Burke–Ernzerhof GGA density functional	VV10	Vydrov and van Voorhis non-local density functional
PBE0	Perdew–Burke–Ernzerhof hybrid density functional	vdW	van der Waals
PES	Potential energy surface	vdW-DF	Dion's van der Waals density functional
PP	Pseudopotential	vdW-DF2	Lundqvist & Langreth's van der Waals density functional
PRO	Percent radial overlap	W n	Weizmann-n methods $n = 1, 2, 3, \dots$
PT(2)	Perturbation theory, (second-order)	WTMAD	Weighted mean absolute deviation (e.g., WTMAD- n , $n = 1, 2, 3, 4$)
PVO	Percent volume overlap	WY	Wu–Yang Fermi-type damping function
PW86	Perdew–Wang PW86 GGA density functional	X	Exchange
p.	Page	X23	Benchmark set of molecular organic solids
QE	Quantum ESPRESSO	XC	Exchange correlation
QHO	Quantum harmonic oscillator	XCDM	Exchange-correlation dipole moment dispersion model
QMC	Quantum Monte Carlo	XDM	Exchange-hole dipole moment dispersion model
RFA	Response-function approximation	Z	Z-damping function (e.g. XDM(Z))
RMSD	Root mean squared deviation	ZORA	Zero-order regular approximation
RMSPD	Root mean squared percent deviation		
RMSE	Root mean squared error		
RMSPE	Root mean squared percent error		
RPA	Random-phase approximation		
RPA-3	RPA's three-body-only energy		
RS	Range separation		
Rel	Relative (e.g. Ice13(Rel) relative energies)		
Ri.	Right-angle triangle		
Ry	Rydberg		
rsSCS	Range-separated self-consistent screening		
rVV10	Revised Vydrov and van Voorhis non-local density functional		
S12L	Grimme's large complexes benchmark		

Symbol	Description	Symbol	Description
Mathematical Symbols (Latin)			
A	Normalization constant for BR hole	\mathbf{d}	Dipole vector
\mathbf{A}	MBD@rsSCS RFA polarizability tensor	$d_{C,\sigma\sigma}$	Same-spin dynamical correlation hole dipole moment
\mathbf{A}	SCS interaction tensor	$d_{C,\sigma\sigma'}$	Opposite-spin dynamical correlation hole dipole moment
A, B, C	Nuclear index values	$d_{X\sigma}$	Exchange-hole dipole moment for spin σ
a	SCAN τ -dependent term	$d_{XC\sigma}$	Exchange-correlation-hole dipole moment for spin σ
\bar{a}	r^2 SCAN τ -dependent term	d, β	MBD@rsSCS Wu–Yang damping parameters
a_σ	Exponent of BR-hole orbital for spin σ	d	PAW sphere separation
a_{latt}	Lattice constant	d_i	Expansion coefficient
a_{latt}^{\min}	Minimum-energy lattice constant	E	Energy (generally)
a_{latt}^{rel}	Relaxed lattice constant	\mathbf{E}	Electric field vector
a_1, a_2	Becke–Johnson damping parameters	$E^{(0)}$	Zeroth-order PT energy
a, b, c	<ul style="list-style-type: none"> · PW86 parameters · Lattice constants 	$E^{(1)}$	First-order PT energy
a_X	Hybrid exchange mixing parameter	$E^{(2)}$	Second-order PT energy
a_C	Double hybrid correlation mixing parameter	E^{1e}	One-electron energy
\mathbf{a}_i	Primitive/Bravais/real-space lattice vectors	E^{2e}	Two-electron energy
b_σ	BR exchange hole displacement for spin σ	E_X	Exchange energy (generally)
\mathbf{b}_i	Reciprocal lattice vectors	E_C	Correlation energy (generally)
b_n, μ	SCAN x -function parameters	E_{cut}	Planewave energy cutoff
C	Vydrov and van Voorhis polarizability functional tunable parameter	E_{base}	Base SCF contribution to the energy
C, d, μ	r^2 SCAN x -function parameters	E_{disp}	Dispersion contribution to the energy
C_6	Dipole-dipole dispersion coefficient	$E_{\text{disp}}^{(2)}$	2-body contribution to the dispersion energy
C_8	Dipole-quadrupole dispersion coefficient	$E_{\text{disp}}^{(3)}$	3-body contribution to the dispersion energy
C_9	ATM 3-body nonadditive dispersion coefficient	$E_{\text{DFT-D}}$	Grimme's DFT-D dispersion energy
C_{10}	Dipole-octupole or quadrupole-quadrupole dispersion coefficient	E_{Dn}	DFT-Dn dispersion energy
C_{12}	Dipole-hexadecapole or quadrupole-octupole dispersion coefficient	E_{MBD}	MBD dispersion energy
C_{14}	Octupole-octupole dispersion coefficient	$E_{\text{SCS MBD}}$	Many-body dispersion energy, using self consistent screening
C_n	General dispersion coefficient	$E_{\text{rsSCS MBD}}$	Many-body dispersion energy, using range-separated self consistent screening
$C_{n,ii}$	Homoatomic dispersion coefficient	E_{TS}	Tkatchenko–Scheffler dispersion energy
$C_{n,ii}^{\text{free}}$	Free-atom homoatomic dispersion coefficient	E_{XDM}	Exchange-hole dipole moment dispersion energy
$C_{n,ij}$	Heteroatomic dispersion coefficient between atoms i and j	E_{XCDM}	Exchange-correlation dipole moment dispersion energy
$C_{n,ij}^{\text{DFT-D}}$	Grimme's DFT-D heteroatomic dispersion coefficient	E_{ACFD}	Adiabatic connection fluctuation-dissipation energy
$C_{n,ij}^{\text{D}}$	DFT-Dn heteroatomic dispersion coefficient	E_{DFT}	Density-functional theory energy
$C_{n,ij}^{\text{TS}}$	TS heteroatomic dispersion coefficient	E_{HF}	Hartree–Fock energy
$C_{n,ij}^{\text{SCS}}$	SCS heteroatomic dispersion coefficient	E_{MP2}	Second-order Møller–Plesset energy
$C_{n,ij}^{\text{XDM}}$	XDM heteroatomic dispersion coefficient	E_{PPT2}	Second-order perturbation theory energy
\mathbf{C}^{MBD}	Second-rank MBD dipolar coupling matrix	E_{PPT2}	Random-phase approximation energy
CN	D3/D4 fractional coordination number	E_{vdW}	Wu and Yang's DFT-D vdW energy
c	Mooij damping parameter	$E_{1,1}^{\text{H}_2}$	Ground-state energy for H_2
$c_{n,r,k}$	Fourier coefficient	$E_{m,n}^{\text{H}_2}$	Zeroth-order energy for H_2
$c_{n,G,k}$	Inverse-Fourier coefficient	$E[\rho]$	Total energy functional (of electron density)
c_i	Expansion coefficient	$E_C[\rho]$	Correlation energy functional
c_x	Functional-dependent parameter	$E_H[\rho]$	Hartree energy functional
D_σ	Difference between σ -spin Kohn–Sham and Weizsäcker kinetic energy densities	$E_X[\rho]$	Exchange energy functional
		$E_{\text{XC}}[\rho]$	Exchange-correlation energy functional

Symbol	Description	Symbol	Description
$E_X^{\text{LDA}}[\rho]$	LDA exchange energy functional	\hat{J}	Coulomb operator
$E_X^{\text{LSDA}}[\rho]$	LSDA exchange energy functional	\hat{K}	Exchange operator
$E_X^{\text{GGA}}[\rho]$	GGA exchange energy functional	k_s	QHO spring constant
E'	First-order perturbative energy correction	\mathbf{k}	Wave vector
E''	Second-order perturbative energy correction	k, ℓ, m	Quantum numbers for the QHO
\mathcal{E}	External field magnitude	k_i	DFT-D fixed scale factors
$ \Delta E $	Average reference energy	\mathbf{L}	Lattice vector
\mathbf{F}	Deformation gradient tensor	\mathcal{L}	Lagrangian operator
$F_{\alpha\beta}$	Deformation gradient tensor components	$L_k^{(\ell+1/2)}$	Generalized Laguerre polynomials
\mathbf{F}_r	Hellmann–Feynman force	MAD_i	Mean absolute deviation on benchmark i
$\mathbf{F}_{k,\alpha}$	α^{th} component of the atomic forces on atom k	$\langle M_\ell^2 \rangle$	Multi-pole (ℓ -pole) moment integral
$F_i(x)$	Normalization functions for BR dynamical correlation hole	m	Mass (generally)
$F(\chi_\sigma)$	General enhancement factor	\mathbf{m}	Induced dipole moment
F^{B86b}	B86b enhancement factor	m_i	Reciprocal lattice coefficients
F^{B88}	B88 enhancement factor	N	<ul style="list-style-type: none"> · Number (e.g., of particles) · Normalization constant (generally)
F^{PBE}	PBE enhancement factor	N_b	Number of basis functions
F^{PW86}	PBE enhancement factor	N_{bench}	Number of benchmarks
\hat{F}	Fock operator	n	Energy state of the QHO
$\mathbf{F}_i^{\text{XDM}}$	XDM dispersion force vector on atom i	n_i	Bravais lattice coefficients
$f(x)$	<ul style="list-style-type: none"> · Function (generally) · Step function of x 	$n(\mathbf{r})$	Alternate notation for electron density
f^d	General damping function	n, ℓ, m	Quantum numbers
f_{ATM}^d	General damping function parametrized for the ATM term	\mathcal{O}	<ul style="list-style-type: none"> · System origin · Big-O notation describing limiting behaviour
f_i^{BJ}	Becke–Johnson damping function	$\tilde{ \mathbf{p}_i\rangle}$	PAW projector function
f^{CHG}	Chai and Head–Gordon damping function	Q_σ	Exact exchange hole curvature for spin σ
f^F	Fermi damping function	q_A	Charge on A
$f^{\text{HF-D}}$	Scoles' damping function	R	Displacement or separation (generally)
f^{WY}	Wu–Yang damping function	\mathbf{R}	Bravais lattice vector
\mathbf{G}	Periodic wave vector	\mathbf{R}_p	Vector pointing toward nucleus p
$g(I, \chi)$	Cutoff function for MBD-NL	\mathbf{R}_p	Vector from origin to oscillator p 's electron
$g_{\sigma\sigma}$	Fixed parameter for same-spin dynamical correlation hole	R_c	Radius of critical separation
$g_{\sigma\sigma'}$	Fixed parameter for opposite-spin dynamical correlation hole	R_m	Scoles' HF-D position of potential minimum
\hat{h}	Single-particle Hamiltonian	R_{sep}	Separation between adjacent atoms
\hat{H}	Hamiltonian	R_{small}	PAW smaller sphere
\hat{H}_I	Interaction Hamiltonian	R_{big}	PAW larger sphere
$\hat{H}^{(0)}$	Zeroth-order PT Hamiltonian	R_{vdW}	van der Wall's radius
$\hat{H}^{(1)}$	First-order PT Hamiltonian	R_{SCS}	SCS vdW radius
$\hat{H}^{(2)}$	Second-order PT Hamiltonian	R_{free}	Free-atom vdW radius
\mathcal{H}	Hilbert space	r, θ, ϕ	Spherical radius, and polar and azimuthal angles
$h_{X\sigma}$	Exchange hole for spin σ	$\hat{\mathbf{r}}, \hat{\theta}, \hat{\phi}$	Spherical unit vectors
$h_{C\sigma\sigma}$	Same-spin dynamical correlation hole	r_{cut}	Cutoff radius
$h_{C\sigma\sigma'}$	Opposite-spin dynamical correlation hole	r_{ij}	Distance between i and j
$h_{XC\sigma}$	Exchange-correlation hole for spin σ	r_{12}	Distance between electrons 1 and 2
I_A	Ionization energy of atom A	r_{1A}	Distance between electron 1 and nucleus A
$I[\rho]$	Local ionization potential	r_{AB}	Distance between nuclei A and B
$J[\rho]$	Coulomb energy density functional	r_i	<ul style="list-style-type: none"> · Radius of sphere i · Distance from nucleus to a BR hole reference electron i
J_{ee}	Alternate notation for $J[\rho]$	r_{onset}	Onset radius

Symbol	Description	Symbol	Description
r'	<ul style="list-style-type: none"> · Radial integration variable · Radial reference point 	x	<ul style="list-style-type: none"> · Transcendental variable for BR hole · SCAN functional x function
\mathbf{r}_p	Vector from oscillator p 's nucleus to its electron	x, y, z	Cartesian directions
s	<ul style="list-style-type: none"> · BR hole reference point · Functional-dependent parameter · Empirical C_n scaling coefficient 	$x_{k,\alpha}$	α^{th} component of the atomic position of atom k
s, w	FHI-aims cutoff potential parameters	$\hat{x}, \hat{y}, \hat{z}$	Cartesian unit vectors
s, d	Wu-Yang empirical parameters	Y_ℓ^m	Spherical harmonic functions
s, γ	Chai and Head-Gordon damping empirical parameters	Z	Nuclear charge
s_n	Grimme-D functional-dependent scale factor	z	FHI-aims effective nuclear charge
\hat{T}	<ul style="list-style-type: none"> · Kinetic energy operator · Cluster operator 	z_{damp}	Z-damping parameter
$T_{\text{KS}}[\rho]$	Kohn-Sham kinetic energy functional	$z_{\sigma\sigma}$	Same-spin correlation length
\mathbf{T}_{ij}	Second-rank dipole-dipole interaction tensor	$z_{\sigma\sigma'}$	Opposite-spin correlation length
\mathbf{T}'_{ij}	General CFDM second-rank dipole-dipole interaction tensor		
$\mathbf{T}_{\text{LR},ij}$	Second-rank dipole-dipole long-range interaction tensor		
$\mathbf{T}_{\text{SR},ij}$	Second-rank dipole-dipole short-range interaction tensor		
\mathcal{T}_{ij}^{ab}	Dipole-dipole interaction tensor elements		
$\mathcal{T}_{\text{LR},ij}^{ab}$	Dipole-dipole long-range interaction tensor elements		
$\mathcal{T}_{\text{SR},ij}^{ab}$	Dipole-dipole short-range interaction tensor elements		
\hat{U}^{en}	Electron-nuclear energy operator		
\hat{U}^{ee}	Electron-electron energy operator		
\hat{U}^{nn}	Nuclear-nuclear energy operator		
$U_{X\sigma}$	Spin-indexed exchange potential		
u_i	FHI-aims radial orbitals		
$u_{n\mathbf{k}}$	Periodic function for Bloch's theorem		
V	<ul style="list-style-type: none"> · Potential (generally) · Volume (generally) 		
v	Alternate notation for potential		
V_{AE}	All-electron pseudopotential		
V_{PP}	General pseudopotential		
V_{US}	Ultrasoft pseudopotential		
\mathcal{V}	Periodic potential		
v_{ext}	External potential		
v_{eff}	Effective potential		
v_H	Hartree potential		
v_{XC}	Exchange-correlation potential		
v_i	Effective volume integral for atom i		
v_{ij}	Dipole-dipole interaction potential		
v_i^{free}	Free-atom effective volume integral for atom i		
$v_{\text{cut}}^{\text{FHI}}$	FHI-aims cutoff potential		
w_i	<ul style="list-style-type: none"> · Hirshfeld atomic-partitioning weight · WTMAD weight 		
w_{int}	Integration weight		

Symbol	Description	Symbol	Description
Mathematical Symbols (Greek)			
α	· Polarizability (Generally) · Gaussian decay exponent	ν_0	Natural frequency of two interacting QHO
α_i	XDM static polarizability for atom i	ξ	MBD mass-weighted displacement
α_i^0	TS static polarizability for atom i	ξ, η	Cartesian components of the Cauchy stress tensor
α^{free}	Free atomic polarizability	ρ	Electron density
α^{TS}	TS frequency-dependent polarizability	ρ_σ	Spin-indexed electron density
α^{SCS}	SCS polarizability	ρ^{free}	Free electron density
α^{rsSCS}	rsSCS polarizability	σ	Cauchy stress tensor
α^{RFA}	Response function approximation polarizability	σ	Spin index
α^{VV}	Vydrov and van Voorhis polarizability	$\sigma_{\alpha\beta}$	Cauchy stress component
α^{rVV}	Ratio-scaled VV polarizability	σ_{ij}	Effective width of the Gaussian charge distribution
$\alpha^{\text{VV}'}$	Cutoff-applied VV polarizability	σ_i	Gaussian charge distribution width of atom i
$\alpha^{\text{rVV}'}$	Cutoff-applied rVV polarizability	τ	Kinetic energy density (general)
α^{H_2}	Dihydrogen polarizability for D3	τ^{KS}	Kohn–Sham kinetic energy density
$\alpha^{\text{A}_m \text{H}_n}$	Hydride polarizability for D3	τ^{W}	Weizsäcker approximation to the kinetic energy density
α^{SCS}	SCS polarizability tensor	τ^{unif}	Uniform electron gas kinetic energy density
β	· Functional-dependent parameter · Range-separation parameter	φ_i	FHI-aims NAO
β_1, γ^A	D4 charge scaling function parameters	$\langle \phi_n $	PAW all-electron partial wavefunction
Γ	· Gamma point · Gamma function	$\langle \tilde{\phi}_n $	PAW pseudo partial wavefunction
$\gamma_{\sigma\sigma}$	Normalization coefficient for same-spin dynamical correlation hole	$\chi_j(\mathbf{r}_i)$	Electron at \mathbf{r}_i in orbital j
$\gamma_{\sigma\sigma'}$	Normalization coefficient for opposite-spin dynamical correlation hole	χ_σ	Reduced density gradient
ΔE_A	Mean excitation energy of particle A	χ_0	Non-interacting response function
Δr_i	Atomic displacement from equilibrium for atom i	χ_λ	Interacting response function at strength λ
δ	Correction term (e.g., $\delta\text{CCSDT}(\mathbf{Q})$)	$\chi[\rho]$	Iso-orbital locator
δ_{ij}	Kronecker delta	Ψ_{vir}	Virtual Kohn–Sham orbitals
ϵ	· Average atomic excitation energy · Fock eigenvalue	Ψ_{occ}	Occupied Kohn–Sham orbitals
ε	Green–Lagrangian strain tensor	Ψ	Total wavefunction (typically N -electron)
$\varepsilon_{\alpha\beta}$	Green–Lagrangian strain component	$\Psi^{(n)}(z)$	Polygamma function
ε_i	Eigenenergy for state i	$\Psi^{(0)}$	Zeroth-order PT wavefunction
ε_{SCF}	SCF convergence threshold	$\Psi^{(1)}$	First-order PT wavefunction
ε_F	Force convergence threshold	$\Psi^{(2)}$	Second-order PT wavefunction
ε_σ	Stress convergence threshold	ψ^{US}	Ultrasoft wavefunction
ε_X	Exchange energy density	ψ^{AE}	All-electron wavefunction
$\varepsilon_X^{\text{LDA}}$	Exchange energy density from the local density approximation	ψ^{NC}	Norm-conserving wavefunction
η	SCAN functional fixed parameter	ψ^{PP}	Pseudowavefunction
λ	· Eigenvalue · Lagrange multiplier · Coupling strength · Hellmann–Feynman continuously-varying parameter	ψ_i	Wavefunction for orbital index i
μ	Reduced mass	ψ^{KS}	Occupied Kohn–Sham orbitals
μ_X	First scalar moment of exchange hole	$\langle \psi_n $	PAW orbital
ν	Grouped QHO constant	$\langle \tilde{\psi}_n $	PAW pseudo orbital
		Ω	Unit-cell volume
		ω	· Angular frequency · Hybrid range-separation parameter
		ω_i	Characteristic excitation frequency for atom i
		ω_i^{SCS}	SCS characteristic excitation frequency for atom i
		ω_i^{rsSCS}	rsSCS characteristic excitation frequency for atom i
		ζ	Minimal basis effective nuclear charge

ACKNOWLEDGEMENTS

I am deeply grateful for the support and guidance I have received from my supervisory committee members, Prof. Jesse Maassen and Prof. Josef Zwanziger; the Johnson Group, past and present; my friends and family; and especially my supervisor and mentor, Prof. Erin Johnson, to whom I owe so much. This thesis could not have been completed without you.

This page will be completed at a later date.

CHAPTER 1

INTRODUCTION

“Thirty-one years ago Dick Feynman told me about his ‘sum over histories’ version of quantum mechanics. ‘The electron does anything it likes,’ he said. ‘It just goes in any direction, at any speed, forward and backward in time, however it likes, and then you add up the amplitudes and it gives you the wave function.’ I said to him ‘You’re crazy.’ But he isn’t.” [1]

~ Prof. Freeman Dyson (1923–2020)

1.1 DISPERSION IN DENSITY-FUNCTIONAL THEORY

When researching new chemical systems, it is important to understand the interactions present within a molecule or material, and also how the system will interact with its surrounding environment. The groundwork for this problem was set back in the 1920s with both correlated-wavefunction methods [2–5], and Hartree–Fock theory [6–11]. Unfortunately, a correlated-wavefunction approach can only work for small molecules, while Hartree–Fock modelling is not accurate enough for use in determining the chemical or physical properties of large systems.

In the 1960s, Hohenberg, Kohn, and Sham greatly simplified the N -electron problem by writing the total energy as a functional of the electron density [12, 13]. This formulation permitted the construction of an effective potential through an initial guess of the electron density, which may be solved for iteratively and self-consistently. This iterative process is known as the self-consistent field (SCF) procedure, and will be discussed further in Section 2.1.

This groundwork has become the foundation for modern-day density-functional theory (DFT), which allows first-principles computational modelling of the electronic structure of large-scale quantum systems by considering only the averaged electron distribution [14, 15]. DFT is widely used across chemistry, physics, and materials science [16], and we owe many advancements in drug-synthesis [17, 18], catalysts [19, 20], and new technologies [21] to improvements in this area of science.

Van der Waals interactions [22], named after Dutch physicist Johannes Diderik van der Waals (1837–1923), describe all intermolecular interactions in quantum systems. Prominent examples of van der Waals interactions include London dispersion interactions [23, 24], Debye induced-dipole interactions [25, 26], and Keesom dipole-dipole interactions [27–30]. London dispersion interactions, named after German physicist Fritz London (1900–1954), are weak, attractive, intermolecular forces that arise between temporary dipoles of neighbouring atoms. These (typically) weak intermolecular forces occur in most quantum systems and become stronger due to factors such as increased intermolecular contact area or polarizability. While weaker than ionic, covalent, or hydrogen bonds, dispersion interactions determine important system properties such as adhesion [31], friction [32], surface adsorption [33], phase-change conditions [34], stability of supramolecular complexes [35], packing in molecular crystals [36], and the shapes of biomolecules [37].

Standard DFT methods [12–15] do not account for London dispersion forces, so a correction must be added. Unfortunately, modelling these forces elegantly has proved to be quite challenging [38]. While there are many choices of dispersion correction, they can generally be divided into two classes. The first class are characterized by a post-SCF additive correction to the base DFT energy, $E_{\text{DFT}} = E_{\text{base}} + E_{\text{disp}}$. These corrections are typically based on the second-order perturbation theory of dispersion and examples include the Grimme-D series [39–43], TS [44, 45], MBD (and its variants) [45–52], and the XDM [53–57] dispersion corrections. The second class are nonlocal density functionals (NLDFs), which contain explicit non-local terms in the exchange-correlation functional, requiring additional computation throughout the SCF procedure [58]. Popular NLDFs include the vDW-DF [59–61], vDW-DF2 [62], VV10 [63], and rVV10 [64] functionals. This thesis will focus exclusively on the first type.

1.2 THE SECOND-ORDER PERTURBATION THEORY OF DISPERSION

Using second-order perturbation theory, it is possible to derive the interaction energy of London dispersion forces for two atoms with internuclear separation R , and show this energy is proportional to $R^{-6} + \mathcal{O}(R^{-8})$. The multipole expansion of this dispersion energy has the form

$$E_{\text{disp}} = -\frac{C_6}{R^6} - \frac{C_8}{R^8} - \frac{C_{10}}{R^{10}} - \dots, \quad (1.2.1)$$

where the C_6 term accounts for dipole-dipole interactions, the C_8 coefficient accounts for dipole-quadrupole interactions, and the C_{10} coefficient accounts for quadrupole-quadrupole and dipole-octupole interactions.¹ This section will briefly derive the dispersion energy contribution for an interacting hydrogen dimer system [66–69]; for the full derivation of Eqs. (1.2.2) to (1.2.5), see Appendix A.1.

Consider two interacting hydrogen atoms with internuclear separation $R \gg a_0$, where a_0 is the Bohr radius. Let (x_1, y_1, z_1) and (x_2, y_2, z_2) represent the coordinates of electrons 1 and 2 with respect to nuclei A and B respectively. The interaction Hamiltonian for the H₂ dimer is

$$\hat{H}_I = \frac{e^2}{4\pi\epsilon_0} \left[-\frac{1}{r_{1B}} - \frac{1}{r_{2A}} + \frac{1}{r_{12}} + \frac{1}{R} \right]. \quad (1.2.2)$$

It is straightforward to expand the $1/r$ terms via their position vectors, and then apply a binomial expansion to Eq. (1.2.2) to arrive at the following approximate interaction Hamiltonian

$$\hat{H}_I \approx \frac{e^2}{4\pi\epsilon_0 R^3} [(x_1 x_2 + y_1 y_2 - 2z_1 z_2)], \quad (1.2.3)$$

where the $\mathcal{O}(R^{-4})$ and lower terms have been neglected. This approximate Hamiltonian no longer involves the $1/r_{12}$ term, greatly reducing the complexity of the problem.

To calculate the interaction energy, we need to consider the ground-state wavefunction, where $\psi = 1s_A(1) \cdot 1s_B(2) = |1, 1\rangle$ is written in terms of the hydrogen 1s

¹We note that there is no consensus in the literature on the sign of the C_n dispersion coefficients [65]. Throughout this work we will write the C_n dispersion coefficients as positive quantities and state the sign explicitly.

orbitals using Dirac notation [70]. Upon applying first-order perturbation theory to the interaction Hamiltonian from Eq. (1.2.3), it is shown that the first-order energy is $E' = 0$ due to the system symmetry. Thus, this problem requires second-order perturbation theory where the ground-state's second-order energy becomes

$$E'' = \sum_{m \neq 1} \sum_{n \neq 1} \frac{\left| \langle 1, 1 | \hat{H}_I | m, n \rangle \right|^2}{E_{1,1}^{\text{H}_2} - E_{m,n}^{\text{H}_2}}. \quad (1.2.4)$$

The zeroth-order energy for the hydrogen dimer is $E_{m,n}^{\text{H}_2} = -(1/m^2 + 1/n^2)/2$ in Hartree atomic units (a.u.), so the second-order energy may be written as

$$E'' = - \sum_{m \neq 1} \sum_{n \neq 1} \frac{2m^2 n^2}{2m^2 n^2 - m^2 - n^2} \left| \left\langle 1, 1 \left| \frac{e^2}{4\pi\epsilon_0 R^3} (x_1 x_2 + y_1 y_2 - 2z_1 z_2) \right| m, n \right\rangle \right|^2. \quad (1.2.5)$$

Appendix A.2 shows how to use Eq. (1.2.5) to arrive at a highly accurate approximation of the interaction energy. The first numerical evaluation of Eq. (1.2.5) was performed in 1930 by Eisenschitz and London [71], who obtained a value of $E'' = -C_6/R^6 = -6.47/R^6$, where C_6 is the dispersion coefficient for dipole-dipole interactions from Eq. (1.2.1). This was later refined by Slater and Kirkwood in 1931 [72], and again by Pauling and Beach in 1935 [73], both of whom obtained a value of ca. $E'' = -6.499/R^6$ Hartree. The accepted value of the hydrogen C_6 dispersion coefficient in the current scientific era is -6.49 ± 0.02 a.u. [44, 74–76].

The closure (or Unsöld) approximation [77] applied to Eq. (1.2.4) gives an approximate second-order energy of the form

$$E'' \approx -\frac{1}{\Delta E_A + \Delta E_B} \left\langle 1, 1 \left| \hat{H}_I^2 \right| 1, 1 \right\rangle, \quad (1.2.6)$$

where ΔE is the mean excitation energy for either particle. It is desirable to write Eq. (1.2.6) in terms of the hydrogen ionization energy and polarizability. Consider a perturbation in the form of a field oriented along the z -direction such that $\hat{H}' = \mathcal{E}e\hat{z}$. The first-order correction will be zero, but the second-order correction will have the form

$$E'' \approx \frac{1}{\Delta E} \left\langle 1 \left| \hat{H}_I^2 \right| 1 \right\rangle = \frac{\mathcal{E}^2 e^2}{3\Delta E} \langle 1 | r^2 | 1 \rangle. \quad (1.2.7)$$

As first shown in Ref. [78], we may take the second derivative of Eq. (1.2.7) with respect to the field to obtain the polarizability

$$\alpha = \frac{d^2 E''}{d\mathcal{E}^2} \approx \frac{2}{3} \frac{e^2}{\Delta E} \langle 1 | r^2 | 1 \rangle , \quad (1.2.8)$$

where $\langle 1 | r^2 | 1 \rangle = 3a_0^2$ for the hydrogen 1s orbital. Finally, substituting Eq. (1.2.3) and Eq. (1.2.8) into Eq. (1.2.6) for both atoms A and B results in the desired form of the second-order energy,

$$E'' = -\frac{1}{R^6} \frac{\alpha_A \alpha_B \langle r^2 \rangle_A \langle r^2 \rangle_B}{\alpha_A \langle r^2 \rangle_B + \alpha_B \langle r^2 \rangle_A} , \quad (1.2.9)$$

which agrees with the literature [57]. If we instead write our expression in terms of the hydrogen ionization energy I (assuming $\Delta E \approx I \approx 0.5$ a.u.), we arrive at the London formula for dispersion between two non-polar atoms,

$$E'' \approx -\frac{3}{2} \frac{I_A I_B}{I_A + I_B} \frac{\alpha_A \alpha_B}{(4\pi\epsilon_0)^2 R^6} . \quad (1.2.10)$$

We note that, for the hydrogen dimer, $\alpha_A = \alpha_B \approx 4.5$ a.u. Thus, this method predicts a second-order energy of $E'' \approx -7.6/R^6$, which is about 17% off of the numerically determined result from Eq. (1.2.5). Eqs. (1.2.9) and (1.2.10) give insight into how highly polarizable atoms will exhibit strong dispersion interactions.

The London formula for dispersion, Eq. (1.2.10), only includes the first non-zero term in the expansion of the interaction Hamiltonian in Eq. (1.2.3). Continuing the expansion to higher powers of $1/R$ would permit the derivation of the C_8 and C_{10} dispersion coefficients as mentioned in Eq. (1.2.1). Using an elaborate variational method, Pauling and Beach [73] derived the first three non-zero terms of the hydrogen multipolar dispersion energy to be

$$E'' \approx -\frac{6.49903}{R^6} - \frac{124.399}{R^8} - \frac{1135.21}{R^{10}} . \quad (1.2.11)$$

Later, using a similar methodology used to arrive at Eq. (1.2.6), Margenau [79] derived an approximate dispersion energy between two hydrogen of the form

$$E'' \approx -\frac{6}{R^6} - \frac{135}{R^8} - \frac{1416}{R^{10}} . \quad (1.2.12)$$

More recent accepted values with error bounds are given by Tang, Norbeck, and

Certain [76] as

$$E'' \approx -\frac{6.49 \pm 0.02}{R^6} - \frac{124.2 \pm 0.4}{R^8} - \frac{3293 \pm 11}{R^{10}}. \quad (1.2.13)$$

Higher-order dispersion coefficients can be derived by including additional terms in the binomial series expansion used to derive Eq. (1.2.3); see Appendix A.1. These higher-order terms account for additional van der Waals contributions, such as quadrupole-octupole (C_{12}) or octupole-octupole (C_{14}) interactions, although, these are not typically relevant for most systems of interest [80, 81].

1.3 EARLY EMPIRICAL DISPERSION CORRECTIONS

Using dispersion corrections in electronic-structure theory is not novel by any means. These corrections have a long history in the community, dating back to the early work of Cohen and Pack in the mid 1970s [82]. The HF-D method introduced by Scoles *et al.* in 1975 [83, 84] was probably the first empirically-corrected dispersion correction. Building on the Hartree–Fock model, the authors used C_6 , C_8 , and C_{10} homoatomic values (or mixed dispersion coefficients using Stwalley’s method [85] when appropriate) alongside Smith’s combination rule [86] to create an empirical dispersion correction to the Hartree–Fock energy of the form:

$$V(R) = \Delta E_{\text{HF}} - \left[\frac{C_6}{R^6} + \frac{C_8}{R^8} + \frac{C_{10}}{R^{10}} \right] f^{\text{HF-D}}(R). \quad (1.3.1)$$

Here, ΔE_{HF} is the HF repulsion, and $f^{\text{HF-D}}(R)$ is an empirically-determined exponential damping function given by

$$f^{\text{HF-D}}(R) = \begin{cases} e^{-(1.28 \frac{R_m}{R} - 1)^2} & \text{for } R < 1.28R_m \\ 1 & \text{for } R \geq 1.28R_m \end{cases}, \quad (1.3.2)$$

where R_m is the position of the potential minimum. This dispersion correction was then matched to available SCF data and experimental results for lighter noble gases and their mixtures. For corrections derived from 2nd-order perturbation theory, it is clear that the dispersion energy will diverge at small internuclear separations due to the R^n in the denominator. Clearly, this is unphysical, and thus damping functions such as those in Eq. (1.3.2) are included. Damping functions will be discussed in more detail in Section 2.5

Another empirical dispersion correction came in the form of Wu and Yang's DFT-D [87], where they added an additional attractive energy,

$$E_{\text{vdW}} = -\frac{C_6 f^{\text{d}}(R)}{R^6}, \quad (1.3.3)$$

to the SCF energy. $f^{\text{d}}(R)$ is a damping function has one of two forms. The first is a modified form of Eq. (1.3.2) as proposed by Mooij *et al.* [88],

$$f^{\text{M}}(R) = \left(1 - e^{-c\left(\frac{R}{R_m}\right)^3}\right)^2, \quad (1.3.4)$$

which makes the second derivative of $f^{\text{d}}(R)$ continuous. Rather than setting $c = 7.19$ as used by [88], a value of 3.54 was used to closer emulate the model used in Ref. [84]. The second damping function is a Fermi-type damping function [89, 90]. The exponential constant's value was chosen to be 23.0 so that $\lim_{R \rightarrow 1.2R_m} f^{\text{d}}(R) = 0.99$.

1.4 MODERN DISPERSION CORRECTIONS

Dispersion-corrected density-functional theory has become a very active research topic, generating tens of thousands of citations over the last two decades [65]. Many dispersion models compute the dispersion energy as a sum of pairwise interactions between atoms. In Section 1.2, we derived this interaction using second-order perturbation theory as

$$E_{\text{disp}}^{(2)} = -\sum_i \sum_{j < i} \sum_{n=6,8,10\dots} \frac{C_{n,ij} f_n^{\text{d}}(R_{ij})}{R_{ij}^n}, \quad (1.4.1)$$

which is summed over all pairs of atoms i and j , and $f_n^{\text{d}}(R_{ij})$ is a damping function, such as those used by Scoles and Mooij in Section 1.3, to prevent the divergence of the dispersion energy as $R \rightarrow 0$. Modern damping functions, such as those of Wu–Yang, Chai and Head-Gordon, and Becke–Johnson are discussed in Section 2.5. It has been shown that the inclusion of C_{12} (and higher) terms yields only modest improvements in the interaction energy and may introduce numerical instabilities [91]. As such, these higher-order terms are universally omitted in practice. The dispersion contribution is then added to the energy determined by the SCF calculation of the base DFT functional.

In 2004, Grimme introduced the DFT-D method [39] to model dispersion in small molecular systems. An updated version was released in 2006 that computed dispersion

coefficients based on geometric means rather than harmonic means, improving its accuracy. At the same time, the number of atomic species supported was increased, broadening its use. This model is known today as DFT-D2 [40]. The widely-used DFT-D3 dispersion model [41, 92] followed in 2010, which uses a recurrence relation to compute higher-order dispersion coefficients while also optionally including the three-body dispersion term. Most recently, the DFT-D4 model [42] extended this framework by incorporating atomic partial charges into the calculation of the atom-in-molecule polarizabilities. The Grimme-D series of dispersion coefficients will be discussed in Section 2.5.1.

In 2009, Tkatchenko and Scheffler presented a post-SCF pairwise dispersion-correction model that was density dependent, known today as the TS model [44]. Considering only the C_6 contribution, the model calculates the dispersion energy via a sum over all electron pairs. The heteroatomic dispersion coefficients are computed from their homoatomic values using the Slater–Kirkwood formula [72], while the homoatomic coefficients are calculated via the effective proportional volume of an atom in the molecule, determined by a Hirshfeld partitioning of the electron density [93, 94]. The TS model and its variant, TS@SCS [48], will be discussed in Section 2.5.2.

The Many-Body Dispersion (MBD) model [45] was introduced by Tkatchenko *et al.* in 2012 as an extension of the TS model, over which it demonstrates significant improvement [46–48]. Through the use of self-consistent screening (SCS) formalism [95–97], the MBD model solves for the atomic and molecular polarizability tensors as well as the characteristic excitation frequencies. Through this process, these quantities contain both short- and long-range electrostatic screening information. Unlike Eq. (1.4.1), the dispersion energy is then calculated as the difference between zero-point energies of coupled and uncoupled quantum harmonic oscillators. The MBD model and its range-separated and (so-called) non-local variants, MBD@rsSCS [46, 47] and MBD-NL [52], will be discussed in Section 2.5.2.

Finally, the exchange-hole dipole moment (XDM) model [55, 57] stands out as one of the most accurate corrections, while also exhibiting stability, low empiricism, and low computational cost [98]. This model is density-dependent like the TS [44] and MBD [45] models, except it derives the dispersion energy through use of the exchange-hole dipole moment. This dispersion model has demonstrated excellent performance for molecular crystals [99–102], inorganic materials [103–108], and crystal structure prediction (CSP) [109, 110], and will be discussed in significant detail in Section 2.5.3.

XDM has been implemented in several codes: Quantum ESPRESSO [56, 99, 111],

CASTEP [112], Q-Chem [113, 114], NWChem [115, 116], SIESTA [117, 118], and recently FHI-aims [119–121]. Also, work is ongoing to implement XDM in AMS (ADF) [122] by A. F. Rumson and E. R. Johnson. Further, XDM can be applied *ad hoc* for any quantum-chemical code that writes `.molden`, `.wfn`, or `.wfx` files via `postg` [123], maintained by Alberto Otero-de-la-Roza and recently updated [124] to incorporate new features introduced in this thesis. Dozens of codes support the `.molden` format [125], with popular examples including Gaussian [126], ORCA [127], TURBOMOL [128], Psi4 [129], PySCF [130], Q-Chem [113, 114], NWChem [115, 116], XTB [131], and AMS (ADF) [122]. Unfortunately, many codes write in slightly different dialects of the `.molden` format; as such, users should verify that this input file type is handled correctly.

1.5 THESIS OVERVIEW

The underlying theory relevant to this work is discussed in Chapter 2. It begins with an in-depth discussion of DFT and its applications, followed by descriptions of the Hartree–Fock method, density-functional approximations (DFAs) to the exchange-correlation energy, and wavefunction methods used as reference data. Solid-state DFT is introduced alongside discussions of planewaves, pseudopotentials, projector-augmented waves (PAW), numerical atom-centred orbitals (NAOs), and basis sets. The concept of geometry optimization is explained, along with the related concepts of forces, stresses, and strains. A detailed comparison of post-SCF dispersion corrections follows, focusing on their theoretical foundations and relevance to this work. Finally, the chapter concludes with an excerpt from a recent article addressing delocalization error, the largest unresolved challenge in modern DFT.

The aim of this thesis is to demonstrate that the XDM model captures dispersion physics accurately, while also exhibiting best-in-class performance with minimal empiricism compared to other dispersion corrections. After establishing these results, we seek to further improve XDM’s physical description by supplementing its exchange-hole dipole moment with contributions from same- and opposite-spin correlation functionals. We also examine a new one-parameter damping function recently proposed by Becke. To this end, the remainder of the thesis is structured as follows:

Chapter 3 discusses the requirements for an accurate dispersion-corrected density functional. This chapter focuses on functional development and the need for it to be guided by physics-based principles. It also highlights how, while highly empirical

functionals can sometimes yield accurate results, they may lead to unphysical or unpredictable behaviour in surprising ways. We detail the essential properties that dispersion-corrected functionals must exhibit for optimal performance.

Chapter 4 studies the highly accurate XDM and MBD dispersion methods in great detail. Despite their similarly strong performance on several molecular and solid-state benchmarks, these two corrections take very different approaches to modelling van der Waals forces. MBD is based on a model of interacting harmonic oscillators, while XDM captures changes in chemical environment through the self-consistent electron density and its derivatives. Further, XDM has been shown to recover the exact asymptotic interaction between harmonic oscillators from perturbation theory [80].² This raises the question: Does the XDM dispersion model accurately capture many-body effects? To address this, model systems of variationally-optimized quantum harmonic oscillators are constructed to test how each correction’s C_6 dispersion coefficients respond to changing chemical environments. Similarly, chains of noble gas atoms are also studied for comparison. Finally, these methods were tested on both molecular and solid-state benchmarks, with key examples studied in depth. This chapter demonstrates how XDM accurately captures dispersion physics.

Chapter 5 presents the first-ever study of the XDM, Grimme-D, and MBD families of dispersion corrections using the same code and basis set. The comparison was conducted on the new DES15K benchmark, containing nearly 15,000 molecular dimers spanning compressed and expanded geometries. The results demonstrate XDM’s best-in-class performance on non-covalent interactions relative to these other leading post-SCF dispersion corrections.

Chapter 6 unveils the new XDM variant, XCDM, which supplements XDM’s exchange-hole dipole moment with contributions from same- and opposite-spin dynamical correlation functionals, thereby improving the description of the physics captured by the model. Further, we study the new, one-parameter Z-damping function recently proposed by Becke, reducing the number of empirically fitted parameters used in the XDM and XCDM models from two to one. Testing of these new variants is performed on the comprehensive benchmark of general main-group thermochemistry, kinetics, and non-covalent interactions (GMTKN55). Comparisons are made to the Grimme-D and MBD family of dispersion corrections, showing excellent performance with our minimally empirical techniques. Notably, this marks the first time

²For the derivation of this quantity, see Appendix A.3 and relevant literature [68, 69].

that XDM or MBD have been tested on GMTKN55. Further, study into the solid-state reveals that these new variants may be of particular interest for crystal-structure prediction and polymorph ranking.

The thesis concludes in Chapter 7 with proposed future developments of the XDM methods and final remarks.

CHAPTER 2

THEORY

“What I cannot create, I do not understand. Know how to solve every problem that has been solved.” [132]
 ~ Prof. Richard Feynman (1918–1988)

2.1 DENSITY-FUNCTIONAL THEORY

Density-functional theory (DFT) has proven to be one of the most accurate ways of calculating the electronic structure of molecules and solids while maintaining sufficiently-low computational requirements to model systems of interest. It comes as no surprise that, over the last 30 years, DFT has become the technique of choice within electronic-structure theory.

In the 1960s, Hohenberg, Kohn, and Sham [12, 13] greatly simplified the N -electron problem by writing the total energy,

$$E[\rho] = T_{\text{KS}}[\rho] + \int v_{\text{ext}}\rho(\mathbf{r})d\mathbf{r} + E_{\text{H}}[\rho] + E_{\text{XC}}[\rho], \quad (2.1.1)$$

as a functional of the electron density¹,

$$\rho(\mathbf{r}) = \sum_{i=1}^N |\psi_i^{\text{KS}}(\mathbf{r})|^2, \quad (2.1.2)$$

for N electrons occupying Kohn–Sham (KS) orbitals $\psi_i^{\text{KS}}(\mathbf{r})$. The remaining terms

¹The electron density, $\rho(\mathbf{r})$, is sometimes denoted as $n(\mathbf{r})$, especially in the solid-state community.

in Eq. (2.1.1) are the Kohn–Sham kinetic energy, written in terms of KS orbitals as

$$T_{\text{KS}}[\rho] = \sum_{i=1}^N \left\langle \psi_i^{\text{KS}}(\mathbf{r}) \left| -\frac{\hbar^2}{2m} \nabla^2 \right| \psi_i^{\text{KS}}(\mathbf{r}) \right\rangle, \quad (2.1.3)$$

the Hartree energy²,

$$E_{\text{H}}[\rho] = \frac{e^2}{2} \iint \frac{\rho(\mathbf{r})\rho(\mathbf{r}')}{|\mathbf{r} - \mathbf{r}'|} d\mathbf{r} d\mathbf{r}', \quad (2.1.4)$$

and the exchange-correlation energy $E_{\text{XC}}[\rho]$. $v_{\text{ext}}(\mathbf{r})$ is the external potential that is acting on the system and can be used to determine the effective Kohn–Sham potential,

$$v_{\text{eff}}(\mathbf{r}) = v_{\text{ext}}(\mathbf{r}) + v_{\text{H}}[\rho] + v_{\text{XC}}[\rho], \quad (2.1.5)$$

where

$$v_{\text{H}}[\rho] = e^2 \int \frac{\rho(\mathbf{r}')}{|\mathbf{r} - \mathbf{r}'|} d\mathbf{r}', \quad (2.1.6)$$

and $v_{\text{XC}}[\rho] = \frac{\delta E_{\text{XC}}[\rho]}{\delta \rho(\mathbf{r})}$ is the functional derivative of the exchange-correlation energy with respect to the electron density. After determining the form of the effective Kohn–Sham potential, the Kohn–Sham equation,

$$\left(-\frac{\hbar^2}{2m} \nabla^2 + v_{\text{eff}}(\mathbf{r}) \right) \psi_i^{\text{KS}}(\mathbf{r}) = \varepsilon_i \psi_i^{\text{KS}}(\mathbf{r}), \quad (2.1.7)$$

may be solved for its eigenenergies, ε_i , and corresponding Kohn–Sham orbital eigenvectors, $\psi_i^{\text{KS}}(\mathbf{r})$.

In modern electronic-structure codes, the Kohn–Sham equations are solved in an iterative process, which starts by choosing a suitable form of the exchange-correlation functional in Eq. (2.1.1) and initially guessing the electron density $\rho(\mathbf{r})$ for the system to calculate the effective potential. The Kohn–Sham equation is then solved for the Kohn–Sham orbitals, which are used to calculate a new electron density. If the energy (or other desired quantity) resulting from this new electron density is within the specified convergence criteria, we say the solution is converged; however, if it is not within the convergence criteria, the newly-calculated electron density is then used as a new initial guess and the procedure starts again. This iterative process is called the self-consistent field (SCF) loop and is the basis of all modern DFT codes.

Density-functional theory is functionally exact in its formulation. The errors in

²The Hartree energy $E_H[\rho]$, is sometimes referred to as the Coulombic energy, denoted as $J[\rho]$.

modern DFT come not from the theory itself, but from density-functional approximations (DFA) [15, 133]. Specifically, these approximations are made to the exchange-correlation functional $E_{XC}[\rho]$, which has no known exact form.

2.2 PERDEW'S LADDER OF DENSITY FUNCTIONAL APPROXIMATIONS

The exchange-correlation energy is the sum of the exchange energy and the correlation energy, $E_{XC} = E_X + E_C$. It has been shown that the atomic exchange energy is one to two orders of magnitude greater than the correlation energy [15, 134, 135], thus the remainder of the section shall focus on the form of exchange rather than correlation functionals.

The quest to determine an exact energy functional is considered to be one of the great outstanding problems of modern-day DFT [136–140]. Such a functional is considered to be perfectly chemically accurate at the top of Perdew's ladder of density functional approximations (DFAs) [133, 141], see Figure 2.1. Until such a time that an exact energy functional is determined, approximate forms of the exchange-correlation functional must be used.

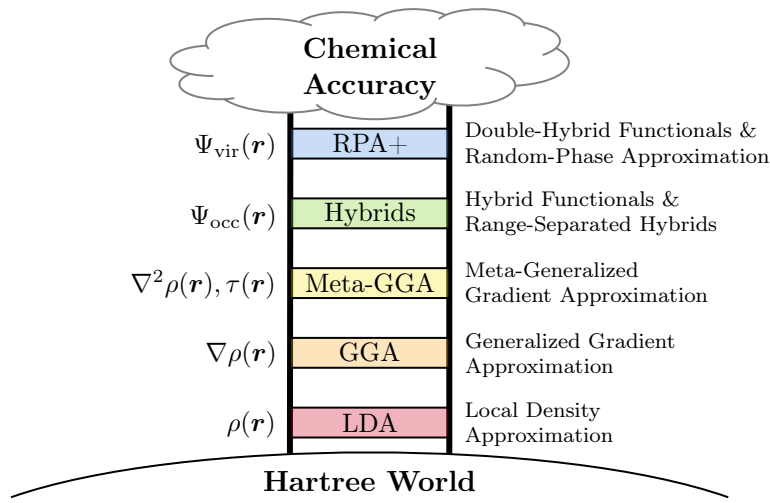


Figure 2.1: Perdew's ladder of density functional approximations (DFAs). Beneath the ladder are the Hartree and Hartree–Fock approximations. Above the ladder is the perfect chemical accuracy obtained using an exact functional, or at the very least, more accurate wavefunction methods. In principle, ascending the ladder leads to higher chemical accuracy at the cost of increased computational resource requirements [141].

2.2.1 THE LADDER'S BASE: HARTREE–FOCK

At the foot of Perdew's ladder is the Hartree–Fock method [6–11]. Consider a general N -electron chemical system. The Hamiltonian (in atomic units) is represented by

$$\hat{H} = -\frac{1}{2} \sum_i \nabla_i^2 - \sum_i \sum_A \frac{Z_A}{r_{iA}} + \frac{1}{2} \sum_{i \neq j} \frac{1}{r_{ij}} \quad (2.2.1)$$

where Z_A is the nuclear charge of nucleus A , r_{iA} is the electron-nuclear distance, and r_{ij} is the interelectron distance. It is well known that the Schrödinger wavefunction must be antisymmetric in accordance with the Pauli exclusion principle [142], the interchange of any two electrons will cause the total wavefunction describing them to change sign: $\Psi(\mathbf{r}_1, \mathbf{r}_2) = -\Psi(\mathbf{r}_2, \mathbf{r}_1)$. The simplest N -electron solution to satisfy this is one that takes the form of a Slater determinant [143],

$$\Psi(\mathbf{r}_1, \mathbf{r}_2, \dots, \mathbf{r}_N) = \frac{1}{N!} \begin{vmatrix} \chi_1(\mathbf{r}_1) & \chi_2(\mathbf{r}_1) & \cdots & \chi_N(\mathbf{r}_1) \\ \chi_1(\mathbf{r}_2) & \chi_2(\mathbf{r}_2) & \cdots & \chi_N(\mathbf{r}_2) \\ \vdots & \vdots & \ddots & \vdots \\ \chi_1(\mathbf{r}_N) & \chi_2(\mathbf{r}_N) & \cdots & \chi_N(\mathbf{r}_N) \end{vmatrix} = |\chi_1, \chi_2, \dots, \chi_N\rangle, \quad (2.2.2)$$

for N electrons occupying N orbitals. Indeed, we see that if any two same-spin electrons occupy the same orbital, the wavefunction vanishes. The Hartree–Fock energy is then given by

$$E^{\text{HF}} = \langle \Psi | \hat{H} | \Psi \rangle. \quad (2.2.3)$$

The key flaw with Hartree–Fock theory is the assumption that a general chemical system can be approximated by a single Slater determinant. This assumption neglects electron correlation, despite exchange being modelled exactly within this framework. For this reason, the Hartree–Fock exchange energy is sometimes referred to as “exact exchange,” and these terms will be used interchangeably throughout this thesis. Through the inclusion of linear combinations of Slater determinants, the energetic effects of virtual (unoccupied) orbitals can be included to capture correlation. This is the premise of the configuration interaction (CI) method and, while it promises incredible accuracy, it also comes with prohibitive computational cost [144]. Unfortunately, due to the neglect of correlation from the Hartree–Fock method, it is not able to compete with even the simplest density-functional approximations to the exchange-correlation energy [141].

2.2.2 RUNG 1: THE LOCAL-DENSITY APPROXIMATION

The first rung of Perdew's Ladder is the local-density approximation (LDA) of Kohn and Sham [13]. It assumes that the contribution to the exchange-correlation energy from each point in the system can be approximated by the exchange-correlation energy contribution from a uniform electron gas with the same density [145]. Specifically, the exchange functional is a function of only electron density with the form

$$E_X^{\text{LDA}}[\rho] = -\frac{3}{2} \left(\frac{3}{\pi} \right)^{1/3} \int \rho^{4/3}(\mathbf{r}) d\mathbf{r}. \quad (2.2.4)$$

The local spin-density approximation (LSDA) is a generalization of the LDA to apply to spin-polarized systems, and the exchange energy is given by

$$E_X^{\text{LSDA}}[\rho_\sigma] = -\frac{3}{2} \left(\frac{3}{4\pi} \right)^{1/3} \sum_\sigma \int \rho_\sigma^{4/3}(\mathbf{r}) d\mathbf{r} \quad (2.2.5)$$

for a spin-dependent density $\rho_\sigma(\mathbf{r})$. The LSDA correlation energy has no closed-form expression, so it is obtained from quantum Monte Carlo simulations of the uniform electron gas [146]. Despite its simplicity, the LSDA model has surprisingly showed to be a decent approximation for solids. Unfortunately, it categorically underestimates exchange energies while overestimating correlation and bond energies [15, 141].

2.2.3 RUNG 2: THE GENERALIZED-GRADIENT APPROXIMATION

The second rung of Perdew's Ladder is the generalized-gradient approximation (GGA). GGAs model systems more physically than the LDA due to incorporating both the electron density (ρ) and its gradient ($\nabla\rho$). There are a number of GGAs that exist in the literature such as the B86b [147], PBE³ [149, 150], PW86 [151, 152], and B88 [134] exchange functionals. The general form of a GGA functional is

$$E_X^{\text{GGA}}[\rho_\sigma] = - \sum_\sigma \int c_x \rho_\sigma^{4/3} F(\chi_\sigma) d\mathbf{r} \quad (2.2.6)$$

where c_x is a functional-dependent constant, and

$$\chi_\sigma = \frac{|\nabla \rho_\sigma|}{\rho_\sigma^{4/3}} \quad (2.2.7)$$

³The PBE functional has the same form as the B86a functional, which was proposed 10 years earlier with slight differences in β and γ [148].

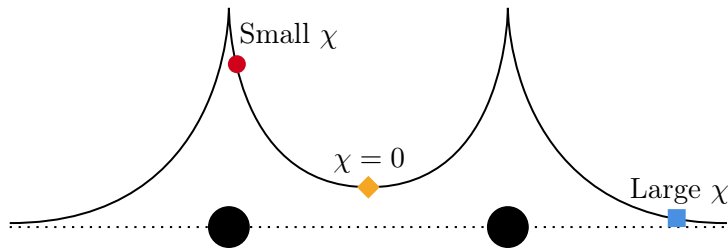


Figure 2.2: Sketch of the electron density for a diatomic molecule (nuclei represented by black circles) with points of interest denoted by coloured points along the curve. At the red circle, the reduced density gradient, χ , is small because the high $\rho^{4/3}$ cancels the high $\nabla\rho$. At the orange diamond, $\chi = 0$ because $\nabla\rho = 0$. At the blue square and far from the nuclei, χ is large because of the dominating $\rho^{4/3}$ in the denominator.

is known as the reduced, or dimensionless, density gradient (sometimes instead denoted as s). $F(\chi_\sigma)$ is the enhancement factor, which is the key difference between each GGA functional. The aforementioned GGA functionals have enhancement factors given by

$$F^{\text{B86b}}(\chi_\sigma) = 1 + \frac{\beta}{c_x} \frac{\chi_\sigma^2}{(1 + \gamma \chi_\sigma^2)^{4/5}}, \quad (2.2.8)$$

$$F^{\text{PBE}}(\chi_\sigma) = 1 + \frac{\beta}{c_x} \frac{\chi_\sigma^2}{1 + \gamma \chi_\sigma^2}, \quad (2.2.9)$$

$$F^{\text{PW86}}(\chi_\sigma) = (1 + a \chi_\sigma^2 + b \chi_\sigma^4 + c \chi_\sigma^6)^{1/15}, \quad (2.2.10)$$

$$F^{\text{B88}}(\chi_\sigma) = 1 + \frac{\beta \chi_\sigma^2}{1 + 6\beta \chi_\sigma \operatorname{arcsinh}(\chi_\sigma)}, \quad (2.2.11)$$

where the values of the functional-dependent parameters— c_x , β , and γ for B86b and PBE; a , b , and c for PW86; and β for B88—may be found in their respective sources.

When selecting a GGA functional, a proper understanding of the reduced density gradient and the enhancement factor are essential. A brief description of the enhancement factor is provided in Figure 2.2. For an accurate description of non-bonded repulsion, the behaviour of the enhancement factor in the limit of large reduced density-gradient should be [153–155]

$$\lim_{\chi_\sigma \rightarrow \infty} F(\chi_\sigma) = \chi_\sigma^{2/5}. \quad (2.2.12)$$

Clearly, from Figure 2.2, a correct description of large reduced density-gradient and its limit plays an important role for long-range effects. Figure 2.3 shows the plots for

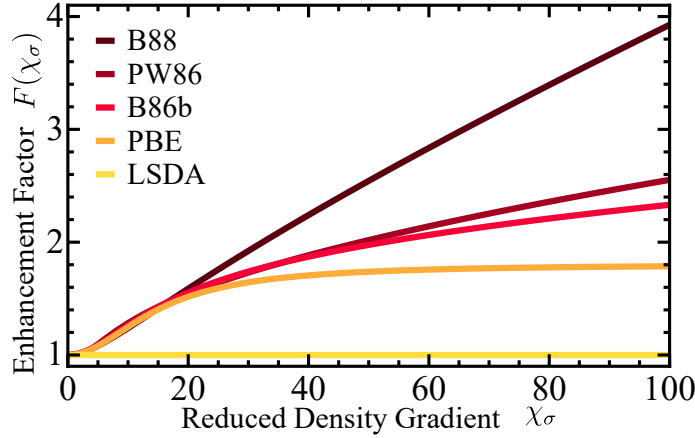


Figure 2.3: The large reduced density gradient behaviour of the LSDA [13] and popular GGA exchange functionals, including the B86b [147], PBE [149, 150], PW86 [151, 152], and the B88 [134] functionals.

each aforementioned enhancement factors from Eqs. (2.2.8) to (2.2.11) as a function of reduced density gradient. Out of the set of considered functionals, only B86b and PW86 have the correct large reduced density gradient limit of $\chi_\sigma^{2/5}$, and only these functionals would correctly predict long-range exchange-repulsion contributions. Further, we can predict that B88 would overestimate these contributions, while LSDA and PBE would underestimate them. Typically, both the B86b and PBE exchange functionals use the PBE correlation functional; the use of the B86b exchange with PBE correlation is known as B86bPBE, and this is the GGA functional of choice to use with the XDM dispersion correction due to its low cost, correct large-gradient limit, and dispersionless behaviour [81].

2.2.4 RUNG 3: META-GENERALIZED GRADIENT APPROXIMATIONS

The third rung on Perdew's Ladder is meta-generalized gradient approximations (meta-GGAs or mGGAs). In addition to the electron density (ρ) and gradient density ($\nabla\rho$), they also use the Laplacian ($\nabla^2\rho$) and/or the kinetic energy density (τ) to describe the system. An example of a meta-GGA is the Becke–Roussel (BR) exchange hole [16] (as used by the XDM dispersion model [55–57, 156]), this will be further discussed in Section 2.5.3. Meta-GGA functionals typically have additional tunable empirical parameters compared to GGA functionals. As such, common issues that are encountered are the effects of overfitting and hampered transferability to types of systems to which they were not fitted. For more discussion on this, see Chapter 3. There is also a recently-developed class of functionals by Janesko and collaborators

termed “Rung 3.5”. These functionals capture non-local information without using exact exchange via the semilocal density matrix [157–159]. Despite the excellent performance of certain meta-GGAs and meta-GGA-based hybrid functionals, some researchers believe that the development of recent highly parametrized functionals is straying from the path towards the exact functional [160].

2.2.5 RUNG 4: HYBRID FUNCTIONALS

The fourth rung on Perdew’s Ladder corresponds to hybrid functionals, which include GGA (or meta-GGA) exchange and incorporate some amount of non-local exact (a.k.a. Hartree–Fock) exchange. One major appeal of hybrid functionals is their usefulness in describing systems characterized by delocalization error [161] (see Section 2.6). Conversely, one major drawback is that hybrid functionals are seen as prohibitively costly for large systems, especially when using planewave basis sets. However, recent advancements in the FHI-aims code have shown that its linear-scaling numerical atom-centred orbital basis functions are capable of modelling large organic-inorganic perovskites, organic crystals, and ice crystals with up to 30,576 atoms using hybrid functionals with unprecedented efficiency [162].

Hybrid functionals can be broadly generalized into three categories: global, range-separated, and local. Global hybrid functionals are the most common, which set the amount of exact-exchange mixing globally, typically between 20% and 50%, via

$$E_{\text{XC}} = a_X E_{\text{X}}^{\text{HF}} + (1 - a_X) E_{\text{X}}^{\text{DFT}} + E_{\text{C}}^{\text{DFT}}, \quad (2.2.13)$$

where $a_X \in [0, 1]$ is known as the hybrid mixing parameter. Popular examples include PBE0 [163], BLYP [164, 165], and our recommended B86bPBE0 [119].

Range-separated hybrid functionals use an exact-exchange mixing strategy based on the inter-electron distance, typically by replacing the Coulomb interaction with

$$\frac{1}{r_{12}} = \frac{\text{erfc}(\omega r_{12})}{r_{12}} + \frac{\text{erf}(\omega r_{12})}{r_{12}}, \quad (2.2.14)$$

where erf is the error function, erfc is the complimentary error function, and ω is the range-separation (RS) parameter that determines the length scale to switch between short- and long-range exchange treatments. One common example is LC- ω PBE [166], a long-range corrected (LC) hybrid that combines exact exchange at long range with GGA exchange from ω PBE at short range. It performs particularly well for fractional-charge systems [167]. Another example is the “screened” range-separated hybrid of

Heyd–Scuseria–Ernzerhof, HSE06 [168]. HSE06 instead mixes exact exchange into the short-range treatment while using PBE for the long-range treatment, proving useful for calculating band gaps in solids without the computational overhead of calculating long-range exact exchange. A recent study by Kokott *et al.* introduces a new screening function that includes long-range exact exchange contributions with greatly improved efficiency [169]. When applied to PBE0, this screened variant (named PBE0') predicts energies and bandgaps close to those of PBE0, but at a significantly reduced computational cost comparable to HSE06.

Lastly, there are local hybrid functionals [170, 171], which use local information to determine the appropriate amount of exact exchange at each grid point. This addresses the significant drawbacks of global or range-separated hybrids where the amount of exact-exchange mixing used is based on thermochemical observations at best, and arbitrary at worst. Local hybrids show incredible promise, but are notoriously difficult to implement in production codes due to requiring the exact-exchange density, prohibiting their widespread usage. Examples include Becke's B05 [172], and Google Deepmind's DM21 [173], which is a machine-learned technique.

2.2.6 RUNG 5: POST-KOHN–SHAM CORRELATION METHODS

Finally, the fifth and highest rung on Perdew's Ladder considers DFT methods that include virtual orbitals. This includes techniques such as the random phase approximation (RPA) [174–179] and double-hybrid functionals [180]. We note that, with the exception of using RPA techniques as reference data and its inclusion in small model systems in Chapter 4, no other fifth-rung techniques were studied in this thesis due to their prohibitive computational demand.

RANDOM-PHASE APPROXIMATION

The random-phase approximation (RPA) is a post-DFT method based on the adiabatic-connection fluctuation-dissipation theorem (ACFDT), which provides a formally exact form for the correlation energy. The ACFDT expresses this energy in terms of a response function $\chi(\mathbf{r}, \mathbf{r}', \omega)$, which quantifies the response at \mathbf{r} due to a change in potential $v(\mathbf{r}')$ at point \mathbf{r}' , as a function of frequency ω . The ACFD correlation energy, in atomic units, is given by

$$E_C^{\text{ACFD}} = -\frac{1}{2\pi} \int_0^\infty d\omega \int_0^1 d\lambda \text{tr}[(\chi_\lambda - \chi_0)v] . \quad (2.2.15)$$

Here, χ_0 is the non-interacting response function and $\chi_\lambda = \chi_0(\lambda v + f_{\text{XC}}^\lambda)\chi_\lambda$ is the interacting response function at Coulomb coupling strength λ . The exchange-correlation kernel, f_{XC}^λ , is not known exactly, and the RPA arises from the assumption that $f_{\text{XC}} = 0$ [181]. This treatment of the correlation energy is the core foundation of the MBD dispersion method [45–48], and this application of the RPA will be discussed further in Section 2.5.2.

DOUBLE-HYBRID FUNCTIONALS

Similar in form to hybrid functionals that supplement the GGA exchange energy using exact exchange, double-hybrid functionals [180] additionally supplement GGA correlation via

$$E_{\text{XC}} = (1 - a_X) E_{\text{X}}^{\text{GGA}} + a_X E_{\text{X}}^{\text{HF}} + (1 - a_C) E_{\text{C}}^{\text{GGA}} + a_C E_{\text{C}}^{\text{PT2}}, \quad (2.2.16)$$

where $E_{\text{C}}^{\text{PT2}}$ is a perturbative second-order Møller–Plesset-type term, and $a_C \in [0, 1]$ is the correlation mixing coefficient. Examples of a double-hybrid functionals include Grimme and Neese's B2PLYP [182], and also Becke's new local double-hybrid functional: DH24 [183].

2.2.7 CHEMICAL ACCURACY AND BEYOND DFT

Since the exact exchange-correlation functional is not known, methods beyond the five rungs of Perdew's ladder are needed for increased accuracy. Thus, we leave the realm of density-functional theory and enter that of correlated-wavefunction techniques. While no wavefunction techniques were used in this work, their results served as reference data to assess the accuracy of DFT techniques. Notable examples of wavefunction methods include second-order Møller–Plesset perturbation theory (MP2) [184–186], coupled-cluster theory (CC) [187, 188], the Weizmann-n (Wn) methods [189], and diffusion Monte Carlo (DMC) [190, 191].

MØLLER–PLESSET PERTURBATION THEORY

Møller–Plesset perturbation theory (MP2) [184–186] is a post-HF method often used to capture electron correlation. The zeroth-order system is described by

$$\hat{H}^{(0)} \left| \Psi_{\text{HF}}^{(0)} \right\rangle = E^{(0)} \left| \Psi_{\text{HF}}^{(0)} \right\rangle, \quad (2.2.17)$$

where the zeroth-order Hamiltonian may be expressed as the sum over one-electron Fock operators,

$$\hat{H}^{(0)} = \sum_p \hat{F}(\mathbf{r}_p), \quad (2.2.18)$$

for an electron at position \mathbf{r}_p . The Fock operator,

$$\hat{F}(\mathbf{r}_p) = \hat{h}(\mathbf{r}_p) + \sum_i \left[\hat{J}_i(\mathbf{r}_p) - \hat{K}_i(\mathbf{r}_p) \right], \quad (2.2.19)$$

is written in terms of the one-electron Hamiltonian (\hat{h}) to capture the kinetic and electron-nuclear energies, and the difference between the Coulomb (\hat{J}_i) and exchange (\hat{K}_i) operators for occupied orbital i . The MP2 correlation energy arises from second-order perturbation theory as

$$E_C^{\text{MP2}} = \sum_{i < j}^{\text{occ}} \sum_{a < b}^{\text{virt}} \frac{|\langle ij | ab \rangle|^2}{\epsilon_i + \epsilon_j - \epsilon_a - \epsilon_b}, \quad (2.2.20)$$

where i, j run over occupied orbitals, a, b run over virtual orbitals, and $\langle ij | ab \rangle$ is the antisymmetrized two-electron integral. These orbitals are eigenfunctions of the Fock operator with corresponding eigenvalues ϵ_i , ϵ_j , ϵ_a , and ϵ_b . The numerator, $|\langle ij | ab \rangle|^2$ represents the interaction strength of the double-excitation from i, j to a, b , while the denominator represents the associated energy cost. We note that single excitations do not contribute to the correlation energy due to Brillouin's theorem [192].

COUPLED-CLUSTER THEORY

Coupled-cluster (CC) theory is primarily a post-HF method that generates correlated wavefunctions through

$$|\Psi_{\text{CC}}\rangle = e^{\hat{T}} |\Psi_{\text{HF}}\rangle, \quad (2.2.21)$$

where \hat{T} is the cluster operator, consisting of linear combinations of excitation operators. This operator can be expanded in terms of excitation levels as

$$\hat{T} = \hat{T}_1 + \hat{T}_2 + \hat{T}_3 + \dots \quad (2.2.22)$$

where $\hat{T}_1 |\Psi_{\text{HF}}\rangle$ would generate a singly-excited Slater determinant, $\hat{T}_2 |\Psi_{\text{HF}}\rangle$ a doubly-excited Slater determinant, and so on. The cluster operator is written in exponential form because one may generate all excitation combinations by considering the Taylor

expansion

$$\begin{aligned}
 e^{\hat{T}} &= 1 + \hat{T} + \frac{1}{2}\hat{T}^2 + \frac{1}{6}\hat{T}^3 + \dots \\
 &= 1 + [\hat{T}_1 + \hat{T}_2 + \dots] + \frac{1}{2} [\hat{T}_1 + \hat{T}_2 + \dots]^2 + \frac{1}{6} [\hat{T}_1 + \hat{T}_2 + \dots]^3 + \dots \\
 &= 1 + \hat{T}_1 + \hat{T}_2 + \hat{T}_1\hat{T}_2 + \frac{1}{2}\hat{T}_1^2 + \frac{1}{2}\hat{T}_2^2 + \frac{1}{2}\hat{T}_1^2\hat{T}_2 + \frac{1}{2}\hat{T}_1\hat{T}_2^2 + \frac{1}{6}\hat{T}_1^3 + \dots. \quad (2.2.23)
 \end{aligned}$$

The most widely used implementation of coupled-cluster theory includes single, double, and perturbative triple excitations, denoted CCSD(T) [188]. In this case, the cluster operator is limited to the first two terms only: $\hat{T} = \hat{T}_1 + \hat{T}_2$. Rather than including \hat{T}_3 explicitly, requiring significant and often prohibitive computational demand, its contribution can be very accurately estimated using a non-iterative correction via second-order equations from Møller–Plesset perturbation theory.

DIFFUSION MONTE CARLO

Diffusion Monte Carlo (DMC), or more generally Quantum Monte Carlo (QMC) [190, 191], is a stochastic quantum method that directly computes the many-electron wavefunction. It starts from a trial wavefunction (typically from HF or DFT) and evolves the wavefunction in imaginary time, τ . Through a diffusion process that is described by Green's function, the algorithm converges to the ground state in the large- τ limit. In order to apply the DMC method to systems of interacting fermions, which create an antisymmetry problem, DMC techniques use the fixed-node (FN) approximation. FN-DMC restricts the sampling process to the nodal regions of a trial wavefunction using a killing procedure, but this can introduce a trial-node error on the energy. While the details of the DMC algorithm are beyond the scope of this thesis, the interested reader is directed to Ref. [193] for an incredibly informative and comprehensive tutorial.

DMC has been shown to have excellent performance for solids, exceeding the accuracy of DFT techniques. [194–196] In recent years, it has been proposed as an alternative reference method for systems that are not accessible to CCSD(T) or other highly-accurate wavefunction methods [197].

MOLECULAR BENCHMARK STANDARDS

Reference data for molecular codes is generally broken into different standards based on how well they approximate the exact result of full configuration interaction

(FCI) at the complete basis set [144]. The aim, ultimately, is for DFT methods to achieve the so-called “chemical accuracy” of 1 kcal/mol that is required for accurate predictions for bond energies, reaction barriers, and conformational energies. If the reader is more familiar with other unit conventions, a conversion table of commonly used energy units in electronic structure theory is provided in Appendix B.1. For small- to medium-sized molecular systems, we list the ranges bronze to platinum, taken from Refs. [198, 199]. Their categorizations, loosely summarized, are

Platinum: CCSD(T)/CBS + δ CCSDT(Q) + core + rel

Gold: CCSD(T)-F12/aTZ

Silver: CCSD(T)-F12/aDZ

Bronze: MP2C-F12/aDZ

where F12 refers to the explicit correlation method [200, 201]. To help approximate the basis-set limit (CBS), F12 is sometimes employed to reduce computational demand, allowing F12/aDZ to perform similarly to aTZ and F12/aTZ to perform similarly to aQZ. This, in combination with basis-set extrapolation [202, 203], is used to approximate the complete basis set (CBS) limit.

The platinum standard requires a finely-converged CBS-limit approximation, going to quintuple- or sextuple-zeta quality with basis-set extrapolation, an approximation of quadruple excitations, core corrections, and inclusion of relativistic effects. Sometimes even the Bohn–Oppenheimer approximation is considered insufficient. The gold standard reports a level of accuracy of 0.05-0.10 kcal/mol compared to the platinum standard on the A24 benchmark [204, 205]. For a benchmark of 345 non-covalent interaction energies by Burns, Marshall, and Sherril [199], the silver standard deviates from gold by another 0.05 kcal/mol, while the bronze standard—the MP2 coupled method (MP2C) by Hefselmann [206, 207]—deviates by 0.16 kcal/mol. It was noted, however, that this level of accuracy is approaching that of the best DFT techniques and, thus, the bronze standard may not be sufficiently accurate for benchmarking purposes. While the Weizmann-n methods are not listed here, these are post-CC methods of similar accuracy.

Finally, we note that for molecular benchmarks of larger systems (>50 atoms), there is currently no general consensus on what constitutes accurate and reliable reference data. As the systems grow in size, methods that claim high accuracy and low uncertainties sometimes report differences in excess of 8 kcal/mol from each other on the same system [208, 209].

SOLID-STATE BENCHMARK STANDARDS

Reference data is difficult to obtain for the solid state, as correlated-wavefunction methods are not widely available to use in periodic codes. As such, most reference data comes in the form of back-corrected experimental data, RPA, or diffusion Monte Carlo (DMC) techniques.

2.3 DFT IN PERIODIC SOLIDS

For the study of condensed-phase materials, we turn to solid-state physics. In theory, we are modelling an effectively endless system with an infinite number of interacting electrons. In practice, we must find a way of modelling a small subsection of this system in a physically realizable way that accurately represents the system as a whole. A solution taken by many electronic-structure codes, such as Quantum ESPRESSO [111], is to use a planewave (PW) basis set and atomic pseudopotentials (PP) to model the system efficiently. This section will explore the necessary theory behind how these types of codes work.

2.3.1 THE BRAVAIS LATTICE AND BLOCH'S THEOREM

It is fortuitous that most solid-state systems are comprised of periodic crystal lattice structures, as it lets us break them into smaller, symmetric pieces. The smallest group of atoms that can form the entire lattice through repetition in all spatial dimensions is known as the unit cell. This unit cell's periodicity can be specified through the use of primitive lattice vectors, \mathbf{a}_i , which generates the Bravais lattice [210],

$$\mathbf{R} = n_1 \mathbf{a}_1 + n_2 \mathbf{a}_2 + n_3 \mathbf{a}_3 , \quad (2.3.1)$$

for integer valued n_i . By enforcing periodicity conditions on the lattice structure, we may then say that the potential $\mathcal{V}(\mathbf{r})$ felt by an electron at point \mathbf{r} would satisfy a translation symmetry when shifted by the Bravais vector such that

$$\mathcal{V}(\mathbf{r}) = \mathcal{V}(\mathbf{r} + \mathbf{R}) . \quad (2.3.2)$$

Thus, only one unit cell (with appropriate periodic boundary conditions) needs to be simulated to effectively model the entire system.

We consider the wavefunction at any point along the infinite lattice would feel this periodic potential \mathcal{V} . The wavefunction must then satisfy the same translation

symmetry as the potential so the probability density of the wavefunction at a point \mathbf{r} would be the same as a point $\mathbf{r} + \mathbf{R}$,

$$|\psi(\mathbf{r})|^2 = |\psi(\mathbf{r} + \mathbf{R})|^2. \quad (2.3.3)$$

This implies $\psi(\mathbf{r} + \mathbf{R}) = c\psi(\mathbf{r})$ where the constant c must satisfy $|c| = 1$. Repeated applications of this periodicity statement forces c to be an N^{th} root of unity, so $c = \exp(i2\pi\theta)$. Further development of this system [211] shows that the wavefunction must be periodic in nature, taking the form of a plane wave. It follows that

$$\psi_{n\mathbf{k}}(\mathbf{r}) = e^{i\mathbf{k}\cdot\mathbf{r}} u_{n\mathbf{k}}(\mathbf{r}), \quad (2.3.4)$$

where n is known as the band index, \mathbf{k} is the wave vector, and $u_{n\mathbf{k}}(\mathbf{r}) = u_{n\mathbf{k}}(\mathbf{r} + \mathbf{R})$ is some periodic function. Eq. (2.3.4) is formally known as Bloch's theorem [212]. Here \mathbf{k} is defined as

$$\mathbf{k} = m_1 \mathbf{b}_1 + m_2 \mathbf{b}_2 + m_3 \mathbf{b}_3, \quad (2.3.5)$$

with reciprocal lattice vectors

$$\mathbf{b}_1 = \frac{2\pi}{\Omega} \mathbf{a}_2 \times \mathbf{a}_3, \quad \mathbf{b}_2 = \frac{2\pi}{\Omega} \mathbf{a}_3 \times \mathbf{a}_1, \quad \mathbf{b}_3 = \frac{2\pi}{\Omega} \mathbf{a}_1 \times \mathbf{a}_2, \quad (2.3.6)$$

where $\Omega = \mathbf{a}_1 \cdot \mathbf{a}_2 \times \mathbf{a}_3$ is the volume of the unit cell, given by scalar triple product of the real-space primitive lattice vectors. The real and reciprocal lattice vectors satisfy the relation $\mathbf{a}_i \cdot \mathbf{b}_j = 2\pi\delta_{ij}$, where δ_{ij} is the Kronecker delta

$$\delta_{ij} = \begin{cases} 1, & \text{if } i = j \\ 0, & \text{if } i \neq j \end{cases}. \quad (2.3.7)$$

The cell-periodic Kohn–Sham wavefunctions may then be written in terms of plane waves using discrete Fourier transforms

$$u_{n,\mathbf{k}}(\mathbf{r}) = \frac{1}{\sqrt{\Omega}} \sum_{\mathbf{G}} c_{n,\mathbf{G},\mathbf{k}} e^{i\mathbf{G}\cdot\mathbf{r}}, \quad \psi_{n,\mathbf{k}}(\mathbf{r}) = \frac{1}{\sqrt{\Omega}} \sum_{\mathbf{G}} c_{n,\mathbf{G},\mathbf{k}} e^{i(\mathbf{G}+\mathbf{k})\cdot\mathbf{r}}. \quad (2.3.8)$$

The Fourier coefficients may be easily transformed between real and reciprocal space via

$$c_{n,\mathbf{r},\mathbf{k}} = \sum_{\mathbf{G}} c_{n,\mathbf{G},\mathbf{k}} e^{i\mathbf{G}\cdot\mathbf{r}} \xleftrightarrow{\text{FFT}} c_{n,\mathbf{G},\mathbf{k}} = \sum_{\mathbf{r}} c_{n,\mathbf{r},\mathbf{k}} e^{-i\mathbf{G}\cdot\mathbf{r}}, \quad (2.3.9)$$

where \mathbf{G} is some periodic wave vector satisfying $\mathbf{G} \cdot \mathbf{R} = 2\pi m$ for some integer m .

To limit the size of our plane-wave basis, as contributions due to higher-energy terms in the Fourier series are diminishing, we may introduce a kinetic energy cutoff and omit plane waves that exceed it. Our plane-wave basis set will include all plane waves satisfying

$$\frac{\hbar^2}{2m} |\mathbf{G} + \mathbf{k}|^2 < E_{\text{cut}}, \quad (2.3.10)$$

where the value of E_{cut} is chosen for the particular system while ensuring that it is set sufficiently high to allow convergence of desired observables.

From here, the reader may question why many DFT methods choose to implement plane-wave bases; there are three reasons for this [213]. The first is that, historically, pseudopotential theory was designed in the framework of plane-waves to cope with the free-electron behaviour that is seen in the band structures of metallic s-block or p-block elements. The second reason is for practicality, as the total energy expressions and the Hamiltonian are easy to implement in terms of plane-wave basis sets. Some quantities are easier to compute in real space, while others are easier to compute in reciprocal space. The use of a plane-wave basis makes it easy to switch between the two via the use of Fourier transformations. The third reason is simply for computational efficiency, as the action of the Hamiltonian on the orbitals is efficiently calculated via the use of fast Fourier transforms (FFT) [214–216], which scales as $\mathcal{O}(N \log N)$ where N is the number of plane waves in the unit cell.

2.3.2 SAMPLING THE BRILLOUIN ZONE

To capture the exact solution to the Kohn–Sham equations, \mathbf{k} -space must be sampled completely. Similarly to how the real-space Bravais lattice can be divided into unit cells, we may divide the reciprocal-space lattice into Brillouin zones [217]. Using symmetry, we then only need to consider sampling the \mathbf{k} -points within the first Brillouin zone, but unfortunately there are still infinitely many of them.

To shed some light on sampling in \mathbf{k} -space, note that a \mathbf{k} -point with coordinates $(1/n, 1/m, 1/p)$ in reciprocal space corresponds to an orbital with periodicity over a real-space supercell of size (n, m, p) . Capturing a long-range electron-electron correlation that spans many unit cells requires a sufficiently fine \mathbf{k} -point mesh. Systems exhibiting long-range electron delocalization such as metals, charge transfer, or those with extended π -conjugation will likely require denser \mathbf{k} -grids to ensure accurate modelling. Convergence testing to ensure your \mathbf{k} -point mesh is sufficiently fine for a given system is required.

While sampling infinitely many \mathbf{k} -points is required for the exact solution, it is not necessary for an accurate solution provided that the sample of \mathbf{k} -points in the crystal is chosen intelligently. The \mathbf{k} -point grid must be positioned such that no vital points in the Brillouin zone are missed, while also being dense enough such that no sharp fluctuations in density are missed due to sampling error. A common sampling scheme was developed by Monkhorst and Pack, known as the MP-scheme [218]. This scheme selects the \mathbf{k} -points using a uniform three-dimensional mesh of points throughout reciprocal-space.

Once the MP mesh has been calculated, it may be shifted (if needed) to incorporate specific points within the Brillouin zone, such as the gamma (central) point. Most solid-state codes will then apply symmetry conditions to the system, extracting it down to an irreducible set of \mathbf{k} -points. This set of \mathbf{k} -points is known as the irreducible Brillouin zone (IBZ). When these points are sampled, they are appropriately weighted to account for the omitted symmetry-equivalent points.

2.3.3 ATOMIC PSEUDOPOTENTIALS

To remedy issues of high computational demand within modern-day DFT calculations, we have approximated the form of the exchange-correlation functional, employed the Born–Oppenheimer (BO) approximation⁴, intelligently selected \mathbf{k} -space integration grids which exploit symmetry, used a plane-wave basis set to take advantage of FFT, and restricted our basis to Fourier components that do not exceed some energy cutoff. Unfortunately, this is still not sufficient. Because we have chosen to use a plane-wave basis, the number of plane waves required to accurately describe orbitals with rapid oscillations and nodes near the nucleus, or tightly bound states, is prohibitively large for any atom with more than a few electrons. Thus, we shall introduce two additional approximations to reduce the number of plane waves required to adequately model our systems.

The first new approximation is known as the frozen-core approximation [219], where the electron density of the core electrons is pre-calculated and kept “frozen” throughout the remainder of the computation. Only the valence electrons are chemically active, so this approximation is justified because these core electrons do not contribute to binding. The second new approximation will be to neglect the exact potential surrounding the nucleus in favour of a pseudopotential [220]. Electrons that contribute to binding may occupy orbitals that exhibit rapid oscillations near the

⁴The Born–Oppenheimer approximation is discussed in Appendix B.2.

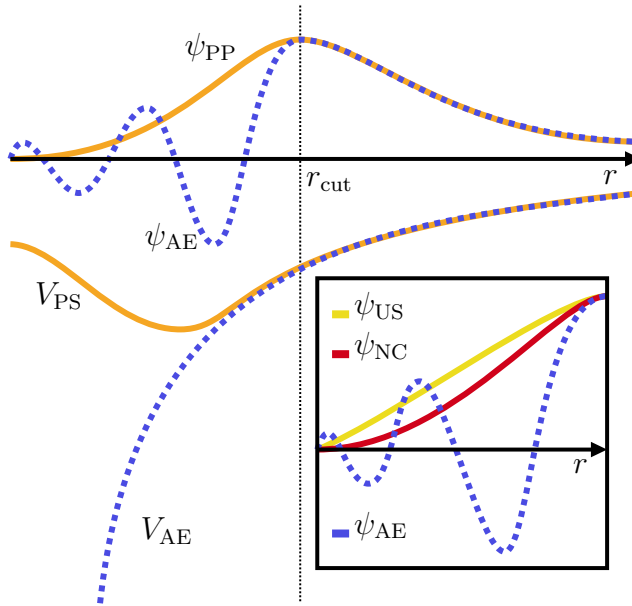


Figure 2.4: Illustration differentiating types of pseudopotentials and pseudowavefunctions. The main plot shows the all-electron potential (V_{AE}) in blue, and pseudopotential (V_{PP}) in orange, demonstrating how the highly oscillatory behaviour of the all-electron wavefunctions (ψ_{AE}) are smoothed (ψ_{PP}), up to the cutoff radius r_{cut} . The inset contrasts norm-conserving wavefunctions (ψ_{NC}) in red versus ultrasoft wavefunctions (ψ_{US}) in yellow, generated by norm-conserving and ultrasoft pseudopotentials V_{NC} and V_{US} respectively (not illustrated).

nucleus, requiring many plane waves to properly describe. Investing computational resources into modelling this area is unnecessary to capture the chemical behaviour in most systems. Pseudopotentials were introduced as a way of smoothing out these rapid oscillations and increasing computational efficiency.

There are two types of pseudopotentials that are commonly used. The first are norm-conserving (NC) pseudopotentials [221–223], which enforce that the norm of each pseudo-orbital is identical to the corresponding all-electron (AE) orbital. The second type are ultrasoft (US) pseudopotentials [224], which do not require norm conservation, so fewer plane waves are required. The goal of ultrasoft pseudopotentials is for calculations to require as low of a cutoff energy as possible to reach chemical accuracy. A graphical representation of pseudopotentials, pseudowavefunctions, and the difference between norm-conserving and ultrasoft pseudopotentials is shown in Figure 2.4.

2.3.4 THE PROJECTOR-AUGMENTED WAVE METHOD

The projector-augmented wave (PAW) method was originally developed by Blöchl [225] and then generalized by Kresse and Joubert [226]. This method was based on Slater's augmented plane-wave (APW) method [227], wherein the Kohn–Sham equations are solved via linearizing the eigenvalue problem using a dual-basis set. This basis set uses plane waves to model the interstitial regions between atoms, while the core regions are modelled using atomic-like radial functions with spherical harmonics. Using a combination of linearized augmented planewaves (LAPW) [228] and pseudopotentials, the PAW method preserves the nodal properties of the highly oscillatory wavefunctions without having to represent them as plane waves. For a detailed overview of the PAW method, the reader is directed to [229] and the references therein.

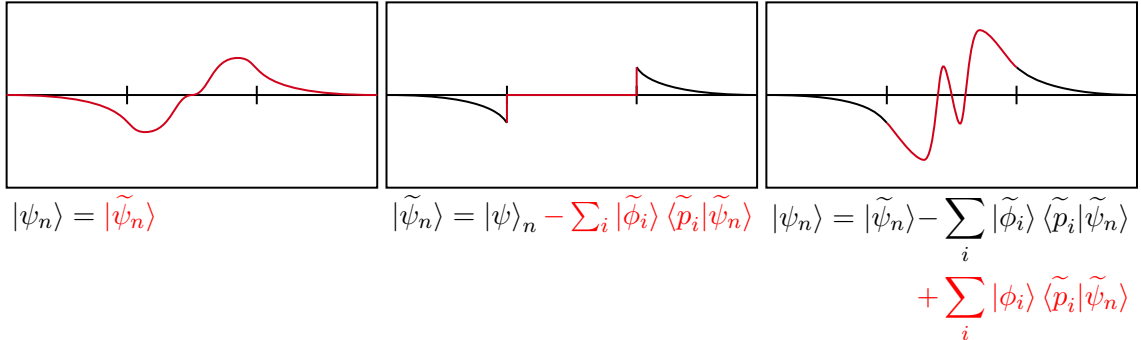


Figure 2.5: Visualization of the projector augmented wave orbital components, adapted from [213]. The components and their graphical representations are highlighted in red. Left: our pseudized orbital. Middle: the subtraction of the pseudized core region. Right: the incorporation of the atomic-like core.

The PAW orbitals are given by

$$|\psi_n\rangle = |\tilde{\psi}_n\rangle + \sum_i \left(|\phi_n\rangle - |\tilde{\phi}_n\rangle \right) \langle \tilde{p}_i | \tilde{\psi}_n\rangle , \quad (2.3.11)$$

where $|\tilde{\psi}_n\rangle$ are our pseudo orbitals, $|\phi_n\rangle$ are our all-electron partial wavefunctions, $|\tilde{\phi}_n\rangle$ are our pseudo partial wavefunctions, and $\langle \tilde{p}_i |$ are known as projector functions. The effect of each of these contributions on the PAW orbital may be visualized in Figure 2.5.

When PAW is used, the base assumption is that the PAW spheres do not overlap. However, in practice, this sometimes is the case. The consequences of PAW overlap are

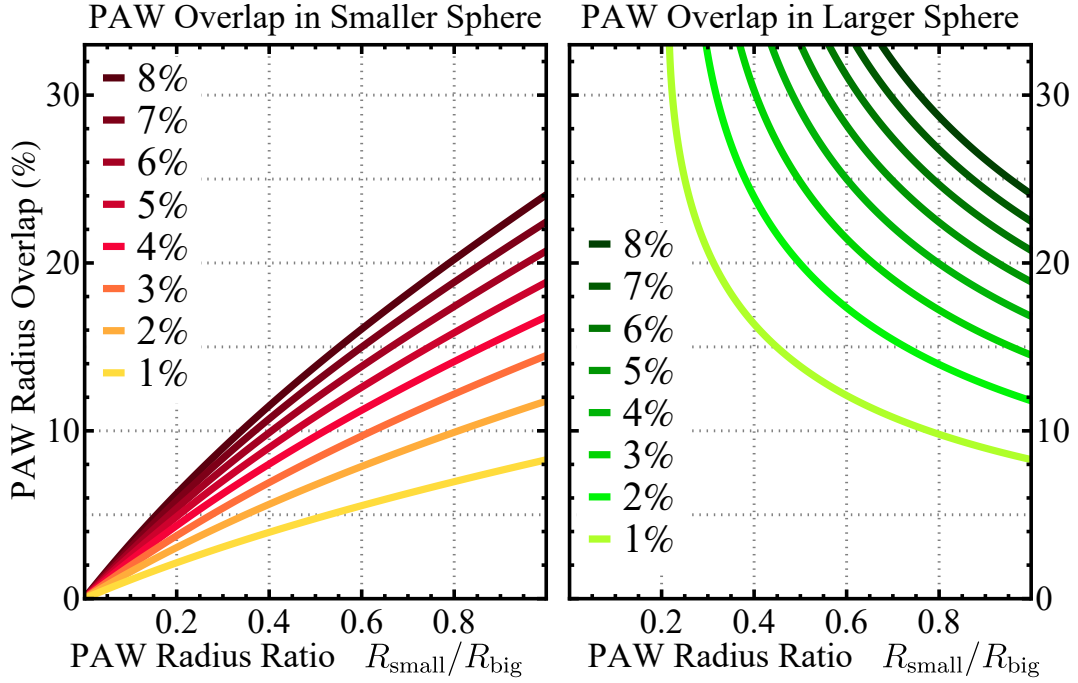


Figure 2.6: Plots showing the percent PAW volume overlap contours as functions of radius ratio and radius overlap for the smaller (left) and larger (right) spheres.

well studied [230] and typically no more than 5% voluminal overlap deemed acceptable [231]. The PAW method was used in Chapter 3, where one system had significant PAW radial overlap: CO₂. The B86bPBE PAW pseudopotentials used for these calculations were UPF version 2.0.1, generated using the “atomic” code by A. Dal Corso [232, 233], packaged with Quantum ESPRESSO [111]. The PAW radii for C and O were 1.1000 and 1.3000 bohr respectively. The minimum separation for CO₂ studied was 2.205 bohr, in a geometry where each unit vector was compressed by 10% from equilibrium. The percent radial overlap (PRO) between two spheres with radii r_i and r_j and separation d is given by

$$\text{PRO} = \left(1 - \frac{d}{r_i + r_j}\right) \times 100\%. \quad (2.3.12)$$

For our compressed CO₂ geometry, we have PRO = 8.125%. The percent volume overlap (PVO) for $r_\alpha \in \{r_i, r_j\}$ is given by

$$\text{PVO}(r_\alpha) = \frac{\pi(r_i + r_j - d)^2 (d^2 + 2dr_i + 2dr_j + 6r_i r_j - 3r_i^2 - 3r_j^2)}{12d} \Big/ \frac{4\pi r_\alpha}{3}. \quad (2.3.13)$$

Thus, there is a 1.24% volume overlap on carbon per oxygen—so 2.48% total—and 0.75% volume overlap on each oxygen. We see that we are well below the 5% voluminal overlap limit. While some codes, such as Abinit [234, 235] (see also: [236–239]), assist with this check automatically, other codes do not. Figure 2.6 was created as a way to visually check for concerning amounts of PAW voluminal overlap for a given PAW sphere radius ratio and easily calculable radius overlap percentage. Walking through our example earlier for CO₂, we know $R_{\text{small}}/R_{\text{big}} = 1.1/1.3 = 0.85$ and our radius overlap was 8.125%. Following the intersection of these two lines on the Figure 2.6 shows the voluminal overlap for carbon is ca. 1.5%. After doubling to account for the two bonded oxygen, this figure informs us at a glance that the voluminal overlap could not be greater than 4%, and thus is within the acceptable range.

2.3.5 NUMERICAL ATOM-CENTRED ORBITALS

While our discussion thus far has focused on the use of planewave basis functions and pseudopotentials, there are many electronic-structure codes that use neither. A notable example is the Fritz Haber Institute *ab initio* molecular simulations (FHI-aims) software package [120, 121], which employs all-electron methods through the use of carefully-constructed numerical atom-centred orbitals (NAOs). The basis within FHI-aims represents single-particle orbitals $\psi_l(\mathbf{r})$ for orbital index l as a basis-set expansion of N_b functions via

$$\psi_l(\mathbf{r}) = \sum_i^{N_b} c_{il} \varphi_i(\mathbf{r}), \quad (2.3.14)$$

with NAOs of the form

$$\varphi_i(\mathbf{r}) = \frac{u_i(r)}{r} Y_m^\ell(\theta, \phi). \quad (2.3.15)$$

Here, $Y_m^\ell(\theta, \phi)$ are the real linear combinations of the spherical harmonics, with azimuthal and magnetic quantum numbers ℓ and m implied by the basis index i . The radial component, $u_i(r)$, is an eigenfunction to the radial wave equation

$$\left[-\frac{1}{2} \frac{d^2}{dr^2} + \frac{\ell(\ell+1)}{r^2} + v_i^{\text{FHI}}(r) + v_{\text{cut}}^{\text{FHI}}(r) \right] u_i(r) = \varepsilon_i u_i(r), \quad (2.3.16)$$

with corresponding eigenenergies ε_i . The potential is given by $v_i^{\text{FHI}}(r) = z/r$ for an effective nuclear charge z . The use of “effective” nuclear charges permits flexibility when constructing a suitable basis. For example, a 1s orbital with an effective nuclear charge of $z = 0.85$ could be used to represent a hydrogen nucleus rather than using

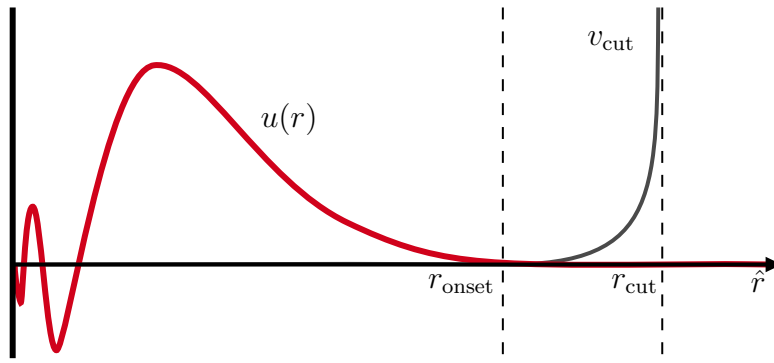


Figure 2.7: Visualization of the numerical atom-centred orbitals used in FHI-aims, adapted from Ref. [240]. The radial basis function is illustrated as a function of distance from an atomic nucleus, depicting how it smoothly decreases to zero at r_{cut} after the cutoff potential activates at r_{onset} .

the typical $Z = 1$. To ensure computational efficiency and $\mathcal{O}(N)$ -like scaling, a cutoff potential smoothly decays all basis functions to zero, localizing the orbitals to approximately atomic width. This cutoff potential, given by

$$v_{\text{cut}}^{\text{FHI}}(r) = \begin{cases} 0 & r \leq r_{\text{onset}} \\ \frac{s}{(r-r_{\text{cut}})^2} \exp\left(\frac{w}{r-r_{\text{onset}}}\right) & r_{\text{onset}} < r < r_{\text{cut}} \\ \infty & r \geq r_{\text{cut}} \end{cases}, \quad (2.3.17)$$

smoothly activates at r_{onset} and gradually increases to infinity at r_{cut} . The width of this activation is $w = r_{\text{cut}} - r_{\text{onset}}$, and the scale is determined by the global scaling parameter s . An illustration of the NAO radial component and its interaction with the cutoff potential at r_{onset} and r_{cut} is shown in Figure 2.7.

The improved scaling of this NAO approach allows for faster GGA computations than planewave codes for large unit cells containing hundreds of atoms. Further still, the NAOs permit hybrid functionals to be practical for solids and can even be applied to very large unit cells containing thousands of atoms or more [162]. Limitations of hybrid functionals largely stem from the incredible computational cost of calculating exact exchange for a planewave basis, which becomes feasible with near-linear-scaling NAOs.

In FHI-aims, the most popular basis functions are `light`, `intermediate`, and `tight`. Blum *et al* [120] studied the performance of these basis sets for the binding energy of a water dimer, with and without a counterpoise (CP) correction [241, 242].

Their results showed that the `light` basis is sufficiently converged such that this correction changed the binding energy by less than 0.4 kcal/mol, and differed from the estimated CBS limit by only 0.7 kcal/mol. For the `tight` basis, it differed by the CBS limit by less than 0.1 kcal/mol. To improve stability in geometry optimizations compared to `light`, but without resorting to the higher cost of `intermediate`, two new basis sets were created. They combine `light` basis functions with denser integration grids like those in `tight`, and are called `lightdense` [119] and `lightdenser` [121, 243, 244]. These two basis sets, along with `tight`, were used for the majority of the calculations in this thesis.

2.3.6 GAUSSIAN-TYPE ORBITALS

While not typically used for solid-state DFT due to common challenges such as basis-set superposition error and linear dependencies in periodic environments, it would be a disservice not to discuss Gaussian-type orbitals (GTOs) given their popularity in molecular codes. Gaussian basis functions are described mathematically as

$$\phi_{ijk} = Nx^i y^j z^k e^{-\alpha r^2}, \quad (2.3.18)$$

where N is a normalization constant, α is a decay exponent, and i , j , and k are non-negative integers. When $i + j + k = 0$, the orbital is spherical and is an *s*-type GTO. If the sum equals 1, it is a *p*-type orbital; if it equals 2, it is a *d*-type orbital, and so on. We will briefly examine three of the most-common nomenclatures used to describe GTOs.

MINIMAL BASIS SETS

The first category is minimal basis sets. These use the smallest possible set of orbitals to accommodate all electrons in each atom's ground state. A natural first guess for a suitable basis function is the hydrogen-like wavefunction of the form

$$R(r) = Nr^{n-1}e^{-\zeta r}, \quad (2.3.19)$$

where n is the principal quantum number, N is the normalization constant, and ζ is the effective charge of the nucleus. This form is known as a Slater-type orbital (STO) [245], and it has the benefits of capturing the true nuclear cusp and exhibiting an appropriate exponential tail. Unfortunately, this form comes with severe limitations. Electron repulsion integrals are not analytically solvable in this basis, and therefore

require costly numerical quadrature. These wavefunctions can instead be approximated using linear combinations of GTO primitives, as first proposed by Pople *et al.* [246]. These follow the naming convention “STO- nG ”, where n indicates the number of primitives used to approximate the Slater-type orbital.

POPLE SPLIT-VALENCE BASIS SETS

The second category is Pople-style split-valence basis sets [247]. Pople basis sets are commonly used in DFT for their computational efficiency. These have the form “ $C\text{-}V_1V_2V_3\dots G$ ”. C represents one basis function, with its value indicating the number of linearly-combined primitive Gaussians used to model the atomic core. Similarly, the value of V_i represents the number of primitives used for the valence orbital, with each V_i corresponding to one basis function. For example, in the 6-31G basis, the “6” indicates six primitives model the core basis function; the “3” indicates three primitives model the first valence basis function; and the “1” indicates that a single primitive models the second valence basis function. This is referred to as a “double-zeta” basis set, as it uses two contracted basis functions to model the valence orbitals. If polarization functions are added, this is typically indicated with one or more asterisks following “G” (e.g. 6-31G*).

DUNNING CORRELATION-CONSISTENT BASIS SETS

The third category is the Dunning-style correlation-consistent basis sets [248]. These are commonly used in post-HF methods due to their ability to systematically converge to the CBS limit through extrapolation techniques [202, 203]. These have the form “cc-pVNZ”, where “cc-p” denotes they are correlation-consistent and polarized, and “VNZ” specifies valence orbitals of N -zeta quality. Typically, N is denoted as D, T, Q, 5, or 6, corresponding to double-, triple-, quadruple-, quintuple-, and sextuple-zeta quality, respectively.

ADDING DIFFUSE FUNCTIONS

Diffuse functions are often added to Pople- or Dunning-style basis sets [249]. These functions improve the accuracy of the basis set for anions, fluorinated compounds, excited states, delocalized systems, and systems described by weak interactions such as van der Waals complexes or hydrogen bonding. In Pople-style basis sets, the addition of diffuse functions is indicated by one or more plus signs before the “G” (e.g., 6-31+G*). In Dunning-style basis sets, this is indicated with the prefix “aug-” (or “aug2-”) at the beginning of the basis name (e.g., aug-cc-pVTZ).

2.4 FORCES AND STRESSES

Most electronic-structure theory programs include a process called a geometry optimization that minimizes the forces on each atom and the stresses on the unit cell. The forces are minimized by shifting atomic positions in the direction of the largest gradient. Simultaneously, the stresses on the unit cell are calculated, and the unit cell is modified to minimize them. These adjustments are made at the end of each SCF cycle, and constitute one step of the geometry optimization process. Once the atomic forces and unit-cell stresses are sufficiently small, the system is considered relaxed and the geometry optimized, indicating it has settled into a minimum on its potential energy surface. An accurate description of forces and stresses in electronic-structure codes is highly desirable; however, proper treatment involves many non-trivial considerations [250]. A flowchart of a typical code's SCF loop and geometry optimization process is illustrated in Figure 2.8.

This section shall derive the Hellmann–Feynman theorem [251–253] and discuss how it may be applied to long-range interatomic forces [254, 255]. Afterwards, the Cauchy stress tensor [256–261], the deformation gradient tensor [261, 262], and the Green–Lagrangian strain tensor [263–267] will be introduced for a discussion of unit cell optimization.

2.4.1 THE HELLMANN–FEYNMAN FORCE THEOREM

The Hellmann–Feynman theorem [251–253] is straightforward to derive. From the well-known Schrödinger equation, $\hat{H}|\psi\rangle = E|\psi\rangle$, we know the expectation value of the Hamiltonian gives the energy, $\langle\psi|\hat{H}|\psi\rangle = E$, due to the normalization condition on the wavefunctions, $\langle\psi|\psi\rangle = 1$. We assume \hat{H} , $\psi(\mathbf{r})$, and E_n are all functions of some continuously varying parameter λ , and take the derivative of both sides,

$$\frac{\partial}{\partial\lambda}\left\langle\psi\left|\hat{H}\right|\psi\right\rangle=\frac{\partial E}{\partial\lambda}. \quad (2.4.1)$$

Via a three-term product rule, the left-hand side expands to

$$\left\langle\frac{\partial\psi}{\partial\lambda}\left|\hat{H}\right|\psi\right\rangle+\left\langle\psi\left|\frac{\partial\hat{H}}{\partial\lambda}\right|\psi\right\rangle+\left\langle\psi\left|\hat{H}\right|\frac{\partial\psi}{\partial\lambda}\right\rangle=\frac{\partial E}{\partial\lambda}. \quad (2.4.2)$$

We shall now show that the sum of the first and third terms of the left-hand side of Eq. (2.4.2) is zero. Using the definition of the Schrödinger equation, we may extract

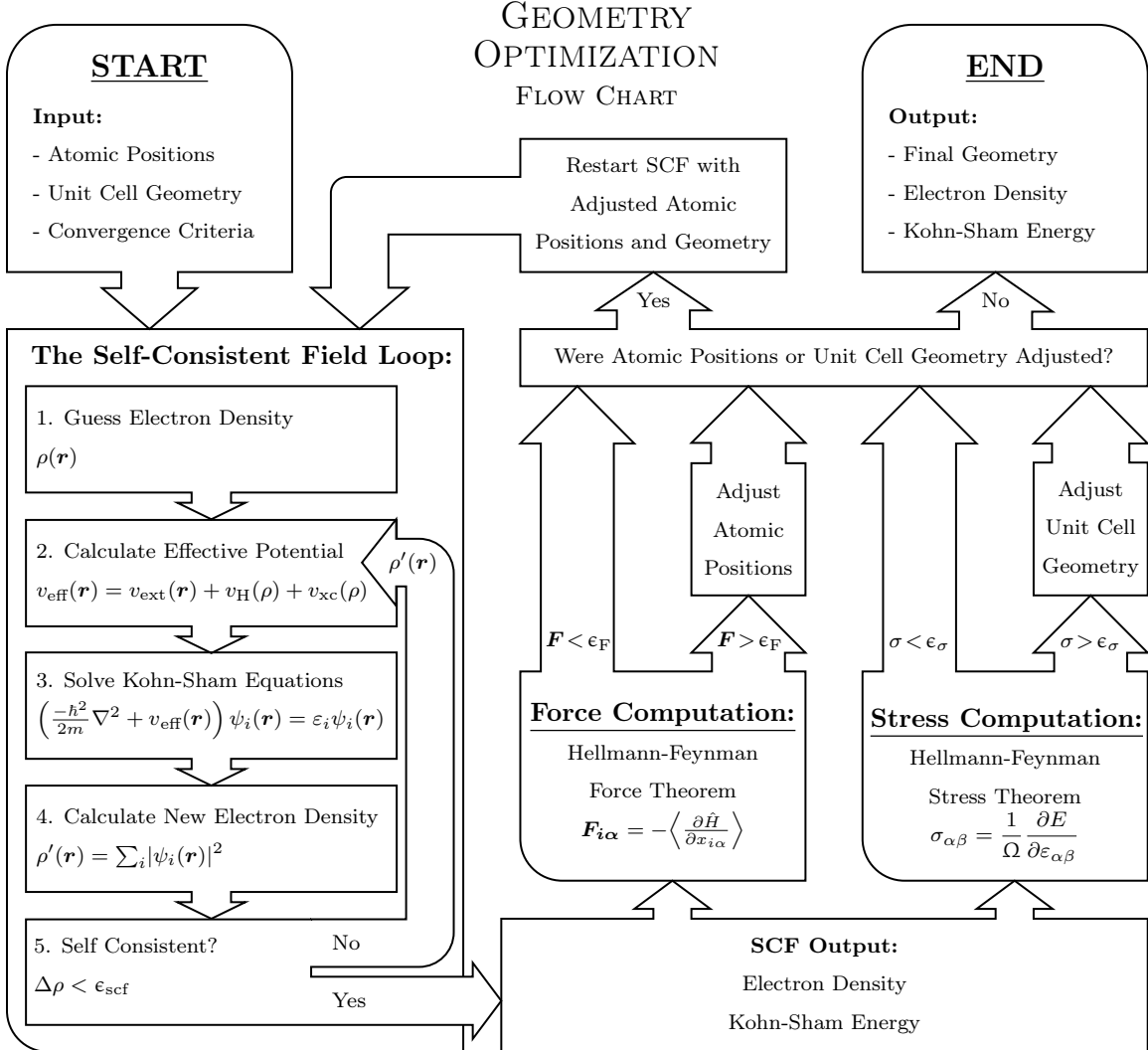


Figure 2.8: A flowchart depicting geometry optimization, as performed by most electronic-structure theory software. Many options for convergence criteria exist in the literature. One of the more common SCF convergence criteria used in practice is to compute the volume-integrated root-mean-square change of charge density between successive SCF iterations.

an energy term from their inner products,

$$\left\langle \frac{\partial \psi}{\partial \lambda} \left| \hat{H} \right| \psi \right\rangle + \left\langle \psi \left| \hat{H} \right| \frac{\partial \psi}{\partial \lambda} \right\rangle = E \left(\left\langle \frac{\partial \psi}{\partial \lambda} \left| \psi \right\rangle \right) + \left\langle \psi \left| \frac{\partial \psi}{\partial \lambda} \right\rangle \right). \quad (2.4.3)$$

The terms in the parentheses on the right-hand side are the result of a simple two-term product rule, $\left\langle \frac{\partial \psi}{\partial \lambda} \left| \psi \right\rangle \right\rangle + \left\langle \psi \left| \frac{\partial \psi}{\partial \lambda} \right\rangle \right\rangle = \frac{d}{d\lambda} \langle \psi | \psi \rangle$. We know that $\langle \psi | \psi \rangle = 1$ is a

constant, thus, taking its derivative with respect to the continuous parameter λ is zero. So we have shown that

$$\left\langle \frac{\partial\psi}{\partial\lambda} \middle| \hat{H} \middle| \psi \right\rangle + \left\langle \psi \middle| \hat{H} \middle| \frac{\partial\psi}{\partial\lambda} \right\rangle = 0. \quad (2.4.4)$$

Finally, substituting Eq. (2.4.4) into Eq. (2.4.2) results in the desired form of the general Hellmann–Feynman theorem

$$\left\langle \psi(\mathbf{r}) \middle| \frac{\partial\hat{H}}{\partial\lambda} \middle| \psi(\mathbf{r}) \right\rangle = \left\langle \frac{\partial\hat{H}}{\partial\lambda} \right\rangle = \frac{\partial E}{\partial\lambda}. \quad (2.4.5)$$

To apply the Hellmann–Feynman theorem to forces⁵, we consider the classical definition of force as an expression of energy. The force can be expressed as the negative of the gradient of the potential energy as

$$\mathbf{F}(\mathbf{r}) = -\nabla V(\mathbf{r}), \quad (2.4.6)$$

and so the Hellmann–Feynman force theorem is given by

$$\mathbf{F}_r = -\left\langle \frac{\partial\hat{H}}{\partial\mathbf{r}} \right\rangle = -\frac{\partial E}{\partial\mathbf{r}}. \quad (2.4.7)$$

2.4.2 STRESSES, STRAINS, AND DEFORMATIONS

Simple deformations to a unit cell may permit direct computation of strain elements. This is illustrated in Figure 2.9 where a system, subject to an applied Cauchy stress of σ_{yy} [256–261], experiences a Green–Lagrangian strain of ε_{yy} [263–267]. However, for more complicated deformations it may be useful (and intuitive) to express these strain elements in terms of the deformation gradient tensor [261, 262], with corresponding elements,

$$F_{\alpha\beta} = \frac{\partial r'_\alpha}{\partial r_\beta}. \quad (2.4.8)$$

The deformation gradient tensor measures the unit-cell's changed configuration, \mathbf{r}' , with respect to the undeformed reference configuration, \mathbf{r} , where $\mathbf{r} = (x, y, z)$ in Cartesian coordinates. In matrix form, the deformation gradient tensor may be written as $\mathbf{F} = \nabla \otimes \mathbf{r}$.⁶ There are four primary types of deformation: rotations, stretching,

⁵This is generally referred to as the Hellmann–Feynman force theorem.

⁶The deformation gradient tensor should not be confused with the force expressions of Eqs. (2.4.6) and (2.4.7).

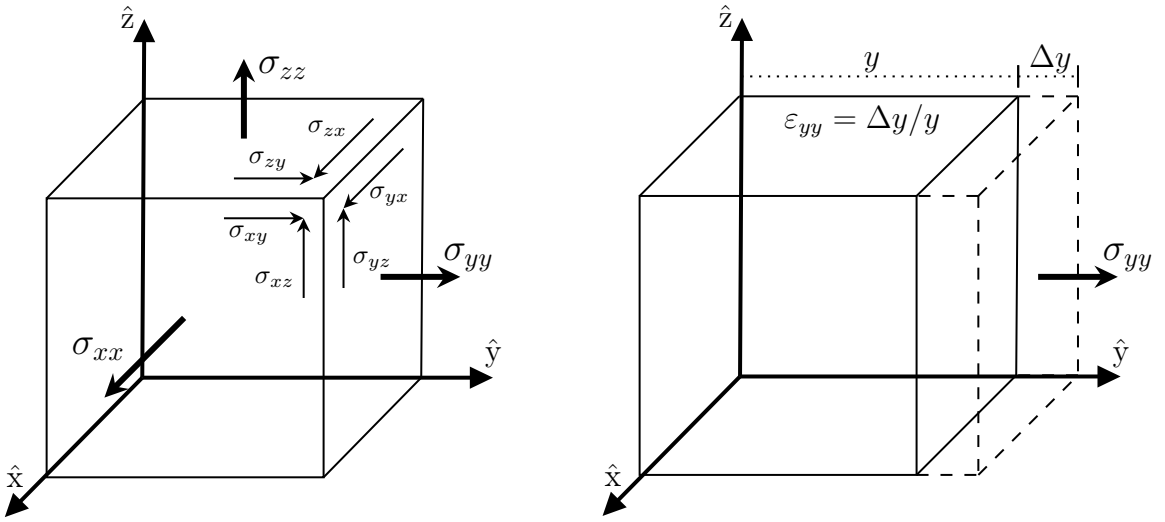


Figure 2.9: A simple cubic lattice with labelled Cauchy stress ($\sigma_{\alpha\beta}$) and Green–Lagrangian strain ($\varepsilon_{\alpha\beta}$) components. Left: A diagram which labels the stress components $\sigma_{\alpha\beta}$. Right: A simple example of a strain component, ε_{yy} , due to an applied stress of σ_{yy} .

shear with rotation, and pure shear. A simple example of deformations and their corresponding deformation gradient tensors can be seen in Figure 2.10. Lastly, we see that displacements yield zero net deformation per Eq. (2.4.8); this makes intuitive sense as displacements do not deform materials.

Should the system be intentionally deformed, the Green–Lagrangian strain elements may be written in terms of deformation gradient tensor elements as

$$\varepsilon_{\alpha\beta} = \frac{1}{2} (F_{\gamma\alpha} F_{\gamma\beta} - \delta_{\alpha\beta}) , \quad (2.4.9)$$

where $\delta_{\alpha\beta}$ is the Kronecker delta as in Eq. (2.3.7). In matrix form, this may be written as $\boldsymbol{\varepsilon} = \frac{1}{2} (\mathbf{F}^T \mathbf{F} - \mathbf{I})$, where \mathbf{I} is the identity matrix, and \mathbf{F}^T is the transpose of \mathbf{F} . Finally, the Cauchy stress tensor, $\boldsymbol{\sigma}$, may be written in terms of Green–Lagrangian strain elements using the Hellmann–Feynman theorem for stresses as

$$\sigma_{\alpha\beta} = \frac{1}{\Omega} \frac{\partial E}{\partial \epsilon_{\alpha\beta}} . \quad (2.4.10)$$

For a different approach, Appendix G of Ref. [261] derives a stress expression from two-body forces in both real and Fourier space using a generalized virial expression.

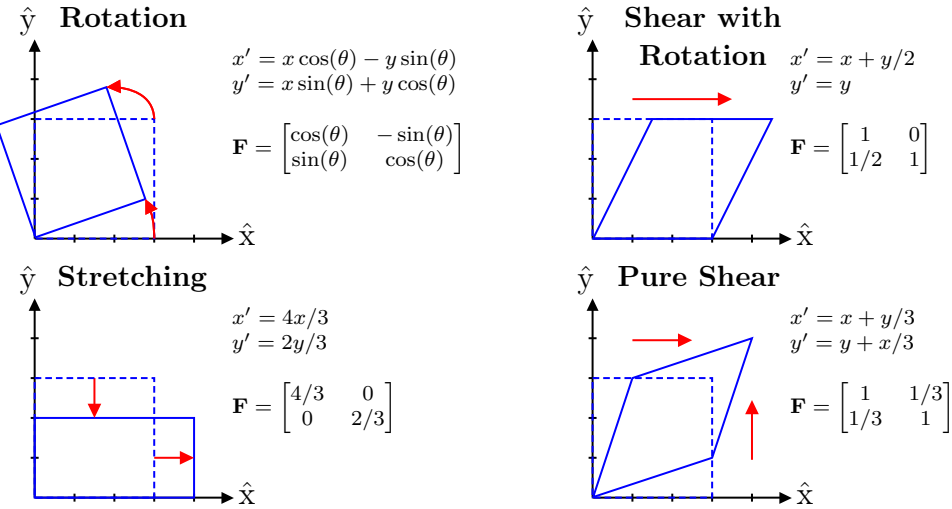


Figure 2.10: Deformations and their corresponding deformation gradient tensors. Pictured are the four basic types of deformations, including rotation (top left), stretching (bottom left), shear with rotation (top right), and pure shear (bottom right).

2.5 DISPERSION CORRECTIONS

In Section 1.3 we introduced the early empirical dispersion corrections of Cohen, Pack, and Scoles, and in Section 1.4 modern dispersion corrections were briefly discussed. Here, we explore the mathematical underpinnings of those post-SCF corrections. The section begins by exploring the Grimme DFT-D series of corrections: D1, D2, D3(0), D3(BJ), and D4. Subsequently, we present a comprehensive and mathematically detailed discussion of the dispersion corrections developed by Tkatchenko and collaborators, including TS, TS@SCS, MBD, MBD@SCS, MBD@rsSCS, and MBD-NL. Finally, this chapter concludes with an in-depth discussion of the XDM method of Johnson and Becke.

2.5.1 GRIMME DFT-D SERIES OF DISPERSION CORRECTIONS

D1 AND D2

In 2004, Grimme introduced the DFT-D method [39] for use in complexes of atoms and small molecules. The post-SCF dispersion energy was given by

$$E_{\text{DFT-D}} = -s_6 \sum_{i=1}^{N-1} \sum_{j=i+1}^N \frac{C_{6,ij}^{\text{DFT-D}}}{R_{ij}^6} f^{\text{WY}}(R_{ij}), \quad (2.5.1)$$

where N is the number of atoms, and s_6 is a functional-dependent empirical scaling factor. This dispersion model uses a Fermi-type [89, 90] damping function proposed by Wu and Yang,

$$f^{\text{WY}}(R_{ij}) = \frac{1}{1 + e^{-d\left(\frac{R_{ij}}{s R_{\text{vdW},ij}} - 1\right)}}, \quad (2.5.2)$$

where s and d are empirically-fitted parameters (for this method, $s = 1$), and $R_{\text{vdW},ij} = R_i^{\text{free}} + R_j^{\text{free}}$ is the sum of the free-atom van der Waal's radii. In this model, the $C_{6,ij}^{\text{DFT-D}}$ are determined via the harmonic mean of the free-atom homoatomic C_6 coefficients of atoms i and j , and averaged over the possible hybridization states. After two years of testing, Grimme released an updated version of the DFT-D model, known today as DFT-D2 [40], which greatly expanded the number of supported atomic species for study, up to and including radon. This time, the dispersion coefficients were calculated via their geometric mean rather than their harmonic mean, as this was shown to improve the accuracy of the method.

D3(0) AND D3(BJ)

The DFT-D3 dispersion model [41] was released in 2010 and improves on the D2 model via the inclusion of the C_8 dipole-quadrupole dispersion term through a recurrence relation [268–270]. The pairwise dispersion energy is thus given by

$$E_{\text{D3}}^{(2)} = - \sum_{ij} \sum_{n=6,8} s_n \frac{C_{6,ij}^{\text{D3}}}{R_{ij}^n} f_n^{\text{d}}(R_{ij}), \quad (2.5.3)$$

where the first sum is over all atom pairs and s_n is a functional-dependent and fitted scale factor. While recurrence relations were proposed up to an arbitrary C_n , only C_6 and C_8 are included, as terms beyond those were shown to lead to instability.

D3 additionally improved on D2 by switching from WY-damping to the damping function of Chai and Head-Gordon (CHG) [271], defined as

$$f^{\text{CHG}}(R_{ij}) = \frac{1}{1 + 6 \left(\frac{R_{ij}}{s R_{\text{vdW},ij}}\right)^{-\gamma}}. \quad (2.5.4)$$

CHG-damping, often referred to as “zero-damping” prevents the discontinuous behaviour at vanishing internuclear separation that is seen in Fermi-type WY damping. When used in combination with “zero-damping” D3 is referred to as D3(0). Further testing showed that the use of Becke–Johnson (BJ) damping [156] yielded improved results [92]. When D3 is used in combination with BJ-damping, it is referred to as

D3(BJ). Becke–Johnson damping is a rational-type damping function written as

$$f_n^{\text{BJ}}(R_{ij}) = \frac{R_{ij}^n}{R_{ij}^n + R_{\text{vdW},ij}^n}, \quad (2.5.5)$$

where $R_{\text{vdW},ij} = (a_1 R_{c,ij} + a_2)$ is the van der Waals radius, a_1 and a_2 are damping parameters that are fit to the particular density-functional, and $R_{c,ij}$ is the “critical” separation for interactions between atoms i and j , determined as the point where successive terms in the dispersion energy expression become equal. For D3(BJ), which uses C_6 and C_8 , this is given by

$$R_{c,ij}^{\text{D3}} = \sqrt{\frac{C_{8,ij}}{C_{6,ij}}}. \quad (2.5.6)$$

This rational-type damping function ensures that the dispersion energy approaches a small, but finite, value for vanishing internuclear separation. Finite damping was inspired by the convergent multipole expansion for two hydrogen atoms showing this finite-damping behaviour at the united-atom limit [272].

The D3 dispersion model calculates fractional coordination numbers (CNs) for all atoms in the system,

$$\text{CN}^A = \sum_{B \neq i}^N \frac{1}{1 + \exp \left[-k_1 \frac{k_2 (R_A^{\text{cov}} + R_B^{\text{cov}})}{R_{AB}} - 1 \right]}, \quad (2.5.7)$$

for fixed scale factors $k_1 = 16$ and $k_2 = 4/3$, and where R_A^{cov} and R_B^{cov} are scaled covalent (single-bond) radii for atoms A and B . These fractional coordination numbers smoothly interpolate between bonded and non-bonded atoms, scaling approximately linearly with the number of bonded interactions. An excellent diagram showing the coordination number of a hypothetical molecule may be found in Fig. 4 of Ref. [41].

Further, the D3 model precalculates reference C_6 values for all atom pairs for combinations of simple hydride molecules, A_mH_n and B_kH_l , using a modified Casimir–Polder formula [273–275] of the form

$$C_{6,AB}^{\text{ref}} = \frac{3}{\pi} \int_0^\infty \frac{\alpha^{\text{A}_m\text{H}_n}(\text{i}\omega) - \frac{n}{2}\alpha^{\text{H}_2}(\text{i}\omega)}{m} \frac{\alpha^{\text{B}_k\text{H}_l}(\text{i}\omega) - \frac{l}{2}\alpha^{\text{H}_2}(\text{i}\omega)}{k} d\omega. \quad (2.5.8)$$

The hydrogen contribution is removed via subtraction of the dihydrogen polarizability, $\alpha^{\text{H}_2}(\text{i}\omega)$, weighted according to the stoichiometric coefficients m , n , k , and l . The

heteroatomic dispersion coefficients are then determined by averaging over a set of reference systems using coordination-number-dependent weights as

$$C_{6,AB}^{\text{D3}} = \frac{\sum_i^{N_A} \sum_j^{N_B} C_{6,AB}^{\text{ref}} (\text{CN}_i^A, \text{CN}_j^B) \exp\left[-k_3 \left([\text{CN}^A - \text{CN}_i^A]^2 + [\text{CN}^B - \text{CN}_i^B]^2 \right)\right]}{\sum_i^{N_A} \sum_j^{N_B} \exp\left[-k_3 \left([\text{CN}^A - \text{CN}_i^A]^2 + [\text{CN}^B - \text{CN}_i^B]^2 \right)\right]}, \quad (2.5.9)$$

where $k_3 = 4$ is an empirical parameter, and N_A and N_B are the number of reference molecules (supporting points) for atoms A and B . Finally, CN_i^A and CN_j^B are coordination numbers for those for reference systems i and j corresponding to the precomputed reference value $C_{6,AB}^{\text{ref}} (\text{CN}_i^A, \text{CN}_j^B)$. Through the use of these fractional coordination numbers, the chemical environment is explicitly modelled through the molecular geometry, rather than using the partitioning of the electron density like other leading dispersion corrections.

Finally, the D3 model may also include Axilrod–Teller–Muto three-body contributions [276, 277] via the summation of two- and three-body energies,

$$E_{\text{D3}} = E_{\text{D3}}^{(2)} + E_{\text{D3}}^{(3)}. \quad (2.5.10)$$

The (undamped) ATM three-body energy for a trio of atoms, ABC , is given by

$$E_{ABC}^{\text{ATM}} = C_{9,ABC} \frac{3 \cos(\theta_a) \cos(\theta_b) \cos(\theta_c) + 1}{R_{AB}^3 R_{BC}^3 R_{CA}^3}, \quad (2.5.11)$$

where R_{AB}^3 is the cube of the interatomic distance between atoms A and B , and θ_a is the internal angle between \mathbf{R}_{AB} and \mathbf{R}_{AC} . As noted by Axilrod and Teller [276], this three-body term predicts repulsion for atoms in equilateral- or right-angle triangular configurations

$$E_{\text{Eq.}}^{\text{ATM}} = C_{9,123} \frac{11/8}{R_{12}^3 R_{23}^3 R_{31}^3}, \quad (2.5.12)$$

$$E_{\text{Ri.}}^{\text{ATM}} = C_{9,123} \frac{1}{R_{12}^3 R_{23}^3 R_{31}^3}, \quad (2.5.13)$$

and maximal attraction for linear configurations,

$$E_{\text{Lin.}}^{\text{ATM}} = C_{9,123} \frac{-2}{R_{12}^3 R_{23}^3 R_{31}^3}. \quad (2.5.14)$$

For D3, the three-body C_9 dispersion coefficient used for the computation of $E_{\text{D3}}^{(3)}$ is

approximated as the geometric mean of the C_6 coefficients as

$$C_{9,ABC}^{\text{D3}} = \sqrt{C_{6,AB} C_{6,BC} C_{6,CA}}. \quad (2.5.15)$$

Thus, the three-body contribution to the D3 energy is given by

$$E_{\text{D3}}^{(3)} = \sum_{ABC} f_{\text{ATM}}^{\text{d}} E_{ABC}^{\text{ATM}}. \quad (2.5.16)$$

where the damping function f^{d} is an ATM-parametrized CHG or BJ damping function. Note that the C_9 coefficient is a positive quantity, and the sign is stated explicitly for consistency with the rest of this thesis. This three-body energy is sometimes omitted for simplicity due to its negligible magnitude.

The DFT-D3 dispersion correction has been thoroughly benchmarked for dozens of density functionals and demonstrated its robustness across a large variety of chemical systems [278], especially on the GMTKN55 database for general main-group thermochemistry, kinetics, and noncovalent interactions [279–281].

D4

The DFT-D4 model [42, 43] was a recent addition to the Grimme-D series of dispersion corrections. This model extends DFT-D3 by estimating atomic partial charges, which are then used to calculate dispersion parameters. This is done through a charge-scaling function of the form

$$\zeta(z^A, z^{A,\text{ref}}) = \exp \left[\beta_1 \left\{ 1 - \exp \left[\gamma^A \left(1 - \frac{z^{A,\text{ref}}}{z^A} \right) \right] \right\} \right], \quad (2.5.17)$$

where $\beta_1 = 3$ and γ^A is taken from Ref. [282]. The effective nuclear charge on atom A is written as the sum of the nuclear charge and the atomic partial charge as $z^A = Z^A + q^A$. This charge-scaling function, in combination with a slightly modified description of the coordination number to capture electronegativity dependence, allows the D4 method to include atomic-charge dependence into the dispersion energy. For brevity, and because the D4 correction was rarely used within this work, the interested reader is directed to Refs. [42, 43] for a complete mathematical description.

Preliminary tests show that the D4 model outperforms its predecessor, D3(BJ), in addition to the TS [44] and various MBD [45, 48, 50] dispersion corrections across a range of periodic systems in terms of both speed and accuracy [43, 281]. We note that, while D4 (and also D3) show strong performance on GMTKN55 [279–281], this can

be partially attributed to the large overlap between their damping parameterization set (S22, S22+, ACONF, SCONF, PCONF, CCONF, ADIM6, RG6) and GMTKN55 itself.

2.5.2 THE TS AND MBD DISPERSION MODELS

The Tkatchenko–Scheffler (TS) model is a pairwise density-dependent dispersion correction that was introduced in 2009 [44]. In 2012, Tkatchenko *et al.* added two significant extensions to the TS model. The first was the use of self-consistent screening (SCS) for determining the screened dynamic polarizabilities of the atoms in the system. The second was the introduction of their many-body dispersion (MBD) model which describes the dispersion interactions between a system’s atoms by modelling them as a system of N -coupled Drude oscillators [283, 284]. These models are explained in incredible detail by DiStasio *et al.* in their 2014 article [48], and this will be the main reference for the theory in this section. We note that the functionals of choice to pair with the TS and MBD models are either the Perdew–Burke–Ernzerhof (PBE) GGA functional [149, 150] or the PBE0 hybrid functional [163], likely due to their low empiricism, and wide popularity for modelling the solid state. For the MBD methods, the S66×8 [285–287] benchmark set is commonly used to fit the damping parameters [46].

THE TKATCHENKO–SCHEFFLER MODEL

The Tkatchenko–Scheffler (TS) model [44] only considers the lowest-order dispersion term, corresponding to instantaneous dipole-dipole contributions of the form

$$E_{\text{TS}} = -\frac{1}{2} \sum_{ij} f^{\text{WY}}(R_{ij}) \frac{C_{6,ij}^{\text{TS}}}{R_{ij}^6}. \quad (2.5.18)$$

Here, the sum is over all electron pairs. Via a Hirshfeld partitioning [93, 94] of the electron density, the Hirshfeld weights,

$$w_i(\mathbf{r}) = \frac{\rho_i^{\text{free}}(\mathbf{r})}{\sum_j \rho_j^{\text{free}}(\mathbf{r})}, \quad (2.5.19)$$

and effective volumes ratios,

$$\frac{v_i}{v_i^{\text{free}}} = \frac{\int r^3 w_i(\mathbf{r}) \rho_i(\mathbf{r}) d\mathbf{r}}{\int r^3 \rho_i^{\text{free}}(\mathbf{r}) d\mathbf{r}}, \quad (2.5.20)$$

for a general atom i are determined. The sum over spin states σ is implied. Using this volume ratio, the effective homoatomic dispersion coefficients ($C_{6,ii}$), static polarizabilities (α_i^0), and vdW radii may be determined via

$$C_{6,ii} = \left(\frac{v_i}{v_i^{\text{free}}} \right)^2 C_{6,ii}^{\text{free}}, \quad (2.5.21)$$

$$\alpha_i^0 = \left(\frac{v_i}{v_i^{\text{free}}} \right) \alpha_i^{\text{free}}, \quad (2.5.22)$$

$$R_i^0 = \left(\frac{v_i}{v_i^{\text{free}}} \right)^{1/3} R_i^{\text{free}}, \quad (2.5.23)$$

where the values of $C_{6,ii}^{\text{free}}$, α_i^{free} , and R_i^{free} are obtained from existing literature [288–290]. We note that TS’s use of the Wu–Yang damping function [87], as defined in Eq. (2.5.2) for D1 and D2, is slightly different. Specifically, unlike these Grimme–D methods that define the heteroatomic vdW radii as the sum of free-atom values, R_i^{free} , TS instead defines it as the sum of the effective vdW radii, R_i^0 . Finally, the heteroatomic dispersion coefficients are obtained from their homoatomic counterparts using the Slater–Kirkwood formula [72, 291–293]:

$$C_{6,ij}^{\text{TS}} = \frac{2C_{6,ii}C_{6,jj}}{\frac{\alpha_j^0}{\alpha_i^0}C_{6,ii} + \frac{\alpha_i^0}{\alpha_j^0}C_{6,jj}}. \quad (2.5.24)$$

The TS model [44] has demonstrated reasonable performance on benchmarks of small molecular systems [44, 294], but has difficulties for molecular-crystal benchmarks such as C21 [99], or its extension X23 [295]. Further, the TS model has shown to overestimate the dispersion energy, resulting in overbinding [35, 51, 295, 296].

SELF-CONSISTENT SCREENING FORMALISM

Through the use of self-consistent screening (SCS) [95–97], the polarizabilities for each atom may be refined via the SCS equation of classical electrodynamics,

$$\boldsymbol{\alpha}_i^{\text{SCS}}(\text{i}\omega) = \alpha_i^{\text{TS}}(\text{i}\omega) + \alpha_i^{\text{TS}}(\text{i}\omega) \sum_{j \neq i} \mathbf{T}_{ij} \boldsymbol{\alpha}_j^{\text{SCS}}(\text{i}\omega), \quad (2.5.25)$$

where $\boldsymbol{\alpha}_i^{\text{SCS}}$ is a tensor that contains the x , y , and z polarizability components for atom i . The frequency-dependent TS polarizability is approximated by considering

the leading term of the Padé series [297–299] as

$$\alpha_i^{\text{TS}}(\omega) = \frac{\alpha_i^0}{1 - (\omega/\omega_i)^2}, \quad (2.5.26)$$

where the characteristic excitation frequency for quantum Drude oscillators, derived from the London dispersion formula [23], is

$$\omega_i = \frac{4}{3} \frac{C_{6,ii}}{(\alpha_i^0)^2}. \quad (2.5.27)$$

The second-rank dipole-dipole interaction tensor [293] in Eq. (2.5.25) is calculated via a tensor product of gradient operators,

$$\mathbf{T}_{ij} = \nabla_{\mathbf{R}_i} \otimes \nabla_{\mathbf{R}_j} v_{ij}, \quad (2.5.28)$$

acting on a potential,

$$v_{ij} = \frac{1}{R_{ij}} \operatorname{erf} \left[\frac{R_{ij}}{\sigma_{ij}} \right], \quad (2.5.29)$$

where $R_{ij} = |\mathbf{R}_i - \mathbf{R}_j|$ is the internuclear distance with components $\mathbf{R}_i = \{x_i, y_i, z_i\}$, $\operatorname{erf}[\dots]$ is the Gauss error function [300, 301], and the effective width of the Gaussian charge distribution is $\sigma_{ij} = (\sigma_i^2 + \sigma_j^2)^{1/2}$ for individual contributions given by $\sigma_i = [\sqrt{2/\pi} (\alpha_i^{\text{TS}}/3)]^{1/3}$. The dipole-dipole interaction tensor elements, \mathcal{T}_{ij}^{ab} , are written explicitly as

$$\mathcal{T}_{ij}^{ab} = -\frac{3R_{ij,a}R_{ij,b} - R_{ij}^2\delta_{ab}}{R_{ij}^5} \left[\operatorname{erf} \left[\frac{R_{ij}}{\sigma_{ij}} \right] - \frac{2}{\sqrt{\pi}} \frac{R_{ij}}{\sigma_{ij}} e^{-(R_{ij}/\sigma_{ij})^2} \right] + \frac{4}{\sqrt{\pi}} \frac{R_{ij,a}R_{ij,b}}{\sigma_{ij}^3 R_{ij}^2} e^{-(R_{ij}/\sigma_{ij})^2}, \quad (2.5.30)$$

where δ_{ij} is the Kronecker delta, and $R_{ij,a}$ is the magnitude of the a^{th} Cartesian component of the internuclear distance between nuclei.

As described in Ref. [48], the SCS equation may be solved using matrix algebra for a series of specific values of angular frequency ω . We construct a $3N \times 3N$ matrix, \mathbf{A} , which is partitioned into 3×3 sub-blocks for each atom i in the system. The i^{th} diagonal 3×3 sub-block will be a diagonal submatrix with non-zero elements of $1/\alpha_i^{\text{TS}}$ from Eq. (2.5.26). The $\{i, j\}^{\text{th}}$ off-diagonal 3×3 sub-block will be the elements of the $\{i, j\}$ -indexed dipole-dipole interaction tensor, \mathbf{T}_{ij} . To illustrate the construction of \mathbf{A} , we consider a system of $N = 3$ particles. The corresponding 9×9 matrix \mathbf{A} will

have the form

$$\mathbf{A} = \begin{bmatrix} 1/\alpha_1^{\text{TS}} & 0 & 0 & \mathcal{T}_{12}^{xx} & \mathcal{T}_{12}^{xy} & \mathcal{T}_{12}^{xz} & \mathcal{T}_{13}^{xx} & \mathcal{T}_{13}^{xy} & \mathcal{T}_{13}^{xz} \\ 0 & 1/\alpha_1^{\text{TS}} & 0 & \mathcal{T}_{12}^{yx} & \mathcal{T}_{12}^{yy} & \mathcal{T}_{12}^{yz} & \mathcal{T}_{13}^{yx} & \mathcal{T}_{13}^{yy} & \mathcal{T}_{13}^{yz} \\ 0 & 0 & 1/\alpha_1^{\text{TS}} & \mathcal{T}_{12}^{zx} & \mathcal{T}_{12}^{zy} & \mathcal{T}_{12}^{zz} & \mathcal{T}_{13}^{zx} & \mathcal{T}_{13}^{zy} & \mathcal{T}_{13}^{zz} \\ \hline \mathcal{T}_{21}^{xx} & \mathcal{T}_{21}^{xy} & \mathcal{T}_{21}^{xz} & 1/\alpha_2^{\text{TS}} & 0 & 0 & \mathcal{T}_{23}^{xx} & \mathcal{T}_{23}^{xy} & \mathcal{T}_{23}^{xz} \\ \mathcal{T}_{21}^{yx} & \mathcal{T}_{21}^{yy} & \mathcal{T}_{21}^{yz} & 0 & 1/\alpha_2^{\text{TS}} & 0 & \mathcal{T}_{23}^{yx} & \mathcal{T}_{23}^{yy} & \mathcal{T}_{23}^{yz} \\ \mathcal{T}_{21}^{zx} & \mathcal{T}_{21}^{zy} & \mathcal{T}_{21}^{zz} & 0 & 0 & 1/\alpha_2^{\text{TS}} & \mathcal{T}_{23}^{zx} & \mathcal{T}_{23}^{zy} & \mathcal{T}_{23}^{zz} \\ \hline \mathcal{T}_{31}^{xx} & \mathcal{T}_{31}^{xy} & \mathcal{T}_{31}^{xz} & \mathcal{T}_{32}^{xx} & \mathcal{T}_{32}^{xy} & \mathcal{T}_{32}^{xz} & 1/\alpha_3^{\text{TS}} & 0 & 0 \\ \mathcal{T}_{31}^{yx} & \mathcal{T}_{31}^{yy} & \mathcal{T}_{31}^{yz} & \mathcal{T}_{32}^{yx} & \mathcal{T}_{32}^{yy} & \mathcal{T}_{32}^{yz} & 0 & 1/\alpha_3^{\text{TS}} & 0 \\ \mathcal{T}_{31}^{zx} & \mathcal{T}_{31}^{zy} & \mathcal{T}_{31}^{zz} & \mathcal{T}_{32}^{zx} & \mathcal{T}_{32}^{zy} & \mathcal{T}_{32}^{zz} & 0 & 0 & 1/\alpha_3^{\text{TS}} \end{bmatrix}. \quad (2.5.31)$$

The i^{th} atom's SCS polarizability tensor may then be determined by the summation of the i^{th} 3×3 sub-block's row of the inverted matrix \mathbf{A}^{-1} ,

$$\boldsymbol{\alpha}_i^{\text{SCS}} = \sum_{j=1}^N [\mathbf{A}^{-1}]_{ij}. \quad (2.5.32)$$

The diagonal and scalar elements (α_i^{SCS}) of the SCS polarizability ($\boldsymbol{\alpha}_i^{\text{SCS}}$) may then be extracted for use in the Casimir–Polder integral [274],

$$C_{6,ij}^{\text{TS@SCS}} = \frac{3}{\pi} \int_0^\infty \alpha_i(\text{i}\omega) \alpha_j(\text{i}\omega) d\omega, \quad (2.5.33)$$

and solved via Gauss-Legendre quadrature [302] or other suitable numerical methods to obtain the SCS dispersion coefficients. These C_6 coefficients may be used in Eq. (2.5.18), giving rise to the TS@SCS method. The SCS vdW radii required for the damping function are $R_i^{\text{SCS}} = (\alpha_i^{\text{SCS}} / \alpha_i^{\text{free}})^{1/3} R_i^{\text{free}}$.

THE MANY-BODY DISPERSION MODEL

The many-body dispersion (MBD) model's energy [45] is computed via the coupled fluctuating dipole model (CFDM) Hamiltonian [303–307], where each atom in the system is represented by a corresponding Drude oscillator [283, 284] (i.e. an isotropic quantum harmonic oscillator). The CFDM Hamiltonian for an arbitrary dipole-dipole interaction tensor, \mathbf{T}'_{ij} , is given by

$$\hat{H} = -\frac{1}{2} \sum_i^N \nabla_{\xi_i}^2 + \frac{1}{2} \sum_i^N (\omega_i^{\text{SCS}} \xi_i)^2 + \sum_i^N \sum_{j < i}^N \omega_i^{\text{SCS}} \omega_j^{\text{SCS}} \sqrt{\alpha_i^{\text{SCS}} \alpha_j^{\text{SCS}}} \xi_i \mathbf{T}'_{ij} \xi_j, \quad (2.5.34)$$

where $\xi_i = \sqrt{m_i} \Delta r_i$ is the mass-weighted displacement from the i^{th} atomic position from equilibrium with $1/m_i = \alpha_i^{\text{SCS}}(\omega_i^{\text{SCS}})^2$ and $\omega_i^{\text{SCS}} = \frac{4}{3}C_{6,ii}^{\text{SCS}}/\alpha_i^{\text{SCS}}$.⁷ The solution of this system requires diagonalizing the $3N \times 3N$ \mathbf{C}^{MBD} matrix, which is composed of 3×3 matrix sub-blocks, $\mathbf{C}_{ij}^{\text{MBD}}$, describing the dipolar coupling between oscillators as

$$\mathbf{C}_{ij}^{\text{MBD}} = \delta_{ij} (\omega_i^{\text{SCS}})^2 + (1 - \delta_{ij}) \omega_i^{\text{SCS}} \omega_j^{\text{SCS}} \sqrt{\alpha_i^{\text{SCS}} \alpha_j^{\text{SCS}}} \mathbf{T}_{ij}. \quad (2.5.35)$$

Further, while Eq. (2.5.34) implies the use of SCS, it is not strictly necessary. As only the lowest-order interactions are considered via the dipole-dipole interaction tensor, \mathbf{T}_{ij} , MBD is considered a C_6 -only method. Although recent work has extended MBD to include quadrupolar terms which would capture C_8 and part of C_{10} [308, 309], this so-called MBDQ variant is not presently implemented in any open-source codes to our knowledge. The diagonalization of the \mathbf{C}^{MBD} matrix yields $3N$ eigenvalues, λ_i , which correspond to the square of the interacting quantum harmonic oscillator frequencies. The MBD interaction energy is then given by the difference of the interacting and non-interacting frequencies as

$$E_{\text{MBD}} = \frac{1}{2} \sum_{i=1}^{3N} \sqrt{\lambda_i} - \frac{3}{2} \sum_{i=1}^N \omega_i^{\text{SCS}}. \quad (2.5.36)$$

The MBD model is based on the adiabatic connection fluctuation-dissipation [310–313] (ACFD) theorem within the random-phase approximation (RPA) framework [174, 175]. This ACFD-RPA approach can be used to obtain the correlation energy for a system of N interacting quantum harmonic oscillators for a dipole-dipole interaction potential [48, 181] via

$$E_{\text{C}}^{\text{RPA}} = -\frac{1}{2\pi} \int_0^\infty d\omega \sum_{n=2}^N \frac{1}{n} \text{tr} \left[(\chi_0 v)^n \right]. \quad (2.5.37)$$

Here, χ_0 is the non-interacting response function, and v is the interaction potential. The $\chi_0 v$ term may be written in matrix form as the product \mathbf{AT} , where \mathbf{A} is a diagonal $3N \times 3N$ matrix with the negative of the frequency-dependent input polarizability for particle i on each of the 3×3 diagonal subblocks, and \mathbf{T} is a dipole-dipole interaction tensor. Eq. (2.5.37) enables one to decompose the MBD energy into each of its n -body contributions.

⁷We note that Eq. (2.5.34) requires α_i^{SCS} and ω_i^{SCS} to be independent of frequency, as indicated within `mbd_methods.f90` in the FHI-aims code, retrieved 2022/12.

MBD [45] has improved performance over the TS [44] model for the S22 [314], S66 [285, 286], S66×8 [285–287], and S66×7 [46] benchmarks of gas-phase molecular dimers both near and away from their equilibrium geometries, indicating a better description of intermolecular noncovalent interactions.

RANGE-SEPARATED SELF-CONSISTENT SCREENING

Tkatchenko *et al.* proposed using a range-separated self-consistent screening variant of MBD, named MBD@rsSCS [46, 47] to damp the dispersion energy at short intermolecular separations. This range-separation is accomplished by introducing a WY-damping function [87], as in Eq. (2.5.2), to modify the dipole-dipole interaction tensor from Eq. (2.5.28) into a short-range version, $\mathbf{T}_{\text{SR},ij}$ with elements

$$\mathcal{T}_{\text{SR},ij}^{ab} = (1 - f^{\text{WY}}(R_{ij})) \mathcal{T}_{ij}^{ab}. \quad (2.5.38)$$

We note that the WY damping function is parameterized using $d = 6$ and different β damping parameters compared to TS. The rsSCS polarizabilities, α_i^{rsSCS} , and characteristic excitation frequencies, ω_i^{rsSCS} , are determined by substitution of $\mathbf{T}_{\text{SR},ij}$ into the SCS equation as given in Eq. (2.5.25). Similarly, the long-range dipole-dipole interaction tensor, $\mathbf{T}_{\text{LR},ij}$, is approximated to have a frequency-independent form with elements described by

$$\mathcal{T}_{\text{LR},ij}^{ab} = f^{\text{WY}}(R_{ij}) \frac{-3R_a R_b + R_{ij}^2 \delta_{ab}}{R_{ij}^5}. \quad (2.5.39)$$

Written generally, the ACFDT-RPA MBD correlation energy is then given by

$$E_{\text{C}}^{\text{MBD}} = \frac{1}{2\pi} \int_0^\infty \text{tr} [\ln(\mathbf{1} - \mathbf{A}\mathbf{T}_{\text{LR}})] d\omega, \quad (2.5.40)$$

where \mathbf{A} is a $3N \times 3N$ diagonal matrix⁸ with elements $\mathbf{A}_{ij} = -\delta_{ij} \alpha_i^{\text{RFA}}(i\omega)$ for the choice of response-function approximation (RFA) determined polarizabilities [174–179]. In practice, the MBD@rsSCS energy may be computed by substituting α^{rsSCS} , ω^{rsSCS} , and \mathbf{T}_{LR} into Eq. (2.5.35) as before.

Extensive benchmarking of MBD@rsSCS has shown slight improvements over MBD across a diverse range of data sets [46, 294, 295]. A fractionally-ionic variant introduced by Gould *et al.* in 2016, named MBD/FI showed improvement over

⁸ \mathbf{A} should not be confused with the SCS matrix \mathbf{A} from Eq. (2.5.31).

MBD@rsSCS across several molecular benchmarks. MBD/FI was not used throughout this thesis and so it will not be detailed; for further discussion related to it, the reader is directed to Refs. [50, 294].

Unfortunately, the MBD methods have significant drawbacks. These corrections are known to be unstable and occasionally experience a “polarization catastrophe”, which manifests as negative eigenvalues in the CFDM Hamiltonian, leading to complex-valued energies and other unphysical behaviour. A polarization catastrophe happens when some dipole interaction tensor elements become similar in magnitude, a situation that becomes more likely if the starting polarizabilities are too large [48, 315].

MBD-NL

A recent addition to the MBD family is the MBD-NL dispersion correction [52]. Instead of relying on the TS@SCS polarizabilities as a starting point, MBD-NL uses Vydrov and van Voorhis’ (VV) semilocal polarizability functional from the nonlocal VV10 dispersion model [63, 316], given by

$$\alpha^{\text{VV}}[n](\mathbf{r}, i\omega) = \frac{\rho(\mathbf{r})}{\frac{4\pi}{3}\rho(\mathbf{r}) + C \frac{|\nabla\rho(\mathbf{r})|^4}{\rho(\mathbf{r})^4} + \omega^2}, \quad (2.5.41)$$

where C is an empirical parameter, and the C_6 coefficients are determined via the Casimir–Polder formula. Because the polarizability functional is not accurate for all elements, the polarizabilities and C_6 coefficients are scaled using the ratio between reference calculations and VV-functional-derived quantities, as follows:

$$\alpha_{0,i}^{\text{rVV}} = \alpha_{0,i}^{\text{VV}} \frac{\alpha_{0,i}^{\text{ref,free}}}{\alpha_{0,i}^{\text{VV,free}}} \quad (2.5.42)$$

$$C_{6,ii}^{\text{rVV}} = C_{6,ii}^{\text{VV}} \frac{C_{6,ii}^{\text{ref,free}}}{C_{6,ii}^{\text{VV,free}}}. \quad (2.5.43)$$

Further, two local electron-density descriptors are used to correct the polarizability. The first is the local ionization potential [317],

$$I[\rho] = \frac{\tau^W[\rho]}{\rho}, \quad (2.5.44)$$

expressed in terms of the von Weizsäcker kinetic energy [318]. The second is the

iso-orbital locator [319–321],

$$\chi[\rho] = \frac{\tau^{\text{KS}}[\rho] - \tau^{\text{W}}[\rho]}{\tau^{\text{UEG}}[\rho]}. \quad (2.5.45)$$

Here, $\tau^{\text{KS}}[\rho] = \sum_i \|\nabla\psi_i^{\text{KS}}\|^2/2$ is the Kohn–Sham kinetic energy, and the kinetic energy of the uniform electron gas is given by $\tau^{\text{UEG}}[\rho] = 3(3\pi^2)^{2/3}\rho^{5/3}/10$. These two descriptors are used as the main components of a carefully-constructed cutoff function,

$$g(I, \chi) = 1 - \frac{1 - f(\chi - 3\sqrt{I/E_h})}{1 + \exp[4(I - 5 \text{ eV})/1 \text{ eV}]} . \quad (2.5.46)$$

Here, E_h is 1.0 Ha. of energy, eV is an electron volt, and $f(x)$ is taken from the SCAN functional [322], given by

$$f(x) = \exp\left[-\frac{\theta(x)x}{10(1-x)}\right]\theta(1-x) \quad (2.5.47)$$

where $\theta(x)$ is a step function of x . Finally, this cutoff function is applied to the polarizability via

$$\alpha^{\text{VV}'}[\rho] = g(I, \chi) \alpha^{\text{VV}}[\rho]. \quad (2.5.48)$$

The resulting effect is the avoidance of double counting long-range electron correlation, as well as density-tail overlap issues observed with the VV functional that can lead to overbinding.

Broadly speaking, one major goal for this model was to remedy the “polarization catastrophe” issues seen in previous MBD methods. As such, these polarizabilities are not further refined via SCS. Except for a small modification to the definition of the van der Waals radii,

$$R_i^{\text{vdW}} = \frac{5}{2} \left(\alpha_{0,i}^{\text{ref,free}} \right)^{\frac{1}{7}} \left(\frac{\alpha_i^{\text{rVV}'}}{\alpha_i^{\text{rVV}',\text{free}}} \right)^{\frac{1}{3}}, \quad (2.5.49)$$

the remainder of the calculation of dispersion energy for MBD-NL follows that of the MBD@rsSCS method.

Preliminary results with MBD-NL [52] show improved performance in metals and ionic solids where MBD@rsSCS and MBD/FI experience instability or crashing. However, MBD-NL does not fully resolve polarization catastrophes, and the CFDM Hamiltonian occasionally still produces negative eigenvalues and complex-valued dispersion

energies. As such, the polarization catastrophe will unfortunately become a recurring theme in this thesis, and will be discussed again in Chapters 4 to 6.

2.5.3 THE EXCHANGE-HOLE DIPOLE MOMENT MODEL

The exchange-hole dipole moment (XDM) model [53–57] is a post-SCF, or *a posteriori*, dispersion correction based on second-order perturbation theory. The XDM model calculates the dispersion energy via

$$E_{\text{XDM}} = - \sum_{i < j} \sum_{n=6,8,10} \frac{f_n^{\text{BJ}}(R_{ij}) C_{n,ij}^{\text{XDM}}}{R_{ij}^n}, \quad (2.5.50)$$

where i and j run over all atom pairs. This model only considers the $n = 6, 8, 10$ terms from the multipole expansion, as it has been shown that the contribution of higher-order terms is negligible [91]. The XDM model is unlike other dispersion corrections in that its foundation is based on the principle that instantaneous dipoles form between reference electrons and their corresponding exchange(-correlation) holes. These instantaneous dipoles create dispersion interactions that manifest as attractive forces between atoms.

Canonically, XDM uses the Becke–Johnson damping function [156],

$$f_n^{\text{BJ}}(R_{ij}) = \frac{R_{ij}^n}{R_{ij}^n + R_{\text{vdW},ij}^n}, \quad (2.5.51)$$

where $R_{\text{vdW},ij} = (a_1 R_{c,ij} + a_2)$ is the van der Waals radius, the definition of which contains two damping parameters a_1 and a_2 . These damping parameters are fitted for a particular basis–functional combination, determined by minimising the root-mean-square percent error (RMSPE) for the binding energies of the KB49 set of small molecular dimers [123, 323]. $R_{c,ij}$ is the “critical” separation for interactions between atoms i and j , at which point the successive terms in the perturbation theory expansion of the dispersion energy become equal. In Section 2.5.1, the DFT-D3 correction only considers the C_6 and C_8 contributions, thus $R_{c,ij} = \sqrt{C_{8,ij}/C_{6,ij}}$. For XDM, however, the C_{10} term is also included so there exist three possible definitions for the “critical” separation

$$R_{c,ij} = \begin{cases} \sqrt{C_{8,ij}/C_{6,ij}} \\ \sqrt{C_{10,ij}/C_{8,ij}} \\ \sqrt[4]{C_{10,ij}/C_{6,ij}} \end{cases} \quad (2.5.52)$$

and so the value is chosen to be their mean,

$$R_{c,ij} = \frac{1}{3} \left[\left(\frac{C_{8,ij}^{\text{XDM}}}{C_{6,ij}^{\text{XDM}}} \right)^{1/2} + \left(\frac{C_{10,ij}^{\text{XDM}}}{C_{6,ij}^{\text{XDM}}} \right)^{1/4} + \left(\frac{C_{10,ij}^{\text{XDM}}}{C_{8,ij}^{\text{XDM}}} \right)^{1/2} \right]. \quad (2.5.53)$$

This section will derive the XDM multipole dispersion coefficients, discuss the use of the Becke–Roussel (BR) hole in XDM, and show how forces and stresses are calculated in the XDM model. For further depth, the reader is directed to excellent existing explanations of the inner workings of XDM [55–57, 156] and the references therein.

MULTIPOLE DISPERSION COEFFICIENTS

The exchange hole (or Fermi hole [68]), $h_{\text{X}\sigma}(\mathbf{r}, \mathbf{s})$, describes the depletion of probability of finding a second same-spin electron at coordinate \mathbf{s} due to the presence of an electron at a reference point \mathbf{r} —an effect caused by the Pauli exclusion principle. Central to the XDM model is the proposal that this depletion of probability is what gives rise to the aforementioned instantaneous dipoles associated with London dispersion. Because the pair probability vanishes when a second same-spin electron is at the same coordinate as the first (i.e., $\mathbf{s} = \mathbf{r}$), the exchange hole must satisfy:

$$h_{\text{X}\sigma}(\mathbf{r}, \mathbf{r}) = -\rho_\sigma(\mathbf{r}). \quad (2.5.54)$$

Further, the exchange hole is normalized to -1 electron so that

$$\int h_{\text{X}\sigma}(\mathbf{r}, \mathbf{s}) d\mathbf{s} = -1. \quad (2.5.55)$$

The exchange-hole dipole moment for a reference point \mathbf{r} is obtained by integrating the exchange hole over \mathbf{s} via

$$\mathbf{d}_{\text{X}\sigma}(\mathbf{r}) = \left(\int \mathbf{s} |h_{\text{X}\sigma}(\mathbf{r}, \mathbf{s})| d\mathbf{s} \right) - \mathbf{r} \quad (2.5.56)$$

where the absolute value arises because the exchange hole is negative everywhere.

To compute the dipole-dipole C_6 dispersion coefficients, first the square of the expectation value of the dipole moment's magnitude is computed,

$$\langle d_{\text{X}}^2 \rangle = \sum_{\sigma} \int w_i(\mathbf{r}) \rho_{\sigma}(\mathbf{r}) d_{\text{X}\sigma}^2(\mathbf{r}) d\mathbf{r}, \quad (2.5.57)$$

which is summed over occupied σ -spin states. Further, the atom-in-molecule polarizabilities are defined equivalently to those of the TS model from Section 2.5.2 as

$$\alpha_i = \alpha_i^{\text{free}} \frac{v_i}{v_i^{\text{free}}} , \quad (2.5.58)$$

where α^{free} is the free atomic polarizability taken from readily available sources [324], and $v_i = \langle r^3 \rangle_i$ is the effective volume computed using the Hirshfeld partitioning weights, via $w_i(\mathbf{r})$, of the electron density. These polarizabilities and exchange-hole dipole moments are determined for each atom i and j in the system. Finally, the heteroatomic C_6 dispersion coefficients may be determined via

$$C_{6,ij} = \frac{\alpha_i \alpha_j \langle d_X^2 \rangle_i \langle d_X^2 \rangle_j}{\alpha_i \langle d_X^2 \rangle_j + \alpha_j \langle d_X^2 \rangle_i} , \quad (2.5.59)$$

which is a key result from the perturbation theory of dispersion, as shown in Eq. (1.2.9).

To compute accurate dispersion energies for realistic systems, we require the inclusion of higher-order ℓ -pole contributions such as quadrupole ($\ell = 2$) or octupole ($\ell = 3$) moments. Consider a reference electron and exchange-hole centre located at distances r and $(r - d_{X\sigma})$ from the nucleus. The strength of that dipole moment is thus $r - (r - d_{X\sigma})$, and so the magnitude of the ℓ -pole moments is then $r^\ell - (r - d_{X\sigma})^\ell$. It follows that the general multipole-moment integral is of the form

$$\langle M_\ell^2 \rangle = \sum_\sigma \int w_i(\mathbf{r}) \rho_\sigma(\mathbf{r}) [r_i^\ell - (r_i - d_{X\sigma})^\ell]^2 d\mathbf{r} , \quad (2.5.60)$$

where $r_i(\mathbf{r}) = |\mathbf{R}_i - \mathbf{r}|$ and R_i is the position of atom i . Finally, the pairwise $C_{n,ij}$ coefficients for Eq. (2.5.50) may be expressed in terms of these multipole-moment integrals as

$$C_{6,ij}^{\text{XDM}} = \frac{\alpha_i \alpha_j \langle M_1^2 \rangle_i \langle M_1^2 \rangle_j}{\alpha_i \langle M_1^2 \rangle_j + \alpha_j \langle M_1^2 \rangle_i} , \quad (2.5.61)$$

$$C_{8,ij}^{\text{XDM}} = \frac{3}{2} \frac{\alpha_i \alpha_j (\langle M_1^2 \rangle_i \langle M_2^2 \rangle_j + \langle M_2^2 \rangle_i \langle M_1^2 \rangle_j)}{\alpha_i \langle M_1^2 \rangle_j + \alpha_j \langle M_1^2 \rangle_i} , \quad (2.5.62)$$

$$C_{10,ij}^{\text{XDM}} = 2 \frac{\alpha_i \alpha_j (\langle M_1^2 \rangle_i \langle M_3^2 \rangle_j + \langle M_3^2 \rangle_i \langle M_1^2 \rangle_j)}{\alpha_i \langle M_1^2 \rangle_j + \alpha_j \langle M_1^2 \rangle_i} + \frac{21}{5} \frac{\alpha_i \alpha_j \langle M_2^2 \rangle_i \langle M_2^2 \rangle_j}{\alpha_i \langle M_1^2 \rangle_j + \alpha_j \langle M_1^2 \rangle_i} . \quad (2.5.63)$$

To capture atomic many-body effects, the XDM model may also, optionally, include the three-body Axilrod–Teller–Muto (ATM) dispersion term [276, 277] as shown in Eq. (2.5.11). Writing this contribution in a familiar form for use in XDM, we arrive at

$$E_{\text{XDM}}^{\text{ATM}} = \sum_{i < j < k} \frac{f_{\text{ATM}}^{\text{BJ}}(R_{ij}, R_{ik}, R_{jk}) C_{9,ijk}^{\text{XDM}} [3 \cos(\theta_i) \cos(\theta_j) \cos(\theta_k) + 1]}{R_{ij}^3 R_{jk}^3 R_{ki}^3}, \quad (2.5.64)$$

with $C_{9,ijk}$ coefficients arising from the nonadditive instantaneous dipole interactions between atoms i , j , and k of the form

$$C_{9,ijk}^{\text{XDM}} = \frac{4}{9} \frac{\epsilon_i + \epsilon_j + \epsilon_k}{(\epsilon_i + \epsilon_j)(\epsilon_j + \epsilon_k)(\epsilon_i + \epsilon_k)} \langle M_1^2 \rangle_i \langle M_1^2 \rangle_j \langle M_1^2 \rangle_k \quad (2.5.65)$$

where ϵ_i is the average atomic excitation energy of atom i . By expressing these excitation energies in terms of polarizabilities, as shown in Section 1.2, the XDM C_9 coefficients may be written as

$$C_{9,ijk}^{\text{XDM}} = \frac{\langle M_1^2 \rangle_i \langle M_1^2 \rangle_j \langle M_1^2 \rangle_k \left(\frac{\langle M_1^2 \rangle_i}{\alpha_i^0} + \frac{\langle M_1^2 \rangle_j}{\alpha_j^0} + \frac{\langle M_1^2 \rangle_k}{\alpha_k^0} \right)}{\left(\frac{\langle M_1^2 \rangle_i}{\alpha_i^0} + \frac{\langle M_1^2 \rangle_j}{\alpha_j^0} \right) \left(\frac{\langle M_1^2 \rangle_i}{\alpha_i^0} + \frac{\langle M_1^2 \rangle_k}{\alpha_k^0} \right) \left(\frac{\langle M_1^2 \rangle_j}{\alpha_j^0} + \frac{\langle M_1^2 \rangle_k}{\alpha_k^0} \right)}. \quad (2.5.66)$$

Lastly, the recommended Becke–Johnson damping function for the ATM term is determined by the product of three f_3^{BJ} damping functions as

$$f_{\text{ATM}}^{\text{BJ}}(R_{ij}, R_{ik}, R_{jk}) = f_3^{\text{BJ}}(R_{ij}) f_3^{\text{BJ}}(R_{ik}) f_3^{\text{BJ}}(R_{jk}). \quad (2.5.67)$$

This corrective term to the dispersion energy is omitted from the default implementation of the XDM method as it has been shown to have no effect on the errors in computed binding energies or can even cause the error to slightly increase [91]. It is believed that this behaviour is due to errors from the base density functional being an order of magnitude larger than the ATM dispersion energy for molecular clusters [57, 325].

THE EXACT-EXCHANGE VERSUS THE BECKE–ROUSSEL HOLE

Early implementations of XDM used the exact exchange, a.k.a. Hartree–Fock, hole [53, 54, 156, 326, 327]. However, using exact exchange is prohibitively costly in solid-state codes due to the double summation over occupied orbitals required to

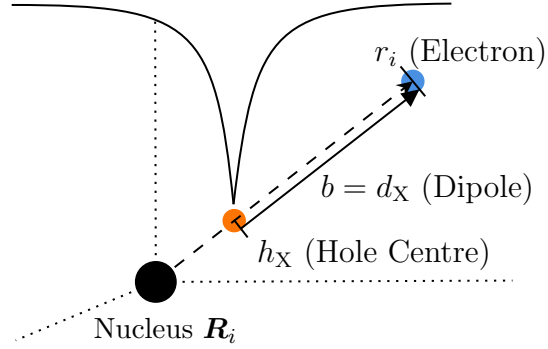


Figure 2.11: An illustration of the Becke–Roussel (BR) exchange hole, adapted from Ref. [80]. The nucleus is at position \mathbf{R}_i and its reference electron is a distance $r_i = |\mathbf{r} - \mathbf{R}_i|$ away. A dipole moment is formed between a reference electron and its exchange hole.

calculate the exact-exchange hole [56], which causes the determination of the expectation value of Eq. (2.5.57) to scale with $\mathcal{O}(N^3)$ [328]. Additionally, it is more accurate for molecular systems to use a local DFA model of the exchange hole that can mimic correlation effects resulting from chemical bonding. Thus, subsequent work has instead used the Becke–Roussel (BR) hole [16] to approximate the exchange hole. This choice results in linear, i.e. $\mathcal{O}(N)$, scaling of the $\langle d_X^2 \rangle$ procedure.

The BR hole is a meta-GGA functional of the spherically-averaged exchange hole that depends on the electron density (ρ_σ), the density gradient ($\nabla\rho_\sigma$), the Laplacian of the density ($\nabla^2\rho_\sigma$), and the kinetic-energy density (τ_σ), where

$$\tau_\sigma = \sum_i |\nabla\psi_{i\sigma}|^2 \quad (2.5.68)$$

is defined in terms of the occupied Kohn–Sham orbitals and follows Becke’s notation where the factor of $1/2$ is omitted. The BR exchange hole itself has the form of an off-center exponential function, $A_\sigma e^{-a_\sigma r}$, centred a distance of $b_\sigma = d_{X\sigma}$ from its reference electron, with normalization constant A_σ . An illustration of the BR hole and associated dipole moment is shown in Figure 2.11. The form of the BR hole is trivially exact for the hydrogen atom, as the exchange hole is simply the negative of the electron density, and this model has shown to be an excellent approximation to the exact exchange hole for many-electron atoms [16].

When constructing model holes of the exact-exchange hole, three conditions must be satisfied:

1. The model hole must be normalized to -1 electron

2. The model hole must deplete to the spin density at the reference point
3. The model hole must have the same curvature as the exact exchange hole at the reference point

where the exact exchange hole curvature is given by

$$Q_\sigma = \frac{1}{6} \left[\nabla^2 \rho_\sigma - 2\tau_\sigma + \frac{1}{2} \frac{(\nabla \rho_\sigma)^2}{\rho_\sigma} \right]. \quad (2.5.69)$$

Condition (1) enforces the normalization condition of the BR hole,

$$A_\sigma = -\frac{a_\sigma^3}{8\pi}, \quad (2.5.70)$$

and (2) enforces a spin density of

$$\rho_\sigma = \frac{a_\sigma^3}{8\pi} e^{-a_\sigma b_\sigma}. \quad (2.5.71)$$

The curvature constraint from condition (3), shown in Ref. [16], yields

$$Q_\sigma = \frac{\rho_\sigma}{6b_\sigma} [a_\sigma^2 b_\sigma - 2a_\sigma]. \quad (2.5.72)$$

We then wish to determine the fixed values of a_σ and b_σ for this system. Substituting Eq. (2.5.71) into Eq. (2.5.72) and letting $x = a_\sigma b_\sigma$ generates the transcendental equation,

$$\frac{x e^{-2x/3}}{x - 2} = \frac{2}{3} \pi^{2/3} \frac{\rho_\sigma^{5/3}}{Q_\sigma}, \quad (2.5.73)$$

where x is solved for numerically via the Newton–Raphson method [16, 329]. Via the rearrangement of Eq. (2.5.71), b_σ may be written as a function of x as

$$b_\sigma^3 = \frac{x^3 e^{-x}}{8\pi \rho_\sigma}. \quad (2.5.74)$$

Finally, once x and b_σ have been determined, a_σ is solved for via $a_\sigma = x/b_\sigma$. By definition $b_\sigma = d_{X\sigma}$ in this model; thus, this exchange-hole dipole moment may be substituted into Eq. (2.5.60) for use in the XDM method. As depicted in Figure 2.11, this model assumes that the electron, hole, and nearest nucleus are collinear; this assumption is reasonable, but note that Hirshfeld atoms are not perfectly symmetric and thus, this is an approximation for atoms in a molecule [54]. In practice, the exchange-hole dipole moment should never exceed the uncorrelated moment, thus,

we require $d_{X\sigma} \equiv b_\sigma \leq r_i$. Should non-physical values of $b_\sigma > r_i$ occur, they are replaced with $b_\sigma = r_i$ to satisfy this limiting condition [56, 330].

The BR hole has the benefit of being localized to an atomic-sized region [99, 170], unlike the exact exchange hole, which is highly delocalized [331]. This localization leads to the assumption that the BR hole may offer a better description of atomic contributions to the combined exchange-correlation hole dipole moment in molecular systems. Indeed, exactly this has been shown with the BR hole implementation of XDM [323, 330]. However, for isolated systems, we expect the exact exchange hole to outperform the BR hole because it is already localized [57].

XDM FORCES AND STRESSES

For use in solid-state codes, the XDM model must provide a description of the dispersion forces and stresses at play in a unit cell. The XDM energy expression in the solid state is given by

$$E_{\text{XDM}} = -\frac{1}{2} \sum_{\mathbf{L}} \sum_{i \neq j'} \sum_{n=6,8,10} \frac{C_{n,ij}^{\text{XDM}}}{R_{\text{vdW},ij}^n + R_{ij,\mathbf{L}}^n}, \quad (2.5.75)$$

where the prime excludes the $i = j$ term for the lattice vector $\mathbf{L} = 0$ [56]. Employing a basic assumption that the dispersion coefficients are approximately constant [113], the Hellmann–Feynman force theorem [251–253] may be applied to the XDM energy to derive an approximate dispersion force expression,

$$\mathbf{F}_i^{\text{XDM}} = \sum_{\mathbf{L}} \sum_{j'} \sum_{n=6,8,10} \frac{n C_{n,ij}^{\text{XDM}} R_{ij,\mathbf{L}}^{n-2}}{(R_{\text{vdW},ij}^n + R_{ij,\mathbf{L}}^n)^2} \mathbf{R}_{ij,\mathbf{L}}, \quad (2.5.76)$$

where $\mathbf{F}_i^{\text{XDM}}$ is the dispersion force vector on atom i . Similarly, the Hellmann–Feynman stress theorem may be applied to arrive at the approximate Cauchy stress tensor components

$$\sigma_{\xi\eta}^{\text{XDM}} = -\frac{1}{2V} \sum_{\mathbf{L}} \sum_{i \neq j'} \sum_{n=6,8,10} \frac{n C_{n,ij}^{\text{XDM}} R_{ij,\mathbf{L}}^{n-2}}{(R_{\text{vdW},ij}^n + R_{ij,\mathbf{L}}^n)^2} (R_{ij,\mathbf{L}})_\xi (R_{ij,\mathbf{L}})_\eta, \quad (2.5.77)$$

where ξ and η are two Cartesian components of the tensor, and V is the volume of the unit cell.

The assumption of constant dispersion coefficients is often reasonable, but not universally valid. XDM’s dispersion coefficients are responsive to changing atomic

environments, and are thus non-constant with changing positions. While the current treatment of dispersion forces is valid in most chemical systems, we will show cases where this approximation breaks down in Chapter 3. In Appendix B.3 we develop the mathematical framework necessary to account for non-constant dispersion coefficients and to arrive at a more rigorous treatment of the XDM forces. However, this framework requires the derivatives of the Hirshfeld weights, which are not currently available in any code where XDM is implemented and thus is left for a future project (see Chapter 7).

2.6 DELOCALIZATION ERROR

This section is adapted from: Bryenton, K. R., Adeleke, A. A., Dale, S. G. & Johnson, E. R. *Delocalization error: The greatest outstanding challenge in density-functional theory*. WIRES: Comp. Mol. Sci., **13**, 2, e1631. (2023) [161]

Author contributions: K.R.B. generated the mathematical model and data shown in this section. K.R.B. and E.R.J. wrote the manuscript, with input from A.A.A. and S.G.D. While A.A.A. and S.G.D. also generated data for this work, those portions of the manuscript are not reproduced here.

2.6.1 INTRODUCTION

Kohn–Sham density-functional theory (KS-DFT) [13] is now the workhorse of computational chemistry, solid-state physics, and materials science. Papers proposing some of the most popular functionals constitute 12 of the top 100 most-cited scientific papers across all fields [332]. For the majority of chemical systems, DFT methods provide an excellent balance between computational cost and accuracy. They are highly successful in modelling reaction thermochemistry and kinetics, proposing reaction mechanisms, investigating dynamics, modelling solid-state structure, and predicting phase transitions, to list a few examples. However, for certain classes of systems, popular KS-DFT methods have the potential to fail dramatically. One such class of system is those with multi-reference character [170, 333–338], meaning that the wavefunction cannot be well represented by a single electronic configuration (i.e. Slater determinant). Development of DFT methods for multi-reference systems has been the subject of much recent research [339–353], although they are relatively rare in ground-state chemistry.

More commonly, errors are seen for systems with highly delocalized electron densities. The most notable examples are H_2^+ , with its bond length stretched far beyond equilibrium [170, 354–357], and analogous stretched ions (He_2^+ , Li_2^+ , Ne_2^+ , etc.). However, similar errors have been identified for many other systems, including charge-transfer complexes [358–361], transition states of radical reactions [362–367], band gaps of semi-conductors [368–374] polarizabilities of long-chain molecules [375–378], systems with extended conjugation [379–388], halogen and chalcogen bonds [389–391], and organic acid/base co-crystals [392]. These are not the result of separate errors, but rather represent many facets of one single error in common density functionals. This error was originally termed self-interaction error (SIE) [393] and discussed in the context of a single electron. However, its definition was later expanded [394–396] and the more general case is known as delocalization error [397]. The latter is the more inclusive term, since delocalization error may still affect results that have been corrected for (one-electron) SIE. While many methods have been proposed over the past four decades to limit delocalization error, no one approach is a panacea and research in this area is ongoing [14, 398–404]. Resolving delocalization error almost certainly remains the greatest outstanding challenge in DFT.

2.6.2 SELF-INTERACTION ERROR

Self interaction arises from the Coulomb energy terms that correspond to interaction of an electron with itself. For a one-electron system, the classical Coulomb energy for electron-electron interactions given by

$$J_{\text{ee}} = \frac{1}{2} \iint \frac{1}{\mathbf{r}_{12}} \rho(\mathbf{r}_1) \rho(\mathbf{r}_2) d\mathbf{r}_1 d\mathbf{r}_2 \quad (2.6.1)$$

is non-zero, which is not physical. However, in Hartree–Fock theory, the non-zero Coulomb energy for interaction of an electron with itself is offset by a corresponding exchange-energy term that is equal in magnitude, but opposite in sign. The exact (Hartree–Fock) exchange energy is

$$E_{\text{X}} = \frac{1}{2} \sum_{\sigma} \iint \frac{1}{r_{12}} \psi_{i\sigma}(\mathbf{r}_1) \psi_{j\sigma}(\mathbf{r}_2) \psi_{j\sigma}(\mathbf{r}_1) \psi_{i\sigma}(\mathbf{r}_2) d\mathbf{r}_1 d\mathbf{r}_2, \quad (2.6.2)$$

where σ indicates electron spin and the ψ 's are the occupied KS orbitals, assumed to be real. Thus, the HF exchange energy is also non-zero for a single electron.

For a one-electron system, with a single occupied orbital, the requirement for

vanishing self-interaction energy is [393]

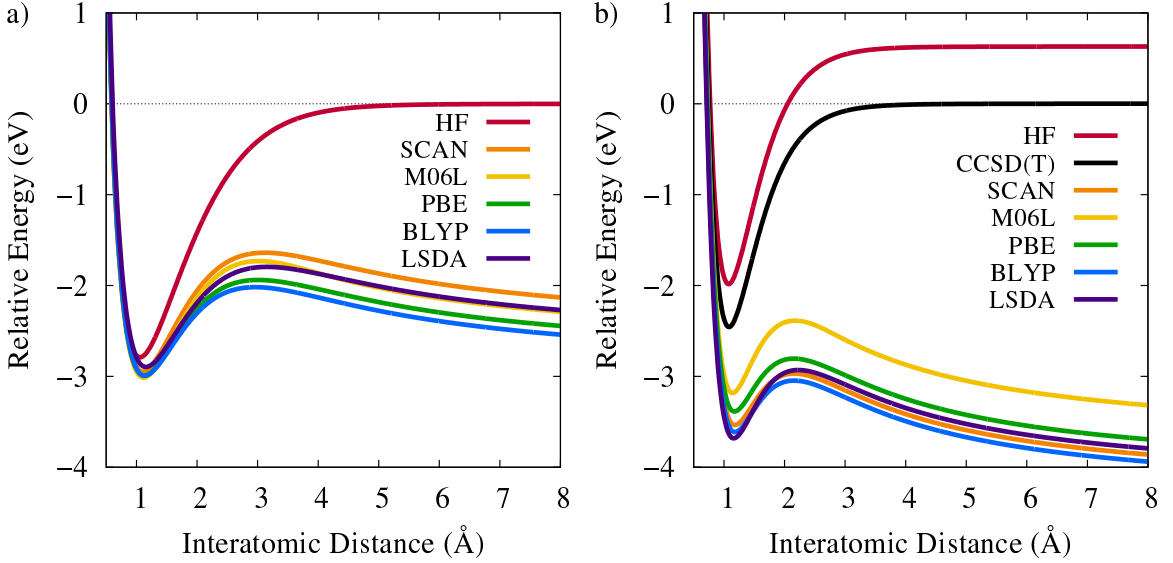
$$J_{ee} + E_X = 0. \quad (2.6.3)$$

This condition is satisfied by the exact (HF) exchange energy due to the offsetting Coulomb and exchange integrals. However, for DFAs such as the LSDA or GGAs, the exchange energy does not offset the self Coulomb energy. Indeed, the DFA exchange energy can be very much larger in magnitude than the exact exchange energy in some systems, resulting in overstabilization.

The classic example of this is the dissociation limit of the H_2^+ potential energy curve, which is described exactly by HF theory. However, this dissociation limit is predicted to be far too low in energy by most DFAs [170, 354, 355, 357], as shown in Figure 2.12(a) for the LSDA [393], and for BLYP [134, 165] and PBE [149], which are representative GGA functionals. Results are also shown for two meta-GGAs: M06L [405] and SCAN [322]. The dissociation limit obtained with each DFA is far below the exact result from HF theory. Figure 2.12(b) shows analogous results for He_2^+ . Here, HF is not exact since He_2^+ is not a one-electron system and, due to neglect of electron correlation effects, it gives a dissociation limit above the CCSD(T) reference. All the DFAs again fail catastrophically, predicting He_2^+ with a highly stretched bond length to be far lower in energy than the separated He atom and He^+ ion. These results are not unique to the specific functionals chosen; all GGAs and meta-GGAs show similar errors [357].

Self-interaction error can be reduced through use of hybrid functionals, since they include some fraction of exact exchange. However the optimum exchange-mixing fraction is clearly system dependent. For a uniform electron gas, the LSDA is exact and there is no self-interaction error. Bulk metals are the systems that most closely resemble a uniform electron gas, and are typically very well treated by the LSDA and GGA functionals. Conversely, for one-electron systems, full exact exchange is needed to eliminate self-interaction error. Most many-electron systems fall somewhere between these two extremes, where some optimal mixing of DFA and HF exchange will minimize SIE. As a result, SIE is identified in practise in cases where the LSDA or GGAs drastically over-stabilize a particular system and the error decreases with increasing exact-exchange mixing, usually up to ca. 50% HF exchange for a global hybrid or 100% long-range HF exchange for a range-separated hybrid.

Figure 2.12: Potential energy curves for (a) H_2^+ and (b) He_2^+ obtained with selected methods and the aug-cc-pVTZ basis set using Gaussian 16 [126] (psi4 [129] for the SCAN calculations).

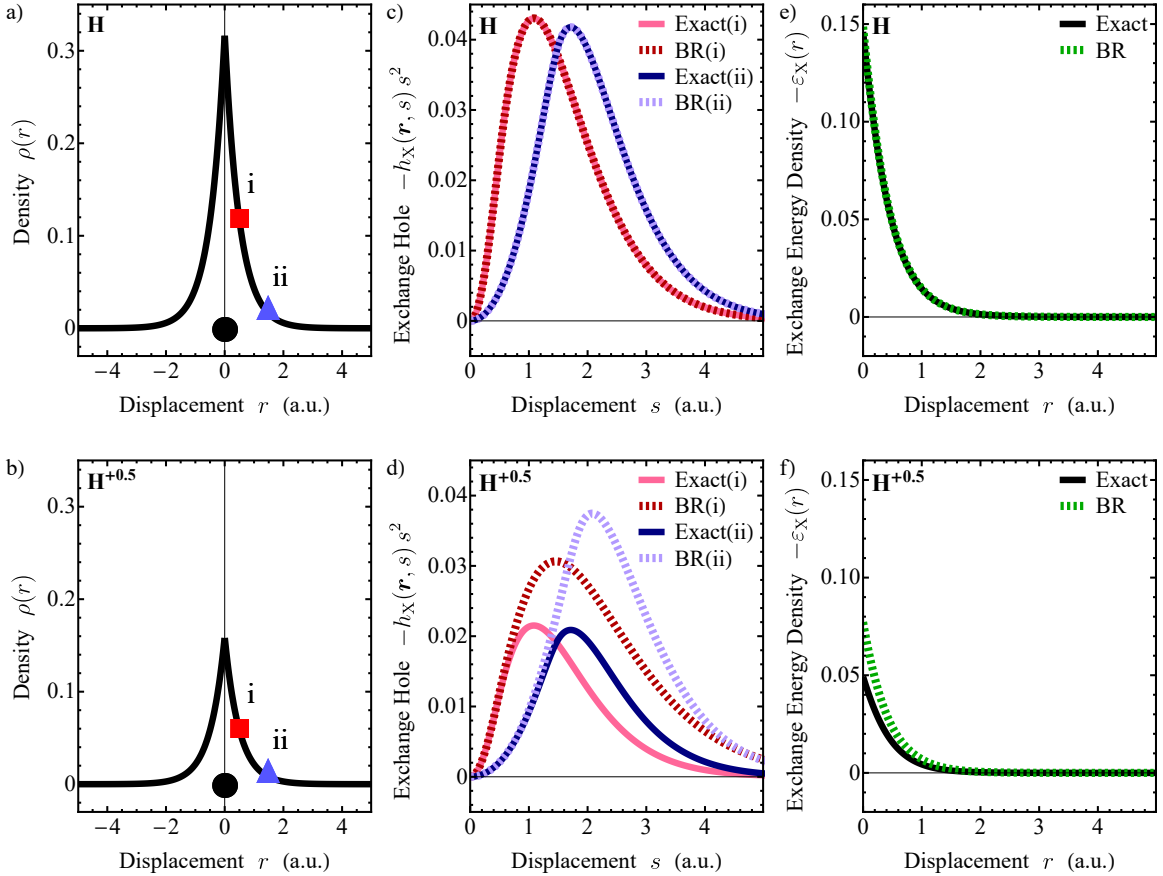


2.6.3 THE EXCHANGE-CORRELATION HOLE PICTURE

One way to understand SIE is through visualization of the exchange-correlation hole [170, 312, 406]. Given an electron at a fixed reference point, the hole measures the depletion in probability of finding a second electron a certain distance away from that point. HF theory gives an exchange hole that is delocalized over all atoms in a system, but correlation usually serves to localize the full exchange-correlation hole to within regions of roughly atomic size [170, 331]. Conversely, most DFAs, and particularly the LSDA and GGAs, already model exchange holes as being fairly localized about each reference point [16, 407, 408]. This is typically advantageous as the model holes implicitly build in non-dynamical correlation effects. However, in situations with significant SIE, non-dynamical correlation is insufficient to localize the hole and the exact exchange-correlation hole remains delocalized, in a similar way to the HF hole. In such cases, the assumptions made in construction of model DFA exchange holes are no longer valid.

As an example, we contrast the hydrogen atom, where DFAs give effectively zero SIE, with the H_2^+ dissociation limit. Note that the dissociation limit of H_2^+ is equivalent to two $\text{H}^{+0.5}$ cations. For simplicity, the electron density of $\text{H}^{+0.5}$ is approximated as half the H-atom density. Figure 2.13(a,b) illustrates these two density distributions.

Figure 2.13: Plots of the total electron density (a,b) and the normalization integrand for spherical averages of BR and exact exchange holes (c,d) about the two shown reference points for H (top row) and $H^{+0.5}$ (bottom row). Also shown are the exchange-energy densities for both species (e,f). All quantities are given in Hartree atomic units (a.u.).



Since there is no electron correlation in either H or $H^{+0.5}$, we can focus entirely on the exchange hole. We use the Becke–Roussel [16] (BR) meta-GGA for this demonstration since it is conveniently based on a real-space representation of the exchange hole as a simple exponential function displaced from the reference point. It is also constrained to recover the density and curvature of the exact exchange hole at the reference point. The DFT exchange energy is uniquely determined by the exchange hole via

$$E_X = \frac{1}{2} \sum_{\sigma} \iint \frac{\rho_{\sigma}(\mathbf{r}_1)}{r_{12}} h_{X\sigma}(\mathbf{r}_1, \mathbf{r}_2) d\mathbf{r}_1 d\mathbf{r}_2. \quad (2.6.4)$$

It can also be shown that the exchange energy is dependent only on the spherical

average of the hole about the reference point [409]:

$$E_X = 2\pi \sum_{\sigma} \iint \frac{\rho_{\sigma}(\mathbf{r})}{s} h_{X\sigma}(\mathbf{r}, s) s^2 ds d\mathbf{r}. \quad (2.6.5)$$

The normalization of the spherically averaged hole is

$$N = 2\pi \sum_{\sigma} \iint h_{X\sigma}(\mathbf{r}, s) s^2 ds d\mathbf{r}, \quad (2.6.6)$$

which is typically constrained to -1 electron in construction of DFAs.

Figure 2.13(c,d) shows the negative integrand of the hole normalization from Eq. (2.6.6) for the spherical average the exact and BR exchange holes for two choices of reference point, \mathbf{r} , in H and $H^{+0.5}$. For the H atom, both the exact and DFA holes are normalized to -1 electron, and the BR hole model is exact by construction, so both curves are overlaid. Conversely, for $H^{+0.5}$, the normalization integrand for the BR hole is larger in magnitude than that of the exact hole away from the reference point. This occurs because DFA holes, including the BR holes shown in Figure 2.13, are always assumed to have unit normalization. However, the exact exchange hole in $H^{+0.5}$ is only normalized to $-1/2$ an electron due to the fractional charge.

Since the exchange energy is determined by the exchange hole via Eq. (2.6.5), having double the normalization from the DFA model hole results in effectively double counting the exchange energy. To illustrate this more clearly, we also plot the exchange-energy density,

$$\varepsilon_X(\mathbf{r}) = 2\pi \rho_{\sigma}(\mathbf{r}) \int h_{X\sigma}(\mathbf{r}, s) s ds, \quad (2.6.7)$$

such that the exchange energy is

$$E_X = \sum_{\sigma} \int \varepsilon_X(\mathbf{r}) d\mathbf{r}. \quad (2.6.8)$$

Results are shown for both H and $H^{+0.5}$ in Figure 2.13(e,f). The BR functional recovers the exact exchange-energy density for H, but gives an exchange-energy density that is too large in magnitude for $H^{+0.5}$, most noticeably near the nucleus. This results in a large total energy error and explains the behaviour seen for the various DFAs for the H_2^+ potential energy surface (PES) in Figure 2.12(a). At equilibrium, the exact exchange hole will have near unit normalization and DFAs provide quite

accurate energies. However, as the dissociation limit is approached, the exact hole normalization will approach $-1/2$ about each nucleus and DFAs will overestimate the magnitude of the exchange contribution to the total energy. An analogous argument can be made for He_2^+ and other stretched odd-electron systems as well [158, 170, 354–357]. Thus, we conclude that delocalization error occurs when the model DFA exchange-correlation hole has a normalization that is too large relative to the exact exchange-correlation hole.

CHAPTER 3

REQUIREMENTS FOR AN ACCURATE DISPERSION-CORRECTED DENSITY FUNCTIONAL

“With four parameters I can fit an elephant, and with five I can make him wiggle his trunk.” [410]

~ Prof. John von Neumann (1903–1957)

This chapter is adapted from: Price, A. J. A., Bryenton, K. R., & Johnson, E. R. *Requirements for an accurate dispersion-corrected density functional.* J. Chem. Phys., **154**, 23, 230902. (2021) [81]

Author contributions: K.R.B. generated the data shown in Section 3.4, E.R.J. generated the data shown in Figure 3.4 and Figure 3.5, while the other data shown was generated by A.J.A.P. E.R.J. wrote the first version of the manuscript, with all authors contributing to editing.

3.1 INTRODUCTION

In this chapter, we opine on the most desirable requirements for a reliable and physically reasonable post-SCF dispersion-corrected density functional. Development of such a method necessitates high accuracy for both components of the total DFT energy: the base density functional and the dispersion correction. Users of dispersion-corrected DFT should be mindful of these requirements when deciding on their computational methodology. Method developers should also consider them when designing new base functionals and dispersion models.

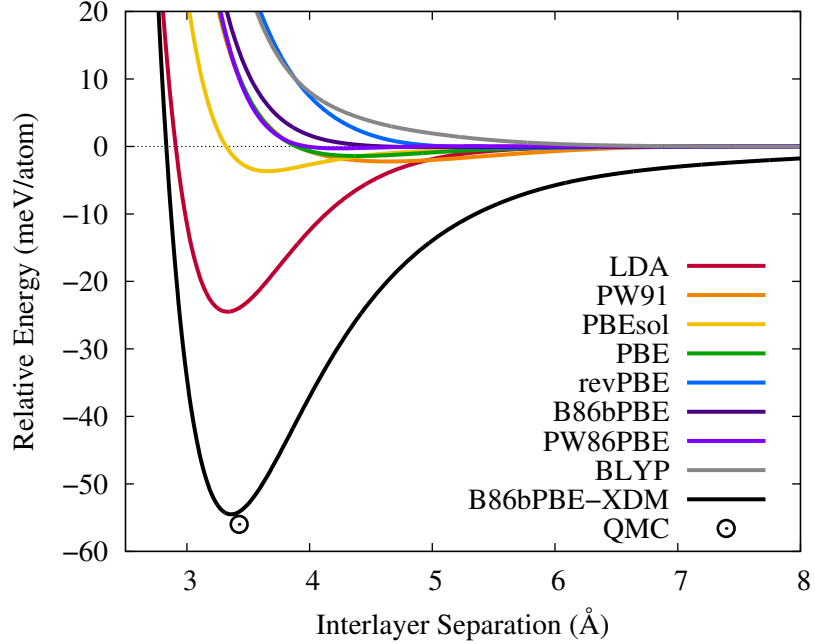
3.2 REQUIREMENTS FOR THE BASE DENSITY FUNCTIONAL

3.2.1 DISPERSIONLESS

The key requirement for a base density functional to pair with a dispersion correction is that it is itself dispersionless [411]. While dispersion is properly a highly non-local correlation effect, the local density approximation (LDA) and many generalized gradient approximation (GGA) functionals capture some dispersion-like binding through their exchange functionals [153–155, 412–415]. This arises because the large-gradient regions in the free atoms (or isolated molecules) do not contribute sufficiently to the exchange energy, and are artificially destabilized relative to the vdW complex. However, this dispersion-like binding is inherently short range and does not recover the proper C_6/R^6 asymptotic behaviour that is characteristic of London dispersion. This is shown by examination of the potential-energy curves for graphite exfoliation, in Figure 3.1, for the LDA and selected GGA functionals without any dispersion correction.

Adding a dispersion correction to an exchange functional that already mimics dispersion-like binding means that there will be some double counting of dispersion at short range [278, 419], resulting in significant overstabilization of vdW complexes. Empirical parameterization to equilibrium binding energies will therefore result in excessive damping of the dispersion correction at short range to reduce this double counting, resulting in under-estimation of dispersion at intermediate ranges. This leads to poor performance for bulk materials, where there are many intermediate-range atomic contacts, such as in molecular crystals [99].

Figure 3.1: Graphite exfoliation energies computed using selected base density functionals [134, 147, 149, 151, 165, 393, 408, 416, 417]. Calculations were performed with Quantum ESPRESSO [111], using the projector-augmented wave (PAW) approach [225, 226] with a $12 \times 12 \times 4$ \mathbf{k} -point mesh. Planewave cut-offs of 100 and 1000 Ry were used for the kinetic energy and electron density, respectively. The B86bPBE-XDM [57, 147, 149] curve and Quantum Monte Carlo equilibrium result [418] are included for reference.



Double-counting of dispersion from the base functional also creates a bias where hydrogen-bonding interactions are favoured relative to dispersion-driven interactions, such as π -stacking [123]. Hydrogen-bond strengths (as in the water dimer) are typically over-estimated with non-dispersionless functionals [420]. In such cases, addition of a dispersion correction unfortunately introduces greater errors for hydrogen bonds, despite being necessary to stabilize dispersion-bound dimers (such as the methane or benzene dimers). Hence, parameterizing the damping function for a non-dispersionless base functional typically leads to over-stabilization of hydrogen-bonded complexes, and under-stabilization of dispersion-bound complexes, to minimize the overall error [123].

To design a dispersionless GGA functional, we must ensure accurate large-gradient

behaviour, which is determined by the functional's enhancement factor. GGA exchange functionals have the general form:

$$E_X^{\text{GGA}} = \sum_{\sigma} \int \varepsilon_{X,\sigma}^{\text{LDA}} F(\chi_{\sigma}) d\mathbf{r}, \quad (3.2.1)$$

where $\varepsilon_{X,\sigma}^{\text{LDA}}$ is the spin-dependent LDA exchange-energy density

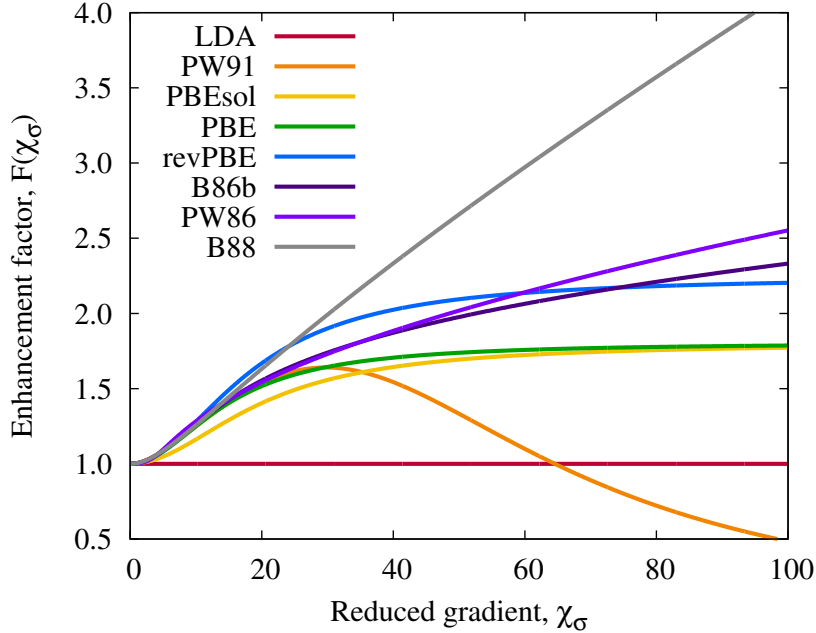
$$\varepsilon_{X,\sigma}^{\text{LDA}} = -\frac{3}{2} \left(\frac{3}{4\pi} \right)^{1/3} \rho_{\sigma}^{4/3}, \quad (3.2.2)$$

ρ_{σ} is the σ -spin density,

$$\chi_{\sigma} = \frac{|\nabla \rho_{\sigma}|}{\rho_{\sigma}^{4/3}} \quad (3.2.3)$$

is the reduced density gradient, and $F(\chi_{\sigma})$ is the enhancement factor. Enhancement factors for several popular GGA exchange functionals [134, 147, 149, 151, 408, 416, 417] are shown in Figure 3.2.

Figure 3.2: Plots of the exchange enhancement factor for the LDA and selected GGA [134, 147, 149, 151, 408, 416, 417] functionals.



For a proper, dispersionless exchange functional, the large-gradient limit of the enhancement factor should be [153–155]

$$\lim_{\chi_{\sigma} \rightarrow \infty} \propto \chi_{\sigma}^{2/5}. \quad (3.2.4)$$

This limit is only obeyed by the PW86 [151] and B86b [147] GGAs. As seen in Figure 3.2, the LDA, PBEsol [416], PW91 [408], and PBE [149] functionals all have enhancement factors converge to a constant value in the large-gradient limit. As a result, these functionals mimic dispersion-like binding at short range to varying extents, making them unsuited for use with asymptotic dispersion corrections. Conversely, the B88 [134] GGA has an enhancement factor that diverges too quickly, proportional to $\chi_\sigma / \ln(\chi_\sigma)$, in the large-gradient limit. While B88 exchange is dispersionless, it notoriously over-estimates non-bonded repulsion. One strategy to obtain a dispersionless GGA functional has been to take linear combinations of PBE and B88 [330], as in the APF [421] functional.

Table 3.1: Mean absolute errors, in kcal/mol, obtained with selected XDM-corrected GGA functionals for the KB49 [123, 323] and X23 [295] benchmarks. All calculations were performed with Quantum ESPRESSO [111] using the projector augmented-wave (PAW) approach [225, 226] and planewave cut-offs of 80 and 800 Ry. A $4 \times 4 \times 4$ \mathbf{k} -point mesh was used for all molecular crystals, while only the Γ point was used to treat the isolated molecules. The B86bPBE, PW86PBE, and PBE results were taken from Ref. [57], while the PW91 and PBEsol results were determined for the present work. The a_1 and a_2 parameters used in the XDM damping function are also shown.

Functional	a_1	a_2 (Å)	KB49	X23
B86bPBE	0.6512	1.4633	0.41	0.85
PW86PBE	0.6836	1.5045	0.41	0.88
PBE	0.3275	2.7673	0.50	1.11
PW91	0.0000	4.0228	0.63	1.89
PBEsol	0.5432	2.3686	0.78	2.11

In light of their correct behaviour in the large-gradient limit, PW86 and B86b are the GGA functionals of choice to pair with dispersion corrections to avoid any double counting of dispersion. Due to their accurate description of non-bonded repulsion, these functionals have demonstrated improved performance for solid-state benchmarks when paired with unscaled dispersion corrections [57, 99], as well as with non-local vdW functionals [62]. This is illustrated in Table 3.1 for several XDM-corrected GGA functionals, which shows mean absolute errors (MAEs) for the KB49 [123, 323] benchmark of molecular-dimer binding energies and the X23 [295] benchmark of molecular-crystal lattice energies. Similar results are obtained with the two dispersionless base functionals, B86bPBE and PW86PBE; however, we tend not to favour PW86PBE for the practical reason that it shows poorer SCF convergence. Larger errors are obtained for the non-dispersionless base functionals: PBE, PBEsol,

and PW91. Further, while non-dispersionless functionals tend to perform better when paired with a zero-damped dispersion correction due to error cancellation (see Section 3.3.1), we note that the largest such error reduction for the KB49 set is only 0.06 kcal/mol for PBEsol. In our opinion, the large-gradient limit of Eq. (3.2.4) is a drastically underutilized constraint in functional development.

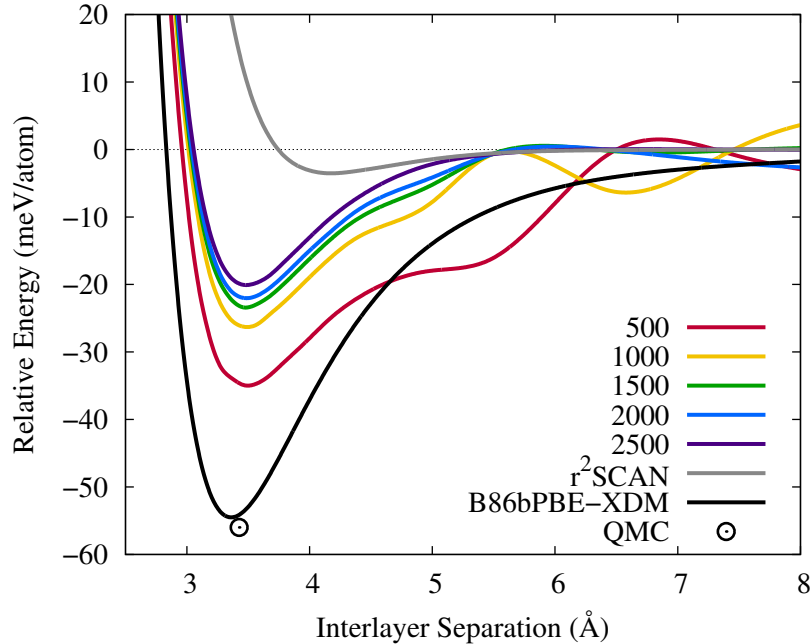
3.2.2 NUMERICALLY STABLE

A further desirable requirement for a base density functional is that it be numerically stable and give smooth potential energy curves for vdW complexes. While this criterion is met by the LDA and GGA functionals, some meta-GGAs display substantial numerical sensitivities that lead to oscillations in potential energy curves of vdW dimers [413, 422–426]. These oscillations can result in errors in vibrational frequencies [427] and geometry optimization to spurious high-energy conformations [428], unless extremely fine integration grids are used. Previous works observing such oscillations have focused on meta-GGA calculations for gas-phase complexes, such as the π -stacked benzene dimer [429]. However, similar behaviour can also be seen for solid-state systems, as shown in Figure 3.3 using the SCAN functional for the example of graphite exfoliation. From the figure, we additionally note that the SCAN functional is not dispersionless and it provides significant, spurious dispersion-like binding for graphite.

In the Quantum ESPRESSO program [111], the real-space integration grid is controlled by the choice of the planewave cut-off for the density expansion (the `ecutrho` parameter). It is common to take this value as only four times the wavefunction planewave kinetic-energy cutoff, `ecutwfc`, when using norm-conserving pseudopotentials. However, as seen in Figure 3.3, low values of `ecutrho` are clearly insufficient and result in massive oscillations of the potential energy curve. Indeed, a smooth potential can only be obtained if `ecutrho` is increased to near 2500 Ry or higher. The need for very large integration grids contributes to the increased computational cost of meta-GGA functionals relative to GGAs, making them unappealing for large systems even if they were dispersionless.

In previous work [422], it has been shown that the numerical sensitivity of meta-GGAs arises from the behaviour of the τ -dependent ratios employed in the functional for the low-density and low-gradient regions near the bond critical points of vdW dimers. Here, we focus on the SCAN meta-GGA functional [322], which is finding increasingly widespread use in solid-state applications. Comparisons will be made to

Figure 3.3: Graphite exfoliation energies computed using the SCAN [322] meta-GGA functional with varying planewave cut-offs (in Ry) for the electron density expansion. Calculations were performed using Quantum ESPRESSO [111], with norm-conserving pseudopotentials [222, 223] and a $12 \times 12 \times 4$ \mathbf{k} -point mesh. A planewave cut-off of 80 Ry was used for the kinetic energy. Results from the r^2 SCAN [430] functional using the same options and a 1000 Ry density cut-off are also shown. The B86bPBE-XDM [57, 147, 149] curve, using the same calculations options described in Figure 3.1, and the Quantum Monte Carlo equilibrium result [418] are included for reference.



a new, more numerically stable modification of SCAN, termed r^2 SCAN [430]. As seen in Figure 3.3, the r^2 SCAN functional remedies the numerical sensitivities seen with SCAN, giving a well-behaved potential energy curve for graphite exfoliation with a modest value of `ecutrho`.

The τ -dependent term used in SCAN is [322]

$$a = \frac{\tau_\sigma - \tau_\sigma^W}{\tau_\sigma^{\text{UEG}}}, \quad (3.2.5)$$

where we have used a , as opposed to the symbol α used in Ref. [322], to avoid confusion with the atomic polarizability. Here,

$$\tau_\sigma^W = \frac{1}{4} \frac{(\nabla \rho_\sigma)^2}{\rho_\sigma} \quad (3.2.6)$$

is the von Weizsäcker kinetic-energy density and

$$\tau_\sigma^{\text{UEG}} = \frac{3}{5} (6\pi^2)^{2/3} \rho_\sigma^{5/3} \quad (3.2.7)$$

is the kinetic-energy density of the uniform electron gas (UEG). A similar τ -dependent ratio is used in the r²SCAN functional:

$$\bar{a} = \frac{\tau_\sigma - \tau_\sigma^W}{\tau_\sigma^{\text{UEG}} + \eta \tau_\sigma^W}, \quad (3.2.8)$$

where $\eta = 10^{-3}$. As seen previously [422] for ingredients of other meta-GGAs, such as VSXC [431], M06-L [405], and TPSS [432], there is sharp variation in both a and \bar{a} near the bond critical point of van der Waals dimers.

The key difference between the two functionals that controls their numerical stability lies in the form of the “ x ” functional, which is one component of the exchange term. In SCAN, this functional is

$$\begin{aligned} x(\chi_\sigma, a) = & \mu \chi_\sigma^2 \left[1 + \left(\frac{b_4}{\mu} \chi_\sigma^2 \right) \exp \left(-\frac{b_4}{\mu} \chi_\sigma^2 \right) \right] \\ & + [b_1 \chi_\sigma^2 + b_2 (1-a) \exp \{-b_3(1-a)^2\}]^2 \end{aligned} \quad (3.2.9)$$

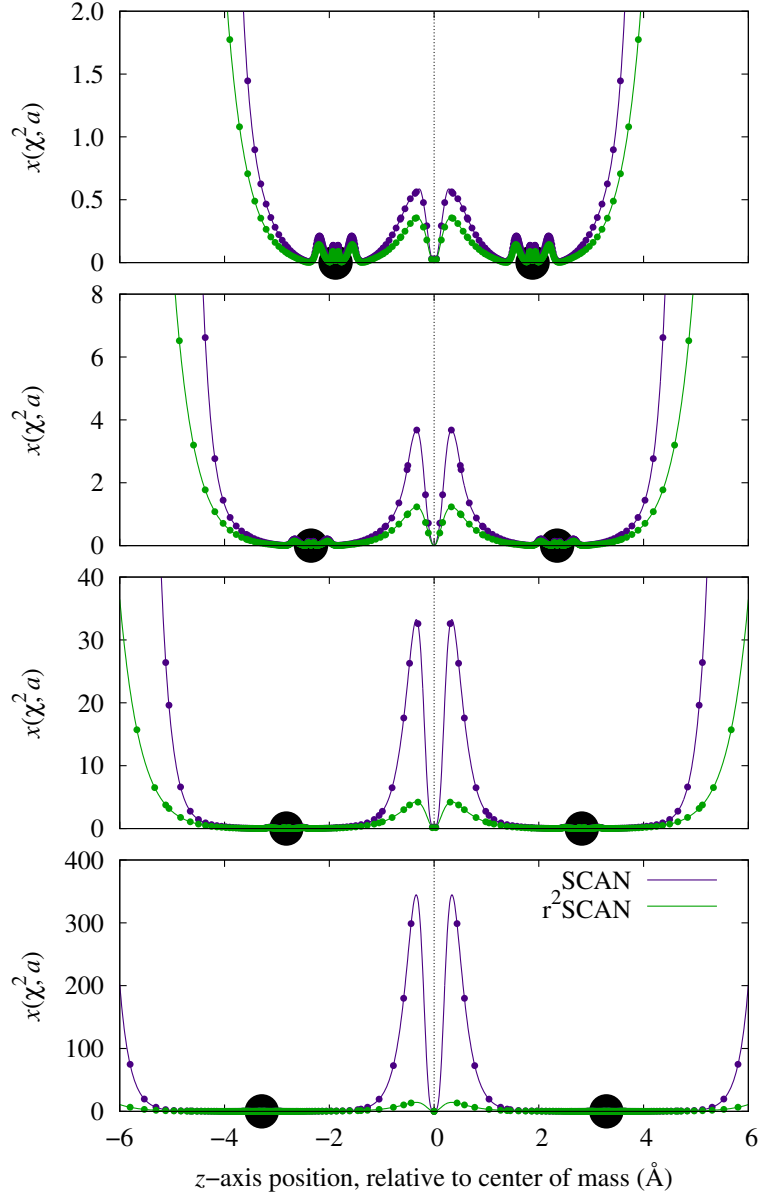
which involves τ_σ dependence. However, in r²SCAN, this functional is replaced by

$$x(\chi_\sigma) = [C \exp(-d\chi_\sigma^4) + \mu] \chi_\sigma^2 \quad (3.2.10)$$

which is independent of τ_σ . Here, C , d , μ , and all the b_n ’s are constants.

Figure 3.4 shows the values of the x functionals used in the SCAN and r²SCAN meta-GGAs along the internuclear coordinate of the argon dimer. While both functionals approach zero at the bond critical point, they give very different behaviour on either side of it. The SCAN results show a divergence that increases with internuclear distance, which is not present in the r²SCAN results. The region surrounding the critical point is only sparsely sampled by atom-centred integration grids [435], and the exchange-energy contributions can vary substantially depending on the precise location of the sampled grid points relative to the peaks of the diverging function. Overall, r²SCAN is well behaved for molecular dimers [436], while SCAN and TPSS show reduced numerical sensitivity [422, 429] compared to VSXC [431] and several of the related Minnesota functionals [405, 437].

Figure 3.4: Values of the x function, Eqs. (3.2.9) and (3.2.10), used in the SCAN [322] and r^2 SCAN [430] functionals along the internuclear axis in Ar_2 . Results are shown for internuclear distances of 1.00, 1.25, 1.50, and 1.75 times its equilibrium separation of 3.76 Å [433]. Calculations were performed using the NUMOL program [434]. The black circles indicate the positions of the Ar nuclei and the points correspond to an integration grid points for a mesh containing 120 radial points per atom.



Care should be taken by developers to select well-behaved τ -dependent terms for use in design of meta-GGA functionals. Meta-GGGAs can offer significant improvements over GGAs for electronic properties, such as the band gap, and tend to give

lower errors for molecular thermochemistry. However, they are much more computationally costly than GGAs for solid-state applications, frequently suffer from poor SCF convergence, and cannot be used for variable-cell relaxations in most planewave codes. Users are strongly cautioned to avoid most meta-GGA functionals for applications where dispersion plays a role since they are frequently numerically unstable. Even meta-GGA functionals that are well-behaved numerically are still not dispersionless, as is shown for r^2 SCAN in Figure 3.3.

3.3 REQUIREMENTS FOR THE DISPERSION CORRECTION

3.3.1 FINITE DAMPING

We now turn to the requirements for the dispersion correction itself. The use of a perturbation-theory expansion for the dispersion energy is correct at infinite separation, but will break down for short interatomic distances. As a result, the dispersion energy for each atom pair is typically multiplied by an empirical damping function, $f(R)$, to avoid divergence as $R \rightarrow 0$. Considering only the leading-order C_6 dispersion term for simplicity, the damped dispersion energy between a single pair of atoms is

$$E_{\text{disp}} = -\frac{C_6 f(R)}{R^6}. \quad (3.3.1)$$

Many possibilities have been proposed for the damping function. The D2 [40] and TS [44] dispersion corrections use a Fermi-type damping function of the form

$$f^{\text{WY}}(R) = \frac{1}{1 + \exp \left[-d \left(\frac{R}{sR_{\text{vdW}}} - 1 \right) \right]} \quad (3.3.2)$$

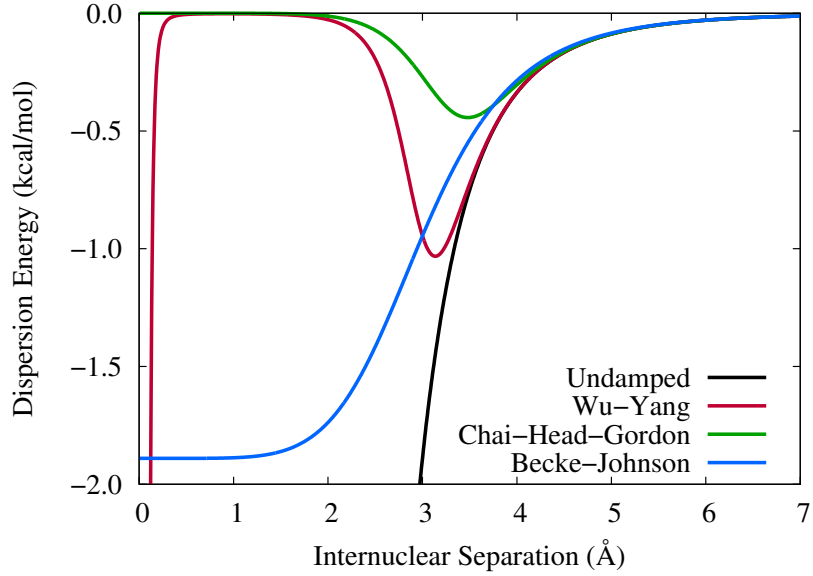
proposed by Wu and Yang [87], where d and s are empirical parameters and R_{vdW} is the sum of the atomic van der Waals radii. In the D3 [41] dispersion correction, an alternative damping function

$$f^{\text{CHG}}(R) = \frac{1}{1 + 6 \left(\frac{R}{sR_{\text{vdW}}} \right)^{-\gamma}} \quad (3.3.3)$$

proposed by Chai and Head-Gordon [271] was used, where γ and s are again empirical parameters. Both the Wu–Yang and Chai–Head-Gordon functions ensure that the

damped dispersion energy reaches zero, as shown in Figure 3.5. However, the Chai–Head–Gordon form prevents the divergence seen with the Wu–Yang damping function at very small internuclear separations. Damping the dispersion energy to zero means that its magnitude will reach a maximum value at some intermediate interatomic distance and, at shorter distances, there will be a non-physical, repulsive dispersion force introduced.

Figure 3.5: Comparison of the effect of various damping functions [87, 156, 271] on the leading-order dispersion energy between two atoms with $C_6 = 100$ a.u. and $R_{\text{vdW}} = 3 \text{ \AA}$. Empirical parameters in the damping functions are set to $s = 1$, $d = 20$, $\gamma = 14$.

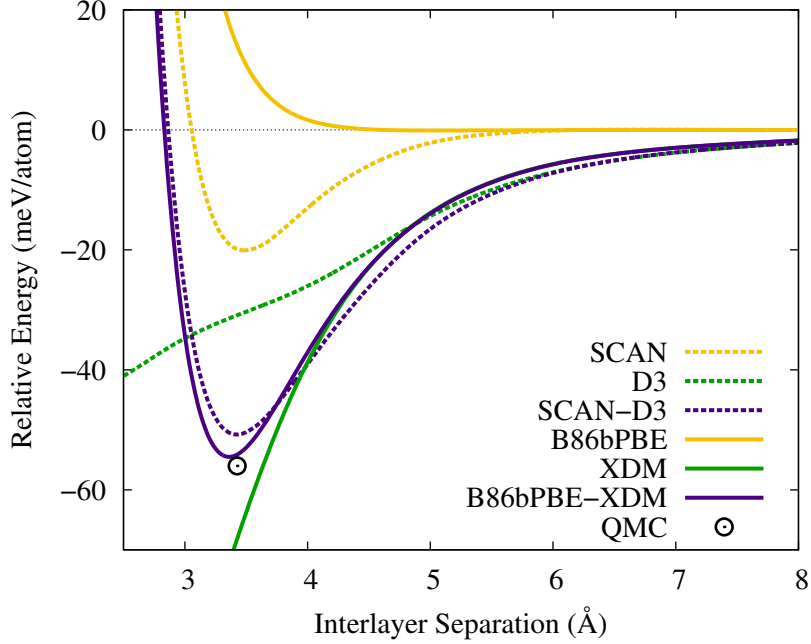


Using a convergent multipole expansion, it can be shown that the dispersion energy should approach a small, but finite, value for two hydrogen atoms in the united-atom limit [272]. As a result, we and others [92] favour damping the dispersion energy to a constant, finite value as $R \rightarrow 0$. One way to achieve this is through the Becke–Johnson damping function [156], which has the form

$$f_n^{\text{BJ}}(R) = \frac{R^n}{R^n + R_{\text{vdW}}^n}, \quad (3.3.4)$$

where $n = 6$ for the leading-order C_6 dispersion term. It should also be noted that the definitions of the vdW radii differ between various damping functions, but will not be discussed further here. The BJ form ensures that the dispersion energy approaches a non-zero constant at short interatomic separations, as shown in Figure 3.5, and the dispersion force is never repulsive.

Figure 3.6: Comparison of SCAN-D3 (dashed lines) and B86bPBE-XDM (solid lines) results for graphite exfoliation. Results are shown for the separate base functionals (yellow) and dispersion corrections (green), as well as for the overall potentials (purple).



The choice of damping function can significantly affect the performance of a dispersion correction, as demonstrated for the D3 dispersion model [92]. When D3 was paired with dispersionless or near-dispersionless base functionals, finite damping produced substantially more accurate results than zero damping for several molecular benchmarks. However, zero-damping does provide improved performance for exchange functionals that mimic short-range dispersion binding [278, 419], such as SCAN [322] and the Minnesota functionals [405]. In these cases, zero damping ensures that the dispersion energy will reach a maximum at intermediate atomic distances, while being significantly damped near equilibrium geometries of vdW complexes to offset the dispersion-like binding from the base functional. This results in accurate potential energy curves through a cancellation of errors. An example of such a cancellation of errors is shown in Figure 3.6. Here, the SCAN meta-GGA is paired with the zero-damped D3 dispersion correction, and the results are compared with B86bPBE-XDM for graphite exfoliation. While the component base functionals and dispersion corrections show very different behaviours, the overall potential energy curves from SCAN-D3 and B86bPBE-XDM are similar.

3.3.2 HIGHER-ORDER DISPERSION TERMS

Force-field implementations [438–440] of the Lennard-Jones (LJ) potential [441], as well as early DFT+D dispersion corrections [39, 87, 328, 442, 443] including the D2 [40] and TS [44] models, limited themselves to inclusion of only the leading-order C_6 dispersion term. If empirical scaling of the dispersion coefficients [40] is introduced, such methods can be capable of very high accuracy for small molecular dimers [40, 80]. However, without empirical scaling, C_6 -only models severely under-bind π -stacked complexes [328]. It has since been shown that inclusion of at least the C_8 dipole-quadrupole term in the dispersion-energy expansion, as in the D3 [41] and XDM [57] models, is required for an accurate treatment of π -stacking [156], graphite exfoliation [80], the S12L benchmark [35] of supermolecular complexes [444], and lattice energies of molecular crystals [80, 99].

Table 3.2 shows a summary of results from Ref. [80], which discussed the importance of higher-order terms in a dispersion model. These calculations employed a damped dispersion-energy, summed over all atom pairs, of the form

$$E_{\text{disp}} = - \sum_{i < j} \sum_{n=6,8,10} \frac{C_{6,ij} f_n^{\text{BJ}}(R_{ij})}{R_{ij}^n}, \quad (3.3.5)$$

truncating it at either the C_6 , C_8 , or C_{10} terms. The BJ damping function involves two parameters (a_1 and a_2) in the definition of the vdW radii, Eq. (3.3.4), that were optimized in each case to minimize the error for the KB49 [123, 323] molecular-dimer benchmark. In the last two rows of Table 3.2, the value of an empirical scaling coefficient multiplying the C_6 or C_8 dispersion-energy terms was also optimized. Errors for the X23 [295] lattice-energy benchmark were then evaluated using these optimized parameters.

The results in Table 3.2 show that the unscaled C_6 dispersion-energy term alone performs poorly for the KB49 molecular benchmark, since neglect of higher-order dispersion terms results in under-estimation of the dispersion energy. This model similarly results in systematic under-binding of the X23 molecular-crystal benchmark, leading to a mean error of -1.59 kcal/mol. Conversely, use of a scaled C_6 terms gives excellent performance for molecules, but this requires doubling of the dispersion coefficients, with $s = 2.09$ [80]. However, the scaled C_6 dispersion correction now results in systematic over-estimation of the molecular-crystal lattice energies, with a mean error of 1.61 kcal/mol. This over-binding occurs because the scaled C_6 term

Table 3.2: Mean absolute errors (MAE), and mean errors (ME), in kcal/mol, for the KB49 [123, 323] and X23 [295] benchmarks using the B86bPBE [147, 149] base functional and selected XDM dispersion terms. Multiplication of a term by s indicates empirical scaling. Table adapted from Ref. [80].

Dispersion Energy Expression	KB49		X23	
	MAE	ME	MAE	ME
$E^{(6)}$	0.83	-0.23	1.97	-1.59
$E^{(6)} + E^{(8)}$	0.48	0.02	0.94	-0.38
$E^{(6)} + E^{(8)} + E^{(10)}$	0.41	0.03	0.86	-0.26
$sE^{(6)}$	0.38	0.01	1.78	1.61
$E^{(6)} + sE^{(8)}$	0.40	0.01	0.84	0.08

has too gradual an asymptotic decay to properly account for higher-order C_8 dispersion, over-estimating the dispersion stabilization for the many atomic contacts in a molecular crystal with large internuclear separations. This error is not seen for small molecular dimers since, unlike for periodic solids, there will be few distant atomic contacts. Overall, inclusion of a C_8 term, either scaled or unscaled, is necessary for simultaneous good performance on both benchmarks.

Interestingly, contrasting the X23 results using scaled and unscaled C_6 dispersion terms provides insight into systematic trends in atomic dispersion coefficients employed in common force fields [438–440]. It was recently found that force-field dispersion coefficients are typically 1.5 times greater than the corresponding XDM values for small organic molecules [445], as well as for biomolecules [446]. It was argued that the 1.5 factor allowed the force fields to approximate contributions from the higher-order C_8 dispersion term using only the C_6 dispersion term available in the LJ potential. From the XDM results above, the mean errors for the X23 set obtained using scaled ($s = 2.09$) and unscaled ($s = 1$) C_6 dispersion terms are equal in magnitude, but opposite in sign. Thus, the scaling of $s = 1.5$ found for the force fields should evenly balance the over- and under-binding tendencies and would be expected to give near zero mean error for the molecular crystals and other condensed-phase systems. However, using a scaled C_6 dispersion term to account for C_8 dispersion contributions neglects important physics and can still result in substantial error. Explicit inclusion of the C_8 term in both DFT dispersion corrections and molecular-mechanics force field is favoured and, for example, can considerably increase the accuracy of a four-point-charge water model [447].

3.3.3 RESPONSE TO ATOMIC ENVIRONMENT, A.K.A. ELECTRONIC MANY-BODY EFFECTS

There has been substantial confusion in the literature regarding the meaning of many-body dispersion. This pertains to deconvoluting non-additivities in the dispersion coefficients themselves, termed electronic many-body effects in our recent work [80], from the triple-dipole Axilrod–Teller–Muto (ATM) [276, 277] and higher-order non-pairwise terms in the perturbation-theory expansion of the dispersion energy. The ATM terms can be modelled even using fixed dispersion coefficients, and can optionally be included in calculations using the D3 dispersion correction [41]. However, such triple-dipole terms are not required for an accurate dispersion correction as they are negligible for most chemical systems [80, 91, 448], although they can be significant in π -stacked dimers depending on the choice of damping function [449]. Conversely, electronic many-body effects are not included in empirical dispersion methods that use fixed dispersion coefficients, but can have massive effects on the dispersion energies [80, 98, 104, 450]. Manifestations of electronic many-body effects include changes in dispersion coefficients due to varying atomic charge state, coordination, and even the presence of neighbouring molecules, which collectively determine an atom’s chemical environment.

A particularly striking example of electronic many-body effects is the change in leading-order C_6 dispersion coefficients for common transition-metal elements when going from a free atom to the bulk metal [98]. Table 3.3 shows computed C_6 dispersion coefficients for five bulk transition metals [451], obtained with various dispersion corrections, compared to the free-atomic values [452]. Unfortunately, there is no accurate reference data for atomic C_6 coefficients in bulk metals. However, XDM [57] and TSsurf [452] (which is a pre-cursor to the MBD [45] method) aim to accurately account for variations in dispersion coefficients with chemical environment. As both of these methods provide highly accurate binding energies for adsorption of benzene on copper, silver, and gold surfaces [98, 452], they should provide the most reasonable C_6 ’s for these metals.

Free transition-metal atoms are highly reactive, possessing loosely bound s -shell electrons. This leads to a much more diffuse and polarizable electron density distribution for a free atom compared to the bulk metal. As a result, one would expect a marked decrease in homoatomic C_6 coefficients for bulk metals; this is exactly what is seen in Table 3.3 with the TSsurf and XDM methods, albeit to varying extents. Conversely, the TS [44] and D3 [41] dispersion models, in which the C_6 coefficients depend

Table 3.3: Homoatomic dispersion coefficients for selected metals, in atomic units; free-atom values [452] are compared with results for the bulk metals [451] using various dispersion corrections. The D3 [41] and D4 [42] dispersion coefficients are determined entirely by the atom positions, while the TSsurf data was taken from Ref. [452]. The XDM results were obtained from B86bPBE calculations using the Quantum ESPRESSO program [111], the PAW [225, 226] approach, a $12 \times 12 \times 12$ \mathbf{k} -point mesh, and a cold smearing [453] parameter of 0.01 Ry. Planewave cutoffs of 120 and 1200 Ry were used for the kinetic energy and electron density, respectively. The TS [44] dispersion coefficients were evaluated by scaling the free-atom values using the ratio of Hirshfeld volumes [93] obtained from the XDM calculations.

Element	Free Atom	Bulk Metal				
		TS	D3	D4	TSsurf	XDM
Cu	253	230	175	62	59	106
Pd	158	172	266	192	102	92
Ag	339	349	269	134	122	180
Pt	347	383	337	331	120	124
Au	298	342	317	41	134	130

only on atomic volumes or local coordination numbers, are too simplistic to correctly account for this physics. In several cases, TS and D3 predict higher C_6 coefficients for the bulk metal than for the free atoms, explaining why they overestimate adsorption energies of benzene on these metal surfaces [98]. The very recent D4 [42, 43] model, which has not yet been comprehensively benchmarked for metal-containing systems, predicts dispersion coefficients that are similar to the free-atom values for Pd and Pt, while showing good agreement with TSsurf for Cu, Ag, and Au.

Prior works have highlighted how the description of molecular surface adsorption [98] and alkali-halide lattice constants [454] is improved due to the leading-order C_6 dispersion coefficients' response to variations in chemical environment. More dramatically, inclusion of electronic many-body effects is essential for accurate prediction of the interlayer distances and exfoliation energies of the transition-metal dichalcogenides [104] using a post-SCF dispersion model. Accounting for changes in dispersion coefficients with atomic environment is also essential for modelling exfoliation of other layered materials, such as inorganic minerals [455]. While simple dispersion models have proved highly successful for organic chemistry, incorporating the physics of electronic many-body effects constitutes an additional requirement for a density-functional dispersion model to attain high accuracy for inorganic chemistry.

3.4 DISPERSION CONTRIBUTIONS TO STRESSES

As discussed in Section 3.3.3, dispersion corrections generally become more accurate as they incorporate more sophisticated dependence on the electron density and, hence, the chemical environment. Unfortunately, density dependence of the dispersion coefficients greatly complicates evaluation of the atomic forces, and the stress tensor for periodic solids, which are required for geometry optimization. Computation of the forces and stress tensor both require differentiation of the dispersion-energy expression with respect to changes in atomic positions. This is trivial for methods like D2 [40] that use fixed, empirical dispersion coefficients. However, it is much more complicated for methods in which the dispersion coefficients involve Hirshfeld [93], or other similar partitioning [296, 456, 457] of the electron density.

For the remainder of this section, we will focus on our XDM model to illustrate the necessity of computing accurate stresses for density-dependent dispersion corrections. In particular, we demonstrate the potential errors that arise from making approximations in evaluating the stress tensor that neglect environmental dependence of the dispersion coefficients. Similar issues are expected for the TS [44] and dDsC [458] dispersion corrections, which also use atomic partitioning. However, stress errors introduced by using approximate derivatives in the TS dispersion correction will be much less than with XDM, since the TS dispersion coefficients display a much weaker dependence on chemical environment effects (see Appendix B.3.1).

For solid-state calculations with XDM (which uses BJ damping), the dispersion energy is [56, 57]

$$E_{\text{disp}} = -\frac{1}{2} \sum_{\mathbf{L}} \sum_{i \neq j'} \sum_{n=6,8,10} \frac{C_{n,ij}}{R_{ij,\mathbf{L}}^n + R_{\text{vdW},ij}^n}, \quad (3.4.1)$$

where the i and j indices provide a sum over all atom pairs and the sum over n includes higher-order dispersion terms from the perturbation-theory expansion of the dispersion energy. The prime excludes the $i = j$ term for lattice vector $\mathbf{L} = 0$ and the $1/2$ factor avoids double counting. We approximate the force on atom i as

$$\mathbf{F}_{\text{disp},i} = \sum_{\mathbf{L}} \sum_{j'} \sum_{n=6,8,10} \frac{n C_{n,ij} R_{ij,\mathbf{L}}^{n-2}}{(R_{ij,\mathbf{L}}^n + R_{\text{vdW},ij}^n)^2} \mathbf{R}_{ij,\mathbf{L}} \quad (3.4.2)$$

and the elements of the stress tensor (where ξ, η are two of x, y, z) as

$$\sigma_{\text{disp},\xi\eta} = -\frac{1}{2V} \sum_{\mathbf{L}} \sum_{i \neq j'} \sum_{n=6,8,10} \frac{n C_{n,ij} R_{ij,\mathbf{L}}^{n-2} (R_{ij,\mathbf{L}})_\xi (R_{ij,\mathbf{L}})_\eta}{(R_{ij,\mathbf{L}}^n + R_{\text{vdW},ij}^n)^2}, \quad (3.4.3)$$

both of which assume constant dispersion coefficients [56]. This assumption results in a mismatch between the energy and the forces and stresses at each step of a geometry optimization. While it has been highly successful for molecular crystals [56, 99], this assumption does break down for non-molecular solids and surfaces, as noted previously for the particular example of graphene adsorption on a nickel surface [103]. As a result, later calculations on layered transition-metal dichalcogenides [104] and on alkali halides [454] with XDM have utilized numerical geometry optimization, in which the interlayer separation or bulk lattice constants were varied over a range of values and the energy minimum found by interpolation.

We consider a set of eight simple cubic solids [451] to illustrate the errors resulting from the assumption of constant dispersion coefficients in stress evaluations Table 3.4 shows the lattice constants resulting from variable-cell relaxation, using Eq. (3.4.3) for the stress evaluation, and the minimum-energy lattice constants obtained from interpolation. Using the approximate stresses from Eq. (3.4.3) results in a systematic under-estimation of the lattice constants, by 0.01–0.08 Å, with the corresponding energy difference between the relaxed and minimum-energy structures ranging from near zero to 0.04 eV.

To highlight the difference between molecular crystals and ionic solids, Figure 3.7 contrasts the examples of CO₂ and NaCl, which shows the largest geometry and energy errors of the cubic solids considered in Table 3.4. The figure shows a steep dependence of the energy on the cell volume for NaCl. Here, the assumption of constant dispersion coefficients leads to comparatively large errors in the minimum energy, cell volume, and stress-tensor components. These errors arise because the C_6 (and higher-order) dispersion coefficients of both Na and Cl are dependent on cell compression, varying by ca. ±4% from their equilibrium values over the range of volumes shown in the Figure. Furthermore, the primary source of variation in the C_6 dispersion coefficients with cell volume can be traced to the exchange-hole dipole moment integrals, which can vary significantly with changes in covalent, metallic, and ionic bond lengths, while the changes in atom-in-solid polarizabilities are minor.

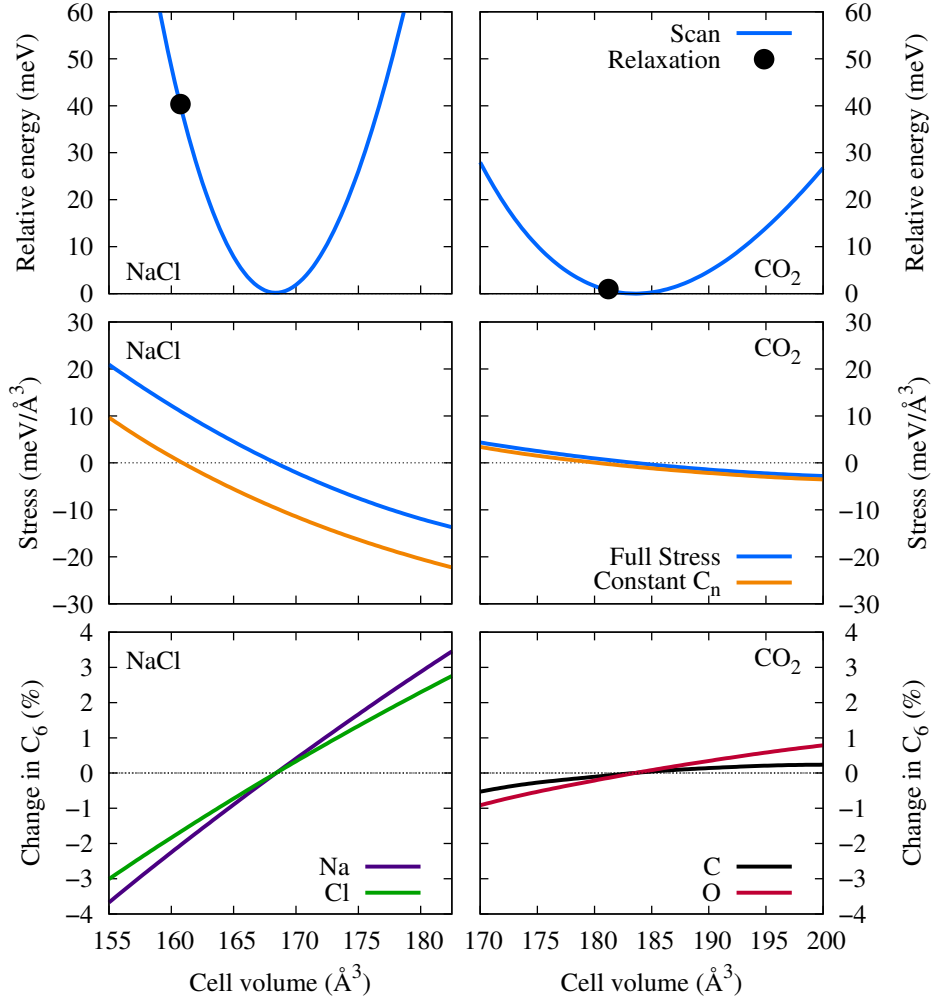
In contrast, for molecular solids such as CO₂, the variations in both moment integrals and dispersion coefficients with expansion or compression are much smaller

Table 3.4: Minimum-energy lattice constants (a_{latt} in Å) of selected materials with cubic unit cells [451]. Results from XDM relaxations assuming constant dispersion coefficients are shown for comparison, along with the corresponding energy error, ΔE . Results were obtained using B86bPBE-XDM [57, 147, 149] with Quantum ESPRESSO [111], the PAW [225, 226] approach and planewave cutoffs of 120 and 1200 Ry for the kinetic energy and electron density, respectively, except for CO₂ where values of 80 and 800 Ry were used. The \mathbf{k} -point meshes were $4 \times 4 \times 4$ for CO₂, $6 \times 6 \times 6$ for C, NaCl, and MgO, and $12 \times 12 \times 12$ for Si, GaAs, Cu, and Ni. A cold smearing [453] parameter of 0.01 Ry was used for Cu and Ni.

Material	a_{latt} (Å)		ΔE (eV)
	Minimum	Relaxed	
CO ₂	5.69	5.66	0.001
C (diamond)	3.57	3.56	0.009
Si	5.46	5.42	0.020
Cu	3.62	3.58	0.026
Ni	3.51	3.47	0.034
GaAs	5.71	5.66	0.036
MgO	4.23	4.19	0.036
NaCl	5.52	5.44	0.040

(< 1%) since altering the cell volume primarily changes the intermolecular distances. Thus, any errors in computed stresses arising from the assumption of constant dispersion coefficients are largely insignificant for molecular crystals, but become quite significant for ionic and network solids. Evaluation of the dispersion contributions to the atomic forces and stress tensor in a way that is fully consistent with the dispersion-energy expression is clearly needed for density-dependent dispersion models, such as XDM. However, the use of Hirshfeld or similar atomic partitioning complicates this task, making it an ongoing challenge for developers of density-dependent dispersion corrections.

Figure 3.7: B86bPBE-XDM results, using the methodology described in Table 3.4, for NaCl (left) and CO₂ (right). Top: potential energy curves showing the energy as a function of lattice constant; the results of variable-cell relaxations assuming constant dispersion coefficients in the stress evaluations are shown for comparison. Middle: comparison of the exact stress and that computed assuming constant dispersion coefficients. Bottom: variation in the homoatomic C₆ dispersion coefficients, relative to their equilibrium values.



3.5 SUMMARY

In this chapter, we have presented what we believe are the key requirements for a general and accurate dispersion-corrected density functional. Accuracy of the base functional and dispersion correction should be enforced separately to ensure that their combination properly describes the physics of both non-bonded repulsion and dispersion attraction, rather than relying on error cancellation.

A reliable dispersion correction should use finite-damping to prevent introduction of an artificial, repulsive dispersion force at short internuclear separations. It should involve minimal empiricism and evaluate the dispersion coefficients in such a way that they are dependent on the electron density and, consequently, can respond to changes in chemical environment. Variations in the dispersion coefficients with chemical environment, including changes in charge state, coordination, and the presence of neighbouring molecules, can be captured through density dependence and are collectively termed electronic many-body effects. Unfortunately, having dispersion coefficients that are intricate functions of the electron density greatly complicates evaluation of the dispersion contributions to the atomic forces and stresses, which are required for geometry optimization. Evaluation of the forces, and particularly stresses, in a way that is fully consistent with the dispersion-energy expression is necessary for proper geometry relaxation with density-dependent dispersion corrections.

A reliable base density functional must be dispersionless, which can be achieved by imposing a constraint on the large-gradient limit of the exchange enhancement factor for GGAs, as well as being numerically stable. These requirements are not met by the majority of meta-GGAs, where the semi-local exchange functionals tend to mimic short-range “dispersion-like” binding, which is properly a non-local correlation effect. Moreover, popular functional forms that build in kinetic-energy dependence result in significant numerical sensitivities to the spacing of the integration mesh relative to low-density bond critical points, as occur in vdW complexes. Finally, an accurate base functional should be free of delocalization error, as discussed in Section 2.6. This error can be reduced through use of global hybrid and range-separated hybrid functionals, although such hybrids do not completely resolve the delocalization error problem and the optimal amount of exact exchange required to minimize it can be highly system dependent [459–461].

CHAPTER 4

MANY-BODY DISPERSION IN MODEL SYSTEMS AND THE SENSITIVITY OF SELF-CONSISTENT SCREENING

“The career of a young theoretical physicist consists of treating the harmonic oscillator in ever-increasing levels of abstraction.” [462]

~ Prof. Sidney Coleman (1937–2007)

This chapter is adapted from: Bryenton, K. R., & Johnson, E. R. *Many-Body Dispersion in Model Systems and the Sensitivity of Self-Consistent Screening*. J. Chem. Phys., **158**, 20, 204110. (2023) [315]

Author contributions: K.R.B. developed the mathematical model, wrote the software, generated all data, and wrote the first draft of the manuscript.

4.1 INTRODUCTION

A number of recent articles have discussed the impact of many-body effects on dispersion interactions and their importance in various chemical or solid-state systems [45, 47, 295, 463–469]. We have argued that many-body effects can be separated into two distinct categories, atomic and electronic, based on the perturbation theory of dispersion [80]. In our definition, atomic many-body effects refer to terms that involve more than two atoms obtained from higher levels of perturbation theory, beyond second order. The most significant of these is the three-body, Axilrod–Teller–Muto (ATM) term [276, 277] that arises from third-order perturbation theory. For a trio of atoms, the ATM energy is given by

$$E_{\text{ATM}} = \frac{C_{9,ijk}}{R_{ij}^3 R_{ik}^3 R_{jk}^3} [3 \cos(\theta_i) \cos(\theta_j) \cos(\theta_k) + 1], \quad (4.1.1)$$

where θ_i is the angle between atoms i, j, k with atom i at the vertex. This term predicts repulsion for atoms in equilateral or right-angle triangular configurations, and maximal attraction for linear configurations. We have, however, argued that contributions from the ATM term are negligible in molecular systems [80, 91].

Electronic many-body effects refer to the responsiveness of the dispersion coefficients, C_n , due to the surrounding atoms. These coefficients will vary from their free-atom values depending on chemical bonding, atomic charge, coordination, hydrogen bonding, and even the presence of distant atoms or molecules [80, 450]. These electronic many-body effects can cause drastic changes in dispersion coefficients, particularly for inorganic solids [80, 104]. Capturing these changes is essential for accurate modelling of a system’s dispersion energy, and will be a focus of this work.

Within the context of density-functional theory (DFT), dispersion terms must be explicitly included either through incorporation in the exchange-correlation functional, or through an additive, post self-consistent field (post-SCF) correction. In this work, we will limit our discussion to post-SCF dispersion corrections, of which the exchange-hole dipole moment (XDM) [55–57, 156] and many-body dispersion (MBD) [45, 46] methods are two of the most accurate. Both of these models involve dispersion coefficients that respond to changes in atomic environment without introduction of empirical parameters, although the origins of their environment dependence are quite different. MBD is based on a model of interacting harmonic oscillators, while XDM captures changes in dispersion coefficients through use of the self-consistent electron

density and its derivatives. There are other essential differences between these two methods, including the form of the dispersion energy, how it is damped for small internuclear separations, whether atomic polarizabilities are treated as isotropic or anisotropic, and whether higher-order terms beyond the leading-order C_6 contribution are taken into account.

While the MBD implementation in FHI-aims computes only the total many-body dispersion energy, it is possible to reformulate the theory in terms of the random-phase approximation (RPA) [181, 470, 471] to obtain a decomposition into two-body, three-body, and higher-order terms. However, this is very different from the partitioning into electronic (changes in the dispersion coefficients due to the presence of all other atoms in the system) and atomic (ATM and analogous terms from higher orders of perturbation theory) many-body effects described above. For example, in the MBD definition, three-body terms will include other contributions in addition to the ATM term [471]. Beyond-pairwise terms in MBD have been shown to have large contributions to the overall dispersion energies of molecular crystals [295], supermolecular complexes [471], and large biomolecules [470]. Much of the debate in the literature concerning the relative importance of beyond-pairwise dispersion effects is likely due to these disparate definitions.

Given the contrasts between the theoretical underpinnings and mathematical forms of XDM and MBD, it is notable that they give quite comparable accuracy for many common benchmarks for intermolecular interactions, molecular crystals, and layered materials. This has prompted us to take a step back and compare the behaviours of these two dispersion methods for a selection of simple model systems, in which the dispersion physics can be examined in the absence of confusing factors such as choices of electronic structure code, basis set, or exchange-correlation functional.

In this chapter, we compare XDM and MBD, as well the Tkatchenko–Scheffler (TS) method [44], for a first-principles interacting quantum harmonic oscillator model at finite separations. Oscillator systems were chosen since they form the basis of the MBD model, while it has been shown that XDM recovers the exact result for the asymptotic interaction between harmonic oscillators from perturbation theory [80] (see also Appendix A.3). We consider linear arrangements of two, three, and four oscillators, where a variational model is used to capture changes in the free-oscillator wavefunction due to interactions with its neighbours. Linear arrangements of these small oscillator systems should serve to maximize the magnitude of the ATM term, as well as the polarization anisotropy [472]. The dispersion energy and C_6

coefficients are computed from the variationally optimized wavefunctions with XDM, and compared to the TS and MBD results for the same quantities. The aim is to determine if the methods provide comparable treatment of dispersion, including many-body effects, despite their different theoretical bases. Additionally, calculations are performed on linear chains of noble gas atoms to connect the oscillator results with real atomic systems. Finally, we consider two homo-molecular dimers (methane and benzene) and two layered materials (graphite and MoS₂) to highlight similarities and differences between our model systems and those more relevant to chemistry and materials science.

4.2 THEORETICAL BACKGROUND: MBD-FREE AND MBD-XDM

For a comprehensive overview of the XDM, TS, MBD@rsSCS, and MBD-NL dispersion corrections that are used in this chapter, the reader is directed to Section 2.5.

The MBD model traditionally uses the polarizabilities and C_6 coefficients from the TS model as a starting point for the SCS and rsSCS schemes. However, this choice is rather arbitrary and it is not clear to what extent it impacts the evaluation of the final dispersion coefficients and energies. Here we considered two new variants, which we call MBD-Free and MBD-XDM. These variants are not intended for production use, but rather, to assess the sensitivity of SCS/rsSCS to the starting conditions.

The MBD-Free variant uses a free-atom starting point, allowing us to visualize the effect of SCS separately from the TS model's volume scaling. This variant would be expected to be well behaved for systems where a free-atom starting point would be reasonable, such as for noble gas atoms. Conversely, MBD-XDM uses the XDM dispersion model as a starting point. Here, the starting C_6 coefficients and polarizabilities are given by

$$C_{6,ii} = C_{6,ii}^{\text{XDM}}, \quad (4.2.1)$$

$$\alpha_i^0 = \alpha_i^{\text{free}} \sqrt{\frac{C_{6,ii}^{\text{XDM}}}{C_{6,ii}^{\text{free}}}}. \quad (4.2.2)$$

These quantities are then used to evaluate the characteristic excitation frequencies and frequency-dependent polarizabilities that are used as input to the SCS or rsSCS process. The final MBD-Free and MBD-XDM dispersion coefficients are then obtained

from the resulting SCS or rsSCS polarizabilities and the Casimir–Polder integral [274].

4.3 INTERACTING OSCILLATOR SYSTEMS

Quantum harmonic oscillators are the classic model system for dispersion. They are at the heart of the MBD method, and XDM has also been shown to be exact for the asymptotic (weakly-interacting) limit for harmonic oscillators [80]. In this work, we aim to model interacting oscillators with XDM over a range of distances and determine if the environment dependence is similar to what is observed for real chemical systems. The ultimate goal will be to compare predicted XDM and MBD energies and dispersion coefficients for harmonic oscillators, and determine if they give equivalent response to surrounding environment/many-body effects.

4.3.1 THE ISOTROPIC QUANTUM HARMONIC OSCILLATOR

To study systems of interacting oscillators we start from the single-oscillator case: the isotropic quantum harmonic oscillator. The corresponding potential has the form

$$V(r) = \frac{1}{2} \mu \omega^2 r^2, \quad (4.3.1)$$

where the angular frequency $\omega = \sqrt{k_s/\mu}$ may be written in terms of the effective spring constant, k_s , and reduced mass, μ . The wavefunctions that satisfy the resulting Schrödinger equation are given by [473]

$$\psi_{k\ell m}(r, \theta, \phi) = N_{k\ell} r^\ell e^{-\nu r^2} L_k^{\ell+\frac{1}{2}}(2\nu r^2) Y_\ell^m(\theta, \phi), \quad (4.3.2)$$

where $N_{k\ell}$ is the normalization constant, $L_k^{(\ell+\frac{1}{2})}(x)$ are the generalized Laguerre polynomials, $Y_\ell^m(\theta, \phi)$ are the spherical harmonic functions, and $\nu = \mu \omega / (2\hbar)$. The corresponding energy eigenvalues for these wavefunctions are given by

$$E = \hbar \omega \left(2k + \ell + \frac{3}{2} \right). \quad (4.3.3)$$

The energy is normally described by the single quantum number $n = 2k + \ell$. Here $k \in \mathbb{N}_0$, $\ell \leq n \in \mathbb{N}_0$, and $-\ell \leq m \leq \ell \in \mathbb{Z}$. The wavefunctions in Eq. (4.3.2) are square-integrable and normalized over their configuration space $\int_{\mathcal{H}} |\psi_{k\ell m}(\mathbf{r})|^2 d\mathbf{r} = 1$, while also satisfying the orthonormality condition for their three quantum numbers: $\langle \psi_{k_1 \ell_1 m_1}(\mathbf{r}) | \psi_{k_2 \ell_2 m_2}(\mathbf{r}) \rangle = \delta_{k_1 k_2} \delta_{\ell_1 \ell_2} \delta_{m_1 m_2}$.

4.3.2 INTERACTION HAMILTONIAN

Dimer, trimer, and tetramer systems of interacting oscillators were aligned along the z -axis, as shown in Figure 4.1, such that each system is symmetric across the $x-y$ plane. Aligning the oscillators as a linear chain comes with numerous benefits: it reduces the computational resources needed as this first-principles model will scale with $O(N^4)$, linear chains will maximize the polarizability anisotropy captured by the SCS model [472], and a linear configuration of oscillators will maximize the ATM term [276]. The distance between any two adjacent oscillators is defined as R_{sep} . \mathbf{R}_p is the vector that points from the system origin to the nucleus of each oscillator, $p = \{A, B, \dots\}$, and \mathbf{r}_p is the vector that points from the nucleus of oscillator p to its respective electron.

To study the properties of these systems, we first must construct the Hamiltonian that describes them. Within the Born–Oppenheimer approximation [474], the non-interacting terms (i.e. kinetic and potential energy terms for a single oscillator) in our Hamiltonian have the form

$$\hat{T}_p + \hat{V}_p = -\frac{\hbar^2}{2\mu_p} \nabla_p^2 + \frac{1}{2}\mu_p\omega_p^2 r_p^2, \quad (4.3.4)$$

for a particular oscillator p . The interactions between the different oscillators will be Coulombic, and will consist of electron-nuclear, electron-electron, and nuclear-nuclear terms. The electron-nuclear term for the electron of oscillator p interacting with the nucleus of oscillator q , with $p \neq q$, is

$$\hat{U}_{pq}^{\text{en}} = \frac{e^2}{4\pi\epsilon_0} \frac{-Z_q}{|(\mathbf{R}_p + \mathbf{r}_p) - \mathbf{R}_q|}, \quad (4.3.5)$$

where e is the charge of the electron, Z_q is the atomic number of oscillator q , and ϵ_0 is the permittivity of free space. Similarly, the interaction between the electrons of two oscillators p and q is described by

$$\hat{U}_{pq}^{\text{ee}} = \frac{e^2}{4\pi\epsilon_0} \frac{1}{|(\mathbf{R}_p + \mathbf{r}_p) - (\mathbf{R}_q + \mathbf{r}_q)|}. \quad (4.3.6)$$

Lastly, nuclear-nuclear contributions have the form

$$\hat{U}_{pq}^{\text{nn}} = \frac{e^2}{4\pi\epsilon_0} \frac{Z_p Z_q}{|\mathbf{R}_p - \mathbf{R}_q|}. \quad (4.3.7)$$

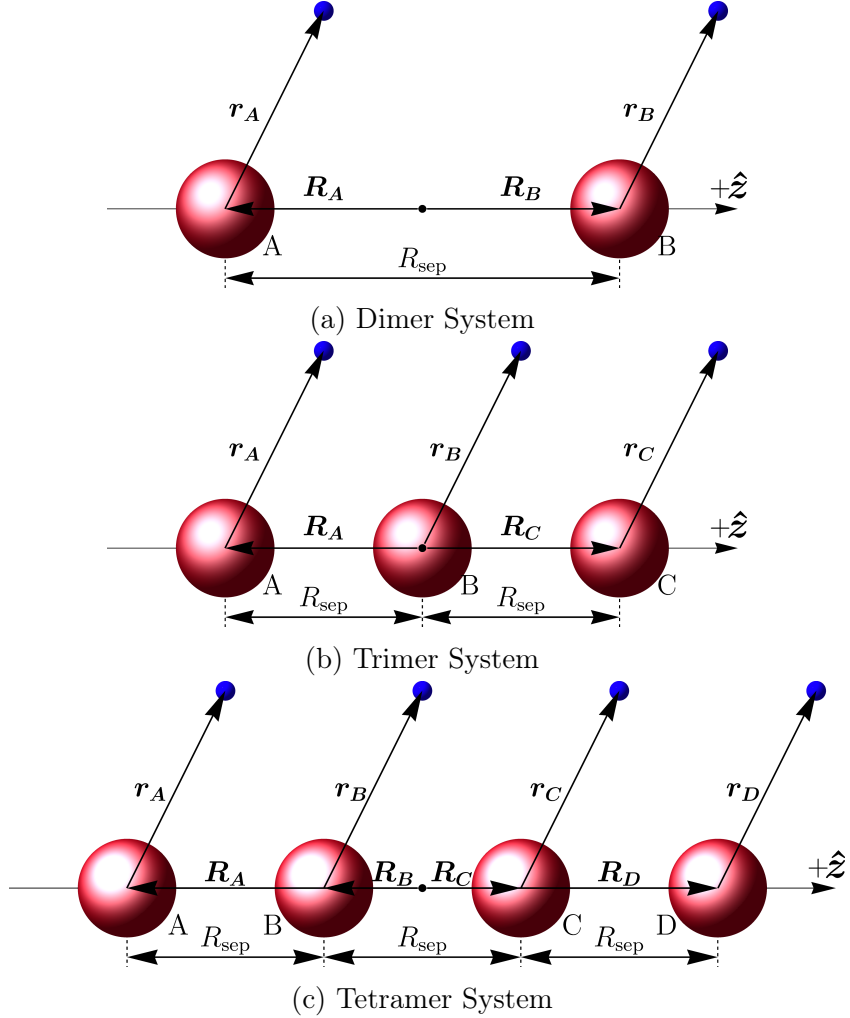


Figure 4.1: The selected geometries for our dimer (a), trimer (b), and tetramer (c) systems of interacting quantum harmonic oscillators, such that all oscillators are aligned along the z -axis. The nucleus of each oscillator is represented by a red sphere, while their corresponding electrons are represented by blue spheres.

Combining these contributions together, the general interaction Hamiltonian is

$$\hat{H} = \sum_p \left(\hat{T}_p + \hat{V}_p \right) + \sum_{q \neq p} \left(\hat{U}_{pq}^{\text{en}} + \frac{1}{2} \hat{U}_{pq}^{\text{ee}} + \frac{1}{2} \hat{U}_{pq}^{\text{nn}} \right). \quad (4.3.8)$$

For the electron-nuclear component, the $p = q$ term is omitted because that interaction has been described by the harmonic coupling in Eq. (4.3.1). For both the electron-electron and nuclear-nuclear terms, the factor of $1/2$ accounts for the double-counting of contributions.

The systems will be modelled after interacting hydrogen atoms, so we will choose $Z_A = Z_B = 1$. The reduced mass of our system then becomes $\mu = {}^{1836}/{}^{1837}$ a.u. We note that the polarizability of a quantum harmonic oscillator may be expressed in terms of the electron charge, e , and the spring constant, k_s , as $\alpha = e^2/k_s$ [69]. Thus, the polarizability and angular frequency are intrinsically linked for this system via

$$\alpha = \frac{e^2}{\omega^2 \mu}, \quad (4.3.9)$$

and choosing $\alpha^{\text{free}} = 4.5$ a.u. to match hydrogen gives a corresponding frequency of $\omega = 0.4715$ a.u. These values were chosen for all calculations unless stated otherwise. Another possible choice is to recall that the first excitation energy for hydrogen is $3/8$ a.u. and the QHO energy level spacing is $\hbar\omega$. Thus, $\omega = 3/8$ a.u. and $\alpha^{\text{free}} = 7.115$ a.u. is reasonable. Alternatively, the SCS routine selects the characteristic excitation frequency via

$$\omega_i = \frac{4}{3} \frac{C_{6,ii}}{(\alpha_i^0)^2}. \quad (4.3.10)$$

Using $C_{6,ii} = 6.5$ a.u. and $\alpha_i^0 = 4.5$ a.u. to match hydrogen yields $\omega = 0.428$ with a corresponding $\alpha^{\text{free}} = 5.4624$ a.u. The effects on C_6 with these alternate values of ω are discussed in Section 4.4.3.

4.3.3 WAVEFUNCTIONS

In constructing the wavefunctions for the interacting oscillators, we use the variational method with a basis of hydrogen-like isolated-oscillator wavefunctions. To help connect with chemical intuition, we will refer to these oscillator wavefunctions by their analogous atomic orbital names, determined by their spherical harmonics. Here, we considered wavefunctions from the ground, first, and second excited states that exhibited bilateral symmetry along the z -axis. The only wavefunctions that satisfied this symmetry were the $1s$ orbital from the ground state, the $2p_z$ orbital from the first excited state, and the $2s$ and $3d_{z^2}$ orbitals from the second excited state. Their explicit forms are given by

$$\psi_{1s}(\mathbf{r}) = \frac{2^{3/4} \nu^{3/4}}{\pi^{3/4}} e^{-\nu r^2} \quad (4.3.11)$$

$$\psi_{2p_z}(\mathbf{r}) = \frac{2^{7/4} \nu^{5/4}}{\pi^{3/4}} e^{-\nu r^2} r \cos(\theta) \quad (4.3.12)$$

$$\psi_{2s}(\mathbf{r}) = \frac{2^{1/4} \nu^{3/4}}{\sqrt{3} \pi^{3/4}} e^{-\nu r^2} (3 - 4\nu r^2) \quad (4.3.13)$$

$$\psi_{3d_{z^2}}(\mathbf{r}) = \frac{2^{3/4} \nu^{7/4}}{\sqrt{3} \pi^{3/4}} e^{-\nu r^2} r^2 (3 \cos(2\theta) + 1) \quad (4.3.14)$$

and plots of these four orbitals are shown in Figure 4.2.

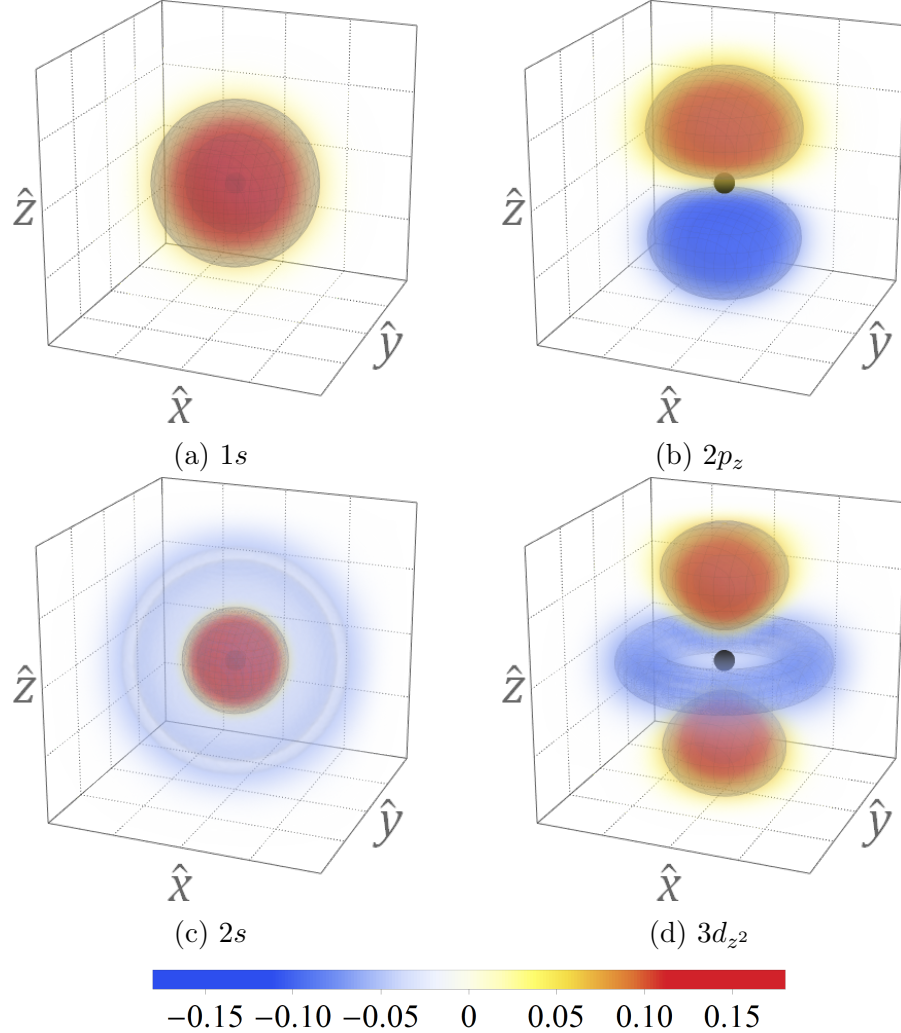


Figure 4.2: The $1s$ (a), $2p_z$ (b), $2s$ (c), and $3d_{z^2}$ (d) free-atomic orbitals for the isotropic quantum harmonic oscillator. From the ground, first, and second excited states, these are the only four orbitals that satisfy the bilateral z -axis symmetry requirement for the interacting oscillator chains.

For each oscillator p , the total wavefunction is given as a linear combination of these four orbitals as

$$\Psi_p = \sum_i c_i \psi_{p,i}. \quad (4.3.15)$$

To ensure symmetry of the wavefunctions across the $x-y$ plane, substitutions of $\theta_p \rightarrow \pi - \theta_p$ were made for certain oscillators: θ_B was substituted for the dimer system, θ_C

for the trimer system, and both θ_B and θ_D for the tetramer system. These choices permitted constructive orbital overlap between adjacent oscillators allowing us to capture the bonding behaviour of the system. Due to symmetry, the central oscillators (trimer oscillator B, and tetramer oscillators B and C) require different expansion coefficients than the terminal oscillators in each system. The expansion coefficients for the terminal oscillators in each system will simply be written as c_i , while the expansion coefficients for the central oscillators will be written as d_i .

Testing was performed using all 10 wavefunctions from the ground, first, and second excited states on our systems; this confirmed that only the four wavefunctions previously discussed had non-zero contributions. Further testing was performed regarding the inclusion of wavefunctions from the higher energy states, specifically the $3p_z$ and $4f_{z^3}$ orbitals. We determined the inclusion of these orbitals added no additional physics to the system, so they were omitted for computational efficiency.

4.3.4 VARIATIONALLY OPTIMIZED ENERGIES

From the total wavefunctions, the one-electron energies (i.e. the kinetic, potential, and electron-nuclear terms) are evaluated via

$$E_p^{1e} = \left\langle \Psi_p \left| \hat{T}_p + \hat{V}_p + \sum_{q \neq p} \hat{U}_{pq}^{\text{en}} \right| \Psi_p \right\rangle. \quad (4.3.16)$$

The two-electron energies (electron-electron) are similarly computed via

$$E_{pq}^{2e} = \left\langle \Psi_p \Psi_q \left| \frac{1}{2} \hat{U}_{pq}^{\text{ee}} \right| \Psi_p \Psi_q \right\rangle. \quad (4.3.17)$$

Thus, the total system energy is given by

$$E = \sum_p E_p^{1e} + \sum_{q \neq p} E_{pq}^{2e} + \sum_{q \neq p} \frac{1}{2} \hat{U}_{pq}^{\text{nn}} \quad (4.3.18)$$

where we note that the nuclear-nuclear terms, \hat{U}_{pq}^{nn} , are constant and may be evaluated separately. The optimal values of the expansion coefficients c_i and d_i have yet to be determined. To solve for them, we variationally optimize the wavefunctions using the method of Lagrange multipliers.

The method of Lagrange multipliers will generate the critical points of a multivariate function that is subject to one or more constraint equations [475]. For our

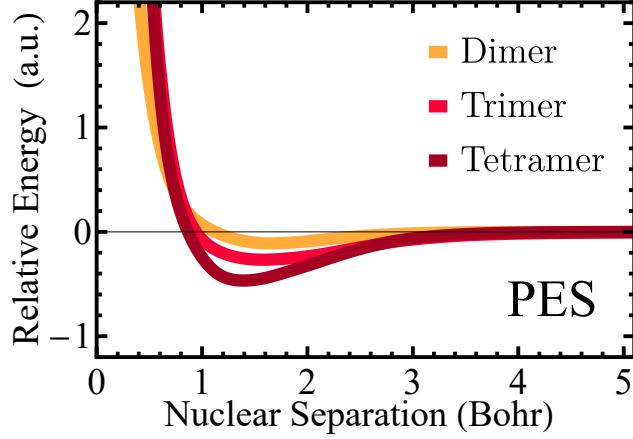


Figure 4.3: Computed potential energy surfaces for the interacting quantum harmonic oscillator systems, calculated from first principles using a variational model.

oscillator systems, the constraint comes from the normalization requirement of the expansion coefficients, $\sum_i c_i^2 = 1$ and $\sum_i d_i^2 = 1$. The Lagrangian for our singly-constrained dimer system is given by

$$\mathcal{L}(\{c_i\}, \lambda) = E - \lambda \left(1 - \sum_i c_i^2 \right), \quad (4.3.19)$$

and for the doubly-constrained trimer and tetramer cases,

$$\begin{aligned} \mathcal{L}(\{c_i\}, \{d_i\}, \lambda_1, \lambda_2) \\ = E - \lambda_1 \left(1 - \sum_i c_i^2 \right) - \lambda_2 \left(1 - \sum_i d_i^2 \right), \end{aligned} \quad (4.3.20)$$

where the λ are Lagrange multipliers. The critical points on our potential energy surface may be found by solving for the expansion coefficients in the equations generated by $\nabla \mathcal{L} = 0$. The total wavefunctions for our oscillators are determined by substituting these coefficients into the relevant set of wavefunctions in Eq. (4.3.15). Thus the coefficients, total wavefunctions, and system energy may be determined for a particular value of R_{sep} . Computing the system energies for a series of separations forms the potential energy surface (PES).

PES for the interacting dimer, trimer, and tetramer systems are shown in Figure 4.3. The curves correctly approach the sum of free-oscillator energies in the

dissociation limit and give the expected bonding, with the tetramer having the deepest potential energy well, followed by the trimer and dimer. We note that the binding energies are comparable to those of covalent bonds.

4.3.5 DISPERSION COEFFICIENTS AND ENERGIES FOR OSCILLATOR MODEL SYSTEMS

From the variationally-optimized total wavefunctions for each electron p , $\Psi_p(\mathbf{r})$, the system's electron density is determined from

$$\rho(\mathbf{r}) = \sum_p^N |\Psi_p(\mathbf{r})|^2 \quad (4.3.21)$$

and a dispersion correction of choice may be used. For XDM, the wavefunctions and electron density are used to calculate the exchange-hole multipole moments, which in turn generate the C_n^{XDM} dispersion coefficients and, thus, the XDM dispersion energy. For TS, the effective volumes determine $C_{6,ii}$, α_i^0 , and R_i^0 for electron i . The $C_{6,ij}^{\text{TS}}$ dispersion coefficient is then obtained via the Slater–Kirkwood formula, and the TS dispersion energy follows. From TS and XDM starting points, the SCS or rsSCS polarizabilities can be determined for MBD, MBD-Free, and MBD-XDM, enabling the use of those corrections as well.

4.4 RESULTS AND DISCUSSION

4.4.1 DISPERSION ENERGIES

We begin by comparing the computed dispersion energies for the harmonic oscillator model systems obtained with the various dispersion methods. Undamped dispersion energies for the interacting dimer, trimer, and tetramer are shown in Figure 4.4 for both the XDM and MBD@SCS dispersion models. We additionally show the contribution to the XDM dispersion energy from only the leading-order C_6 dispersion term. The results indicate that the undamped TS, MBD, and C_6 -only XDM dispersion energies are in excellent agreement and all three curves are superimposed in the figure. This shows that MBD does not implicitly capture higher-order effects through its self-consistent screening procedure or its model Hamiltonian. It is notable that TS is in agreement with both XDM- C_6 and MBD. This indicates that neither

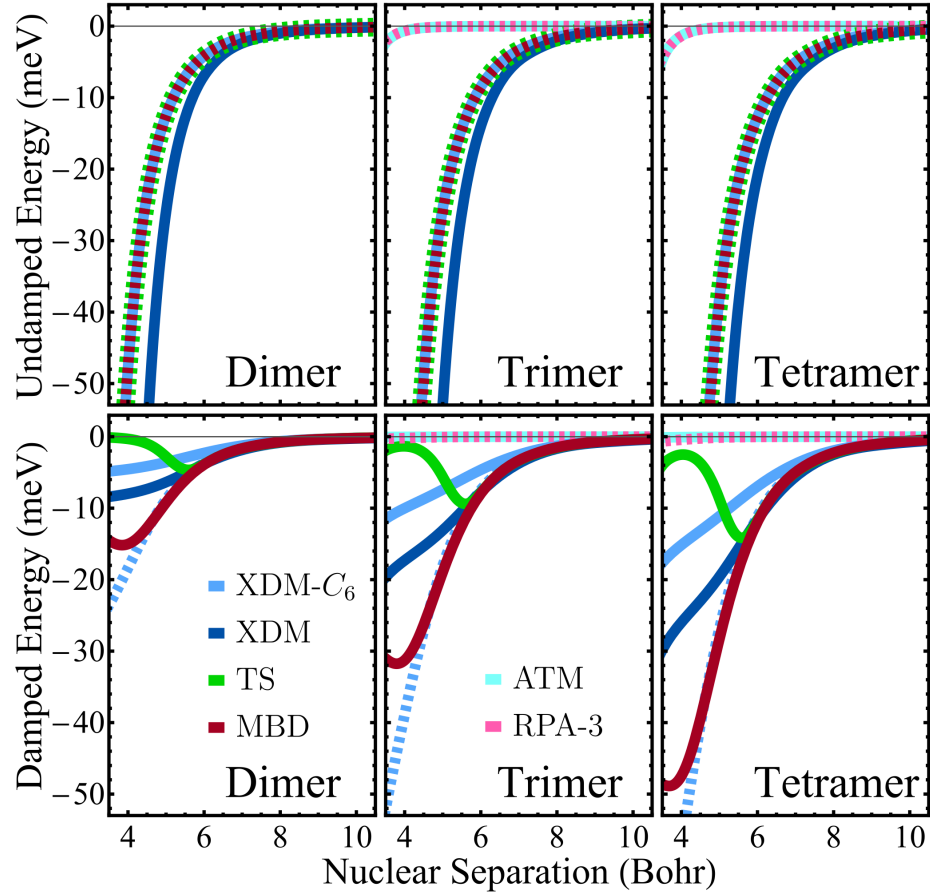


Figure 4.4: Computed undamped (top) and damped (bottom) dispersion energies for the harmonic oscillator model systems. The three-body ATM term was evaluated for XDM but this energy contribution is plotted separately. RPA-3 represents RPA’s three-body-only energy contribution. For the damped XDM- C_6 energies, the typical BJ damping with $a_1 = 0.65$ and $a_2 = 1.68 \text{ \AA}$ is shown as a solid line, and with $a_1 = 0$ and $a_2 = 2.30 \text{ \AA}$ as a dashed line.

the effects of the exchange-hole dipole for XDM, nor the additional n -body contributions from MBD, are significantly contributing to the dispersion energy for this model system of oscillators.

In previous work using XDM, we established that the C_6 term is responsible for only ca. 60% of the dispersion binding [156]. One may therefore wonder how MBD manages accuracy that rivals that of XDM when neglecting higher-order dispersion terms. To understand this, we consider the damped dispersion energies, which requires an informed choice of damping parameters.

The damping parameters used in any dispersion model are sensitive to the choice

of base DFT method, since they correct in part for errors in the description of non-bonded repulsion provided by the exchange-correlation functional, as well as basis-set incompleteness. To obtain “ideal” damping parameters, we consider the set of six noble-gas dimers consisting of all combinations of He, Ne, and Ar, studied by Kannemann [476]. In that work, the PW86PBE exchange-correlation functional [149, 151] with the aug-cc-pV5Z basis set and counterpoise correction [241] was chosen to give as accurate as possible a treatment of non-bonded repulsion to pair with a dispersion correction. The optimal parameters were determined by minimizing the root-mean-square percent error in the binding energies for all six dimers.

The ideal BJ damping parameters for use with XDM were found to be $a_1 = 0.65$ and $a_2 = 1.68 \text{ \AA}$ [476]. For the current study, we optimized the β parameter from the Wu–Yang damping function for both TS and MBD@rsSCS. Here, the TS and MBD@rsSCS dispersion energies were evaluated with FHI-aims using the PBE functional and **tight** basis sets. The dispersion energies were then combined with the literature PW86PBE/aug-cc-pV5Z counterpoise-corrected electronic energies. This ensured that the damping functions were parameterized in as similar a way as possible to allow direct comparison. The optimal damping parameters for TS and MBD@rsSCS were determined to be $\beta_{\text{TS}} = 0.86$ and $\beta_{\text{rsSCS}} = 0.62$ respectively. Lastly, we wanted to see how TS and MBD@rsSCS compare to XDM- C_6 , the C_6 -only contribution to the damped XDM energy. Using the same methodology, reparameterizing XDM- C_6 resulted in optimal BJ damping parameters of $a_1 = 0$ and $a_2 = 2.30 \text{ \AA}$, since a_1 must have a non-negative value.

Using these ideal damping parameters, a comparison of the damped dispersion energies from XDM, TS, and MBD is shown in Figure 4.4. Interestingly, the MBD, TS, and XDM damped dispersion energies track each other closely at large internuclear separations (>6 bohr). This is also the case for XDM- C_6 when the BJ damping parameters are optimized for the C_6 -only energy, but not when using the full-XDM parameterization. At short range, the TS dispersion energy is strongly damped, while MBD actually provides greater dispersion stabilization than the full XDM dispersion energy, and is in notably high agreement with the reparameterized XDM- C_6 for >4 bohr. Thus, the choice of damping can cause the MBD dispersion energy to resemble the full XDM dispersion energy rather than only the C_6 term, in the same way that a weaker damping function on XDM- C_6 can achieve similar results.

For the trimer and tetramer, the contributions of both the ATM term and the 3-body energy from RPA are included. The ATM contribution to the energy was

calculated with XDM. For the RPA contribution, each of the n -body contributions to the correlation energy were extracted from the ACFD-RPA approach for the correlation energy of the MBD method. This is described in Section 2.5.2. We compare these 3-body contributions for undamped and damped trimer and tetramer systems at all computed separations beyond 4 bohr. To ensure fair comparison between the RPA energy and MBD, the SCS starting point was used for the undamped energies, and rsSCS was used for the damped energies. The individual n -body RPA and MBD energies were compared, and found to be within 1% of each other. Further, the 2-body RPA energy captured no less than 97.9% of the total many-body energy. There is remarkably high agreement between the undamped ATM and 3-body RPA energies, as seen from the nearly superimposed curves in Figure 4.4, differing by no more than 3.2%. These results agree with our previous finding [80] that the ATM term represents a negligible contribution to the overall dispersion energy.

4.4.2 ANALYSIS OF C_6 BEHAVIOUR

Next, we analyze the changes in C_6 coefficients themselves. The computed C_6 coefficients are plotted in Figure 4.5 as a function of internuclear separation for the dimer, trimer, and tetramer models, with separate plots for the symmetry distinct (central and terminal) oscillators. Results are shown for the TS and XDM dispersion models, as well as for the SCS and rsSCS schemes used in MBD with the usual TS (MBD), free-atom (MBD-Free), or XDM (MBD-XDM) starting points. While the SCS and rsSCS C_6 coefficients do not explicitly appear in the MBD energy expression, their magnitude is directly related to the dispersion stabilization.

Overall, all of the methods give dispersion coefficients that are responsive to changes in the local environment of each oscillator. The C_6 coefficients all correctly approach the free-oscillator limit at large separations. They then reach a maximum value as the separation decreases to between 2–3 bohr. While there is some variation depending on the particular model system and internuclear separation, the dispersion coefficients follow the rough trend of MBD > MBD-XDM > TS > XDM \gg MBD-Free. Thus, the SCS and rsSCS schemes are surprisingly sensitive to the choice of starting polarizabilities and dispersion coefficients. This stands in sharp contrast to the usual self-consistent evaluation of DFT energies, which are typically insensitive to the choice of starting guess (provided convergence can be reached). A more subtle trend is that SCS tends to give larger changes in C_6 than rsSCS.

The increase in C_6 (relative to the infinitely separated limit) is smallest for the

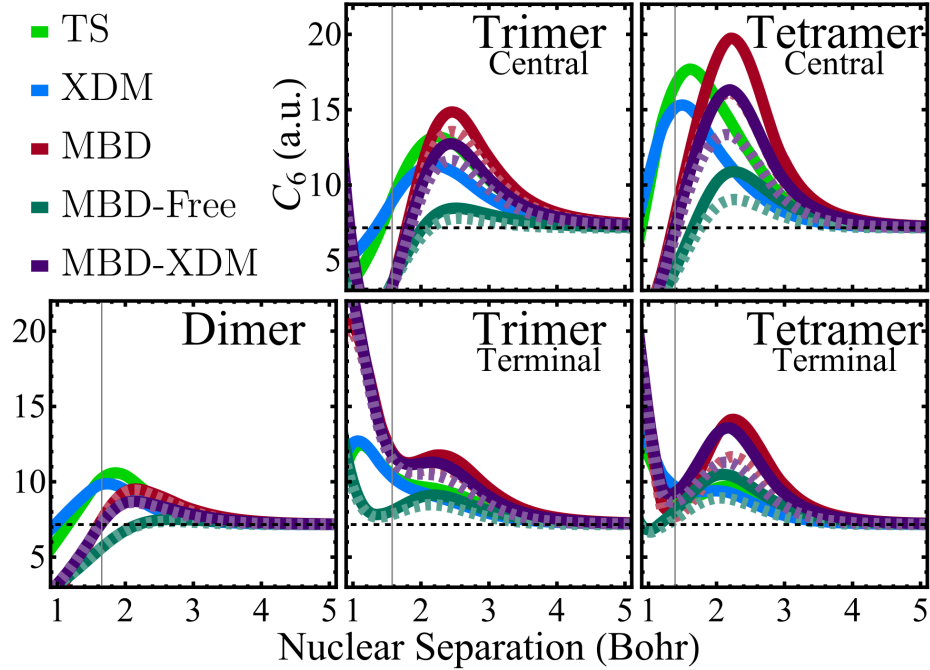


Figure 4.5: The analysis of C_6 for the oscillator chains. For the MBD methods, solid lines are C_6 coefficients derived from SCS polarizabilities and dashed lines are derived from rsSCS polarizabilities. The vertical lines indicate the equilibrium bond distances for each system.

terminal oscillators, followed by the central oscillator in the trimer and tetramer, with the latter showing the highest C_6 values. This change with environment is captured by all of the models. The C_6 increase between the free oscillators, terminal oscillators, and central oscillators is an example of what we mean by electronic many-body effects. Additionally, the higher C_6 for the central oscillators of the tetramer, relative to the trimer, would not be captured by a simple coordination number descriptor.

To connect with the oscillator data, we performed calculations on a similar chemical system: linear argon chains. The geometries were analogous to those shown in Figure 4.1, with the separation between each Ar atom held fixed at the same R_{sep} . These calculations were performed with the XDM, TS, and MBD dispersion models, all using the PBE density functional [149] and the **tight** basis sets in the FHI-aims package [119, 120]. Here, the PBE functional was chosen because it is the recommended GGA to pair with MBD. As such, PBE was used for all calculations in this study to ensure a fair comparison between dispersion methods, despite the fact that combining XDM with a dispersionless base functional such as B86bPBE [147, 149] results in higher accuracy [81]. For these calculations, we also modified the code to implement MBD-Free, which was expected to give similar results to MBD for noble

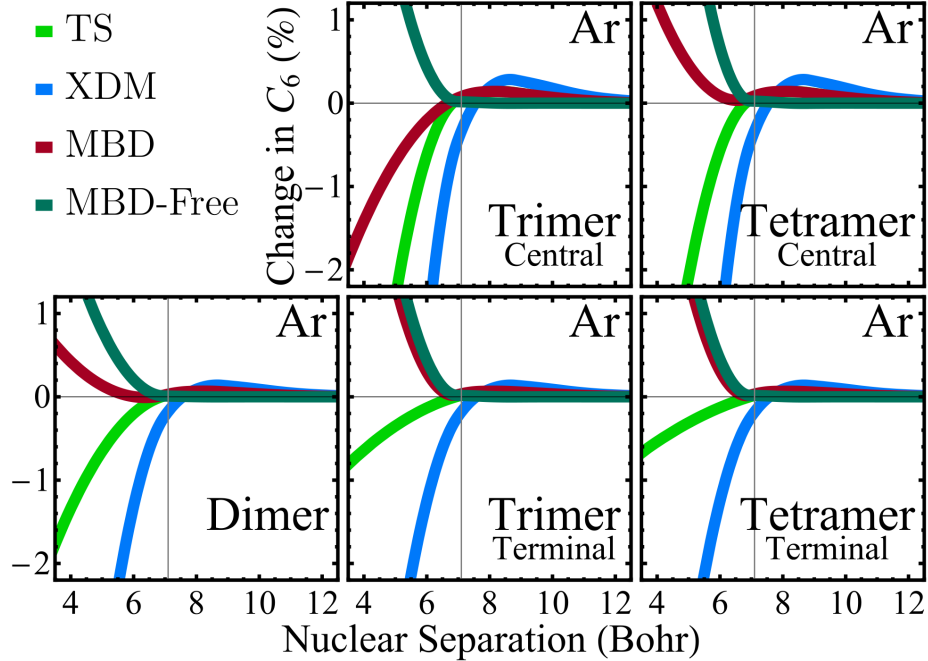


Figure 4.6: Variation in C_6 for argon chains, from FHI-aims calculations using the PBE density functional with tight basis sets. For the MBD methods, the rsSCS routine was used. The vertical lines indicate the reference equilibrium separation for the Ar dimer [433].

gases where a free-atom reference is highly intuitive. The computed dispersion coefficients for the argon dimer, trimer, and tetramer are shown in Figure 4.6, where all MBD methods used the rsSCS routine.

The argon-chain results show that the dependence on surrounding environment is qualitatively similar to that seen for the quantum harmonic oscillators. The XDM, TS, and MBD dispersion coefficients again increase beyond their free-atom values as the internuclear distance is shortened and reach maximum values. However, these maximum values are obtained at much larger separations of roughly 8–9 bohr, which is reasonable given the larger atomic size and far weaker binding. The maximum C_6 coefficients are again lower for the terminal atoms than the central atoms, although the results are quite similar for the central atoms of the trimer and tetramer, unlike for the oscillators.

At short separations in Figure 4.6 (and in some cases in Figure 4.5 as well), MBD and MBD-Free's dispersion coefficients show unusual behaviour as they begin to sharply increase. We believe this is a symptom of a “polarization catastrophe,” which is a known issue with self-consistent screening. MBD's SCS routine relies on

Applequist's interactive dipole model which predicts the divergence of polarizabilities at low separation [477]. For chemical systems, the use of cutoffs or damping functions to address this issue is considered essential [97].

The MBD model attempts to address the issue of excessive polarization by smearing interacting point dipoles into spherical Gaussian charge distributions. This choice of interaction potential attenuates the polarizability to converge to a finite value at zero separation [48]. The rsSCS routine further damps the MBD energy at short range via a Wu–Yang damping function [46]. Despite these efforts, we see that MBD@rsSCS still suffers from unphysical polarizabilities. Focusing on Figure 4.6's results for the central atom in the Ar trimer, MBD-Free exhibits a “polarization catastrophe,” but not regular MBD. This again illustrates how sensitive the MBD method is to the starting point and indicates that modifications of MBD to avoid the (rs)SCS scheme [52] may provide some much-needed stability.

Further, despite the MBD and MBD-Free C_6 coefficients being reported at short-range in Figure 4.5, at separations below the equilibrium bond length, MBD and MBD-Free typically generated complex-valued energies. This behaviour will be discussed further in Section 4.4.4 but, as a result, the short-range MBD results presented above should only be interpreted qualitatively.

4.4.3 EFFECT OF OSCILLATOR FREQUENCY

For the oscillator models, the results shown so far have all used $\alpha^{\text{free}} = 9/2$ a.u. and the corresponding $\omega = 0.4715$ a.u. The oscillator frequency controls the spring constant for the interaction between the electron and nucleus, which then determines the oscillator polarizability. To investigate how the environmental/electronic many-body effects change with element, we performed additional calculations for the dimer model in which the oscillation frequency, ω , was systematically varied. The considered values of ω correspond to the various starting points discussed in Section 4.3.2. Additionally, $\omega = 0.525$ was also used to test a higher frequency, corresponding to a more strongly-bound electron. For each ω , the polarizability, α , was adjusted appropriately using Eq. (4.3.9).

The C_6 results for variable ω are shown in the top row of Figure 4.7. For large frequencies, the electron is strongly bound to the oscillator (high excitation energy), resulting in low polarizability. Conversely, for low frequencies, the electron is weakly

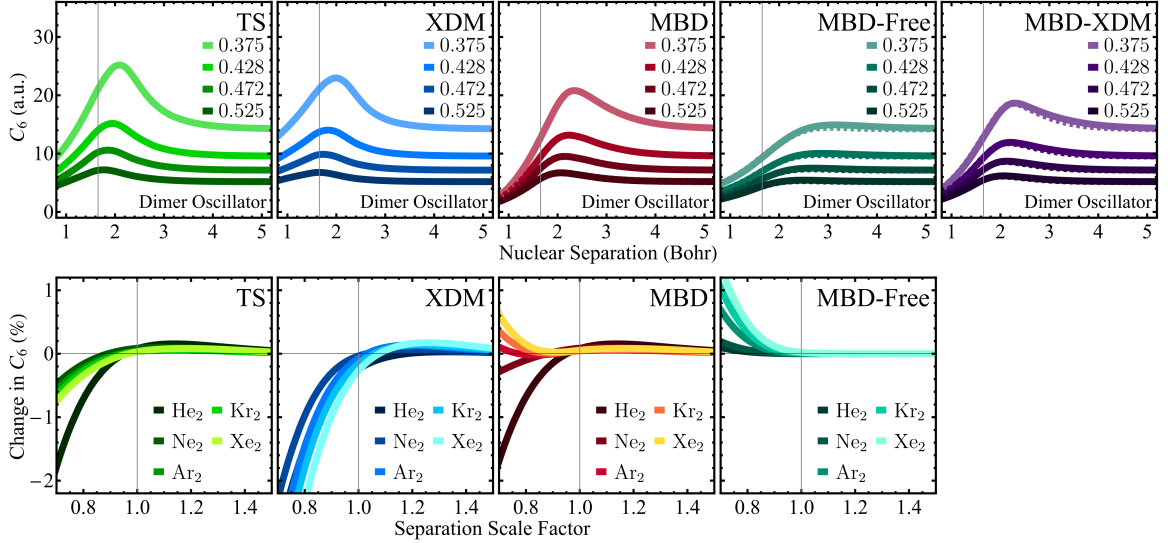


Figure 4.7: Top: Effect of changing ω on C_6 on the dispersion corrections for the oscillator system’s dimers. For the MBD methods, solid lines are C_6 coefficients derived from SCS polarizabilities and dashed lines are derived from rsSCS polarizabilities. Bottom: Variation in C_6 for noble-gas dimers with the internuclear separation ranging from $0.7 \times$ to $1.5 \times$ the reference equilibrium distance of the dimer [433]. Calculations were performed with FHI-aims for various dispersion models, using PBE with `tight` basis sets. For the MBD methods, the rsSCS routine was used. The vertical lines indicate the equilibrium bond distances for each system.

bound to the oscillator (low excitation energy), resulting in high polarizability. Therefore, we expect larger variability in C_6 with environment for more polarizable oscillators, corresponding to small ω . This is exactly what is seen in Figure 4.7 for all methods, although MBD-Free shows less dependence of C_6 on ω values than the other corrections.

To connect this result with real atomic systems, we also computed dispersion coefficients for the series of homoatomic noble-gas dimers from He₂ to Xe₂. The calculations were performed for the TS, XDM, MBD, and MBD-Free dispersion models with FHI-aims using the `tight` basis sets and the PBE density functional. The results are shown in the bottom row of Figure 4.7. Since the noble-gas atoms all have very strongly bound electrons (high ionization potentials), the results are similar to those obtained with the oscillators for the highest ω . There is only a modest increase in C_6 near the equilibrium separation, relative to the free-atom limit. XDM most clearly recovers the trend seen for the oscillators, with the variability in C_6 increasing with higher polarizability down the noble-gas group. Further, we note that only XDM

predicts non-constant C_6 gradients near the equilibrium bond distance for both the oscillator and noble-gas systems, which has implications for the calculation of dispersion forces [81]. At short separations, the MBD and MBD-Free results again show a polarization catastrophe, with more rapid divergence of the dispersion coefficients occurring for more polarizable elements down the group. Notably, MBD only shows a polarization catastrophe for Ar_2 , Kr_2 , and Xe_2 , while it occurs for all 5 noble-gas dimers with MBD-Free.

4.4.4 CONNECTION WITH MOLECULAR DIMERS AND LAYERED MATERIALS

To this point, we have seen that TS, XDM and MBD all give a consistent description of electronic many-body effects (i.e. changes in C_6 for varying atomic positions) in oscillator and atomic model systems. This stands in sharp contrast with previously observed behaviour for graphite [104]. In this section, we extend our comparison of various dispersion models to two molecular dimers (methane dimer and π -stacked benzene dimer in a parallel-displaced configuration) and two layered, solid-state materials (graphite and MoS_2).

The geometries of the molecular dimers were obtained from the S22 \times 5 benchmark [478] and correspond to separations both at and away from equilibrium. The geometries of the periodic solids were obtained from Refs. [104, 479] and the c lattice parameter systematically varied relative to the experimental reference value to consider expanded and compressed interlayer separations. Calculations using the PBE functional, `light` basis settings, `dense` integration grids, and each of the TS, XDM, MBD, and MBD-NL [52] dispersion methods, were performed with FHI-aims. For brevity, the @rsSCS label on MBD will be implied throughout in this section. For the layered materials, 12 \times 12 \times 4 \mathbf{k} -point meshes were used. The resulting potential energy surfaces are shown in the top row of Figure 4.8.

Note that the MBD-NL method [52] represents yet another possible starting point for MBD. In MBD@rsSCS, there is a related problem to the “polarization catastrophe” where some dipole interaction tensor elements become similar in magnitude to the inverse values of the polarizabilities when the starting polarizability is too high, typically occurring at small separations, or in ionic or metallic systems. This behaviour results in negative eigenvalues, suggesting that these induced dipoles are (unphysically) aligned anti-parallel to the applied field [480], and leads to complex-valued energies. A number of notable MBD variants that have been proposed to help with

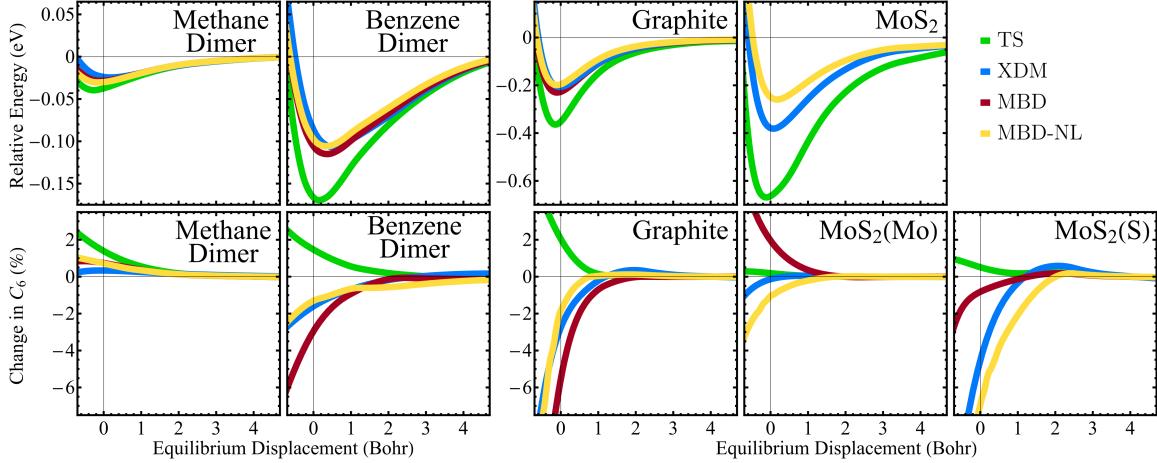


Figure 4.8: Potential energy curves (top) and changes in dispersion coefficients (bottom) for selected molecular dimers and layered materials, computed using the PBE functional, `light` basis sets and `dense` integration grids with FHI-aims. For MBD, the rsSCS routine was used. Evaluation of the MBD energies failed to converge for MoS₂, so those results are omitted. The vertical lines indicate the reference equilibrium separation for each system [478, 479].

this problem include the fractionally ionic variant [50] (MBD/FI), the use of iterative Hirshfeld partitioning [296, 481] (MBD/HI), or the use of a polarizability functional [52] (MBD-NL). In MBD-NL, the initial polarizabilities and dispersion coefficients are taken from the non-local VV10 dispersion model [63, 316]. Unlike other MBD variants, MBD-NL does not refine the polarizabilities with SCS, thus avoiding the polarization catastrophe. Instead, the VV10 polarizabilities are refined with cutoffs and used to obtain the characteristic excitation frequency. The polarizabilities, characteristic excitation frequencies, and the damped long-range dipole potential are then used to compute the MBD-NL energy via the matrix methods described in Section 2.5.2. This variant of MBD is recommended specifically for layered materials, such as the transition-metal dichalcogenides, where the rsSCS scheme cannot provide converged energies from the usual TS starting point.

With each method, homoatomic dispersion coefficients were evaluated at each point along the PES and their relative values are shown in Figure 4.8 as a function of intermolecular or interlayer separation. The methane dimer, the parallel-displaced benzene dimer, and graphite results are all qualitatively similar. XDM and MBD show similar behaviour to each other, with an initial increase in C_6 as the molecules/layers approach each other, followed by a sharp decrease. Again, this is similar to the results of these methods for the oscillator models and noble-gas systems. The outlier is the

Table 4.1: Computed binding energies, in kcal/mol for the molecular dimers and in meV/Å² for the layered materials. Literature reference data [478, 479] is shown for comparison. Also included are mean absolute errors (MAE) for the S66×8 benchmark [287] of molecular complexes and two benchmarks of layered materials [38, 479].

System	TS	MBD	MBD-NL	XDM	Ref.
(CH ₄) ₂	0.91	0.66	0.70	0.57	0.53
(C ₆ H ₆) ₂	3.91	2.65	2.44	2.46	2.81
Graphite	34.47	21.78	18.82	19.56	18.32
MoS ₂	38.62	—	14.98	22.01	20.53
S66×8 (kcal/mol)	0.60	0.44	0.43	0.45	—
LM11 (meV/Å ²)	12.5	—	5.0	3.7	—
LM26 (meV/Å ²)	13.1	—	4.6	4.9	—

TS method, which shows starkly different behaviour for the molecular dimers and graphite than seen above for the oscillators and noble gases. Specifically, TS shows a sharp increase in C_6 at small separations. It is not immediately clear why TS gives such different behaviour for molecules than for atomic dimers or chains; the increased Hirshfeld volumes upon compression may perhaps be due to the presence of covalently bonded atoms or the greater contact area between the interacting molecules/layers.

For MoS₂, only XDM and MBD-NL predict similar changes in C_6 with interlayer separation for both bulk materials. Here, the MBD method strongly over polarizes and the Mo dispersion coefficients sharply increase for separations near the equilibrium displacement. This is because the TS starting point gives very high initial C_6 coefficients and polarizabilities for the Mo atoms, as we will see. Conversely, MBD-NL is well behaved due to having a much lower input polarizability and avoiding the SCS routine, therefore avoiding these polarization issues for MoS₂ and showing a decrease in C_6 at short separations similar to XDM. We note, however, that MBD-NL exhibits small oscillations in its C_6 dispersion coefficients' curves in Figure 4.8, suggesting that there may be some numerical instability.

To quantitatively assess the quality of the PES, the computed binding energies are compared with high-level reference data in Table 4.1. The XDM, MBD, and MBD-NL results are generally in fairly close agreement, while TS strongly overbinds. The greatest spread between the methods occurs for MoS₂. To provide a better statistical comparison, we also report mean absolute errors (MAEs) obtained with the same collection of methods for the binding energies of the S66×8 set of molecular complexes [287] and the exfoliation energies of Bojkman's LM26 set [479] (and its

Table 4.2: Computed homoatomic C_6 dispersion coefficients, in a.u. for single isolated molecules and selected layered materials at large interlayer separation. The homoatomic free C_6 values for C and S [288], and Mo [480], were taken from available reference data. Also included are mean absolute percent errors (MAPE) and mean percent errors (MPE) for a set of 20 homomolecular C_6 dispersion coefficients (MolC6).

System	Atom	Free	TS	MBD	MBD-NL	XDM
CH ₄	C	46.6	26.0	31.7	27.6	18.7
C ₆ H ₆	C	46.6	32.6	30.7	28.6	21.4
Graphite	C	46.6	35.4	33.3	27.7	20.2
MoS ₂	Mo	1029	1060	627	260	388
MoS ₂	S	134.0	132	80.3	101	78.5
MolC6 MAPE (%)		—	12.7	13.1	7.3	20.1
MolC6 MPE (%)		—	2.5	-3.2	-2.2	-18.2

smaller LM11 subset considered by Tawfik *et al.* [38]) of layered materials in Table 4.1. These benchmarks were computed in FHI-aims using the PBE base functional, **light** basis settings, and **dense** integration grids. Again, for layered materials, $12 \times 12 \times 4$ \mathbf{k} -point meshes were used throughout. MBD, MBD-NL, and XDM all give comparable performance for the S66 \times 8 benchmark when paired with the PBE base functional. The interested reader is directed to Ref. [119] for the results with differing functionals and with the **tight** basis settings. No MBD result is given for the layered benchmark since the MBD energy evaluation consistently predicted complex-valued energies for transition metal dichalcogenides. Here, TS massively overbinds, similar to what was seen for the specific case of MoS₂, while MBD-NL and XDM again give comparable, good performance.

To evaluate the accuracy of the various methods for homomolecular C_6 dispersion coefficients, we constructed a C_6 benchmark using a set of 20 molecules: H₂, N₂, O₂, Cl₂, CO₂, methane, CCl₄, SiH₄, SiF₄, SF₆, ethyne, ethene, propene, propane, butene, butane, pentane, hexane, and benzene. Reference data was collected from Ref. [326], and computations were performed using FHI-aims with the PBE functional and **tight** basis settings. During the initial development of XDM, it was found to give a mean (absolute) percent error of only 0.3% (3.4%) for the C_6 dispersion coefficients of all combinations of H, He, Ne, Ar, Kr, and Xe [55]. Conversely, for this set of 20 molecules, the results in Table 4.2 show that XDM systematically underestimates the homomolecular C_6 dispersion coefficients, while TS, MBD, and MBD-NL give mean percent errors much closer to zero. The systematic underestimation of molecular

C_6 dispersion coefficients with XDM, despite its excellent performance for isolated atoms, is likely because of its use of simplistic volume scaling to obtain isotropic atomic polarizabilities. Similar to how MBD likely relies on its damping function to compensate for missing C_8 and higher-order dispersion terms, XDM likely relies on its damping function to compensate for underestimation of C_6 .

Finally, selected homoatomic dispersion coefficients for the non-hydrogen atoms in methane, benzene, graphite, and MoS₂ are collected in Table 4.2 and show much larger differences between methods than were seen for the benchmark of 20 homomolecular C_6 coefficients. Particularly for MoS₂, the chemical bonding causes large changes in C_6 relative to the free-atomic values, as noted previously [104]. The coefficients follow the general trend of Free > TS ≈ MBD > MBD-NL > XDM for C, and Free ≈ TS > MBD > MBD-NL ≈ XDM for S and Mo, which explains the trends in MoS₂ exfoliation energies in Table 4.1. While there is no reference data for accurate C_6 coefficients of Mo and S in MoS₂, the XDM and MBD-NL values would be expected to be the most reliable estimates given the good performance of these two methods for the exfoliation energy benchmarks (Table 4.1).

CONCLUSION

In this work, we constructed and variationally optimized wavefunctions for a series of model systems composed of interacting quantum harmonic oscillators. From these wavefunctions, we evaluated dispersion coefficients and energies with the XDM, TS, and several variants of the MBD dispersion methods. The results showed a significant difference in dispersion energies between XDM, which includes higher-order C_8 and C_{10} contributions, and the TS and MBD methods that do not. Conversely, when considering the damped dispersion energies, all give nearly identical results at long range and, at intermediate range, MBD is in excellent agreement with a reparameterized version of XDM that uses only the C_6 term.

Turning to the dispersion coefficients, the rsSCS modification of MBD seems to provide a stabilizing effect, reducing the variation of the dispersion coefficients with surrounding environment. All the dispersion models considered showed similar behaviour for the variation in C_6 with nuclear separation, although the MBD-based methods showed evidence of a “polarization catastrophe” at short distances. Qualitatively similar results to those for the quantum harmonic oscillators were obtained for dimers, trimers, and tetramers of Ar atoms, with the MBD-based methods again

exhibiting a polarization catastrophe at short internuclear separations. We additionally investigated how the dispersion coefficients of two interacting oscillators change with their vibrational frequency. In general, we found greater variations in C_6 with surrounding environment (i.e. the distance between the coupled oscillators) for lower vibrational frequencies, which corresponds to higher polarizability. Similar behaviour was observed for DFT calculations on noble gas dimers, where the polarizability increases down the group.

Finally, we performed calculations on the homomolecular dimers of methane and benzene, as well as graphite and MoS₂ to determine if the results obtained for the oscillators and noble gases were transferable to larger chemical systems. Overall, we found similar dependence of the dispersion coefficients on centre-of-mass or interlayer separation. The exception to this was the TS method, where the dispersion coefficients would increase sharply at small distances, resembling the polarization catastrophe, but occurring due to increases in the Hirshfeld atomic volumes. This behaviour would appear to make the TS dispersion coefficients and polarizabilities a less-than-optimal starting point for the MBD method.

A key finding of this work is that the SCS/rsSCS schemes used in MBD show a concerning sensitivity to the choice of input polarizabilities and dispersion coefficients. While a TS starting point is the usual choice, this is by no means the only option and it can result in unphysical polarizabilities, and generating complex-valued energies in cases like MoS₂. This occurs because TS gives dispersion coefficients and polarizabilities that are similar to, or higher than, the free-atom values for Mo atoms for the bulk solid. The NL variant of MBD, which is recommended for layered materials and metals, avoids these polarization issues, and is suitable for all chemical systems considered in this work. We therefore recommend MBD-NL over MBD@rsSCS generally. Perhaps the VV10 polarizability functional used in MBD-NL could also be integrated into XDM to improve the model's treatment of dynamic dipole polarizability. Indeed, this could be an interesting avenue to explore in a future study.

The original purpose of this work was to compare and contrast the different dispersion corrections to understand how each accounted for electronic and atomic many-body effects. Our results show that TS, XDM, and MBD all exhibit roughly the same magnitude of variation in C_6 with changing environment for weak interactions between oscillators or noble gases, demonstrating that they all capture electronic many-body effects for these systems. The agreement of TS with XDM- C_6 and MBD for undamped and damped dispersion energies of the oscillator model systems, when

it shows very different behaviour for molecules and materials, limits our ability to draw further conclusions.

For the oscillator model systems, we see that XDM- C_6 and MBD@rsSCS (when parameterized similarly) give effectively identical damped dispersion energies for both intermediate- and long-range interactions. Further, MBD's 3-body energy contribution, computed via the ACFD-RPA correlation energy, is in near perfect agreement with the ATM energy calculated via XDM. In both cases, these 3-body energy contributions proved to be negligible for the model oscillator systems, although MBD's 3-body contributions are reported to become significant for some supermolecular complexes and biochemical systems [470]. These results suggest that it would be of pedagogical interest to study these 3-body contributions for larger systems. For now, this further confirms our previous conclusion [80] that electronic many-body effects and the inclusion of higher-order, pairwise dispersion energies represent far more important contributions to the physics of London dispersion than the triple-dipole ATM term. Overall, our findings suggest that quantum harmonic oscillators may be too simple to assess the performance of dispersion models, since they are missing many of the intricacies of dispersion interactions in molecular and solid-state systems.

CHAPTER 5

COMPARISON OF DENSITY-FUNCTIONAL THEORY DISPERSION CORRECTIONS FOR THE DES15K DATABASE

“Something unknown is doing we don’t know what.” [482]
~ Sir. Arthur Eddington (1882–1944)

This chapter is adapted from: Nickerson, C. J., Bryenton, K. R., Price, A. J. A., & Johnson, E. R. *Comparison of Density-Functional Theory Dispersion Corrections for the DES15K Database*. *J. Phys. Chem. A*, **127**, 41, 8712–8722. (2023) [483]

Author contributions: K.R.B. was responsible for the data analysis related to Section 5.3.3, including modifications to FHI-aims. The computational data was generated by C.J.N., who also wrote the first draft of the manuscript. A.J.A.P. conceived the initial study. E.R.J. generated the final figures and edited the manuscript.

5.1 INTRODUCTION

DES15K [484] is a 2021 benchmark collection of high-level quantum mechanical reference data, containing interaction energies for close to 15,000 different atomic and molecular dimer geometries. These interaction energies were computed using basis-set extrapolated MP2 calculations, combined with CCSD(T) calculations using augmented quadruple-zeta, triple-zeta, or double-zeta basis sets, depending on the system size [484]. This corresponds to either “gold” or “silver” standards in electronic-structure theory [199, 204], which have estimated accuracies of ca. 0.1 kcal/mol [198] or 0.5 kJ/mol [485], although this will naturally be system dependent and may increase for larger molecular dimers [486]. While most benchmarks cover only a narrow range of systems [285, 314, 478, 487–492], the DES15K benchmark is extremely broad and covers many intermolecular interaction types, such as dispersion, H-bonding, ion-molecule, and ion-ion, over a range of geometries from compressed to expanded. Consequently, the DES15K dataset provides an excellent benchmark for comparing the performance and limitations of the various dispersion corrections for small molecular systems.

In this study, we present a head-to-head comparison of several of the most popular dispersion corrections by using them to predict interaction energies for the DES15K benchmark set. In particular, we study the XDM [55, 57, 156], D3BJ [41, 92], D4 [42], TS [44], MBD [45, 46], and MBD-NL [52] models, providing the first-ever comparison of these methods using the same electronic structure code, basis set, and functional. The breadth of the DES15K benchmark allows us to gain new insight into the strengths and weaknesses of these dispersion corrections. By considering the outliers showing the largest deviation from the reference data, we are able to identify the areas where improvements are most needed. Finally, we apply these dispersion corrections to a model cation- π complex at stretched and compressed geometries to further assess how these dispersion methods behave for an example of a problematic system.

5.2 COMPUTATIONAL METHODS

5.2.1 DFT CALCULATIONS

Geometries of the 14,651 complexes comprising the DES15K benchmark were obtained from the `.csv` file provided in the supporting information of Ref. [484], along with the reference binding energies, which correspond to the CCSD(T) results extrapolated to the complete basis-set limit. The geometries, in the more standard `.xyz` format, are available in the supplementary material of Ref. [483].

We computed interaction energies for all of the complexes in the DES15K benchmark by performing single-point energy calculations on the complex and the two isolated monomer fragments and evaluating the resulting electronic energy difference. These calculations used each of the XDM, D3BJ, D4, TS, MBD, and MBD-NL dispersion methods, paired with the PBE0 [149, 163, 493] density functional. This is the recommended hybrid functional for use with TS, MBD, and MBD-NL, and the damping functions of XDM, D3BJ, and D4 have also been parameterized for use with PBE0. Using this same functional across the board has the benefit of allowing comparison of the various dispersion methods on an equal footing.

We have previously argued that correct large-gradient behaviour of the DFT exchange functional is important for an accurate description of intermolecular chemistry [56, 81, 414] and we consequently recommend the use of B86b [147] (as opposed to PBE) [149] exchange when using the XDM dispersion correction. Given this, we also tested the XDM dispersion model paired with the B86bPBE0 hybrid functional [119] to assess the relative importance of changing the base functional compared to the dispersion method for this benchmark. It should be noted that B86bPBE0 and PBE0 have the same exact-exchange mixing fraction and correlation functional, and differ only in replacing PBE with B86b for the semi-local exchange component.

All electronic structure calculations were performed using a modified copy of version 230214 of the Fritz Haber Institute – *ab initio* materials simulations (FHI-aims) program [120, 494–497]. The calculations used the default settings for a `tight` basis for each species, as well as the “atomic ZORA” scalar relativity correction [120]. The damping function parameters used with XDM were set to the recommended values for use with the tight basis ($a_1 = 0.7268$, $a_2 = 1.3825$ Å for B86bPBE0 and $a_1 = 0.4710$, $a_2 = 2.3857$ Å for PBE0), while the default values present in FHI-aims for use with PBE0 were assigned for TS, MBD, and MBD-NL.

Notably, the D3BJ and D4 dispersion methods were not yet implemented within FHI-aims at the time this work was carried out, although D3 has since been implemented [121]. However, as the dispersion energy depends only on the atomic positions (and not on the electron density) with these two methods, it could be evaluated separately and added to the uncorrected PBE0 energy obtained from FHI-aims. To evaluate the D3BJ and D4 dispersion energies, one can use the standalone dftd3 [498] and dftd4 [499] programs, respectively. These require only the Cartesian coordinates, damping function parameters, and net charge as input. Note that the ATM term was not included in either the D3BJ or D4 dispersion energies reported here. This choice was made since repeating the calculations using D4+ATM showed that it has a negligible effect on the binding energies, changing the mean (absolute) errors by at most 0.02 kcal/mol, and not changing the maximum errors, for the full DES15K set and all subsets considered herein.

For the final part of this study, we performed analogous FHI-aims calculations to generate potential energy curves for a cation- π complex of Li^+ and benzene with C_{6v} symmetry. Here, the distance between the Li and the centre-of-mass of the benzene ring was varied from 1–5 Å in 0.1 Å increments. To obtain the C_6 coefficients along this potential with TS, MBD, and MBD-NL, the FHI-aims code was modified by adding some print statements, while Grimme’s stand-alone dftd3 [498] and dftd4 [499] programs were used to obtain the C_6 dispersion coefficients with D3BJ and D4, respectively.

5.2.2 CORRELATED-WAVEFUNCTION CALCULATIONS

To obtain high-level reference data for the Li^+ –benzene potential energy curve, we also performed single-point energy calculations with MP2 and CCSD(T) using the Gaussian program [126]. These calculations used the aug-cc-pVXZ basis sets [248, 500] for C and H and the aug-cc-pCVXZ basis [501, 502] for Li, which we abbreviate as aXZ. Effectively complete-basis MP2 binding energies were evaluated from basis-set extrapolation [503] using the aTZ (X=3) and aQZ (X=4) results. Higher-order correlation effects were included by adding the difference between the CCSD(T) and MP2 binding energies at the aTZ level:

$$\Delta E = \Delta E(\text{MP2}/[\text{aTZ},\text{aQZ}]) + \Delta E(\text{CCSD(T)}/\text{aTZ}) - \Delta E(\text{MP2}/\text{aTZ}). \quad (5.2.1)$$

Frozen cores were not employed, and the final reference binding energies were taken as an equal weighting of the results with and without counterpoise correction [241].

5.3 RESULTS AND DISCUSSION

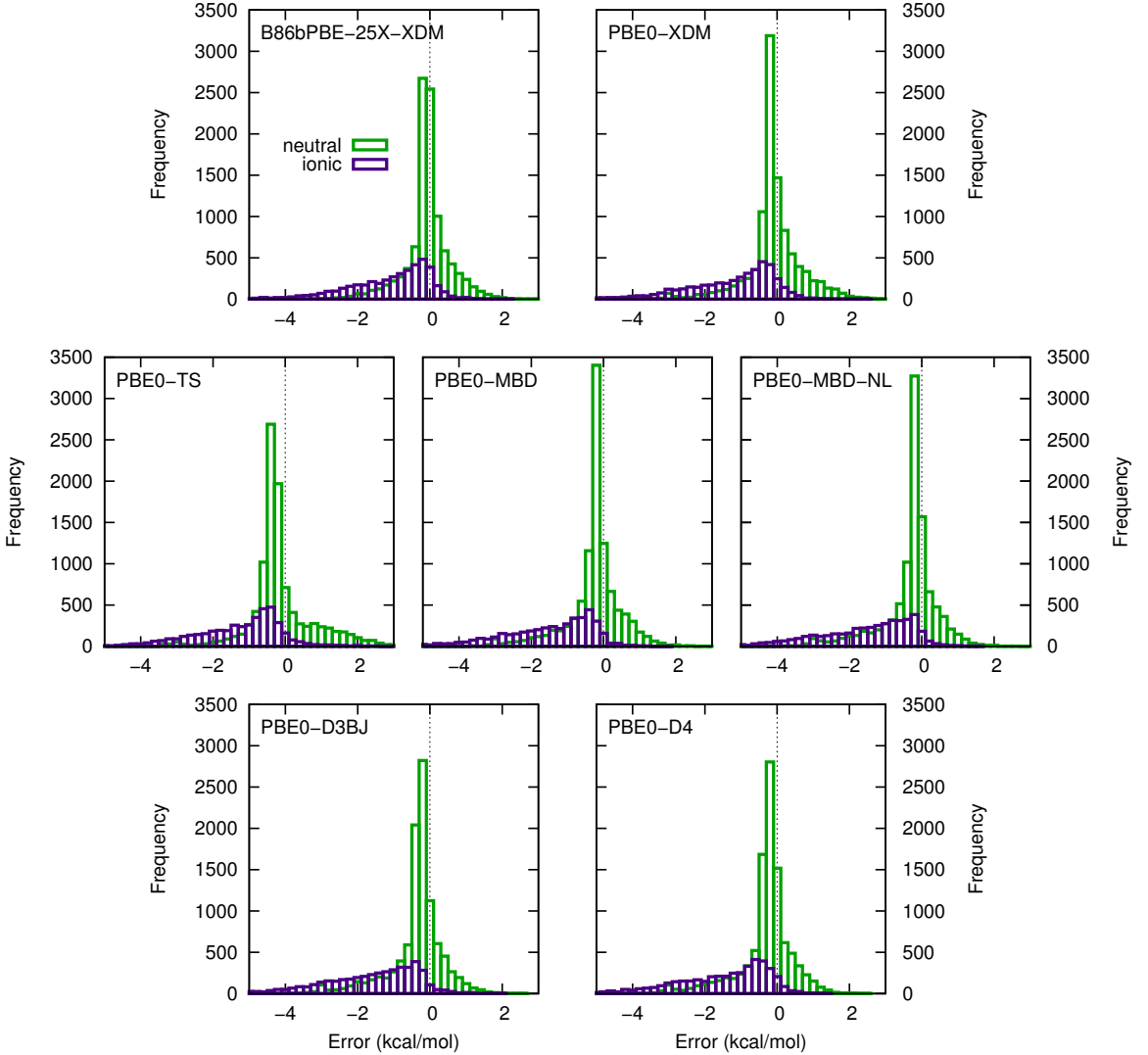


Figure 5.1: Histograms showing the error distributions obtained with each functional and dispersion correction. The data has been split into neutral (green) and ionic (purple) complexes. Negative errors indicate overbinding and positive errors indicate underbinding.

5.3.1 ANALYSIS OF THE FULL BENCHMARK

Figure 5.1 shows histograms of the error distributions for the computed binding energies comprising the DES15K benchmark, obtained with each of the seven pairings of density functional and dispersion correction considered. The results for the overall data set are decomposed into separate subsets of neutral and ionic complexes to better

reveal the differing behaviours of our tested methods. From the histograms, we see that all of the methods perform quite well for the neutral complexes where, in general, we see narrow peaks with the errors clustered roughly symmetrically about zero. For the ionic complexes, however, we see that all of the methods tend to give larger errors and considerably overbind many of the complexes.

The error statistics for the full DES15K set, as well as the neutral and ionic subsets, are summarized in Table 5.1. The errors for the neutral complexes are comparable to those for other, smaller intermolecular interaction benchmarks, such as S22 \times 5 and S66 \times 8 [119]. For these neutral complexes, we see that TS displayed the largest MAE (in agreement with our previous work [119]), while all other dispersion methods gave similar errors to each other. Specifically, when paired with PBE0, the XDM, D3BJ, D4, MBD, and MBD-NL models all gave mean absolute errors (MAEs) of 0.49–0.50 kcal/mol. We also observe that the choice of base density functional had a larger impact on the results than the choice of dispersion method, as seen from the decrease in MAE from 0.49 to 0.40 kcal/mol with XDM upon changing the functional from PBE0 to B86bPBE0. Additionally, this change in base functional has the effect of shifting the highest peak to better centre the error distribution in Figure 5.1 for the neutral complexes.

Table 5.1: Error statistics for the full DES15K benchmark set and for selected subsets, all in kcal/mol.*

Functional	Dispersion	Neutral (<i>n</i> =10,263)				Ionic (<i>n</i> =4,388)				Full (<i>n</i> =14,651)			
		MAE	ME	RMS	MAX	MAE	ME	RMS	MAX	MAE	ME	RMS	MAX
B86bPBE0	XDM	0.40	0.03	0.62	3.78	1.13	-1.03	1.57	7.49	0.62	-0.29	1.01	7.49
PBE0	XDM	0.49	0.00	0.77	5.87	1.31	-1.22	1.80	7.85	0.74	-0.36	1.18	7.85
PBE0	D3BJ	0.50	-0.27	0.80	5.87	1.58	-1.54	2.04	9.34	0.83	-0.64	1.30	9.34
PBE0	D4	0.49	-0.23	0.79	5.86	1.48	-1.43	1.96	7.17	0.79	-0.59	1.26	7.17
PBE0	TS	0.61	-0.01	0.90	5.89	1.33	-1.21	1.75	8.26	0.83	-0.37	1.22	8.26
PBE0	MBD	0.49	-0.16	0.78	5.87	1.55	-1.52	2.09	17.20	0.81	-0.57	1.32	17.20
PBE0	MBD-NL	0.50	-0.21	0.81	5.88	1.56	-1.52	2.09	10.63	0.82	-0.60	1.33	10.63

Functional	Dispersion	Ionic, No Metals (<i>n</i> =3,426)				Alkali Cations (<i>n</i> =907)				Alkaline Earth Dications (<i>n</i> =55)			
		MAE	ME	RMS	MAX	MAE	ME	RMS	MAX	MAE	ME	RMS	MAX
B86bPBE0	XDM	1.12	-1.01	1.57	6.62	1.04	-0.97	1.34	5.67	3.30	-3.30	3.91	7.49
PBE0	XDM	1.28	-1.18	1.79	7.21	1.25	-1.22	1.58	6.22	3.71	-3.71	4.35	7.85
PBE0	D3BJ	1.51	-1.46	1.96	7.01	1.67	-1.65	2.09	6.33	4.58	-4.58	5.20	9.34
PBE0	D4	1.49	-1.45	1.98	7.17	1.28	-1.21	1.60	6.17	3.75	-3.75	4.17	7.11
PBE0	TS	1.19	-1.04	1.57	6.43	1.73	-1.71	2.09	5.93	3.79	-3.79	4.45	8.26
PBE0	MBD	1.33	-1.29	1.75	6.71	2.22	-2.22	2.86	17.20	4.25	-4.25	5.05	9.46
PBE0	MBD-NL	1.37	-1.31	1.80	6.66	2.11	-2.10	2.60	8.12	4.90	-4.90	5.73	10.63

* *n* indicates the number of complexes present in each (sub)set; MAE: mean absolute error; ME: mean error; RMS: root-mean-square error; MAX: maximum absolute error.

The ionic complexes are where we observed the highest degree of error among the tested dispersion methods. In particular, the maximum errors from MBD and MBD-NL seen in Table 5.1 are significantly larger than with the other dispersion methods. This prompted us to further decompose the set of ionic complexes into three subsets: those that contain no metal cations, those that contain alkali metal cations (Li^+ , Na^+ , K^+), and those that contain alkaline earth metal dications (Mg^{2+} , Ca^{2+}). The error statistics for these further subsets are also reported in Table 5.1. This decomposition shows that, like the neutral complexes, the errors for the ionic complexes without metals are fairly comparable with all of the methods considered. While D3BJ and D4 perform similarly for the ionic complexes without metals, D4 does give lower errors compared to D3BJ for the metal-containing complexes due to its dependence on partial atomic charges. Further, we see some much larger errors for the complexes containing metal cations and dications with MBD and MBD-NL compared to the other methods; we will return to this observation later in this work.

From Table 5.1, we see that the MAEs and RMS errors are much higher for the dications than for the other two classes of ionic complexes. This observation is consistent with the findings of a previous study [504] where we assessed the performance of several XDM-corrected functionals for the SSI set [505] of pairs of interacting amino-acid side chains and also found large systematic errors for dications. While, in that work, the DFT methods overestimated the repulsion between two monocations, here they are overestimating the binding between a dication and a neutral molecule. The large amount of error that we observe for the dications can be attributed to a need for an improved description of polarization and electrostatic interactions within density functionals, which we believe to be an important area for further research. It is, of course, possible that this error may be corrected with more complex meta-GGA, range-separated hybrid, or double-hybrid density functionals. However, a survey of the vast range of possible base functionals now available is not our aim and is beyond the scope of this study, which is focused on dispersion corrections.

5.3.2 EXAMINATION OF OUTLIERS

To get a sense as to the nature of the complexes responsible for the largest errors, the signed errors for each of the tested methods were plotted against the reference binding energies. These plots are shown in Figure 5.2, where the results are grouped into the same subsets used in Table 5.1.

For the neutral complexes, we see that the largest errors occur for systems with

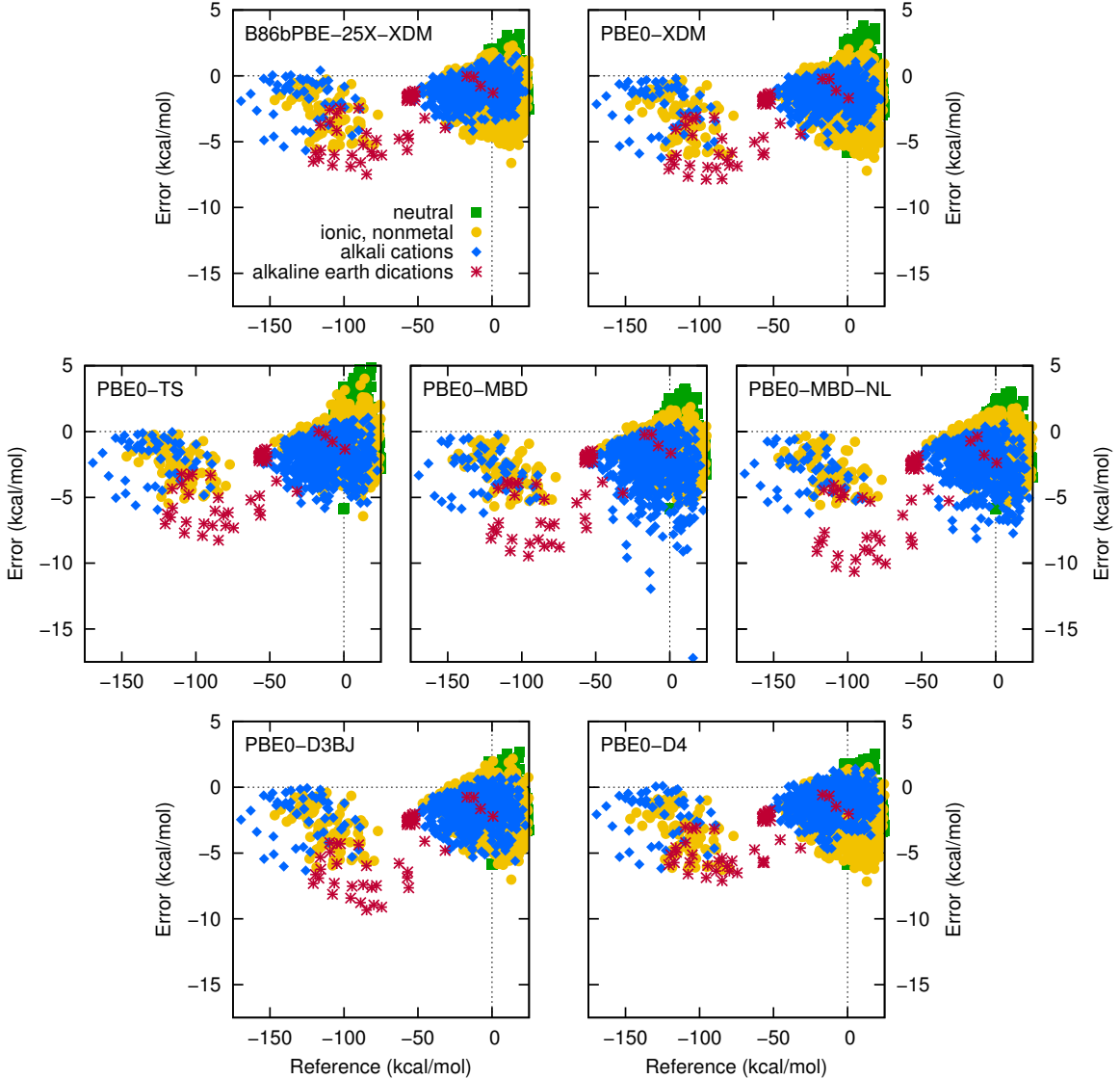


Figure 5.2: Scatter plots showing the errors obtained with each functional and dispersion correction for each system in the benchmark set, as a function of the reference binding energies.

highly-compressed separations, i.e. the systems with positive binding energies. The TS method, in particular, appears to be susceptible to this kind of error, likely due to the steep onset of its WY damping function that zeros the dispersion energy and results in too little dispersion stabilization at compressed geometries. Also, at compressed geometries, the repulsive part of the potential becomes important, explaining the improved behaviour of B86bPBE0 (which has a more accurate repulsive term [56, 81, 414]), relative to PBE0, when paired with XDM.

Also apparent from Figure 5.2 is the significant overbinding seen for the already

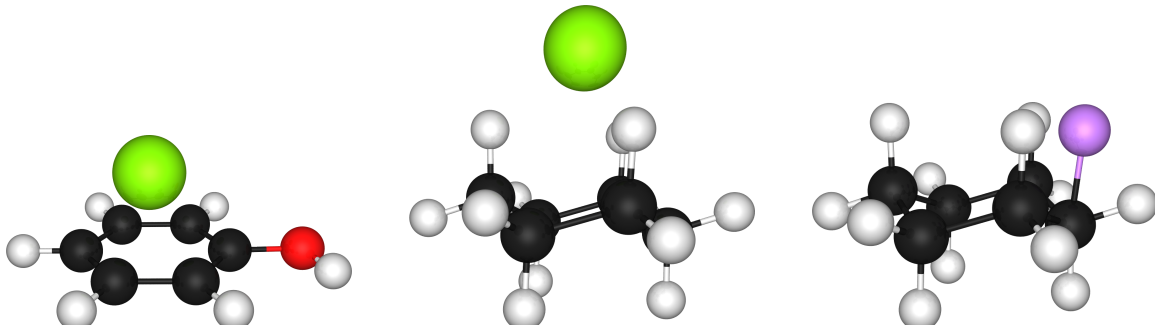


Figure 5.3: Structures of the complexes exhibiting the maximum errors listed in Table 5.1. From left to right: the complex of Mg^{2+} with phenol gives the maximum error for PBE0-XDM and PBE0-MBD-NL; the complex of Mg^{2+} with cyclohexane gives the maximum error for B86bPBE0-XDM, PBE0-D3BJ, PBE-D4, and PBE0-TS; the complex of Li^+ with cyclohexane gives the maximum error for PBE0-MBD.

strongly bound complexes involving the alkaline earth dications. For these complexes, D4 appears to provide somewhat improved performance relative to the other dispersion corrections. However, the alkaline earth dication complexes still exhibit the largest errors for all methods considered, except for MBD. Depending on the dispersion correction, the largest errors were observed for either the interaction of Mg^{2+} with cyclohexane, or Mg^{2+} with phenol (see Figure 5.3). As noted above, this is primarily due to systematic overbinding from PBE0 (or B86bPBE0) even in the absence of dispersion. Similar, although less severe, overbinding is also apparent for the other strongly bound ionic complexes (i.e. those with binding energies of greater than ca. 60 kcal/mol in magnitude).

Finally, by looking at the blue points on the right-hand side of Figure 5.2, we observe that the maximum errors obtained with MBD arise from alkali-metal complexes with positive, or slightly negative, binding energies. Examination of these structures shows that they correspond to compressed geometries, which experience a repulsive potential. One would not expect large amounts of dispersion stabilization in such complexes due to the small atomic size and low polarizabilities of alkali-metal cations. However, for several of these compressed complexes, the MBD dispersion energies are greater than the corresponding TS dispersion energies by more than 5 kcal/mol, and by as much as 11.8 kcal/mol for the compressed complex of Li^+ with cyclohexane shown in Figure 5.3. Prediction of large dispersion energies for compressed alkali-metal complexes is also a problem for MBD-NL, although to a lesser extent. Here, the maximum increase in dispersion stabilization relative to the TS method is

5.1 kcal/mol. This behaviour seems unphysical and prompted us to investigate its origins in more detail for a simple model system.

5.3.3 MODEL CATION- π COMPLEX

To investigate the unexpected behaviour of the MBD-based dispersion methods for compressed geometries of alkali-metal complexes in more detail, we consider the example of the Li⁺-benzene complex with C_{6v} symmetry. This model system was selected for several reasons. First, there is a long history of studying such cation- π complexes in the DFT and computational chemistry literature [506–508] due to their importance in biochemistry and materials science [509]. Additionally, this complex is already present within the DES15K set and showed the fourth largest increase in dispersion energy going from TS to MBD. Finally, the high symmetry means that we need only consider the interaction between the lithium and one of the six equivalent carbon atoms, or one of the six equivalent hydrogen atoms, to capture the entirety of the dispersion energy.

Calculations were performed to generate potential energy curves for the Li⁺-benzene complex by systematically varying the distance between the Li cation and the centre-of-mass of the benzene ring. Figure 5.4 displays the results for each dispersion method by plotting the error in the computed binding energy relative to our correlated-wavefunction reference data. Since the same base density functional (PBE0) is used in all cases, the differences between the six curves are entirely due to the approximations used to compute the dispersion energies, which are also plotted as a function of distance in the figure. The results show a sharp divergence in the MBD dispersion energy at compressed distances, beyond the equilibrium separation. This appears to be non-physical as dispersion interactions involving the Li⁺ cation should be quite weak due to its tightly bound electrons and low polarizability. Similarly, MBD-NL predicts a large dispersion stabilization for compressed distances; however, here we see that the dispersion energy levels out, approaching a constant value, instead of diverging as seen for MBD.

The divergence of the MBD dispersion energy as $R \rightarrow 0$ made us wonder if it was experiencing a polarization catastrophe, as seen previously for noble-gas dimers, trimers, and tetramers at compressed geometries [315]. To investigate this possibility, we also plot the heteroatomic C_6 dispersion coefficients for the Li-C and Li-H interactions as a function of distance in Figure 5.4. The results show that the TS and MBD dispersion coefficients are fairly similar, which is not unexpected since MBD

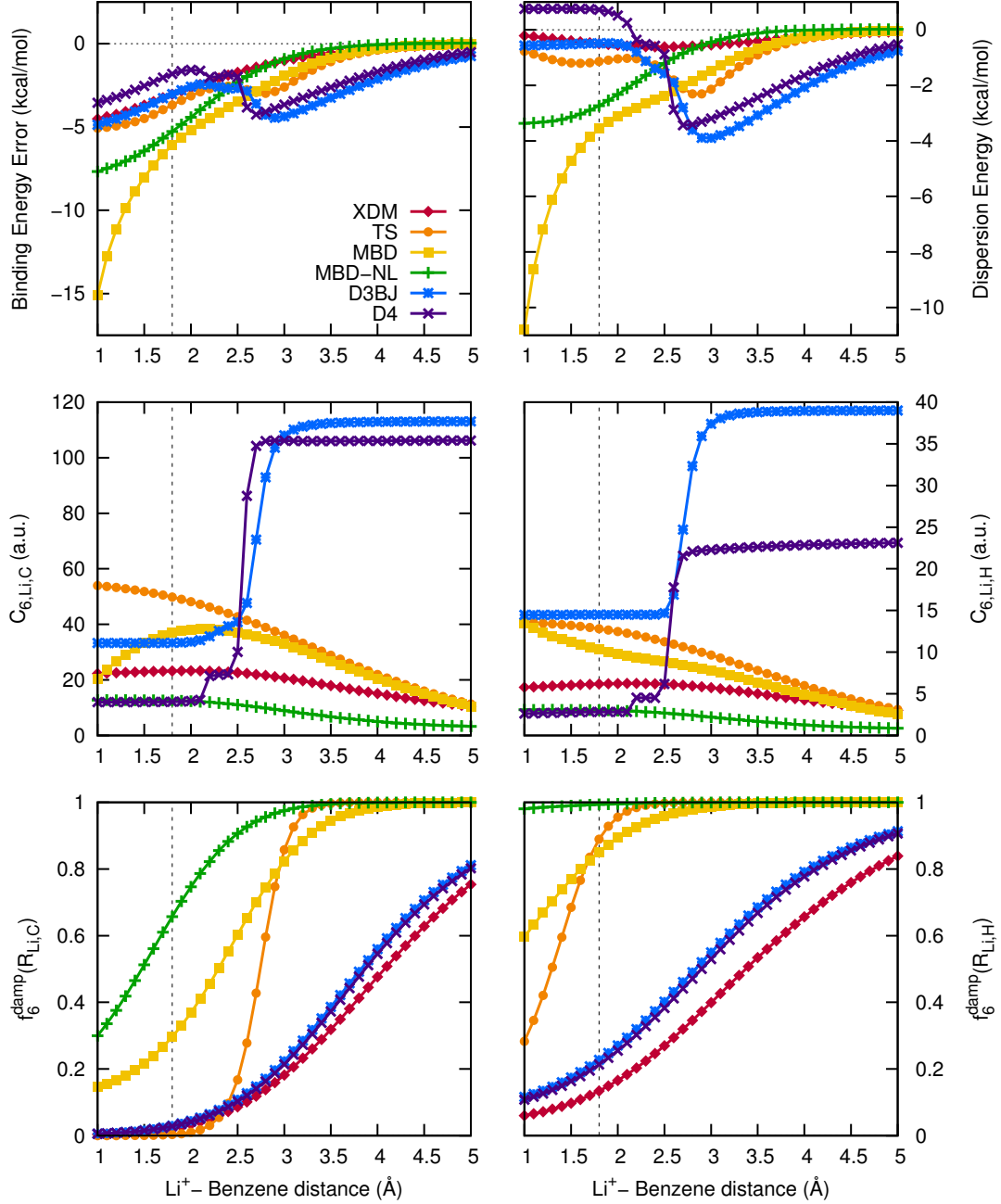


Figure 5.4: Errors in the computed binding energies, relative to correlated wavefunction reference data, and computed dispersion energies for a C_{6v} Li^+ –benzene complex as a function of the distance between the cation and the benzene ring’s centre of mass (top). Also shown are the heteroatomic C_6 dispersion coefficient between the Li and C or H atoms (middle), and the corresponding damping function (bottom). For XDM, D3BJ, and D4, this is the BJ damping function for the C_6 term using the PBE0 parameters while, for TS, MBD, and MBD-NL, it is the WY damping function. The dashed vertical line indicates the reference equilibrium distance.

uses TS as the starting point for its rsSCS scheme. However, this observation rules out the possibility that MBD experiences a polarization catastrophe for this system.

The most striking feature of the C_6 plots is that the D3BJ and D4 methods give a massive dispersion coefficient that decreases sharply once the separation falls below a certain threshold. This behaviour can be explained by the dependence of the D3BJ and D4 methods on the coordination number of the atom. At large separations, the Li is modelled as an uncoordinated neutral atom, which is highly polarizable and capable of strong dispersion interactions. It is only when the Li–C distances are sufficiently small that the coordination number increases and the Li is correctly modelled as a cation, yielding a much lower dispersion coefficient. It is the sharp decrease in dispersion coefficient from $2.5 \text{ \AA} < R < 3.0 \text{ \AA}$ that causes the sudden damping of the dispersion energy over this same distance range.

In contrast to D3BJ and D4, the other dispersion methods yield low dispersion coefficients at large distances due to these models' dependence on the SCF electron density. The trend in dispersion coefficients at separations larger than 3 \AA in Figure 5.4 is D3BJ > D4 \gg TS \sim MBD > XDM > MBD-NL, which explains the trends in the asymptotic dispersion energy. It is our opinion that MBD-NL is likely giving the most reasonable treatment of the Li cation's dispersion coefficients through its polarizability functional, while the other methods are likely somewhat overestimating the C_6 due to their use of the free neutral-atom reference polarizability for Li, as opposed to a free cation reference.

The behaviour of the C_6 coefficients alone does not explain the much larger dispersion stabilization predicted by MBD and MBD-NL compared to the other methods, particularly since MBD-NL consistently gives the lowest dispersion coefficients. This prompted us to consider the behaviour of the damping functions, which are also plotted for the Li–C and Li–H interactions in Figure 5.4. At short separations, the XDM, D3BJ, and D4 methods are strongly damped due to their use of BJ damping functions. The TS dispersion energy is also very strongly damped, with the WY damping function having a sudden onset in the range $2.5 \text{ \AA} < R < 3.0 \text{ \AA}$. While MBD and MBD-NL also use WY damping functions, their parameters were chosen to make the damping far more gradual than for TS. It appears that this choice may be a problem for the present system, with incomplete damping of only ca. 70-80% of the Li–C dispersion energy at compressed geometries. As the dispersion energy diverges as $-C_6/R^6$, and the Li–C distances fall below the sum of their covalent radii, this is likely insufficient. Additionally, less than 40% of the Li–H dispersion energy

is damped with MBD, and less than 5% is damped with MBD-NL. This latter result is likely sufficient to explain the large dispersion stabilization predicted for MBD-NL at short separations, despite yielding relatively small dispersion coefficients. Thus, the large errors observed with the MBD and MBD-NL methods for alkali-cation complexes at compressed geometries seem to be due to insufficient damping for dispersion interactions involving these cations.

5.4 CONCLUSION

In this study, we used the recent DES15K [484] benchmark of neutral and charged intermolecular complexes, at expanded and compressed geometries, to assess the performance of five popular dispersion corrections within density-functional theory. By using the same electronic-structure code, density functional, basis sets, and integration grids, this represents the first head-to-head comparison of the XDM [55, 57, 156], D3BJ [41, 92], D4 [42], TS [44], MBD [45, 46], and MBD-NL [52] dispersion corrections. Furthermore, the size of this benchmark and the breadth of chemical systems present within it give us a high level of confidence in our findings and reveals some unexpected errors not seen for narrower data sets. It should be noted, however, that the DES15K set is limited to relatively small, gas-phase molecular dimers and significant errors with one or more density-functional dispersion corrections can and do occur for systems not sampled here, including supermolecular complexes [486], inorganic solids [38, 479], and surface adsorption [510, 511].

For the neutral complexes, and ionic complexes without metal cations, the XDM, D3BJ, D4, MBD, and MBD-NL dispersion methods all performed similarly. For these types of systems, we found no strong reason to choose any of these methods over any other. Indeed, the choice of base functional matters more for computational accuracy than the choice of dispersion correction. This was demonstrated by the fact that B86bPBE0-XDM gave lower errors than PBE0-XDM for complexes at compressed geometries due to better treatment of non-bonded repulsion. It is our opinion that a more accurate treatment of non-bonded repulsion should be an ongoing aim in DFT development. We additionally found that systems containing alkaline earth metal dication pose a consistent problem for both of the base functionals considered here, although it is possible that other base functionals may perform better.

MBD and MBD-NL were found to give consistently larger errors than obtained with the other dispersion methods for complexes containing alkali cations and alkaline

earth dications. Analysis of the outliers revealed that MBD and MBD-NL tend to significantly overbind these species, particularly at compressed geometries. We therefore decided to investigate this problem further by studying a model cation- π complex. This showed that the error is not a result of a polarization catastrophe, but rather, seems to be a problem with the dispersion energy evaluation, likely due to an overly weak damping function. Presently, we do not recommend MBD-based methods for intermolecular chemistry involving metal cations. It is possible that MBD/FI [50], the fractionally ionic variant of MBD, may show improved performance for such systems. However, the MBD/FI dispersion correction has yet to be implemented in FHI-aims, preventing a fair comparison in this work. While the worst errors occur for highly compressed geometries that are not encountered in most thermochemistry studies, compressed geometries do arise in molecular dynamics simulations or when modelling systems at high applied pressure. A particular application that may prove problematic would be modelling intercalation of Li (or other alkali metals) into graphite anodes for Li-ion battery applications [512–516].

As a final remark, this work demonstrates how analysing the outliers from large benchmarks can provide valuable insight into where popular methods succeed and fail. It is by examination of the outliers that benchmarking studies can provide value and new physical insight, although this is, unfortunately, often overlooked.

CHAPTER 6

THE EXCHANGE-CORRELATION DIPOLE MOMENT DISPERSION METHOD

“I think there is a moral to this story, namely that it is more important to have beauty in one’s equations than to have them fit experiment. It seems that if one is working from the point of view of getting beauty in one’s equations, and if one has really a sound insight, one is on a sure line of progress.” [517]

~ Prof. Paul A. M. Dirac (1902–1984)

This chapter is adapted from: **Bryenton, K. R.**, & Johnson, E. R. *The exchange-correlation dipole moment dispersion method*. Submitted To: Phys. Chem. Chem. Phys., (2025) [244]

Author contributions: K.R.B. developed the mathematical model, wrote the software, generated all data, and wrote the first draft of the manuscript.

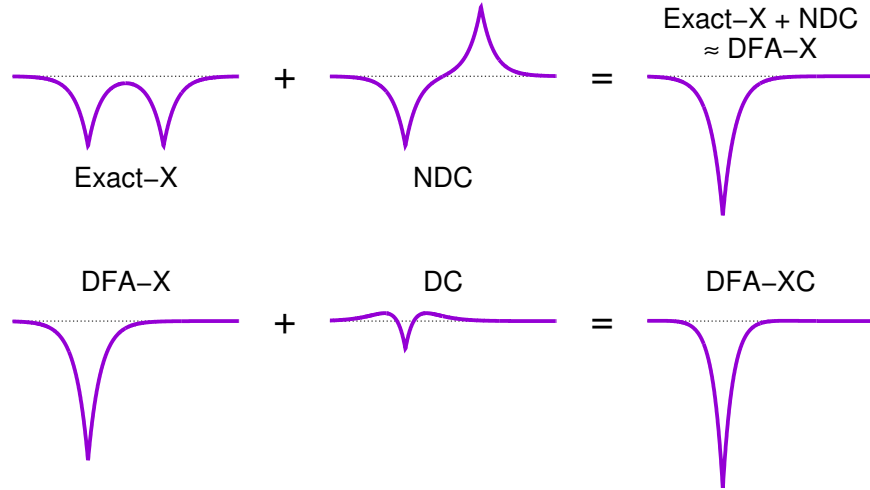
6.1 INTRODUCTION

The XDM model uses second-order perturbation theory to obtain the dispersion energy in terms of atomic multipole-moment integrals and polarizabilities [78, 518]. One key approximation is that the multipole moments are taken to be those of a reference electron and its associated DFA exchange hole [55], which serves as a convenient and simple proxy for the full exchange-correlation (XC) hole. Indeed, shortly after the formulation of XDM, three papers sought to provide a more rigorous link between the XC hole and the London dispersion energy [519–521]. The rationale for the good performance of a dispersion model based on the DFA exchange-hole multipole moments, without further correlation terms, is that the chosen Becke–Roussel model [16] is inherently local and confines the hole to a region of roughly atomic size. This implicitly accounts for the effects of non-dynamical correlation (NDC) [170], which serves to localise the highly non-local exact exchange hole and produce a localised XC hole [331], as illustrated in Figure 6.1. Thus, NDC is expected to account for the vast majority of the total correlation contribution to the XC hole, while the more local, dynamical correlation (DC) is thought to have only a small contribution [55] and has been neglected in XDM to date. However, given the high accuracy achieved by existing DFA dispersion models, inclusion of the DC contribution is becoming increasingly relevant.

Additionally, Becke recently showed [183] that XDM fails to accurately predict the binding energies of two alkali-metal clusters (Li_8 and Na_8) in the ALK8 subset of the GMTKN55 thermochemistry benchmark [280]. The error was traced to the Becke–Johnson (BJ) damping function [156] used in XDM (as well as in the D3(BJ) and D4 dispersion models) to damp the dispersion energy to a small negative value at short interatomic separations. An alternative damping function based on atomic numbers, Z , was proposed and found to provide good accuracy for these metal clusters, and the GMTKN55 benchmark as a whole [183]. Notably, the Z -dependent damping function is simpler, relying on only one empirical parameter for use with a given DFA, as opposed to the two parameters used in BJ-damping. However, the performance of Z -damping has not yet been assessed on solid-state systems or on molecular systems beyond those comprising the GMTKN55 data set.

In this chapter, dynamical correlation is added to XDM dispersion through the use of a real-space correlation-hole model [135, 522], yielding the exchange-correlation dipole moment (XCDM) dispersion method. The effects of dynamical correlation on

Figure 6.1: Sketch (modelled after H₂ from Ref. [331]) of the exact exchange hole and non-dynamical correlation hole in a diatomic molecule, the sum of which is approximated by the DFA exchange hole. Also shown is the dynamical correlation hole and its sum with the DFA exchange hole to give the DFA exchange-correlation hole. Note that the exchange holes have a normalization of -1, while the correlation holes have a normalization of 0.



the resulting atomic and molecular dispersion coefficients are quantified for the first time. The performance of XDM and XCDM, paired with both BJ- and Z-damping, is assessed for selected isolated-molecule and periodic-solid benchmarks. Overall, XCDM is found to outperform XDM for computation of molecular dispersion coefficients, as well as for all molecular benchmarks, although it significantly overbinds layered materials. XDM with Z-damping appears to be a Pauling point [523], providing consistently reliable results for all benchmarks considered with a minimum of empiricism.

6.2 THEORY

6.2.1 INCLUSION OF DYNAMICAL CORRELATION: XCDM

As previously stated, since XDM uses the BR hole model it is able to capture the effects of non-dynamical correlation as well as exchange. However, the BR model does not account for dynamical correlation, so it must be added. This is intended; it has long been argued that the role of DFA exchange functionals is to also capture this non-dynamical contribution to correlation, and that dynamical correlation should be captured explicitly through dedicated correlation functionals [522, 524]. We consider

the same-spin ($\sigma\sigma$) and opposite-spin ($\sigma\sigma'$ for $\sigma \neq \sigma'$) dynamical correlation holes proposed by Becke [135]:

$$h_{C\sigma\sigma}(\mathbf{r}, s) = \frac{s^2 (s - z_{\sigma\sigma}) D_\sigma(\mathbf{r})}{6(1 + z_{\sigma\sigma}/2)} F(\gamma_{\sigma\sigma}s), \quad (6.2.1)$$

$$h_{C\sigma\sigma'}(\mathbf{r}, s) = \frac{(s - z_{\sigma\sigma'}) \rho_{\sigma'}(\mathbf{r})}{1 + z_{\sigma\sigma'}} F(\gamma_{\sigma\sigma'}s). \quad (6.2.2)$$

Here, z is the correlation length, which is the radial distance from the reference electron at which the correlation hole becomes zero. This length is determined using the inverse of the spin-indexed exchange potentials,

$$z_{\sigma\sigma} = 2c_{\sigma\sigma}|U_{X\sigma}|^{-1}, \quad (6.2.3)$$

$$z_{\sigma\sigma'} = c_{\sigma\sigma'}(|U_{X\sigma}|^{-1} + |U_{X\sigma'}|^{-1}), \quad (6.2.4)$$

where the dimensionless quantities $c_{\sigma\sigma} = 0.88$ and $c_{\sigma\sigma'} = 0.63$ were obtained from fits to atomic correlation energies [522]. For the case of the BR exchange functional, the exchange potential is [16]

$$|U_{X\sigma}| = \frac{1}{b_\sigma} \left(1 - e^{-x} - \frac{1}{2}x e^{-x} \right). \quad (6.2.5)$$

Returning to Eq. (6.2.1), $D_\sigma = \tau_\sigma - \tau_\sigma^w$ is the difference between the exact kinetic-energy density,

$$\tau_\sigma = \sum_i |\nabla \psi_{i\sigma}|^2, \quad (6.2.6)$$

written in terms of occupied Kohn–Sham orbitals, $\psi_{i\sigma}$, and the von Weizsäcker approximation [318],

$$\tau_\sigma^w = \frac{1}{4} \frac{(\nabla \rho_\sigma)^2}{\rho_\sigma}. \quad (6.2.7)$$

The prefactor is $1/4$, as opposed to $1/8$, to be commensurate with our definition of the kinetic-energy density where the usual $1/2$ factor is omitted. Finally, $F(\gamma s)$ is a function that describes the hole shape and involves an adjustable parameter to enforce normalization.

In his work, Becke suggested three forms for this normalization function [135]:

$$F_1(x) = \operatorname{sech}(x), \quad (6.2.8)$$

$$F_2(x) = (1 + x) e^{-x}, \quad (6.2.9)$$

$$F_3(x) = e^{-x^2}. \quad (6.2.10)$$

If the exchange and exchange-correlation holes both normalize to -1 electrons, then the correlation hole must normalize to zero. Thus, the first step is to solve for the value of γ in these functions to enforce the zero normalization constraint of

$$\int h_C(\mathbf{r}, s) s^2 \sin(\theta) ds d\theta d\phi = 0. \quad (6.2.11)$$

For the same-spin hole, it can be shown that

$$\gamma_{\sigma\sigma,1} = \frac{\Psi^{(5)}(1/4) - \Psi^{(5)}(3/4)}{360\pi^5 z_{\sigma\sigma}}, \quad (6.2.12)$$

$$\gamma_{\sigma\sigma,2} = \frac{35}{6 z_{\sigma\sigma}}, \quad (6.2.13)$$

$$\gamma_{\sigma\sigma,3} = \frac{8}{3\sqrt{\pi} z_{\sigma\sigma}}, \quad (6.2.14)$$

and for the opposite-spin hole

$$\gamma_{\sigma\sigma',1} = \frac{\Psi^{(3)}(1/4) - \Psi^{(3)}(3/4)}{16\pi^3 z_{\sigma\sigma'}}, \quad (6.2.15)$$

$$\gamma_{\sigma\sigma',2} = \frac{15}{4 z_{\sigma\sigma'}}, \quad (6.2.16)$$

$$\gamma_{\sigma\sigma',3} = \frac{2}{\sqrt{\pi} z_{\sigma\sigma'}}, \quad (6.2.17)$$

where $\Psi^{(n)}(z) = \frac{d^n}{dz^n} \frac{\Gamma'(z)}{\Gamma(z)}$ is the polygamma function, not to be confused with a wavefunction.

The correlation hole models presented above are all spherically symmetric about the reference point (as the correlation energy depends only on the spherical average) and will, therefore, not possess a dipole moment. However, the actual correlation holes will not be spherically symmetric in general. While the spherically symmetric hole is centred about the reference electron at position, \mathbf{r} , one can envision an asymmetric hole shifted by some displacement, d , towards the nearest nucleus (where there is more electron density to deplete) that would give the same spherical average. This is indeed the case for the BR exchange hole, as illustrated in Figure 6.2, where the magnitude of this shift, d_X , is determined from the BR exchange-hole dipole moment. However, for the correlation hole, we use its radial size as a proxy for the extent of polarisation, d_C . The first scalar moments of the same- and opposite-spin dynamical correlation

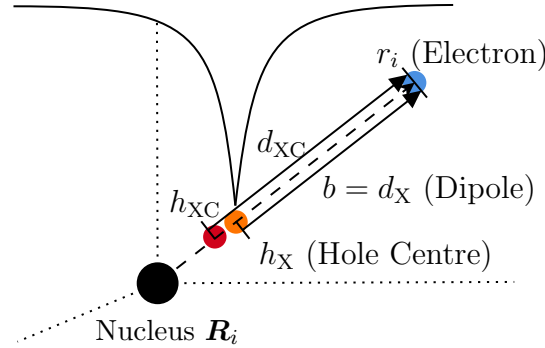


Figure 6.2: An illustration of the Becke–Roussel (BR) exchange hole, adapted from Ref. [80]. The nucleus is at position \mathbf{R}_i and its reference electron is a distance $r_i = |\mathbf{r} - \mathbf{R}_i|$ away. A dipole moment is formed between the reference electron and the centre of its associated exchange hole. Also depicted is the BR exchange-correlation hole, which is shifted slightly further towards the nucleus, increasing the dipole moment strength compared to using only the exchange hole.

holes are ultimately used to shift the hole even closer to the nucleus, as illustrated in Figure 6.2, increasing the dipole strength. The resulting exchange-correlation-hole dipole moment is used to calculate the XCDM dispersion coefficients. The validity of this model will be assessed by testing its performance for molecular and solid state systems.

The first scalar moment of the correlation hole,

$$d_C(\mathbf{r}) \approx \int h_C(\mathbf{r}, s) s d\mathbf{s}, \quad (6.2.18)$$

should provide a measure of the average distance between the reference electron and hole centre and will be used to approximate the correlation-hole dipole moment. The quality of this approximation is assessed for the BR exchange-hole dipole moments in Appendix C.1. Using Eq. (6.2.18), our same- and opposite-spin correlation-hole dipole moment contributions are then

$$d_{C\sigma\sigma}(\mathbf{r}) = \left[\frac{g_{\sigma\sigma} z_{\sigma\sigma}^7}{2 + z_{\sigma\sigma}} D_\sigma(\mathbf{r}) \right], \quad (6.2.19)$$

$$d_{C\sigma\sigma'}(\mathbf{r}) = \left[\frac{g_{\sigma\sigma'} z_{\sigma\sigma'}^5}{1 + z_{\sigma\sigma'}} \rho_{\sigma'}(\mathbf{r}) \right], \quad (6.2.20)$$

where the value of the dimensionless constant g depends on the chosen normalization function, F , and is thus a function of γ . XCDM was tested using each normalization

function on a molecular C_6 benchmark (see Section 6.3.1), and the values from the sech-type form of Eq. (6.2.8) were ultimately chosen, specifically $g_{\sigma\sigma} = 0.01243$ and $g_{\sigma\sigma'} = 0.5360$.

Finally, the correlation-hole contributions are combined with the exchange-hole dipole contribution to form the σ -spin exchange-correlation dipole, given by

$$d_{XC\sigma}(\mathbf{r}) = d_{X\sigma}(\mathbf{r}) + d_{C\sigma\sigma}(\mathbf{r}) + d_{C\sigma\sigma'}(\mathbf{r}) \quad (6.2.21)$$

$$\approx b_\sigma + \left[\frac{g_{\sigma\sigma} z_{\sigma\sigma}^7}{2 + z_{\sigma\sigma}} D_\sigma \right] + \left[\frac{g_{\sigma\sigma'} z_{\sigma\sigma'}^5}{1 + z_{\sigma\sigma'}} \rho_{\sigma'} \right], \quad (6.2.22)$$

and $r_i - d_{XC\sigma} \geq 0$ is now enforced. The addition of correlation deepens the total XC hole compared to the exchange hole. In the limit of two opposite point charges, the dipole strength is maximized. Thus, the addition of dynamical correlation (which localizes the hole) should increase the dipole strength such that $d_{XC} \geq d_X$. This would shift the location of d_{XC} closer to the nucleus, as illustrated in Figure 6.2. This result is substituted into the multipole-moment integrals in order to evaluate the XCDM dispersion coefficients.

Figure 6.3 shows the radial distribution of the exchange hole, correlation hole, and total XC hole about a reference electron for three positions within an isolated helium atom. Naturally, all three holes are deeper when the reference electron is closer to the nucleus, as the overall electron density is higher. Addition of dynamical correlation deepens the overall hole near the reference point, but its effect is rather short range and limited by the correlation length, which is ca. 1 a.u. in this particular example. The figure also shows the magnitudes of the exchange-, correlation-, and XC-hole dipole moments. Due to the localised nature of the dynamical correlation hole about the reference electron, it gives rise to a small first scalar moment. Thus, the XC-hole dipole moment is only slightly larger than the exchange-hole dipole moment, justifying the previous neglect of the dynamical correlation contribution in XDM. However, the dynamical correlation contribution is non-negligible, and its inclusion does result in a ca. 10% decrease in the mean absolute percent error (MAPE) in molecular C_6 dispersion coefficients. Further, as shown in Table 6.1, the XCDM mean percent error (MPE) all but vanishes, eliminating the systematic underestimation of the molecular C_6 dispersion coefficients observed with XDM. Tabulated MAPE and MPE values for the F_2 and F_3 normalization functions, as well as the rounded mean of all three normalization functions, can be found in Table C.1.

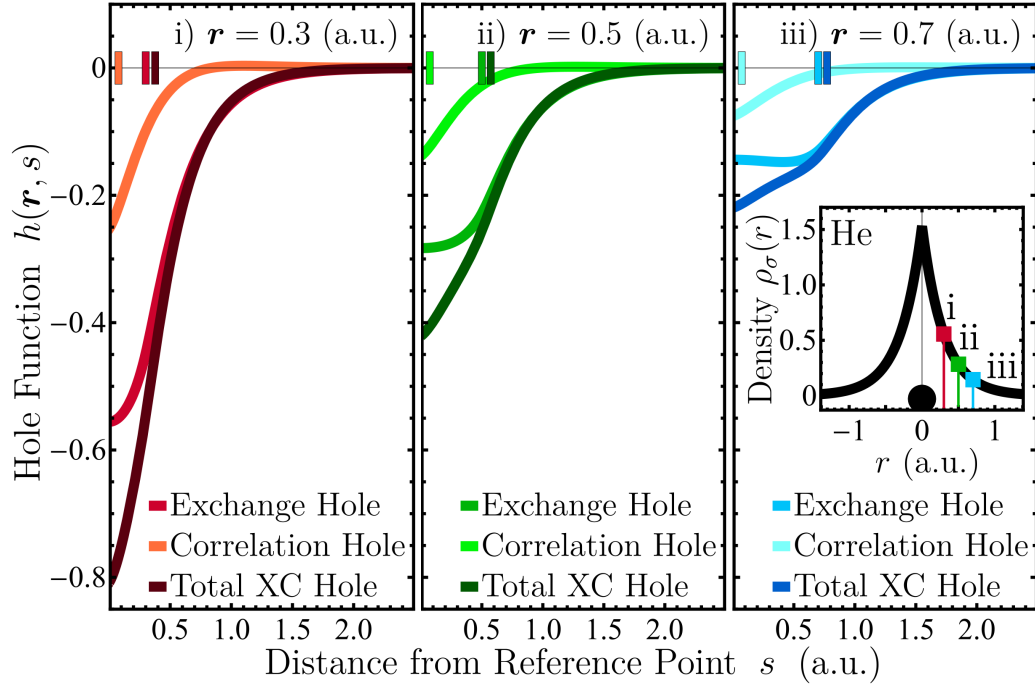


Figure 6.3: The exchange hole, opposite-spin correlation hole, and combined XC hole are plotted as a function of the distance from the reference electron, s . The associated dipole moment strengths are indicated with coloured bars along the s -axis. Results are shown for the helium atom, with the reference electron at three selected displacements, r (in bohr), from the nucleus, as shown in the inset.

6.2.2 DAMPING FUNCTIONS

Conventionally, XDM uses the Becke–Johnson (BJ) damping function [156], which is also used in the D3(BJ) and D4 dispersion methods of Grimme and co-workers. The BJ-damping function is

$$f_n^{\text{BJ}}(R_{ij}) = \frac{R_{ij}^n}{R_{ij}^n + R_{\text{vdW},ij}^n}, \quad (6.2.23)$$

where $R_{\text{vdW},ij}$ is the sum of approximate van der Waals radii of atoms i and j . It is determined as

$$R_{\text{vdW},ij} = a_1 R_{c,ij} + a_2, \quad (6.2.24)$$

where a_1 and a_2 are empirical parameters that are not element-dependent but are fitted for use with a particular combination of density functional and basis set. $R_{c,ij}$ is a “critical” interatomic distance at which successive terms in the perturbation theory expansion of the dispersion energy become equal. If the dispersion energy only

Table 6.1: Results for the MolC6 benchmark of homomolecular C_6 coefficients, computed using XDM and XCDM in FHI-aims [120] using **tight** basis settings. Mean percent errors (MPE) and mean absolute percent errors (MAPE) are shown for the B86bPBE and PBE functionals, as well as their 25% and 50% hybrid variants.

Functional	XDM		XCDM	
	MAPE	MPE	MAPE	MPE
B86bPBE	18.4	-16.4	8.5	2.7
B86bPBE0	19.6	-18.1	8.6	0.6
B86bPBE50	17.0	-14.5	9.0	-1.2
PBE	18.1	-16.1	8.4	3.3
PBE0	19.4	-17.9	8.5	1.1
PBE50	16.6	-14.0	8.9	-0.9

includes the C_6 and C_8 terms, then

$$R_{c,ij} = \sqrt{\frac{C_{8,ij}}{C_{6,ij}}} . \quad (6.2.25)$$

However, if the C_{10} term is also included in the dispersion energy, two other possible definitions for $R_{c,ij}$ arise:

$$R_{c,ij} = \begin{cases} \sqrt{\frac{C_{10,ij}}{C_{8,ij}}} \\ \sqrt[4]{\frac{C_{10,ij}}{C_{6,ij}}} \end{cases} . \quad (6.2.26)$$

In XDM, the value of $R_{c,ij}$ is taken to be the average of these three results.

Becke recently proposed an alternative damping function for use with XDM that, unlike BJ damping, involves only one empirical fit parameter [183]. In this work, it will be referred to as Z-damping, due to the dependence on the atomic number. The Z-damping function is

$$f_n^Z(R_{ij}) = \frac{R_{ij}^n}{R_{ij}^n + z_{\text{damp}} \frac{C_{n,ij}}{Z_i + Z_j}} , \quad (6.2.27)$$

where Z_i and Z_j are the atomic numbers of atoms i and j , respectively. This definition was chosen because the resulting contribution to the correlation energy in the united-atom limit would be

$$\lim_{R_{ij} \rightarrow 0} \left(\frac{C_{n,ij}}{R_{ij}^n + z_{\text{damp}} \frac{C_{n,ij}}{Z_i + Z_j}} \right) = \frac{Z_i + Z_j}{z_{\text{damp}}} , \quad (6.2.28)$$

and atomic correlation energies are roughly proportional to atomic number. Similar

to BJ damping, the single empirical parameter, z_{damp} , is atom-independent and fitted for use with a particular density functional and basis set. A typical value of z_{damp} is around 10^5 Ha^{-1} .

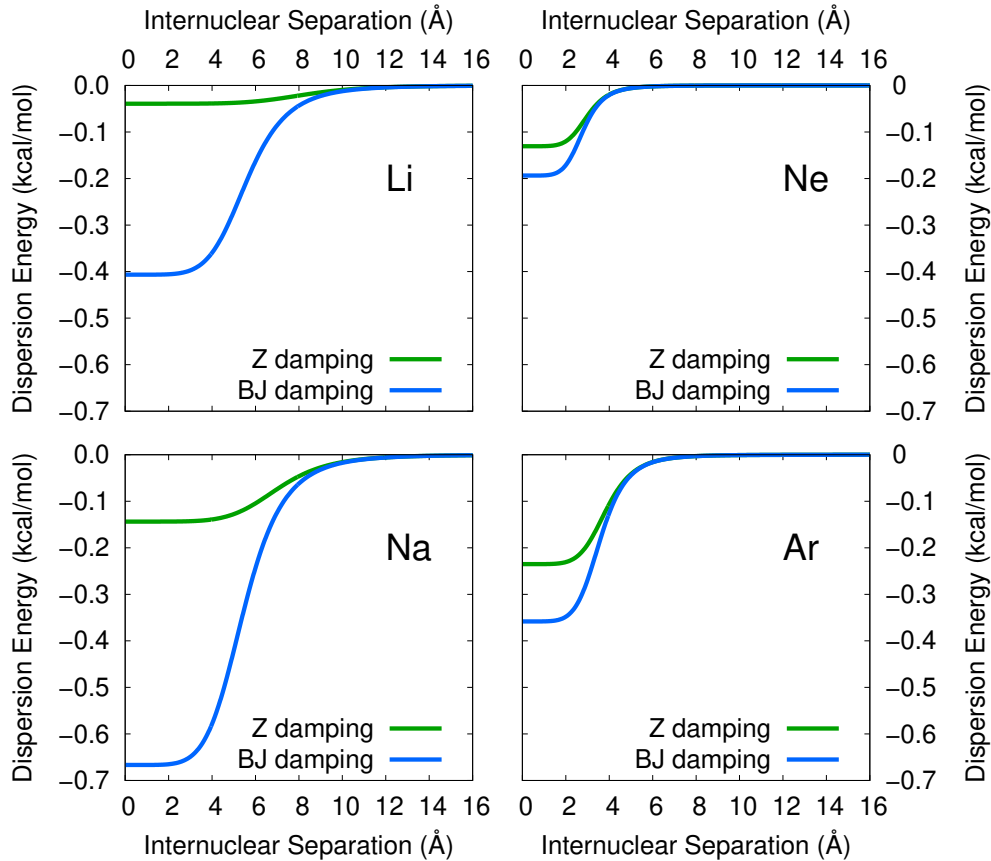


Figure 6.4: Comparison of BJ- and Z-damping functions. The plots use XDM data for the free atoms only, computed with the B86bPBE functional and *tight* basis settings using FHI-aims.

To illustrate the differences in damping functions, BJ- and Z-damping are compared for homonuclear interactions between Li, Na, Ne, and Ar atoms in Figure 6.4. The Li and Na calculations are spin-polarized, with a net spin of 1 electron. For simplicity, the curves use only data for the free atoms, which omit changes in dispersion coefficients with internuclear separation that would be observed in the dimer systems due to varying electron densities. The results in Figure 6.4 show that Z-damping consistently reduces the magnitude of the dispersion energy compared to BJ-damping. However, this effect is fairly minor for Ne and Ar, while there is a very large increase in damping strength for Li and Na. This allows correction of the overbinding seen with BJ-damping for the Li_8 and Na_8 clusters, while preserving high

accuracy for main-group elements. With BJ-damping, the magnitudes of the dispersion energies in the united-atom limit follow the trend Na>Li>Ar>Ne, but this changes to Ar>Na≈Ne>Li for Z-damping. The latter appears more physical because, in the united-atom limit, the dispersion energy would become a correlation energy and should increase with the number of electrons and, hence, atomic number.

6.3 DATA SETS

To evaluate the performance of XDM and XCDM, both with BJ- and Z-damping, a comprehensive list of benchmarks has been selected for testing. These are categorised into three groups: those used to optimize parameters for dispersion coefficients and damping functions, finite-molecule benchmarks, and periodic-solid benchmarks. The benchmark content, geometry sources, and reference data quality are summarised below.

6.3.1 C_6 BENCHMARK AND FIT SET

MolC6: Benchmark of 20 homomolecular C_6 dispersion coefficients originally studied by Becke and Johnson [326]. Systems include H₂, N₂, O₂, Cl₂, CO₂, methane, CCl₄, SiH₄, SiF₄, SF₆, ethyne, ethene, ethane, propene, propane, butene, butane, pentane, hexane, and benzene. Reference values were obtained from experimental dipole oscillator strength (DOS) data and subsequently refined using the dipole oscillator strength distribution (DOSD) method [87, 326, 525–530]. These C_6 reference values were used to assess the accuracy of XCDM relative to XDM and to guide the optimal determination of the $g_{\sigma\sigma}$ and $g_{\sigma\sigma'}$ parameters, as described in Section 6.2.1.

KB49: Binding energies of 49 molecular dimers with reference values from basis-set extrapolated CCSD(T) calculations [323]. Dimer geometries are available from the `refdata` GitHub repository [531]. The BJ-damping parameters, a_1 and a_2 (in Å), as well as the Z-damping parameter, z_{damp} , were fitted separately for XDM and XCDM for each combination of DFA and basis set. Optimal parameters were determined by minimising the root-mean-square percent error (RMSPE) for the KB49 set and may be found in Table C.2 and Table C.3.

6.3.2 MOLECULAR BENCHMARKS

GMTKN55: A collection of 55 individual benchmarks spanning the thermochemistry of small and large molecules, reaction barriers, and both intramolecular

and intermolecular non-covalent interactions (NCI). Typically, error metrics are reported for seven categories: “Basic + Small”, “Iso + Large”, “Barriers”, “Intermolecular NCI”, “Intramolecular NCI”, “All NCI”, and GMTKN55 as a whole. The interested reader is directed to Ref. [280] for detailed information regarding the individual benchmarks. Geometries for FHI-aims may be obtained from the `gmtkn55-fhiaims` GitHub repository [532].

Due to the wide range of energy scales of the component benchmarks within the GMTKN55, the overall error for the set is reported as a weighted mean absolute deviation (WTMAD). Several definitions for such a weighted error have been proposed. The first proposed metric, WTMAD-1, is not commonly used. In this scheme, each subset is assigned an arbitrary weight, denoted w_i , where $w_i = 10$ when $|\Delta E|_i < 7.5$ kcal/mol, $w_i = 0.1$ when $|\Delta E|_i > 75$ kcal/mol, and $w_i = 1$ otherwise. The WTMAD-1 is then calculated as

$$\text{WTMAD-1} = \frac{1}{N_{\text{bench}}} \sum_{i=1}^{N_{\text{bench}}} w_i \cdot \text{MAD}_i. \quad (6.3.1)$$

The most widely used metric for the GMTKN55 benchmark is the WTMAD-2, introduced in Ref. [280] and defined as

$$\text{WTMAD-2} = \sum_{i=1}^{N_{\text{bench}}} \frac{N_i}{N_{\text{total}}} \cdot \frac{\overline{|\Delta E|}_{\text{mean}}}{\overline{|\Delta E|}_i} \cdot \text{MAD}_i, \quad (6.3.2)$$

where the sum runs over all 55 benchmarks. Here, N_i is the number of data points in the i th benchmark, $\overline{|\Delta E|}_i$ is the average reference energy for that benchmark, $N_{\text{total}} = \sum_{j=1}^{N_{\text{bench}}} N_j$, $\overline{|\Delta E|}_{\text{mean}}$ is the average of all $\overline{|\Delta E|}_i$ values (approximately 56.84 kcal/mol if all 55 subsets are considered), and MAD_i is the mean absolute deviation between the computed and reference data. Additionally, Whittmann *et al.* recently proposed the WTMAD-3 weighting scheme, which is identical to WTMAD-2 except that it attenuates the weights for a subset to be no more than 1% of the total reactions considered [533].

As shown in Table C.4, all three of these metrics result in a number of benchmarks having a disproportionately large contribution to the overall WTMAD, while others have near-zero contribution. Upon review, we determined that calculating weights based on the MAD relative to the reference energy $\overline{|\Delta E|}_i$ was not representative. For example, IL16’s average reference energy is 109.04 kcal/mol—171 times larger than

its mean MAE across our methods of 0.63 kcal/mol—resulting in severe undercontribution (0.05%) in WTMAD-2. Subsets such as PA26 (0.21%) and DIPCS10 (0.04%) are similarly affected. There also exist cases where the inverse is true and the ratio is small, causing overcontribution of subsets such as PCONF21 (4.5%), HEAVY28 (4.7%), and BH76 (9.6%).

To address these issues, we propose yet another metric, WTMAD-4. This scheme is identical to WTMAD-1 in its construction, but the weights are based on the magnitudes of expected errors rather than on the absolute energy scales. As a result, each benchmark contributes meaningfully and appropriately to the overall WTMAD-4, with contributions ranging approximately between 1.0 to 3.5%. The weights are given by

$$w_i = \begin{cases} 50 & \text{ACONF, RG18} \\ 25 & \text{ADIM6, Amino20x4, BUT14DIOL,} \\ & \text{HEAVY28, ICONF, MCONF, S66} \\ 10 & \text{BHROT27, HAL59, IL16, PCONF21,} \\ & \text{PNICO23, RSE43, S22, SCONF, UPU23} \\ 5 & \text{AHB21, CARBHB12, CDIE20,} \\ & \text{CHB6, ISO34, Parel, TAUT15} \\ 2.5 & \text{AL2X6, BH76, BH76RC, BHPERI,} \\ & \text{BSR36, FH51, G21EA, HEAVYSB11,} \\ & \text{IDISP, INV24, ISOL24, NBPRC,} \\ & \text{PA26, YBDE18} \\ 1 & \text{ALK8, ALKBDE10, BHDIV10, DARC,} \\ & \text{DIPCS10, G21IP, G2RC, PX13,} \\ & \text{RC21, W4-11, WATER27, WCPT18} \\ 0.5 & \text{C60ISO, DC13, MB16-43, SIE4x4} \end{cases} \quad (6.3.3)$$

Considerations for each subset, such as its total fraction of reactions within its category, and the quality of its reference data, were taken into account when determining the appropriate weights. For additional information on the reasoning and construction of WTMAD-4, the reader is directed to Appendix C.4.

6.3.3 SOLID-STATE BENCHMARKS

X23: Lattice energies of 23 molecular crystals [99, 295], using updated “X23b” reference energies [534]. Geometries are available from the `refdata` repository [531].

Unlike the previous benchmarks, X23 requires geometry optimizations with each functional and basis combination considered.

HalCrys4: Lattice energies of four halogen crystals— Cl_2 , Br_2 , I_2 , and ICl [535]. These lattice energies are compared to back-corrected experimental results from Ref. [536]. As with the X23, geometries are optimised for each reported functional and basis set. Geometries are available from the `refdata` repository [531].

ICE13: Absolute lattice energies of ice polymorphs [537] (Abs), along with their relative energy differences (Rel) using diffusion Monte Carlo (DMC) reference data [196]. ICE13 requires geometry optimizations for all systems except the isolated water molecule, which uses a fixed geometry. Geometries are available from the `refdata` repository [531].

LM26: Exfoliation energies of 26 layered materials, predominantly transition-metal dichalcogenides, but also including graphite and hexagonal boron nitride [479]. We also provide statistics for the LM11 subset studied by Tawfik [38]. Reference data was obtained using the random-phase approximation (RPA), and geometries may be obtained from the Inorganic Crystal Structure Database [538]. Since small deviations in the in-plane lattice constant, a , do not significantly affect the equilibrium interlayer separation and binding energy, the in-plane lattice constants are fixed to their experimental values. The binding energies and c lattice constant are determined by unit-cell relaxation [38] or interpolation [315, 479].

6.4 COMPUTATIONAL METHODS

Unless otherwise stated, all calculations were performed using version 250425 of FHI-aims (commit b38a7049) [119, 120, 162, 494–497, 539]. As noted above, the BJ- and Z-damping coefficients were determined for each functional and basis combination by least-squares fitting to minimise the RMSPE for the KB49 benchmark set of intermolecular binding energies. Parameters for the XDM(BJ), XDM(Z), XCDM(BJ), and XCDM(Z) dispersion corrections, optimised for all combinations of eleven density functionals and five basis sets, are included in Table C.2 and Table C.3.

Herein, we will focus on only nine representative functionals, using data near the basis-set limit to avoid any conflating effects of basis-set incompleteness errors. At the GGA level of theory, we considered the PBE [148–150] and B86bPBE [147] functionals. At the global hybrid level, we selected six GGA-based hybrids including

B3LYP [134, 165, 540–542], popular for molecular thermochemistry, PBE0 [163], popular in solid-state chemistry, and our recommended B86bPBE0 [119]; we also used their analogues with 50% exact exchange—BHLYP [164], PBE50, and B86bPBE50—which should exhibit reduced delocalization error [161]. Finally, we also considered the range-separated GGA-based hybrid LC- ω PBE ($\omega = 0.4 \text{ bohr}^{-1}$) [166, 167], which has previously demonstrated excellent performance on GMTKN55 as a minimally empirical functional when paired with the D3(BJ) dispersion correction [280]. Our focus is limited to methods with simple functional forms as this is consistent with an “Occam’s Razor” approach to DFA development. We explicitly do not consider any exchange-correlation functionals involving empirically fit parameters, with the exception of B3LYP, which involves three parameters and was fit to the G1 [543, 544] thermochemistry set only. We similarly do not consider any double-hybrid functionals due to their reliance on virtual orbitals.

For GMTKN55, all FHI-aims calculations used the `tight` basis, except for subsets containing anions. HB21, BH76, BH76RC, and G21EA used `tier2_aug2` for all atoms; IL16 used `tier2_aug2` for all O, F, S, and Cl atoms; and WATER27 used `tier2_aug2` for O atoms only for reactions involving anions, as this basis caused linear dependencies in the SCF for some of the larger, neutral water clusters. In all cases, the damping parameters were kept at the same values optimised for the `tight` basis settings as these are already sufficiently converged as to approach the basis-set limit. As some SCF convergence problems were encountered for the range-separated hybrid functionals in FHI-aims (see Appendix C.3), the LC- ω PBE data were obtained in combination with the aug-cc-pVTZ basis set using the Gaussian16 program [126], with the dispersion corrections applied *ad hoc* using the postg code [124].

Turning to the solid-state, only FHI-aims calculations were performed and only the two GGA and four global-hybrid functionals were considered (B3LYP and BHLYP were omitted as the asymptotic constraint used in the construction of the B88 exchange functional [134] is not relevant for solid-state systems). For the X23, ICE13, and HalCrys4 benchmarks, GGA calculations used both `tight` and `lightdenser` [243] basis settings. The latter is our recommended basis for most solid-state calculations, particularly geometry optimizations, although there will be some residual basis-set incompleteness error. As hybrid calculations with the `tight` basis require prohibitive amounts of memory, only `lightdenser` calculations were performed. Hybrid results

Table 6.2: Timing comparisons for XDM and its variants are reported as the mean of the percent van der Waals (vdW) time per system. For the “1 SCF Step” column, each GMTKN55 system was reinitialized from a converged SCF using the `elsi_restart` feature, and was allowed to converge—typically one SCF step—using the B86bPBE0 hybrid functional and `tight` basis settings. For the “1 Opt Step” column, each system in the X23 benchmark was started from a pre-converged geometry, thus a single geometry optimization step was calculated. The results combine data from PBE, B86bPBE, and their associated 25% and 50% hybrid functionals, all using the `lightdenser` basis.

Method	1 SCF Step	1 Opt Step
XDM(BJ)	9.42%	3.20%
XDM(Z)	9.16%	3.20%
XCDM(BJ)	9.44%	3.24%
XCDM(Z)	9.17%	3.28%

with the `tight` basis were approximated using an additive basis set correction evaluated at the converged GGA/`lightdenser` geometries [119, 545]:

$$\begin{aligned} E(\text{hybrid/tight}) &\approx E(\text{hybrid/lightdenser}) \\ &+ E(\text{GGA/tight}) \\ &- E(\text{GGA/lightdenser}). \end{aligned} \quad (6.4.1)$$

For the LM26 benchmark (and its LM11 subset), only GGA calculations using the `lightdenser` and `tight` basis settings were performed. Hybrid results are not reported due to SCF convergence issues, likely arising due to the small band gaps in these semiconducting materials.

Lastly, we highlight the computational efficiency of the XDM-based post-SCF dispersion corrections. As shown in Table 6.2, these corrections account for only a small fraction of the total CPU time compared to even a single SCF step. The increased overhead to compute XCDM is negligible relative to XDM, and Z-damping is slightly quicker than BJ-damping, although not enough to be significant during a geometry optimization.

6.5 RESULTS AND DISCUSSION

6.5.1 MOLECULAR BENCHMARKS

The focus of this section is the GMTKN55 set, comprised of 55 diverse molecular benchmarks. The summarized results are presented below, while full statistics for each benchmark with all functionals and dispersion corrections, as well as the WTMAD values for each category, are provided in Appendix C.5. A recent study by Becke demonstrated the improved performance of Z-damping compared to BJ-damping for alkali metal clusters in the ALK8 benchmark when paired with a double-hybrid functional [183]. However, in that work, the Z-damping parameter was fitted to the GMTKN55 itself, which may have introduced a confounding variable. Here, we fitted XDM(Z) to the canonical KB49 set and extended the comparison to a range of common, minimally empirical, density functionals.

Figure 6.5 shows the best-performing dispersion correction among XDM(BJ), XDM(Z), XCDM(BJ), and XCDM(Z) for each functional and benchmark alongside the corresponding MAE. While XCDM(BJ) clearly performs better for most systems, Z-damping shows clear improvements for specific cases, including ALK8 (dissociation and other reactions of alkaline compounds), HEAVYSB11 (dissociation energies in heavy-element compounds), YBDE18 (bond-dissociation energies in ylides), and much of the “Iso+Large” category (reaction energies for large systems and isomerization reactions). LC- ω PBE also tends to pair better with Z-damping, although further testing is needed to see if this is broadly applicable to range-separated hybrid functionals.

To quantify the differences between the four dispersion corrections, the MAE difference of XDM(Z), XCDM(BJ), and XCDM(Z) compared to XDM(BJ) for each benchmark is shown in Figure 6.6. The B86bPBE0 and LC- ω PBE functionals were selected for this assessment because B86bPBE0 is representative of most other global hybrids tested, while LC- ω PBE should reduce delocalization error due to its range separation. As expected, Z-damping alleviates the issues with alkali metal clusters and substantially improves performance on the ALK8 set, lowering the MAE by >6 kcal/mol with B86bPBE0. However, the ALK8 set is not an outlier for BJ-damping when paired with LC- ω PBE, indicating that there is considerable interplay between the base functional and dispersion damping for this data set. Additionally, XCDM(BJ) at least partially alleviates the overbinding of ALK8, although not to the same extent as Z-damping. It is also notable that the large improvement in

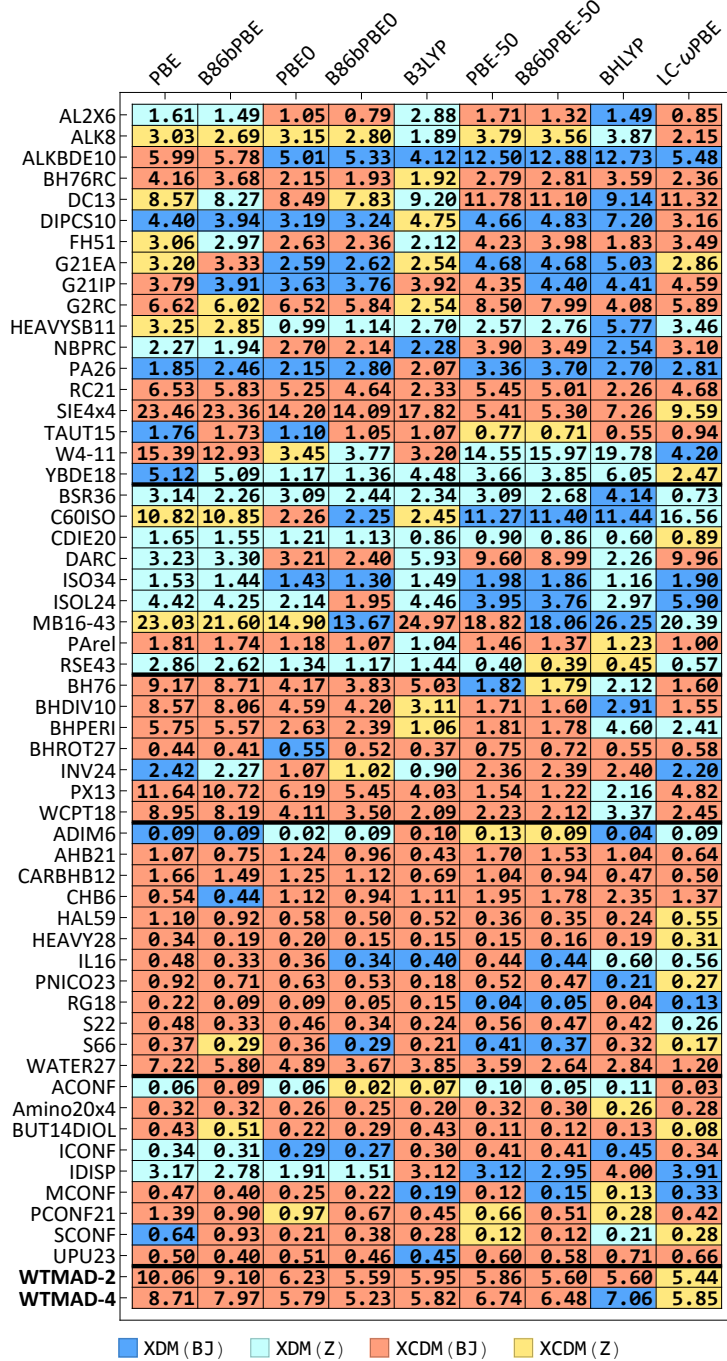


Figure 6.5: Minimum MAEs, in kcal/mol, obtained for each benchmark within the GMTKN55 set for each DFA considered. The dispersion correction yielding this MAE is indicated by the colour. WTMAD-2 and WTMAD-4 results for the entire benchmark are also shown. Thick black lines partition GMTKN55 into its composite categories: (from top to bottom) “Basic + Small”, “Iso + Large”, “Barriers”, “Intermolecular NCI”, and “Intramolecular NCI”.

	XDM(Z)	XCDM(BJ)	XCDM(Z)			
	B86bPBE0	LC- ω PBE	B86bPBE0	LC- ω PBE	B86bPBE0	LC- ω PBE
AL2X6	-0.30	-0.81	0.12	0.19	-0.23	-0.69
ALK8	6.39	0.75	3.39	1.27	6.63	0.93
ALKBDE10	-0.03	-0.02	-0.08	-0.01	-0.05	-0.02
BH76RC	-0.02	-0.02	0.02	0.01	-0.01	-0.01
DC13	-0.07	-0.63	0.10	0.08	0.11	-0.43
DIPCS10	-0.09	0.07	-0.06	0.10	-0.09	0.08
FH51	-0.19	-0.17	0.06	0.07	-0.12	-0.10
G21EA	-0.02	0.00	-0.02	-0.01	-0.02	0.00
G21IP	-0.02	0.00	-0.01	0.00	-0.02	0.00
G2RC	-0.05	-0.12	0.13	0.08	0.02	-0.06
HEAVYSB11	0.44	1.01	-0.37	-0.35	0.39	0.89
NBPRC	-0.34	-0.36	0.14	0.18	-0.23	-0.25
PA26	-0.35	-0.09	-0.11	-0.11	-0.33	-0.07
RC21	-0.37	-0.23	0.10	0.07	-0.23	-0.12
SIE4x4	-0.07	-0.01	0.01	-0.01	-0.05	0.00
TAUT15	-0.05	-0.03	0.00	0.00	-0.04	-0.03
W4-11	0.11	0.00	-0.10	-0.06	0.04	-0.01
YBDE18	0.31	0.03	-0.24	0.03	0.14	0.04
BSR36	0.74	1.10	0.05	0.03	0.56	0.94
C60ISO	-0.04	0.22	-0.01	-0.10	-0.05	0.17
CDIE20	0.08	0.01	-0.04	-0.02	0.05	0.01
DARC	-1.06	-0.99	0.15	0.14	-0.66	-0.67
ISO34	-0.01	-0.01	-0.02	-0.02	-0.02	-0.01
ISOL24	0.00	-0.47	0.04	-0.07	0.03	-0.40
MB16-43	-0.33	2.00	-0.09	-1.12	-0.21	1.74
PArel	-0.04	-0.04	0.00	0.00	-0.03	-0.03
RSE43	0.17	0.01	-0.01	0.00	0.14	0.00
BH76	-0.15	0.00	0.09	0.02	-0.09	0.01
BHDIV10	-0.07	-0.18	0.07	0.02	0.00	-0.14
BHPERI	-0.18	0.09	0.24	-0.16	0.05	-0.03
BHROT27	-0.02	0.00	0.00	0.00	-0.02	0.00
INV24	0.00	-0.01	-0.01	-0.04	0.00	-0.01
PX13	-0.35	-0.22	0.08	0.05	-0.26	-0.15
WCPT18	-0.24	-0.13	0.12	0.08	-0.14	-0.07
ADM6	0.09	0.05	-0.18	-0.25	0.03	0.02
AHB21	-0.20	-0.07	0.16	0.01	-0.12	-0.03
CARBHB12	-0.06	-0.03	0.06	0.05	-0.02	0.01
CHB6	-0.23	-0.30	0.21	0.14	-0.12	-0.22
HAL59	-0.34	0.02	0.06	-0.11	-0.29	0.03
HEAVY28	-0.38	-0.01	0.06	-0.15	-0.35	0.01
IL16	-0.42	0.78	-0.01	-0.25	-0.28	0.70
PNICO23	-0.10	0.02	0.06	-0.07	-0.05	0.03
RG18	-0.04	0.00	0.00	-0.03	-0.04	-0.01
S22	-0.06	0.08	0.04	0.01	-0.03	0.07
S66	-0.04	0.04	-0.01	-0.05	-0.02	0.04
WATER27	-1.61	-0.63	0.84	0.44	-1.16	-0.25
ACONF	0.00	-0.01	0.00	0.06	0.02	0.04
Amino20x4	-0.02	-0.02	0.00	0.03	-0.02	-0.02
BUT14DIOL	-0.03	-0.01	0.01	0.00	0.00	0.01
ICONF	-0.01	-0.03	-0.01	0.00	-0.01	-0.03
IDISP	0.18	-0.06	0.13	-0.15	0.02	-0.24
MCONF	-0.02	-0.08	0.00	-0.04	-0.03	-0.08
PCONF21	0.01	0.00	0.06	0.05	0.02	0.01
SCONF	-0.14	-0.02	0.00	-0.04	-0.08	0.04
UPU23	-0.04	-0.13	0.04	0.04	-0.03	-0.11
WTMAD-2	-0.65	-0.03	0.19	-0.19	-0.51	0.04
WTMAD-4	-0.39	0.06	0.11	-0.22	-0.26	0.13

Figure 6.6: MAE differences, in kcal/mol, relative to XDM(BJ) results for each GMTKN55 benchmark, with the three new XDM variants. Data is shown only for the two generally best-performing functionals: B86bPBE0 and LC- ω PBE. The red/green colours indicate increases/decreases in the MAE for a particular data set. The WTMAD-2 and WTMAD-4 differences for the entire benchmark are also shown. Thick black lines partition GMTKN55 into its composite categories: (from top to bottom) “Basic + Small”, “Iso + Large”, “Barriers”, “Intermolecular NCI”, and “Intramolecular NCI”.

the ALK8 MAE with Z-damping does not carry over to the WTMAD values, likely due to it providing slightly worse performance for most of the other benchmarks. It would perhaps be desirable to consider a weighted root-mean-square deviation, or some other metric that would reward consistency across the subsets while punishing extreme outliers more harshly in its evaluation.

The largest worsening of performance seen with Z-damping is for the WATER27 set, where the MAD rose by >1 kcal/mol with B86bPBE0, showing increased overbinding relative to BJ-damping. This is partially due to delocalization error in the base functional as WATER27 exhibits cooperative hydrogen bonding, in many cases involving ions; the observed overbinding is consistent with the ICE13 benchmark results in Section 6.5.2 as well. However, worsening performance with Z-damping, relative to BJ-damping, is also seen for WATER27 with LC- ω PBE. Perhaps the $(Z_i + Z_j)$ term appearing in the Z-damping function (Eq. (6.2.27)) is somewhat too weak for hydrogen, and this could be investigated in future work.

In addition to our four XDM variants, we also evaluated the performance of the MBD family of DCs available in FHI-aims (TS, MBD@rsSCS, and MBD-NL), and compare with literature D3(BJ) results [280]. Due to the limited availability of damping parameters, only the PBE and PBE0 DFAs were considered. WTMAD values and per-category breakdowns are provided in Appendix C.5. Qualitatively, the TS method appears to struggle with the Iso+Large category and D3(BJ) with the reaction barriers, while MBD@rsSCS, MBD-NL, XDM, and XCDM are more consistently accurate across all categories. XCDM(BJ) yields the best results of any of the DCs for the GMTKN55, according to both WTMAD-2 and WTMAD-4 metrics.

To this point, we have focused on comparing only the various dispersion corrections, but the overall performance for the GMTKN55 is heavily reliant on the choice the underlying base density functional. The WTMAD-2 and WTMAD-4 results obtained for all nine functionals with the XDM(BJ), XDM(Z), XCDM(BJ), and XCDM(Z) dispersion corrections are collected in Table 6.3. As expected, the GGA functionals show larger errors than the hybrid and range-separated hybrid functionals. B86b exchange generally outperforms PBE exchange, which reinforces our previous conclusion as to the importance of using a dispersionless DFA in combination with post-SCF dispersion corrections [81]. The best performing methods overall are B86bPBE0-XCDM(BJ) and LC- ω PBE-XCDM(Z), with the WTMAD-4 favouring the former and WTMAD-2 favouring the latter, due to its greater weighting of the BH76 set. It is particularly notable that B86bPBE0 consistently achieves the minimum error

Table 6.3: WTMAD-2 and WTMAD-4 results in kcal/mol for the GMTKN55 benchmark with selected functionals and dispersion corrections.

WTMAD-2	XDM(BJ)	XDM(Z)	XCDM(BJ)	XCDM(Z)
PBE	10.40	10.78	10.06	10.70
B86bPBE	9.38	10.00	9.10	9.87
PBE0	6.55	6.96	6.23	6.88
B86bPBE0	5.78	6.43	5.59	6.29
B3LYP	6.27	6.88	5.95	6.76
PBE50	6.06	6.44	5.86	6.37
B86bPBE50	5.67	6.20	5.60	6.11
BHLYP	5.72	6.09	5.60	6.08
LC- ω PBE	5.48	5.51	5.67	5.44

WTMAD-4	XDM(BJ)	XDM(Z)	XCDM(BJ)	XCDM(Z)
PBE	8.99	9.10	8.71	9.05
B86bPBE	8.13	8.52	7.97	8.42
PBE0	6.06	6.12	5.79	6.06
B86bPBE0	5.34	5.73	5.23	5.60
B3LYP	6.12	6.44	5.82	6.37
PBE50	6.92	6.95	6.74	6.90
B86bPBE50	6.50	6.74	6.48	6.66
BHLYP	7.06	7.16	7.08	7.25
LC- ω PBE	5.98	5.92	6.20	5.85

on the MB16-43 “mindless benchmarking” set, yielding MAEs of 13.6–14.0 kcal/mol for all four dispersion corrections considered. For comparison, it has been noted that “MADs for MB16-43 usually exceed 15 kcal/mol for most dispersion-corrected hybrid DFAs [280].” This strongly indicates that the B86bPBE0 functional, in combination with any XDM or XCDM dispersion correction, captures the relevant physics well.

While we recommend the new WTMAD-4 going forward, use of the WTMAD-2 metric allows comparison of the results in Table 6.3 with previous literature [280, 281]. Our results on GMTKN55 show consistently strong performance for both GGA-based global hybrids and range-separated hybrids. While lower WTMAD-2 values can be obtained by functionals with 10 or more fit parameters [280], these have much more complicated functional forms, relying on power-series expansions and either range-separation or meta-GGA ingredients. While fitting no parameters in the base DFAs whatsoever, our results rank 2nd through 6th among all GGA-based global hybrids, surpassed only by revPBE0-D3(BJ)/def2-QZVPP(D), which achieved a WTMAD-2 of 5.43 [281]. Despite being slightly higher, the WTMAD-2 of 5.59

with B86bPBE0-XCDM(BJ)/`tight` is notable for a number of reasons. First, the strong performance of D3(BJ) and D4 on GMTKN55 can be partially attributed to the large overlap between their damping parameterization set (S22, S22+, ACONF, SCONF, PCONF, CCONF, ADIM6, RG6) and GMTKN55 itself, whereas XDM and XCDM are parameterized using the external KB49 set. Second, the `tight` basis set in FHI-aims includes fewer functions than the typical def2-QZVPP(D) basis for this benchmark (thanks to using numerical atom-centred orbitals, rather than Gaussian-type orbitals), yet delivers comparable performance [121]. Finally, the B86bPBE0-XCDM(BJ)/`tight` functional yields results comparable to the best minimally empirical range-separated hybrids: LC- ω hPBE-D3(BJ)/(aug-)def2-QZVP with a WTMAD-2 of 5.56 [280] and, now, LC- ω PBE-XCDM(Z)/aug-cc-pVTZ with a WTMAD-2 of 5.44.

6.5.2 SOLID-STATE BENCHMARKS

While both XCDM and Z-damping appear to be consistently reliable across the GMTKN55, it is crucial to also examine their performance in the solid state. Therefore, we examine the following solid-state benchmarks: the molecular crystal structures of X23, HalCrys4, ICE13-Abs, and ICE13-Rel, as well as the layered materials of LM26. For the molecular crystal structures, tabulated results for XDM(BJ), XDM(Z), XCDM(BJ), and XCDM(Z) using the basis-set correction of Eq. (6.4.1) are presented in Table 6.4.

Conventionally, only results from the largest basis set are reported to avoid confounding variables such as error cancellation. However, as shown in Appendix C.5, the various DCs also perform with exceptional accuracy and consistency for the molecular crystal benchmarks with the `lightdenser` basis setting, rivalling—or even exceeding—the basis-set-corrected results in Table 6.4. In particular, XCDM(BJ) gives MAEs for the X23 set of 0.50–0.65 kcal/mol across all functionals considered. This performance is worth noting, as these benchmarks are indicative of a method’s effectiveness for crystal structure prediction (CSP). In CSP workflows, basis-set corrections are often used only for final energy refinement due to time and computational constraints; in practice, geometry optimizations and preliminary energy ranking typically employ a smaller basis such as `lightdenser`.

Looking at the basis-set corrected data for X23 specifically, we see that XDM(BJ), XCDM(Z), and XDM(Z) performed similarly, while XCDM(BJ) performed slightly better. The signed mean errors (shown in Appendix C.5) reveal that XDM(BJ)

Table 6.4: Mean absolute errors, in kcal/mol, for the X23, HalCrys4, and ICE13 (absolute and relative) lattice-energy benchmarks. All results are shown for `tight` basis settings at `lightdenser` geometries; for the hybrid functionals, this involved the basis-set correction of Eq. (6.4.1).

Functional	X23				HalCrys4				ICE13-Abs				ICE13-Rel			
	XDM		XCDM		XDM		XCDM		XDM		XCDM		XDM		XCDM	
	BJ	Z	BJ	Z	BJ	Z	BJ	Z	BJ	Z	BJ	Z	BJ	Z	BJ	Z
PBE	1.13	0.92	0.63	0.98	5.49	4.12	5.97	4.73	1.44	2.10	1.43	2.13	0.82	0.61	0.83	0.59
B86bPBE	0.70	0.81	0.63	1.20	4.70	5.03	5.66	5.68	1.56	1.88	1.29	1.87	0.52	0.41	0.60	0.40
PBE0	1.00	0.66	0.53	0.74	1.61	0.57	1.99	0.59	0.43	0.50	0.43	0.52	0.48	0.29	0.49	0.29
B86bPBE0	0.48	0.61	0.65	1.19	1.21	0.86	1.84	1.30	0.30	0.36	0.40	0.35	0.31	0.17	0.36	0.17
PBE50	0.87	0.75	0.60	0.79	1.78	3.78	1.19	3.38	1.30	0.69	1.33	0.66	0.21	0.24	0.22	0.25
B86bPBE50	0.51	0.73	0.73	1.24	1.10	3.36	0.87	2.90	1.25	0.73	1.37	0.73	0.18	0.33	0.19	0.34

underbound on average, where XCDM(BJ) and XDM(Z) both shifted the mean error closer to zero. Combining both into XCDM(Z) overcorrected and led to slight overbinding. For the ICE13 and HalCrys4 datasets, hybrid functionals tend to outperform GGAs, due to reduction of delocalization error [161]. ICE13, which involves co-operative hydrogen-bonding networks, and HalCrys4, which involves halogen bonding, are paradigmatic examples of systems affected by this error. While XDM(BJ) and XCDM(BJ) performed equivalently for HalCrys4, we note that Z-damping performed better for 25% hybrids, and worse for 50% hybrids, indicating an interplay between dispersion binding and delocalization error in the base DFA. Also, there was an improvement for the relative ICE13 lattice energies for Z-damping when paired with B86bPBE0 and PBE0, which may be beneficial for polymorph ranking.

The performance of XDM(Z) with the 25% hybrid functionals on all four molecular-crystal benchmarks is notable. There is only slight degradation for X23 and ICE13-Abs relative to BJ-damping, a small improvement for ICE13-Rel, and a large net improvement for HalCrys4 (which contains heavier elements). This performance is impressive considering that one empirical parameter was eliminated from the damping function. To unify our GMTKN55 and molecular-crystal results, we have compiled the WTMAD-4 and the basis-set-corrected solid-state (X23, ICE13, ICE13-Rel, HalCrys4) data for the PBE and B86bPBE GGA functionals, and their 25% and 50% hybrid counterparts Figure 6.7. The results highlight the greater importance of exact-exchange mixing than the choice of dispersion correction. Exactly which XDM variant is the best performing depends on the base functional and benchmark set, but we recommend XDM(Z) as a good general method for both molecular and solid-state applications due to its overall reliability and need for only a single damping parameter.

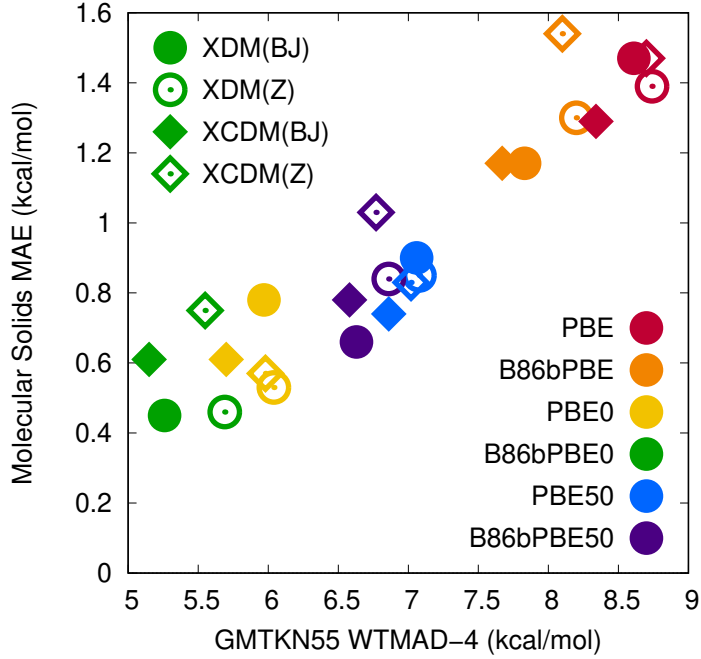


Figure 6.7: A scatter plot showing the GMTKN55 WTMAD-4 values (in kcal/mol) on the x -axis, and the overall mean absolute error (MAEs) for the basis-set-corrected solid-state data from Table 6.4 on the y -axis. XDM is indicated by circles and XCDM by diamonds; solid and hollow shapes denote BJ- and Z-damping respectively. The overall MAE was computed as the mean of all individual reaction errors across all four benchmarks.

Table 6.5: Mean absolute errors, in kcal/mol/cell, for the LM26 benchmark and Tawfik’s subset, LM11, calculated using the `tight` basis set in FHI-aims. Analogous results in meV/ \AA^2 units are given in Table C.16.

Method	B86bPBE		PBE	
	LM11	LM26	LM11	LM26
XDM(BJ)	1.5	2.0	1.3	1.8
XDM(Z)	1.4	2.0	1.0	1.4
XCDM(BJ)	3.6	4.2	3.3	4.0
XCDM(Z)	3.3	4.0	2.5	3.1

Finally, we turn to the layered materials benchmark presented in Table 6.5, where XDM(Z) yields notable improvements over XDM(BJ), consistent with its good behaviour in the GMTKN55 for metal clusters. Unfortunately the XCDM methods exhibit markedly worse performance. Our analysis reveals that XDM slightly overbinds these layered materials, and this error is exacerbated by the dynamical correlation contributions introduced in XCDM. We attribute this to two main factors. First,

XDM relies on a semi-empirical treatment of atom-in-molecule polarizabilities derived via a Hirshfeld partitioning of the electron density. While this approximation is valid for most molecular systems—as evidenced by the excellent performance on MolC6—it tends to overestimate polarizabilities for metals, such as those within the LM26 benchmark. Second, our use of the first scalar moment of the correlation hole to approximate the correlation-hole dipole moment may be much less valid for layered materials and metals than for molecular systems. As illustrated in Figure C.1 for the case of the BR exchange hole, this approximation is exact in the exponentially decaying density tails far from atoms or molecules, but is poorer in bonding regions, which will account for far more of the integration grid points in inorganic solids. A final (but likely lesser) factor is that the canonical implementation of the XDM method neglects the Axilrod–Teller–Muto (ATM) three-body dispersion term [276, 277]. This omission was intentional due to the ATM term contributing negligibly to the dispersion binding of intermolecular complexes when combined with XDM, coupled with the added computational complexity of summing over atomic trimers [80, 91]. However, the ATM term is known to be repulsive for equilateral and right-angle atom configurations, while maximally attractive in linear arrangements [276]. Perhaps neglect of dynamical correlation and use of approximate atomic polarizabilities previously offset the missing repulsion from the ATM term for these layered materials.

6.6 SUMMARY

This chapter improves the dispersion physics of the XDM model, introducing new variants that include dynamical correlation effects and address previous overbinding of metal clusters. It is also the first to test the XDM (and MBD) methods for the GMTKN55 data set, enabling a direct, head-to-head comparison of the most widely-used dispersion corrections on a comprehensive benchmark for general main-group thermochemistry, kinetics, and non-covalent interactions. Additionally, we identified unintended behaviour in previous WTMAD weighting schemes and have introduced WTMAD-4 to ensure each benchmark within GMTKN55 is treated fairly.

XDM and its variants performed extremely well for molecular systems, with the results typically being more sensitive to the choice of base functional than dispersion correction. B86bPBE0 is generally the best exchange-correlation functional among those tested and, despite its simplicity, gives WTMAD values on par with the best minimally empirical global and range-separated hybrids in the literature [280, 281]

when paired with any of our XDM variants. We attribute the exceptional performance of B86bPBE0 to its adherence to known physical limits [81].

Comparing the dispersion corrections, the canonical XDM(BJ) method showed strong results in all cases with the exception of the ALK8 benchmark, which originally motivated the study into Z-damping. XDM(Z) completely resolved this error and, despite eliminating one empirical parameter, it still performed on par with other leading dispersion corrections on GMTKN55. Notably, it yielded our third lowest WTMAD-2 when paired with LC- ω PBE. The inclusion of dynamical correlation effects in XCDM eliminated the systematic underestimation of molecular dispersion coefficients, giving improved agreement with available reference data. Consequently, XCDM(BJ) was the most accurate dispersion method tested for molecular systems, providing the lowest WTMAD values when paired with most DFAs considered. However, its drawback is its poor performance on the layered-material benchmark, LM26, which we attribute to the semi-empirical treatment of XDM polarizabilities and overestimation of the correlation-hole dipole contributions, causing inflated dispersion coefficients for metals, and possibly to the omission of the Axilrod–Teller–Muto (ATM) three-body term. In contrast, XDM(Z) was consistently accurate for all solid-state benchmarks, including LM26 and LM11. It may be an example of a Pauling point [523] for the XDM methods, rarely the best but consistently reliable across the widest range of systems. With only one fit parameter, B86bPBE0-XDM(Z) is an excellent choice for a simple, minimally empirical density functional.

CHAPTER 7

CONCLUSIONS

“One never notices what has been done; one can only see what remains to be done.” [546]
~ Prof. Marie Curie (1867–1934)

The work presented in this thesis establishes the exchange-hole dipole moment (XDM) model as a leading approach to modelling dispersion interactions within density-functional theory (DFT). This model has demonstrated its ability to capture the physics of London dispersion, to deliver best-in-class energies across many diverse systems, and has a stable implementation that avoids crashes that affect some competing methods. In addition, new, physics-guided implementations of XDM were introduced, incorporating the missing contributions from dynamical correlation (XCDM), and reducing empiricism by using a one-parameter damping function based on atomic numbers that uses only one tunable parameter. These developments were rigorously tested and implemented in open-source software.

7.1 DISSERTATION SUMMARY

The dissertation began in Chapter 1 with a historical and qualitative overview of dispersion in density-functional theory, tracing how the early ideas of van der Waals and London were incorporated into the pioneering work of Hohenberg, Kohn, and Sham over half a century ago. Dispersion was introduced through the principles of second-order perturbation theory, and the equations of Eisenshitz and London were

derived from first principles. Early empirical dispersion corrections of Cohen, Pack, and Scoles were discussed, followed by an overview of modern dispersion methods developed by Grimme; Tkatchenko and Scheffler; and Johnson and Becke.

The second chapter focuses on the theory that supports and provides the framework for the thesis. Chapter 2 begins by outlining the mathematics of Kohn–Sham DFT, introducing the concepts of quantum mechanical exchange and correlation, and describing the self-consistent field (SCF) process. A detailed discussion of Perdew’s ladder of density functional approximations (DFA) to the exchange-correlation energy follows. Here, we discuss Hartree–Fock, the local-density approximation (LDA), generalized-gradient approximations (GGAs), meta-GGAs, various types of hybrid functionals, and post-Kohn–Sham correlation methods such as random-phase approximations and double-hybrid functionals. Methods beyond DFT are also presented, including Møller–Plesset perturbation theory (MP2), coupled-cluster theory (CC), and diffusion Monte Carlo (DMC), discussed in the context of their use as reference data for benchmarking DFT techniques in both molecular systems and the solid state. The section continues by exploring the application of DFT to periodic solids, detailing crystal lattice structures, \mathbf{k} -space, plane waves, and the Brillouin zone. Techniques that make periodic DFT calculations practical—such as the use of atomic pseudopotentials, the projector-augmented wave (PAW) method, and numerical atom-centred orbitals (NAOs)—are discussed, along with the nomenclature of commonly used basis sets in the literature. The mathematical treatment of forces, stresses, strains, and deformations is also presented. The mathematical frameworks of popular post-SCF dispersion corrections are presented in full, including the Grimme-D series (D1, D2, D3(0), D3(BJ), and D4); Tkatchenko’s many-body dispersion methods (TS, TS@SCS, MBD, MBD@rsSCS, and MBD-NL); and the exchange-hole dipole moment (XDM) model of Becke and Johnson. Finally, the chapter closes with a discussion of delocalization error.

To lay the groundwork for the development of more accurate dispersion corrections, a comprehensive understanding of what is being corrected (i.e., the base density functional) is required. This challenge is compounded by the fact that, over the past few decades, hundreds of density functional approximations have been developed. This has earned the current state of development the nickname “density-functional zoo” among many in the field. Chapter 3 discusses the role of the base density functional in the context of dispersion-corrected (DC) DFT. The requirements for

ensuring that the base functional and dispersion correction are individually as accurate as possible in their respective treatments of non-bonded repulsion and dispersion attraction were presented. We showed why the base functional should be dispersionless, numerically stable, and involve minimal delocalization error. For the dispersion correction, we explained that it should be damped to a finite quantity at small internuclear separations, account for higher-order contributions such as quadrupole and octupole effects, and that dispersion coefficients should dynamically respond to changing chemical environments via electronic many-body effects. However, capturing many-body effects complicates the form of the dispersion coefficients, which necessarily become non-constant. To calculate the dispersion forces and stresses, derivatives of these coefficients must be taken. Presently, all post-SCF dispersion corrections assume these are constant in order to simplify the expressions. This assumption was shown to break down, leading to false minima in geometry optimizations and variable-cell relaxations, especially for ionic and network solids. We posit that the development of dispersion corrections and density functionals is best guided through physics-based approaches, with the goal of achieving accurate, minimally empirical DC-DFT that does not rely on error cancellation. B86bPBE-XDM was presented as a minimally-empirical method that adheres to these principles.

Now that the requirements for accurate dispersion-corrected DFT have been established, and a suitable DFA to pair with XDM has been proposed, we wanted to deepen the investigation into the dispersion correction itself. Recent literature has highlighted the importance of many-body effects in dispersion and raised questions as to which corrections accurately capture them. Chapter 4 responds to these questions, and a model system of variationally-optimized quantum harmonic oscillators is constructed to study electronic and atomic many-body effects. The XDM, Tkatchenko–Scheffler (TS), and many-body dispersion (MBD) corrections were applied to this model system, with leading-order atomic three-body contributions calculated explicitly via both Axilrod–Teller–Muto (ATM) and random-phase approximation (RPA) techniques. These two techniques agreed on the amount of three-body dispersion energy, while also showing that this contribution was negligible relative to the total dispersion energy. Further, the undamped TS and MBD energies closely followed the C_6 -only contribution to the XDM energy, implying that MBD did not capture significant atomic many-body effects for this system, nor did it capture higher-order quadrupolar or octupolar contributions. Next, the dispersion coefficients themselves were considered for the model oscillator systems, argon chains, and noble gas dimers He_2 through Xe_2 . Here, we observed the “polarization catastrophe” that plagues the

MBD methods, where the behaviour of the C_6 coefficients at compressed geometries becomes erratic, and at even shorter separations, the MBD dispersion energy becomes complex-valued. To address these polarization issues, we tested MBD-Free and MBD-XDM, which use free-atom and XDM starting points, respectively, for the range-separated SCS method. Unfortunately, neither starting point resolved these issues, which were present in both cases. In contrast, the XDM model behaves consistently across these systems. Finally, we studied benchmarks of molecular dimers and layered materials, and included the new MBD-NL variant that uses a semi-local polarizability functional in place of SCS. Overall, TS overbound across all systems, MBD crashed due to polarization catastrophes in layered materials, and XDM and MBD-NL performed similarly well. Clearly, XDM proved its ability to consistently capture electronic many-body effects, while atomic many-body effects were negligible in these model systems. Further, XDM displayed high accuracy and stability across all systems considered.

Chapter 5 presents the first-ever head-to-head comparison of leading post-SCF dispersion corrections using the same code and basis set, including Becke and Johnson’s XDM; Tkatchenko’s TS, MBD, and MBD-NL; and Grimme’s D3(BJ) and D4 corrections. The selected benchmark for this comparison was DES15K, which contains an impressive 14,651 noncovalently bonded, small molecular complexes. The scope of this benchmark is broad, covering dispersion, hydrogen bonding, ion–molecule, and ion–ion intermolecular interactions across compressed and expanded geometries. The electronic-structure code used for this study was the Fritz Haber Institute *ab initio* materials simulation (FHI-aims) program. Calculations employed the well-converged **tight** numerical atom-centred orbital (NAO) all-electron basis set, and PBE0 and B86bPBE0 hybrid functionals. For neutral and ionic complexes without metal ions, all methods, with the exception of TS, performed similarly. The analysis of outliers proved especially revealing, showing how MBD and MBD-NL significantly overbound complexes of organic molecules with alkali cations and alkaline earth dications, particularly at compressed geometries. This issue was traced not to polarization catastrophes, but rather to the dispersion energy evaluation itself, likely due to their weak damping functions. Ultimately, B86bPBE0-XDM delivered best-in-class performance, followed by PBE0-XDM. These results reinforce and validate the physics-guided principles outlined in the previous two chapters.

The preceding chapters establish XDM as a leading post-SCF dispersion correction, notable not only for its accuracy and stability, but also its ability to correctly

capture the intricate physics of London dispersion. This forms a solid foundation for further development. Chapter 6 introduces a new physics-guided variant, the exchange-correlation dipole moment (XCDM) model, which supplements the XDM exchange-hole dipole moment with missing contributions from same- and opposite-spin dynamical correlation holes. We show that this inclusion all but eliminates XDM’s systematic 15-20% underestimation of molecular C_6 dispersion coefficients. We also studied Z-damping, a one-parameter damping function based on atomic numbers, recently proposed by Becke to address overbinding in Li_8 and Na_8 clusters observed with Becke–Johnson (BJ) damping. XCDM and Z-damping were implemented in both FHI-aims and postg, and comprehensively tested for molecular and solid-state systems. For molecular systems, we used the GMTKN55 benchmark of general main-group thermochemistry, kinetics, and non-covalent interactions, and compared to the D3, TS, MBD, and MBD-NL dispersion corrections. Notably, this marks the first time that either XDM or MBD has been tested for GMTKN55. Z-damping resolved the issues seen with alkali metal clusters, and pairs well with the LC- ω PBE functional for both XDM and XCDM. Meanwhile, XCDM(BJ) was the most accurate dispersion method tested on GMTKN55, providing the lowest weighted mean absolute deviation (WTMAD) values when paired with most of the DFAs considered in the study. We also identified unintended behaviour in previous WTMAD weighting schemes and introduced the WTMAD-4, which is a new scheme based on relative errors seen for typical, minimally-empirical functionals to ensure each benchmark within GMTKN55 is treated fairly. For the solid state, we examined the performance of XCDM and Z-damping on five benchmarks consisting of molecular crystals and layered materials. When paired with the `lightdenser` basis, XCDM(BJ) performed accurately and consistently for molecular-crystal benchmarks, rivalling or even exceeding the basis-set-corrected results. This performance suggests a possible use-case for XCDM(BJ) in crystal structure prediction (CSP), where preliminary energy rankings typically employ a smaller basis such as `lightdenser` and basis-set corrections are only used for final refinement. However, XCDM(BJ)’s drawback is its poor performance for layered materials, which we attribute to the semi-empirical treatment of polarizabilities. Finally, XDM(Z) may represent a Pauling point for the XDM methods: while it is rarely the most accurate, it is consistently reliable across all systems. With only one fit parameter, B86bPBE0-XDM(Z) is an excellent choice for a simple, reliable, minimally empirical density functional.

7.2 FUTURE WORK

There are a number of avenues that could be explored to continue the development of the XDM methods.

7.2.1 IMPROVEMENT OF DISPERSION FORCES IN XDM

The current implementations of post-SCF dispersion forces, including XDM, assume that the dispersion coefficients are constant with respect to changing atomic positions and lattice vectors. While this assumption is reasonable for most systems, we showed in Chapter 3 that it can cause dispersion corrections to converge to false minima during geometry optimizations and variable-cell relaxations, particularly for ionic or network solids. XDM is disproportionately affected by this assumption compared to other dispersion corrections due to typically having steeper gradients in its dispersion coefficients near equilibrium geometries. This poor assumption also results in force–energy inconsistencies that prevent accurate dispersion treatment in molecular dynamics. The underlying mathematics for this correction to the XDM dispersion forces has already been developed (see Appendix B.3); however, its implementation hinges on access to the derivatives of the Hirshfeld weights. Unfortunately, none of the codes in which XDM is currently available contain a working implementation of these requisite Hirshfeld weight derivatives.

7.2.2 CONTINUED DEVELOPMENT OF XDM AND XCDM

XDM’s largest remaining source of empiricism comes from its semi-empirical treatment of atom-in-molecule polarizabilities. Unfortunately, this is also one of the largest sources of error, causing an overprediction of dispersion coefficients for metals and leading to overbinding. As shown in Chapter 6, this issue was compounded when the exchange-hole dipole moment was supplemented with contributions from same- and opposite-spin correlation functionals. One potential solution would be to adopt the approach used in MBD-NL: employing a polarizability functional (such as VV10’s) alongside local electron-density descriptors to correct errors in XDM’s polarizability.

XCDM’s poor performance on layered materials is partially explained by its semi-empirical polarizabilities, but this is unlikely the full story. Certainly, while the transition-metal species in LM26 likely suffer from polarizability-related issues, this does not explain the decreased performance and overbinding observed for graphite. In

fact, the MolC6 benchmark is heavily weighted towards systems that contain carbon, where XCDM successfully eliminated the systematic underestimation of C_6 coefficients. This suggests that there could be an additional interlayer energy contribution that is not explained by the C_6 coefficients themselves. One plausible source could be the neglected Axilrod–Teller–Muto three-body dispersion term. This term is known to be attractive for linear configurations, but repulsive in right- and equilateral-triangle configurations. In principle, this term would cause a slight increase the equilibrium layer separation and reduce the interlayer binding energy.

Regarding the Z-damping function, while a slight worsening of performance was observed, this is not unexpected given it has one fewer tunable parameter. However, examination of outliers revealed that the largest error increase was for the WATER27 set. When paired with B86bPBE0, the MAD increased by over 1 kcal/mol compared to BJ-damping. Although this may partly stem from delocalization error in the base density functional, the issue persisted (albeit, to a lesser degree) with LC- ω PBE, which is expected to perform well for these systems. Further investigation revealed that systems with numerous hydrogen atoms exhibited larger changes in dispersion energy relative to BJ-damping. Perhaps the $(Z_i + Z_j)$ term appearing in the Z-damping function is too weak for very light nuclei such as hydrogen, and this should be investigated.

7.2.3 EXPANDED XDM AND XCDM IMPLEMENTATION

As mentioned in Chapter 1, the current state of XDM implementation is as follows:

“XDM has been implemented in several codes: Quantum ESPRESSO [56, 99, 111], CASTEP [112], Q-Chem [113, 114], NWChem [115, 116], SIESTA [117, 118], and recently FHI-aims [119–121]. Also, work is ongoing to implement XDM in AMS (ADF) [122] by A. F. Rumson and E. R. Johnson. Further, XDM can be applied *ad hoc* for any quantum-chemical code that writes `.molden`, `.wfn`, or `.wfx` files via `postg` [123], maintained by Alberto Otero-de-la-Roza and recently updated [124] to incorporate new features introduced in this thesis. Dozens of codes support the `.molden` format [125], with popular examples including Gaussian [126], ORCA [127], TURBOMOL [128], Psi4 [129], PySCF [130], Q-Chem [113, 114], NWChem [115, 116], XTB [131], and AMS (ADF) [122].”

As of the time of writing, XCDM and Z-damping are currently only implemented

in postg and FHI-aims. It would be beneficial to port these features to the other codes that already support XDM to improve accessibility for the community. While postg technically broadens the range of codes that support XDM, it also creates a barrier by requiring users to rely on an external tool. Ideally, XDM and XC_{DM} would be natively supported by popular codes such as VASP, ORCA, and Gaussian. However, this is a lower priority (unless requested) until further theoretical developments to XDM and XC_{DM} are complete.

Lastly, to further improve accessibility, the number of supported functionals could be expanded to include most or all of LibXC [547]. Although fitting XDM to hundreds of functionals across various basis sets would be a significant undertaking from high-throughput and data management perspectives, the KB49 benchmark consists of small molecular dimers and, therefore, would not require prohibitive CPU time.

BIBLIOGRAPHY

1. Rioux, F. *Quantum Tutorials: Section 1.55 - Using a Mach-Zehnder Interferometer to Illustrate Feynman's Sum Over Histories Approach to Quantum Mechanics* [Accessed 2025-06-12]. 2023. <https://chem.libretexts.org/@go/page/5119> (p. 1).
2. Hylleraas, E. A. Über den grundzustand des heliumatoms. *Z. Angew. Phys.* **48**, 469–494. doi:[10.1007/BF01340013](https://doi.org/10.1007/BF01340013) (1928) (p. 1).
3. Hylleraas, E. A. Neue berechnung der energie des heliums im grundzustande, sowie des tiefsten terms von ortho-helium. *Z. Angew. Phys.* **54**, 347–366. doi:[10.1007/BF01375457](https://doi.org/10.1007/BF01375457) (1929) (p. 1).
4. Fulde, P. Wavefunction methods in electronic-structure theory of solids. *Adv. Phys.* **51**, 909–948. doi:[10.1080/00018730110116371](https://doi.org/10.1080/00018730110116371) (2002) (p. 1).
5. Grüneis, A., Hirata, S., Ohnishi, Y.-y. & Ten-No, S. Perspective: Explicitly correlated electronic structure theory for complex systems. *J. Chem. Phys.* **146**, 080901. doi:[10.1063/1.4976974](https://doi.org/10.1063/1.4976974) (2017) (p. 1).
6. Hartree, D. R. *The wave mechanics of an atom with a non-coulomb central field. Part II. Some results and discussion in Math. Proc. Cambridge Philos. Soc.* **24** (1928), 111–132. doi:[10.1017/S0305004100011920](https://doi.org/10.1017/S0305004100011920) (p. 1, 15).
7. Fock, V. “Selfconsistent field” mit Austausch für Natrium. *Z. Angew. Phys.* **62**, 795–805. doi:[10.1007/BF01330439](https://doi.org/10.1007/BF01330439) (1930) (p. 1, 15).
8. Hartree, D. R. & Hartree, W. Self-consistent field, with exchange, for beryllium. *Proc. R. Soc. London, Ser. A* **150**, 9–33. doi:[10.1098/rspa.1935.0085](https://doi.org/10.1098/rspa.1935.0085) (1935) (p. 1, 15).
9. Hartree, D. R. & Hartree, W. Self-consistent field with exchange for potassium and argon. *Proc. R. Soc. London, Ser. A* **166**, 450–464. doi:[10.1098/rspa.1938.0103](https://doi.org/10.1098/rspa.1938.0103) (1938) (p. 1, 15).
10. Hartree, D. R. & Hartree, W. Self-consistent field, with exchange, for nitrogen and sodium. *Proc. R. Soc. London, Ser. A* **193**, 299–304. doi:[10.1098/rspa.1948.0047](https://doi.org/10.1098/rspa.1948.0047) (1948) (p. 1, 15).
11. Slater, J. C. A simplification of the Hartree-Fock method. *Phys. Rev.* **81**, 385. doi:[10.1103/PhysRev.81.385](https://doi.org/10.1103/PhysRev.81.385) (1951) (p. 1, 15).
12. Hohenberg, P. & Kohn, W. Inhomogeneous electron gas. *Phys. Rev.* **136**, B864. doi:[10.1103/PhysRev.136.B864](https://doi.org/10.1103/PhysRev.136.B864) (1964) (p. 1–2, 12).
13. Kohn, W. & Sham, L. J. Self-consistent equations including exchange and correlation effects. *Phys. Rev.* **140**, A1133. doi:[10.1103/PhysRev.140.A1133](https://doi.org/10.1103/PhysRev.140.A1133) (1965) (p. 1–2, 12, 16, 18, 60).
14. Burke, K. Perspective on density functional theory. *J. Chem. Phys.* **136**, 150901. doi:[10.1063/1.4704546](https://doi.org/10.1063/1.4704546) (2012) (p. 2, 61).

15. Becke, A. D. Perspective: Fifty years of density-functional theory in chemical physics. *J. Chem. Phys.* **140**, 18A301. doi:[10.1063/1.4869598](https://doi.org/10.1063/1.4869598) (2014) (p. 2, 14, 16).
16. Becke, A. D. & Roussel, M. R. Exchange holes in inhomogeneous systems: A coordinate-space model. *Phys. Rev. A* **39**, 3761. doi:[10.1103/PhysRevA.39.3761](https://doi.org/10.1103/PhysRevA.39.3761) (1989) (p. 2, 18, 57–58, 63–64, 129, 131, 223).
17. LaPointe, S. M. & Weaver, D. F. A review of density functional theory quantum mechanics as applied to pharmaceutically relevant systems. *Curr. Comput.-Aided Drug Des.* **3**, 290–296. doi:[10.2174/157340907782799390](https://doi.org/10.2174/157340907782799390) (2007) (p. 2).
18. Tandon, H., Chakraborty, T. & Suhag, V. A brief review on importance of DFT in drug design. *Res. Med. Eng. Sci.* **39**, 46. doi:[10.31031/RMES.2019.07.000668](https://doi.org/10.31031/RMES.2019.07.000668) (2019) (p. 2).
19. Weijing, D., Weihong, Z., Xiaodong, Z., Baofeng, Z., Lei, C., Laizhi, S., Shuangxia, Y., Haibin, G., Guanyi, C., Liang, Z., *et al.* The application of DFT in catalysis and adsorption reaction system. *Energy Procedia* **152**, 997–1002. doi:[10.1016/j.egypro.2018.09.106](https://doi.org/10.1016/j.egypro.2018.09.106) (2018) (p. 2).
20. Chen, Z., Chen, L., Wen, Z. & Jiang, Q. Understanding electro-catalysis by using density functional theory. *Phys. Chem. Chem. Phys.* **21**, 23782–23802. doi:[10.1039/C9CP04430B](https://doi.org/10.1039/C9CP04430B) (2019) (p. 2).
21. Neugebauer, J. & Hickel, T. Density functional theory in materials science. *Wiley Interdiscip. Rev.: Comput. Mol. Sci.* **3**, 438–448. doi:[10.1002/wcms.1125](https://doi.org/10.1002/wcms.1125) (2013) (p. 2).
22. van der Waals, J. D. On the continuity of the gas and liquid state. *Leiden University, Leiden, Netherlands*, 301 (1873) (p. 2).
23. London, F. On the theory and systematics of molecular forces. *Z. Phys.* **63**, 245–279. doi:[10.1007/BF01421741](https://doi.org/10.1007/BF01421741) (1930) (p. 2, 47).
24. London, F. The general theory of molecular forces. *Trans. Faraday Soc.* **33**, 8b–26. doi:[10.1039/TF937330008B](https://doi.org/10.1039/TF937330008B) (1937) (p. 2).
25. Debye, P. Van der Waals cohesion forces. *Phys. Z.* **21**, 178–187 (1920) (p. 2).
26. Debye, P. Molecular forces and their electrical interpretation. *Phys. Z.* **22**, 302–308 (1921) (p. 2).
27. Keesom, W. H. The second viral coefficient for rigid spherical molecules, whose mutual attraction is equivalent to that of a quadruplet placed at their centre. *Proc. R. Acad. Sci.* **18**, 636–646 (1915) (p. 2).
28. Keesom, W. H. The quadrupole moments of the oxygen and nitrogen molecules. *Proc. R. Acad. Sci.* **23**, 939–942 (1921) (p. 2).
29. Keesom, W. H. Van der Waals attractive force. *Phys. Z.* **22**, 129–141 (1921) (p. 2).
30. Keesom, W. H. Van der Waals attractive force. *Phys. Z.* **22**, 643–644 (1921) (p. 2).

31. Autumn, K., Sitti, M., Liang, Y. A., Peattie, A. M., Hansen, W. R., Sponberg, S., Kenny, T. W., Fearing, R., Israelachvili, J. N. & Full, R. J. Evidence for van der Waals adhesion in gecko setae. *Proc. Natl. Acad. Sci.* **99**, 12252–12256. doi:[10.1073/pnas.192252799](https://doi.org/10.1073/pnas.192252799) (2002) (p. 2).
32. Lessel, M., Loskill, P., Hausen, F., Gosvami, N. N., Bennewitz, R. & Jacobs, K. Impact of van der Waals interactions on single asperity friction. *Phys. Rev. Lett.* **111**, 035502. doi:[10.1103/PhysRevLett.111.035502](https://doi.org/10.1103/PhysRevLett.111.035502) (2013) (p. 2).
33. Liu, W., Tkatchenko, A. & Scheffler, M. Modeling adsorption and reactions of organic molecules at metal surfaces. *Acc. Chem. Res.* **47**, 3369–3377. doi:[10.1021/ar500118y](https://doi.org/10.1021/ar500118y) (2014) (p. 2).
34. Micoulaut, M., Piarristeguy, A., Flores-Ruiz, H. & Pradel, A. Towards accurate models for amorphous GeTe: Crucial effect of dispersive van der Waals corrections on the structural properties involved in the phase-change mechanism. *Phys. Rev. B* **96**, 184204. doi:[10.1103/PhysRevB.96.184204](https://doi.org/10.1103/PhysRevB.96.184204) (2017) (p. 2).
35. Risthaus, T. & Grimme, S. Benchmarking of London dispersion-accounting density functional theory methods on very large molecular complexes. *J. Chem. Theory Comput.* **9**, 1580–1591. doi:[10.1021/ct301081n](https://doi.org/10.1021/ct301081n) (2013) (p. 2, 46, 79).
36. Moellmann, J. & Grimme, S. Importance of London dispersion effects for the packing of molecular crystals: a case study for intramolecular stacking in a bis-thiophene derivative. *Phys. Chem. Chem. Phys.* **12**, 8500–8504. doi:[10.1039/c003432k](https://doi.org/10.1039/c003432k) (2010) (p. 2).
37. Kolář, M., Kubař, T. & Hobza, P. On the role of London dispersion forces in biomolecular structure determination. *J. Phys. Chem. B* **115**, 8038–8046. doi:[10.1021/jp202878d](https://doi.org/10.1021/jp202878d) (2011) (p. 2).
38. Tawfik, S. A., Gould, T., Stampfl, C. & Ford, M. J. Evaluation of van der Waals density functionals for layered materials. *Phys. Rev. Mater.* **2**, 034005. doi:[10.1103/PhysRevMaterials.2.034005](https://doi.org/10.1103/PhysRevMaterials.2.034005) (2018) (p. 2, 109–110, 126, 141).
39. Grimme, S. Accurate description of van der Waals complexes by density functional theory including empirical corrections. *J. Comput. Chem.* **25**, 1463–1473. doi:[10.1002/jcc.20078](https://doi.org/10.1002/jcc.20078) (2004) (p. 2, 7, 40, 79).
40. Grimme, S. Semiempirical GGA-type density functional constructed with a long-range dispersion correction. *J. Comput. Chem.* **27**, 1787–1799. doi:[10.1002/jcc.20495](https://doi.org/10.1002/jcc.20495) (2006) (p. 2, 8, 41, 76, 79, 83).
41. Grimme, S., Antony, J., Ehrlich, S. & Krieg, H. A consistent and accurate ab initio parametrization of density functional dispersion correction (DFT-D) for the 94 elements H-Pu. *J. Chem. Phys.* **132**, 154104. doi:[10.1063/1.3382344](https://doi.org/10.1063/1.3382344) (2010) (p. 2, 8, 41–42, 76, 79, 81–82, 115, 126).

42. Caldeweyher, E., Ehlert, S., Hansen, A., Neugebauer, H., Spicher, S., Banwarth, C. & Grimme, S. A generally applicable atomic-charge dependent London dispersion correction. *J. Chem. Phys.* **150**, 154122. doi:[10.1063/1.5090222](https://doi.org/10.1063/1.5090222) (2019) (p. 2, 8, 44, 82, 115, 126).
43. Caldeweyher, E., Mewes, J.-M., Ehlert, S. & Grimme, S. Extension and evaluation of the D4 London-dispersion model for periodic systems. *Phys. Chem. Chem. Phys.* **22**, 8499–8512. doi:[10.1039/D0CP00502A](https://doi.org/10.1039/D0CP00502A) (2020) (p. 2, 44, 82).
44. Tkatchenko, A. & Scheffler, M. Accurate molecular van der Waals interactions from ground-state electron density and free-atom reference data. *Phys. Rev. Lett.* **102**, 073005. doi:[10.1103/PhysRevLett.102.073005](https://doi.org/10.1103/PhysRevLett.102.073005) (2009) (p. 2, 4, 8, 44–46, 50, 76, 79, 81–83, 90, 115, 126).
45. Tkatchenko, A., DiStasio Jr, R. A., Car, R. & Scheffler, M. Accurate and efficient method for many-body van der Waals interactions. *Phys. Rev. Lett.* **108**, 236402. doi:[10.1103/PhysRevLett.108.236402](https://doi.org/10.1103/PhysRevLett.108.236402) (2012) (p. 2, 8, 21, 44, 48, 50, 81, 89, 115, 126).
46. Ambrosetti, A., Reilly, A. M., DiStasio Jr, R. A. & Tkatchenko, A. Long-range correlation energy calculated from coupled atomic response functions. *J. Chem. Phys.* **140**, 18A508. doi:[10.1063/1.4865104](https://doi.org/10.1063/1.4865104) (2014) (p. 2, 8, 21, 45, 50, 89, 105, 115, 126).
47. Ambrosetti, A., Alfè, D., DiStasio Jr, R. A. & Tkatchenko, A. Hard numbers for large molecules: Toward exact energetics for supramolecular systems. *J. Phys. Chem. Lett.* **5**, 849–855. doi:[10.1021/jz402663k](https://doi.org/10.1021/jz402663k) (2014) (p. 2, 8, 21, 50, 89).
48. DiStasio, R. A., Gobre, V. V. & Tkatchenko, A. Many-body van der Waals interactions in molecules and condensed matter. *J. Phys.: Condens. Matter* **26**, 213202. doi:[10.1088/0953-8984/26/21/213202](https://doi.org/10.1088/0953-8984/26/21/213202) (2014) (p. 2, 8, 21, 44–45, 47, 49, 51, 105).
49. Ruiz, V. G., Liu, W. & Tkatchenko, A. Density-functional theory with screened van der Waals interactions applied to atomic and molecular adsorbates on close-packed and non-close-packed surfaces. *Phys. Rev. B* **93**, 035118. doi:[10.1103/PhysRevB.93.035118](https://doi.org/10.1103/PhysRevB.93.035118) (2016) (p. 2).
50. Gould, T., Lebegue, S., Ángyán, J. G. & Tomáš, B. A fractionally ionic approach to polarizability and van der Waals many-body dispersion calculations. *J. Chem. Theory Comput.* **12**, 5920–5930. doi:[10.1021/acs.jctc.6b00925](https://doi.org/10.1021/acs.jctc.6b00925) (2016) (p. 2, 44, 51, 108, 127).
51. Kim, M., Kim, W. J., Gould, T., Lee, E. K., Lebegue, S. & Kim, H. uMBD: A Materials-Ready Dispersion Correction That Uniformly Treats Metallic, Ionic, and van der Waals Bonding. *J. Am. Chem. Soc.* **142**, 2346–2354. doi:[10.1021/jacs.9b11589](https://doi.org/10.1021/jacs.9b11589) (2020) (p. 2, 46).

52. Hermann, J. & Tkatchenko, A. Density functional model for van der Waals interactions: unifying many-body atomic approaches with nonlocal functionals. *Phys. Rev. Lett.* **124**, 146401. doi:[10.1103/PhysRevLett.124.146401](https://doi.org/10.1103/PhysRevLett.124.146401) (2020) (p. 2, 8, 51–52, 105, 107–108, 115, 126).
53. Becke, A. D. & Johnson, E. R. Exchange-hole dipole moment and the dispersion interaction. *J. Chem. Phys.* **122**, 154104. doi:[10.1063/1.1884601](https://doi.org/10.1063/1.1884601) (2005) (p. 2, 53, 56).
54. Becke, A. D. & Johnson, E. R. Exchange-hole dipole moment and the dispersion interaction: High-order dispersion coefficients. *J. Chem. Phys.* **124**, 014104. doi:[10.1063/1.2139668](https://doi.org/10.1063/1.2139668) (2006) (p. 2, 53, 56, 58).
55. Becke, A. D. & Johnson, E. R. Exchange-hole dipole moment and the dispersion interaction revisited. *J. Chem. Phys.* **127**, 154108. doi:[10.1063/1.2795701](https://doi.org/10.1063/1.2795701) (2007) (p. 2, 8, 18, 53–54, 89, 110, 115, 126, 129).
56. Otero-de-la-Roza, A. & Johnson, E. R. Van der Waals interactions in solids using the exchange-hole dipole moment model. *J. Chem. Phys.* **136**, 174109. doi:[10.1063/1.4705760](https://doi.org/10.1063/1.4705760) (2012) (p. 2, 8, 18, 53–54, 57, 59, 83–84, 89, 116, 121, 160).
57. Johnson, E. R. *The Exchange-Hole Dipole Moment Dispersion Model in Non-covalent Interactions in Quantum Chemistry and Physics: Theory and Applications* Edited by A. Otero-de-la-Roza and G. A. DiLabio, 169–194 (Elsevier, 2017). doi:[10.1016/C2015-0-06383-3](https://doi.org/10.1016/C2015-0-06383-3) (p. 2, 5, 8, 18, 53–54, 56, 59, 69, 71, 73, 79, 81, 83, 85, 89, 115, 126).
58. Andersson, Y., Langreth, D. & Lundqvist, B. van der Waals Interactions in Density-Functional Theory. *Phys. Rev. Lett.* **76**, 102. doi:[10.1103/PhysRevLett.76.102](https://doi.org/10.1103/PhysRevLett.76.102) (1996) (p. 2).
59. Dion, M., Rydberg, H., Schröder, E., Langreth, D. C. & Lundqvist, B. I. Van der Waals density functional for general geometries. *Phys. Rev. Lett.* **92**, 246401. doi:[10.1103/PhysRevLett.92.246401](https://doi.org/10.1103/PhysRevLett.92.246401) (2004) (p. 2).
60. Dion, M., Rydberg, H., Schröder, E., Langreth, D. C. & Lundqvist, B. I. Erratum: Van der Waals density functional for general geometries [Phys. Rev. Lett. 92, 246401 (2004)]. *Phys. Rev. Lett.* **95**, 109902. doi:[10.1103/PhysRevLett.95.109902](https://doi.org/10.1103/PhysRevLett.95.109902) (2005) (p. 2).
61. Román-Pérez, G. & Soler, J. M. Efficient implementation of a van der Waals density functional: application to double-wall carbon nanotubes. *Phys. Rev. Lett.* **103**, 096102. doi:[10.1103/PhysRevLett.103.096102](https://doi.org/10.1103/PhysRevLett.103.096102) (2009) (p. 2).
62. Lee, K., Murray, É. D., Kong, L., Lundqvist, B. I. & Langreth, D. C. Higher-accuracy van der Waals density functional. *Phys. Rev. B* **82**, 081101. doi:[10.1103/PhysRevB.82.081101](https://doi.org/10.1103/PhysRevB.82.081101) (2010) (p. 2, 71).
63. Vydrov, O. A. & Van Voorhis, T. Nonlocal van der Waals density functional: The simpler the better. *J. Chem. Phys.* **133**, 244103. doi:[10.1063/1.3521275](https://doi.org/10.1063/1.3521275) (2010) (p. 2, 51, 108).

64. Sabatini, R., Gorni, T. & De Gironcoli, S. Nonlocal van der Waals density functional made simple and efficient. *Phys. Rev. B* **87**, 041108. doi:[10.1103/PhysRevB.87.041108](https://doi.org/10.1103/PhysRevB.87.041108) (2013) (p. 2).
65. Grimme, S., Hansen, A., Brandenburg, J. G. & Bannwarth, C. Dispersion-corrected mean-field electronic structure methods. *Chem. Rev.* **116**, 5105–5154. doi:[10.1021/acs.chemrev.5b00533](https://doi.org/10.1021/acs.chemrev.5b00533) (2016) (p. 3, 7).
66. Johnson, C. S. & Pedersen, L. G. *Problems and solutions in Quantum Chemistry and Physics* ISBN: 048665236X (Courier Corporation, 1986) (p. 3, 207).
67. Eyring, H., Walter, J. & Kimball, G. E. *Quantum chemistry* ISBN: 1298492742 (Wiley New York, 1944) (p. 3, 207).
68. Atkins, P. W. & Friedman, R. S. *Molecular Quantum Mechanics* ISBN: 0199541426 (Oxford University Press, Oxford, 2011) (p. 3, 10, 54, 207).
69. Kauzmann, W. *Quantum chemistry: an introduction* ISBN: 1483250709 (Elsevier, 2013) (p. 3, 10, 95, 207).
70. Dirac, P. A. M. *A new notation for quantum mechanics* in *Math. Proc. Cambridge Philos. Soc.* **35** (1939), 416–418. doi:[10.1017/S0305004100021162](https://doi.org/10.1017/S0305004100021162) (p. 4).
71. Eisenschitz, R. & London, F. On the ratio of the van der Waals forces and the homo-polar binding forces. *Phys. Z.* **60**, 491–527. doi:[10.1142/9789812795762_0022](https://doi.org/10.1142/9789812795762_0022) (1930) (p. 4).
72. Slater, J. C. & Kirkwood, J. G. The van der Waals forces in gases. *Phys. Rev.* **37**, 682. doi:[10.1103/PhysRev.37.682](https://doi.org/10.1103/PhysRev.37.682) (1931) (p. 4, 8, 46).
73. Pauling, L. & Beach, J. Y. The van der Waals interaction of hydrogen atoms. *Phys. Rev.* **47**, 686. doi:[10.1103/PhysRev.47.686](https://doi.org/10.1103/PhysRev.47.686) (1935) (p. 4–5).
74. Gould, T. & Bucko, T. C6 coefficients and dipole polarizabilities for all atoms and many ions in rows 1–6 of the periodic table. *J. Chem. Theory Comput.* **12**, 3603–3613. doi:[10.1021/acs.jctc.6b00361](https://doi.org/10.1021/acs.jctc.6b00361) (2016) (p. 4).
75. Gould, T. How polarizabilities and C6 coefficients actually vary with atomic volume. *J. Chem. Phys.* **145**, 084308. doi:[10.1063/1.4961643](https://doi.org/10.1063/1.4961643) (2016) (p. 4).
76. Tang, K. T., Norbeck, J. M. & Certain, P. R. Upper and lower bounds of two- and three-body dipole, quadrupole, and octupole van der Waals coefficients for hydrogen, noble gas, and alkali atom interactions. *J. Chem. Phys.* **64**, 3063–3074. doi:[10.1063/1.432569](https://doi.org/10.1063/1.432569) (1976) (p. 4, 6).
77. Unsöld, A. Quantentheorie des Wasserstoffmoleküls und der Born-Landéschen Abstoßungskräfte. *Z. Angew. Phys.* **43**, 563–574. doi:[10.1007/BF01397633](https://doi.org/10.1007/BF01397633) (1927) (p. 4, 211).
78. Salem, L. The calculation of dispersion forces. *Mol. Phys.* **3**, 441–452. doi:[10.1080/00268976000100481](https://doi.org/10.1080/00268976000100481) (1960) (p. 5, 129).
79. Margenau, H. Van der Waals forces. *Rev. Mod. Phys.* **11**, 1. doi:[10.1103/RevModPhys.11.1](https://doi.org/10.1103/RevModPhys.11.1) (1939) (p. 5).

80. Otero-de-la-Roza, A., LeBlanc, L. M. & Johnson, E. R. What is “many-body” dispersion and should I worry about it? *Phys. Chem. Chem. Phys.* **22**, 8266–8276. doi:[10.1039/DQCP01213K](https://doi.org/10.1039/DQCP01213K) (2020) (p. 6, 10, 57, 79–81, 89–90, 92, 102, 113, 133, 152, 217).
81. Price, A. J. A., Bryenton, K. R. & Johnson, E. R. Requirements for an accurate dispersion-corrected density functional. *J. Chem. Phys.* **154**. (Chapter 3 in this thesis), 230902. doi:[10.1063/5.0050993](https://doi.org/10.1063/5.0050993) (2021) (p. 6, 18, 67, 103, 107, 116, 121, 147, 153).
82. Cohen, J. S. & Pack, R. T. Modified statistical method for intermolecular potentials. Combining rules for higher van der Waals coefficients. *J. Chem. Phys.* **61**, 2372–2382. doi:[10.1063/1.1682318](https://doi.org/10.1063/1.1682318) (1974) (p. 6).
83. Hepburn, J., Scoles, G. & Penco, R. A simple but reliable method for the prediction of intermolecular potentials. *Chem. Phys. Lett.* **36**, 451–456. doi:[10.1016/0009-2614\(75\)80278-8](https://doi.org/10.1016/0009-2614(75)80278-8) (1975) (p. 6).
84. Ahlrichs, R., Penco, R. & Scoles, G. Intermolecular forces in simple systems. *Chem. Phys.* **19**, 119–130. doi:[10.1016/0301-0104\(77\)85124-0](https://doi.org/10.1016/0301-0104(77)85124-0) (1977) (p. 6–7).
85. Stwalley, W. C. Higher-order long-range interactions between rare gas and hydrogen atoms. *J. Chem. Phys.* **61**, 3840–3841. doi:[10.1063/1.1682573](https://doi.org/10.1063/1.1682573) (1974) (p. 6).
86. Smith, F. T. Atomic distortion and the combining rule for repulsive potentials. *Phys. Rev. A* **5**, 1708. doi:[10.1103/PhysRevA.5.1708](https://doi.org/10.1103/PhysRevA.5.1708) (1972) (p. 6).
87. Wu, Q. & Yang, W. Empirical correction to density functional theory for van der Waals interactions. *J. Chem. Phys.* **116**, 515–524. doi:[10.1063/1.1424928](https://doi.org/10.1063/1.1424928) (2002) (p. 7, 46, 50, 76–77, 79, 138).
88. Mooij, W. T. M., van Duijneveldt, F. B., van Duijneveldt-van de Rijdt, J. G. C. M. & van Eijck, B. P. Transferable ab initio intermolecular potentials. 1. Derivation from methanol dimer and trimer calculations. *J. Phys. Chem. A* **103**, 9872–9882. doi:[10.1021/jp991641n](https://doi.org/10.1021/jp991641n) (1999) (p. 7).
89. Fermi, E. Sulla quantizzazione del gas perfetto monoatomico. *Rend. Lincei* **145** (1926) (p. 7, 41).
90. Dirac, P. A. M. On the theory of quantum mechanics. *Proc. R. Soc. London, Ser. A* **112**, 661–677. doi:[10.1098/rspa.1926.0133](https://doi.org/10.1098/rspa.1926.0133) (1926) (p. 7, 41).
91. Otero-de-la-Roza, A. & Johnson, E. R. Many-body dispersion interactions from the exchange-hole dipole moment model. *J. Chem. Phys.* **138**, 054103. doi:[10.1063/1.4789421](https://doi.org/10.1063/1.4789421) (2013) (p. 7, 53, 56, 81, 89, 152).
92. Grimme, S., Ehrlich, S. & Goerigk, L. Effect of the damping function in dispersion corrected density functional theory. *J. Comput. Chem.* **32**, 1456–1465. doi:[10.1002/jcc.21759](https://doi.org/10.1002/jcc.21759) (2011) (p. 8, 41, 77–78, 115, 126).

93. Hirshfeld, F. L. Bonded-atom fragments for describing molecular charge densities. *Theor. Chim. Acta* **44**, 129–138. doi:[10.1007/BF00549096](https://doi.org/10.1007/BF00549096) (1977) (p. 8, 45, 82–83).
94. Heidar-Zadeh, F., Ayers, P. W., Verstraelen, T., Vinogradov, I., Vöhringer-Martinez, E. & Bultinck, P. Information-theoretic approaches to atoms-in-molecules: Hirshfeld family of partitioning schemes. *J. Phys. Chem. A* **122**, 4219–4245. doi:[10.1021/acs.jpca.7b08966](https://doi.org/10.1021/acs.jpca.7b08966) (2017) (p. 8, 45).
95. Felderhof, B. U. On the propagation and scattering of light in fluids. *Physica* **76**, 486–502. doi:[10.1016/0031-8914\(74\)90155-4](https://doi.org/10.1016/0031-8914(74)90155-4) (1974) (p. 8, 46).
96. Oxtoby, D. W. & Gelbart, W. M. Collisional polarizability anisotropies of the noble gases. *Mol. Phys.* **29**, 1569–1576. doi:[10.1080/00268977500101371](https://doi.org/10.1080/00268977500101371) (1975) (p. 8, 46).
97. Thole, B. T. Molecular polarizabilities calculated with a modified dipole interaction. *Chem. Phys.* **59**, 341–350. doi:[10.1016/0301-0104\(81\)85176-2](https://doi.org/10.1016/0301-0104(81)85176-2) (1981) (p. 8, 46, 105).
98. Christian, M. S., Otero-de-la-Roza, A. & Johnson, E. R. Surface adsorption from the exchange-hole dipole moment dispersion model. *J. Chem. Theory Comput.* **12**, 3305–3315. doi:[10.1021/acs.jctc.6b00222](https://doi.org/10.1021/acs.jctc.6b00222) (2016) (p. 8, 81–82, 217).
99. Otero-de-la-Roza, A. & Johnson, E. R. A benchmark for non-covalent interactions in solids. *J. Chem. Phys.* **137**, 054103. doi:[10.1063/1.4738961](https://doi.org/10.1063/1.4738961) (2012) (p. 8, 46, 59, 68, 71, 79, 84, 140, 160).
100. Otero-de-la-Roza, A., Cao, B. H., Price, I. K., Hein, J. E. & Johnson, E. R. Predicting the Relative Solubilities of Racemic and Enantiopure Crystals by Density-Functional Theory. *Angew. Chem. Int. Ed.* **53**, 7879–7882. doi:[10.1002/ange.201403541](https://doi.org/10.1002/ange.201403541) (2014) (p. 8).
101. Whittleton, S. R., Otero-de-la-Roza, A. & Johnson, E. R. Exchange-hole dipole dispersion model for accurate energy ranking in molecular crystal structure prediction. *J. Chem. Theory Comput.* **13**, 441–450. doi:[10.1021/acs.jctc.6b00679](https://doi.org/10.1021/acs.jctc.6b00679) (2017) (p. 8).
102. Whittleton, S. R., Otero-de-la-Roza, A. & Johnson, E. R. Exchange-hole dipole dispersion model for accurate energy ranking in molecular crystal structure prediction ii: Nonplanar molecules. *J. Chem. Theory Comput.* **13**, 5332–5342. doi:[10.1021/acs.jctc.7b00715](https://doi.org/10.1021/acs.jctc.7b00715) (2017) (p. 8).
103. Christian, M. S., Otero-de-la-Roza, A. & Johnson, E. R. Adsorption of graphene to nickel (111) using the exchange-hole dipole moment model. *Carbon* **118**, 184–191. doi:[10.1016/j.carbon.2017.03.024](https://doi.org/10.1016/j.carbon.2017.03.024) (2017) (p. 8, 84).
104. Otero-de-la-Roza, A., LeBlanc, L. M. & Johnson, E. R. Asymptotic Pairwise Dispersion Corrections Can Describe Layered Materials Accurately. *J. Phys. Chem. Lett.* **11**, 2298–2302. doi:[10.1021/acs.jpcllett.0c00348](https://doi.org/10.1021/acs.jpcllett.0c00348) (2020) (p. 8, 81–82, 84, 89, 107, 111).

105. Kaadou, F., Maassen, J. & Johnson, E. R. Improved Charge Transfer and Barrier Lowering across a Au–MoS₂ Interface through Insertion of a Layered Ca₂N Electride. *J. Phys. Chem. C*. doi:[10.1021/acs.jpcc.1c02142](https://doi.org/10.1021/acs.jpcc.1c02142) (2021) (p. 8).
106. Vazirisereshk, M. R., Ye, H., Ye, Z., Otero-de-la-Roza, A., Zhao, M.-Q., Gao, Z., Johnson, A. T. C., Johnson, E. R., Carpick, R. W. & Martini, A. Origin of nanoscale friction contrast between supported graphene, MoS₂, and a graphene/MoS₂ heterostructure. *Nano Lett.* **19**, 5496–5505. doi:[10.1021/acs.nanolett.9b02035](https://doi.org/10.1021/acs.nanolett.9b02035) (2019) (p. 8).
107. Kabengele, T. & Johnson, E. R. Theoretical modeling of structural superlubricity in rotated bilayer graphene, hexagonal boron nitride, molybdenum disulfide, and blue phosphorene. *Nanoscale* **13**, 14399–14407. doi:[10.1039/D1NR03001A](https://doi.org/10.1039/D1NR03001A) (2021) (p. 8).
108. Christian, M. S., Johnson, E. R. & Besmann, T. M. Interplay between London Dispersion, Hubbard U, and Metastable States for Uranium Compounds. *J. Phys. Chem. A* **125**, 2791–2799. doi:[10.1021/acs.jpca.0c10533](https://doi.org/10.1021/acs.jpca.0c10533) (2021) (p. 8).
109. Price, A. J., Mayo, R. A., Otero-de-la-Roza, A. & Johnson, E. R. Accurate and efficient polymorph energy ranking with XDM-corrected hybrid DFT. *CrysEngComm* **25**, 953–960. doi:[10.1039/D2CE01594C](https://doi.org/10.1039/D2CE01594C) (2023) (p. 8).
110. Mayo, R. A., Price, A. J., Otero-de-la-Roza, A. & Johnson, E. R. Assessment of the exchange-hole dipole moment dispersion correction for the energy ranking stage of the seventh crystal structure prediction blind test. *Acta Crystallogr.* **80**. doi:[10.1107/S2052520624002774](https://doi.org/10.1107/S2052520624002774) (2024) (p. 8).
111. Giannozzi, P., Andreussi, O., Brumme, T., Bunau, O., Nardelli, M. B., Calandra, M., Car, R., Cavazzoni, C., Ceresoli, D., Cococcioni, M., *et al.* Advanced capabilities for materials modelling with Quantum ESPRESSO. *J. Phys.: Condens. Matter* **29**, 465901. doi:[10.1088/1361-648X/aa8f79](https://doi.org/10.1088/1361-648X/aa8f79) (2017) (p. 8, 25, 31, 69, 71–73, 82, 85, 160, 216–217).
112. Clark, S. J., Segall, M. D., Pickard, C. J., Hasnip, P. J., Probert, M. I., Refson, K. & Payne, M. C. First principles methods using CASTEP. *Z. Kristallogr. - Cryst. Mater.* **220**, 567–570. doi:[10.1524/zkri.220.5.567.65075](https://doi.org/10.1524/zkri.220.5.567.65075) (2005) (p. 9, 160).
113. Kong, J., Gan, Z., Proynov, E., Freindorf, M. & Furlani, T. R. Efficient computation of the dispersion interaction with density-functional theory. *Phys. Rev. A: At. Mol. Opt. Phys.* **79**, 042510. doi:[10.1103/PhysRevA.79.042510](https://doi.org/10.1103/PhysRevA.79.042510) (2009) (p. 9, 59, 160).
114. Shao, Y., Gan, Z., Epifanovsky, E., Gilbert, A. T., Wormit, M., Kussmann, J., Lange, A. W., Behn, A., Deng, J., Feng, X., *et al.* Advances in molecular quantum chemistry contained in the Q-Chem 4 program package. *Mol. Phys.* **113**, 184–215. doi:[10.1080/00268976.2014.952696](https://doi.org/10.1080/00268976.2014.952696) (2015) (p. 9, 160).

115. Valiev, M., Bylaska, E. J., Govind, N., Kowalski, K., Straatsma, T. P., Van Dam, H. J. J., Wang, D., Nieplocha, J., Aprà, E., Windus, T. L., *et al.* NWChem: A comprehensive and scalable open-source solution for large scale molecular simulations. *Comput. Phys. Commun.* **181**, 1477–1489. doi:[10.1016/j.cpc.2010.04.018](https://doi.org/10.1016/j.cpc.2010.04.018) (2010) (p. 9, 160).
116. Aprà, E., Bylaska, E. J., de Jong, W. A., Govind, N., Kowalski, K., Straatsma, T. P., Valiev, M., van Dam, H. J. J., Alexeev, Y., Anchell, J., *et al.* NWChem: Past, present, and future. *J. Chem. Phys.* **152**. doi:[10.1063/5.0004997](https://doi.org/10.1063/5.0004997) (2020) (p. 9, 160).
117. LeBlanc, L. M., Weatherby, J. A., Otero-de-la-Roza, A. & Johnson, E. R. Non-covalent interactions in molecular crystals: Exploring the accuracy of the exchange-hole dipole moment model with local orbitals. *J. Chem. Theory Comput.* **14**, 5715–5724. doi:[10.1021/acs.jctc.8b00797](https://doi.org/10.1021/acs.jctc.8b00797) (2018) (p. 9, 160).
118. Soler, J. M., Artacho, E., Gale, J. D., García, A., Junquera, J., Ordejón, P. & Sánchez-Portal, D. The SIESTA method for ab initio order-N materials simulation. *J. Phys.: Condens. Matter* **14**, 2745. doi:[10.1088/0953-8984/14/11/302](https://doi.org/10.1088/0953-8984/14/11/302) (2002) (p. 9, 160).
119. Price, A. J. A., Otero-de-la-Roza, A. & Johnson, E. R. XDM-corrected hybrid DFT with numerical atomic orbitals predicts molecular crystal lattice energies with unprecedented accuracy. *Chem. Sci.* **14**, 1252–1262. doi:[10.1039/D2SC05997E](https://doi.org/10.1039/D2SC05997E) (2023) (p. 9, 19, 34, 103, 110, 116, 119, 141–143, 160, 225, 231).
120. Blum, V., Gehrke, R., Hanke, F., Havu, P., Havu, V., Ren, X., Reuter, K. & Scheffler, M. Ab initio molecular simulations with numeric atom-centered orbitals. *Comput. Phys. Commun.* **180**, 2175–2196. doi:[10.1016/j.cpc.2009.06.022](https://doi.org/10.1016/j.cpc.2009.06.022) (2009) (p. 9, 32–33, 103, 116, 136, 141, 160, 216–217, 230–231, 234–246).
121. Abbott, J. W., Acosta, C. M., Akkoush, A., Ambrosetti, A., Atalla, V., Bagrets, A., Behler, J., Berger, D., Bieniek, B., Björk, J., *et al.* Roadmap on Advancements of the FHI-aims Software Package. *arXiv preprint arXiv:2505.00125*. doi:[10.48550/arXiv.2505.00125](https://doi.org/10.48550/arXiv.2505.00125) (2025) (p. 9, 32, 34, 117, 149, 160).
122. Baerends, E. J., Aguirre, N. F., Austin, N. D., Autschbach, J., Bickelhaupt, F. M., Bulo, R., Cappelli, C., van Duin, A. C. T., Egidi, F., Guerra, C. F., *et al.* The Amsterdam Modeling Suite. *J. Chem. Phys.* **162**, 162501. doi:[10.1063/5.0258496](https://doi.org/10.1063/5.0258496) (2025) (p. 9, 160).
123. Otero-de-la-Roza, A. & Johnson, E. R. Non-covalent interactions and thermochemistry using XDM-corrected hybrid and range-separated hybrid density functionals. *J. Chem. Phys.* **138**, 204109. doi:[10.1063/1.4807330](https://doi.org/10.1063/1.4807330) (2013) (p. 9, 53, 69, 71, 79–80, 160).

124. Otero-de-la-Roza, A., Bryenton, K. R., Kannemann, F., Johnson, E. R., Dickson, R. M., Schmider, H. & Becke, A. D. *postg* (*release: XCDM(Z)*) version 2025-05-23. Sept. 2015. <https://github.com/aoterodelaroza/postg> (p. 9, 142, 160, 225, 232, 234–237).
125. Zou, W. *Molden2Aim* version 2024-03-09. Dec. 2015. <https://github.com/zorkzou/Molden2AIM?tab=readme-ov-file%5C#about-the-molden-file> (p. 9, 160).
126. Frisch, M. J., Trucks, G. W., Schlegel, H. B., Scuseria, G. E., Robb, M. A., Cheeseman, J. R., Scalmani, G., Barone, V., Petersson, G. A., Nakatsuji, H., *et al.* *Gaussian 16 Revision B.01* Gaussian Inc. Wallingford CT. 2016 (p. 9, 63, 117, 142, 160, 225, 232, 234–237).
127. Neese, F., Wennmohs, F., Becker, U. & Ripplinger, C. The ORCA quantum chemistry program package. *J. Chem. Phys.* **152**, 224108. doi:[10.1063/5.0004608](https://doi.org/10.1063/5.0004608) (2020) (p. 9, 160).
128. Balasubramani, S. G., Chen, G. P., Coriani, S., Diedenhofen, M., Frank, M. S., Franzke, Y. J., Furche, F., Grotjahn, R., Harding, M. E., Hättig, C., *et al.* TURBOMOLE: Modular program suite for ab initio quantum-chemical and condensed-matter simulations. *J. Chem. Phys.* **152**, 184107. doi:[10.1063/5.0004635](https://doi.org/10.1063/5.0004635) (2020) (p. 9, 160).
129. Smith, D. G. A., Burns, L. A., Simmonett, A. C., Parrish, R. M., Schieber, M. C., Galvelis, R., Kraus, P., Kruse, H., Remigio, R. D., Alenaizan, A., *et al.* PSI4 1.4: Open-source software for high-throughput quantum chemistry. *J. Chem. Phys.* **152**. doi:[10.1063/5.0006002](https://doi.org/10.1063/5.0006002) (2020) (p. 9, 63, 160).
130. Sun, Q., Zhang, X., Banerjee, S., Bao, P., Barbry, M., Blunt, N. S., Bogdanov, N. A., Booth, G. H., Chen, J., Cui, Z.-H., *et al.* Recent developments in the PySCF program package. *J. Chem. Phys.* **153**, 024109. doi:[10.1063/5.0006074](https://doi.org/10.1063/5.0006074) (2020) (p. 9, 160).
131. Bannwarth, C., Caldeweyher, E., Ehlert, S., Hansen, A., Pracht, P., Seibert, J., Spicher, S. & Grimme, S. Extended tight-binding quantum chemistry methods. *WIREs: Comput. Mol. Sci.* **11**, e1493. doi:[10.1002/wcms.1493](https://doi.org/10.1002/wcms.1493) (2021) (p. 9, 160).
132. Feynman, R. *Richard Feynman's Blackboard at Time of His Death. Photo ID 1. 1029* <https://digital.archives.caltech.edu/collections/Images/1.10-29/>. [Accessed: 2025-06-12]. 1988 (p. 12).
133. Maurer, R. J., Freysoldt, C., Reilly, A. M., Brandenburg, J. G., Hofmann, O. T., Björkman, T., Lebègue, S. & Tkatchenko, A. Advances in density-functional calculations for materials modeling. *Annu. Rev. Mater. Res.* **49**, 1–30. doi:[10.1146/annurev-matsci-070218-010143](https://doi.org/10.1146/annurev-matsci-070218-010143) (2019) (p. 14).
134. Becke, A. D. Density-functional exchange-energy approximation with correct asymptotic behavior. *Phys. Rev. A* **38**, 3098. doi:[10.1103/PhysRevA.38.3098](https://doi.org/10.1103/PhysRevA.38.3098) (1988) (p. 14, 16, 18, 62, 69–71, 142).

135. Becke, A. D. Correlation energy of an inhomogeneous electron gas: A coordinate-space model. *J. Chem. Phys.* **88**, 1053–1062. doi:[10.1063/1.454274](https://doi.org/10.1063/1.454274) (1988) (p. 14, 129, 131, 223–224).
136. Gilbert, T. L. Hohenberg-Kohn theorem for nonlocal external potentials. *Phys. Rev. B* **12**, 2111. doi:[10.1103/PhysRevB.12.2111](https://doi.org/10.1103/PhysRevB.12.2111) (1975) (p. 14).
137. Percus, J. The role of model systems in the few-body reduction of the N-fermion problem. *Int. J. Quantum Chem.* **13**, 89–124. doi:[10.1002/qua.560130108](https://doi.org/10.1002/qua.560130108) (1978) (p. 14).
138. Levy, M. Universal variational functionals of electron densities, first-order density matrices, and natural spin-orbitals and solution of the v-representability problem. *Proc. Natl. Acad. Sci.* **76**, 6062–6065. doi:[10.1073/pnas.76.12.6062](https://doi.org/10.1073/pnas.76.12.6062) (1979) (p. 14).
139. Lieb, E. H. *Density functionals for Coulomb systems* in *Inequalities* 269–303 (Springer, 2002). doi:[10.1002/qua.560240302](https://doi.org/10.1002/qua.560240302) (p. 14).
140. Cohen, A. J. & Mori-Sánchez, P. Landscape of an exact energy functional. *Phys. Rev. A* **93**, 042511. doi:[10.1103/PhysRevA.93.042511](https://doi.org/10.1103/PhysRevA.93.042511) (2016) (p. 14).
141. Perdew, J. P. & Schmidt, K. *Jacob's ladder of density functional approximations for the exchange-correlation energy* in *AIP Conf. Proc.* **577** (2001), 1–20. doi:[10.1063/1.1390175](https://doi.org/10.1063/1.1390175) (p. 14–16).
142. Pauli, W. Über den Verbindung zwischen der Abschluss des Elektronengruppen in die Atom und der Complexstruktur des Spectra. *Z. Physik* **31**, 765–783. doi:[10.1007/BF02980631](https://doi.org/10.1007/BF02980631) (1925) (p. 15).
143. The theory of complex spectra. *Phys. Rev.* **34**, 1293. doi:[10.1103/PhysRev.34.1293](https://doi.org/10.1103/PhysRev.34.1293) (1929) (p. 15).
144. Sherrill, C. D. & Schaefer III, H. F. *The configuration interaction method: Advances in highly correlated approaches* in *Advances in Quantum Chemistry* 143–269 (Elsevier, 1999). doi:[10.1016/S0065-3276\(08\)60532-8](https://doi.org/10.1016/S0065-3276(08)60532-8) (p. 15, 24).
145. Dirac, P. A. *Note on exchange phenomena in the Thomas atom* in *Math. Proc. Cambridge Philos. Soc.* **26** (1930), 376–385. doi:[10.1017/S0305004100016108](https://doi.org/10.1017/S0305004100016108) (p. 16).
146. Ceperley, D. M. & Alder, B. J. Ground state of the electron gas by a stochastic method. *Phys. Rev. Lett.* **45**, 566. doi:[10.1103/PhysRevLett.45.566](https://doi.org/10.1103/PhysRevLett.45.566) (1980) (p. 16).
147. Becke, A. D. On the large-gradient behavior of the density functional exchange energy. *J. Chem. Phys.* **85**, 7184–7187. doi:[10.1063/1.451353](https://doi.org/10.1063/1.451353) (1986) (p. 16, 18, 69–71, 73, 80, 85, 103, 116, 141).
148. Becke, A. D. Density functional calculations of molecular bond energies. *J. Chem. Phys.* **84**, 4524–4529. doi:[10.1063/1.450025](https://doi.org/10.1063/1.450025) (1986) (p. 16, 141).
149. Perdew, J. P., Burke, K. & Ernzerhof, M. Generalized gradient approximation made simple. *Phys. Rev. Lett.* **77**, 3865. doi:[10.1103/PhysRevLett.77.3865](https://doi.org/10.1103/PhysRevLett.77.3865) (1996) (p. 16, 18, 45, 62, 69–71, 73, 80, 85, 101, 103, 116, 141, 217).

150. Perdew, J. P., Burke, K. & Ernzerhof, M. Erratum: "Generalized gradient approximation made simple" (vol 77, pg 3865, 1996). *Phys. Rev. Lett.* **78**, 1396–1396. doi:[10.1103/PhysRevLett.78.1396](https://doi.org/10.1103/PhysRevLett.78.1396) (1997) (p. 16, 18, 45, 141, 217).
151. Perdew, J. P. & Yue, W. Accurate and simple density functional for the electronic exchange energy: Generalized gradient approximation. *Phys. Rev. B* **33**, 8800. doi:[10.1103/physrevb.33.8800](https://doi.org/10.1103/physrevb.33.8800) (1986) (p. 16, 18, 69–71, 101).
152. Perdew, J. & Yue, W. Erratum: accurate and simple density functional for the electronic exchange energy: generalized gradient approximation 40: 3399 (E)-3399 (E); Perdew JP, Wang Y (1992) Accurate and simple analytic representation of the electron-gas correlation energy. *Phys. Rev. B* **45**, 13244–13249. doi:[10.1103/PhysRevB.40.3399](https://doi.org/10.1103/PhysRevB.40.3399) (1989) (p. 16, 18).
153. Lacks, D. J. & Gordon, R. G. Pair interactions of rare-gas atoms as a test of exchange-energy-density functionals in regions of large density gradients. *Phys. Rev. A* **47**, 4681. doi:[10.1103/PhysRevA.47.4681](https://doi.org/10.1103/PhysRevA.47.4681) (1993) (p. 17, 68, 70).
154. Zhang, Y., Pan, W. & Yang, W. Describing van der Waals Interaction in diatomic molecules with generalized gradient approximations: The role of the exchange functional. *J. Chem. Phys.* **107**, 7921–7925. doi:[10.1063/1.475105](https://doi.org/10.1063/1.475105) (1997) (p. 17, 68, 70).
155. Murray, É. D., Lee, K. & Langreth, D. C. Investigation of exchange energy density functional accuracy for interacting molecules. *J. Chem. Theory Comput.* **5**, 2754–2762. doi:[10.1021/ct900365q](https://doi.org/10.1021/ct900365q) (2009) (p. 17, 68, 70).
156. Johnson, E. R. & Becke, A. D. A post-Hartree-Fock model of intermolecular interactions: Inclusion of higher-order corrections. *J. Chem. Phys.* **124**, 174104. doi:[10.1063/1.2190220](https://doi.org/10.1063/1.2190220) (2006) (p. 18, 41, 53–54, 56, 77, 79, 89, 100, 115, 126, 129, 135).
157. Janesko, B. G. Rung 3.5 density functionals: Another step on Jacob's ladder. *Int. J. Quantum Chem.* **113**, 83–88. doi:[10.1002/qua.24256](https://doi.org/10.1002/qua.24256) (2013) (p. 19).
158. Janesko, B. G., Proynov, E., Scalmani, G. & Frisch, M. J. Long-range-corrected Rung 3.5 density functional approximations. *J. Chem. Phys.* **148**. doi:[10.1063/1.5017981](https://doi.org/10.1063/1.5017981) (2018) (p. 19, 66).
159. Ramos, C. & Janesko, B. G. Nonlocal rung-3.5 correlation from the density matrix expansion: Flat-plane condition, thermochemistry, and kinetics. *J. Chem. Phys.* **153**. doi:[10.1063/5.0025160](https://doi.org/10.1063/5.0025160) (2020) (p. 19).
160. Medvedev, M. G., Bushmarinov, I. S., Sun, J., Perdew, J. P. & Lyssenko, K. A. Density functional theory is straying from the path toward the exact functional. *Science* **355**, 49–52. doi:[10.1126/science.aah5975](https://doi.org/10.1126/science.aah5975) (2017) (p. 19).
161. Bryenton, K. R., Adeleke, A. A., Dale, S. G. & Johnson, E. R. Delocalization error: The greatest outstanding challenge in density-functional theory. *WIREs: Comput. Mol. Sci.* **13**, e1631. doi:[10.1002/wcms.1631](https://doi.org/10.1002/wcms.1631) (2023) (p. 19, 60, 142, 150).

162. Kokott, S., Merz, F., Yao, Y., Carbogno, C., Rossi, M., Havu, V., Rampp, M., Scheffler, M. & Blum, V. Efficient All-electron Hybrid Density Functionals for Atomistic Simulations Beyond 10,000 Atoms. *J. Chem. Phys.* **161**. doi:[10.1063/5.0208103](https://doi.org/10.1063/5.0208103) (2024) (p. 19, 33, 141, 231).
163. Adamo, C. & Barone, V. Toward reliable density functional methods without adjustable parameters: The PBE0 model. *J. Chem. Phys.* **110**, 6158–6170. doi:[10.1063/1.478522](https://doi.org/10.1063/1.478522) (1999) (p. 19, 45, 116, 142).
164. Becke, A. D. A new mixing of Hartree-Fock and local density-functional theories. *J. Chem. Phys.* **98**, 1372–1377. doi:[10.1063/1.464304](https://doi.org/10.1063/1.464304) (1993) (p. 19, 142).
165. Lee, C., Yang, W. & Parr, R. G. Development of the Colle-Salvetti correlation-energy formula into a functional of the electron density. *Phys. Rev. B* **37**, 785. doi:[10.1103/PhysRevB.37.785](https://doi.org/10.1103/PhysRevB.37.785) (1988) (p. 19, 62, 69, 142).
166. Vydrov, O. A. & Scuseria, G. E. Assessment of a long-range corrected hybrid functional. *J. Chem. Phys.* **125**, 234109. doi:[10.1063/1.2409292](https://doi.org/10.1063/1.2409292) (2006) (p. 19, 142).
167. Vydrov, O. A., Scuseria, G. E. & Perdew, J. P. Tests of functionals for systems with fractional electron number. *J. Chem. Phys.* **126**, 234109. doi:[10.1063/1.2723119](https://doi.org/10.1063/1.2723119) (2007) (p. 19, 142).
168. Kruckau, A. V., Vydrov, O. A., Izmaylov, A. F. & Scuseria, G. E. Influence of the exchange screening parameter on the performance of screened hybrid functionals. *J. Chem. Phys.* **125**. doi:[10.1063/1.2404663](https://doi.org/10.1063/1.2404663) (2006) (p. 20, 224).
169. Kokott, S., Blum, V. & Scheffler, M. Efficient computation of the long-range exact exchange using an extended screening function. *J. Chem. Phys.* **162**, 224103. doi:[10.1063/5.0262451](https://doi.org/10.1063/5.0262451) (2025) (p. 20).
170. Becke, A. D. A real-space model of nondynamical correlation. *J. Chem. Phys.* **119**, 2972–2977. doi:[10.1063/1.1589733](https://doi.org/10.1063/1.1589733) (2003) (p. 20, 59–63, 66, 129).
171. Jaramillo, J., Scuseria, G. E. & Ernzerhof, M. Local hybrid functionals. *J. Chem. Phys.* **118**, 1068–1073. doi:[10.1063/1.1528936](https://doi.org/10.1063/1.1528936) (2003) (p. 20).
172. Becke, A. D. Real-space post-Hartree–Fock correlation models. *J. Chem. Phys.* **122**, 064101. doi:[10.1063/1.1844493](https://doi.org/10.1063/1.1844493) (2005) (p. 20).
173. Kirkpatrick, J., McMorrow, B., Turban, D. H., Gaunt, A. L., Spencer, J. S., Matthews, A. G., Obika, A., Thiry, L., Fortunato, M., Pfau, D., *et al.* Pushing the frontiers of density functionals by solving the fractional electron problem. *Science* **374**, 1385–1389. doi:[10.1126/science.abj6511](https://doi.org/10.1126/science.abj6511) (2021) (p. 20).
174. Bohm, D. & Pines, D. A collective description of electron interactions: III. Coulomb interactions in a degenerate electron gas. *Phys. Rev.* **92**, 609. doi:[10.1103/PhysRev.92.609](https://doi.org/10.1103/PhysRev.92.609) (1953) (p. 20, 49–50).

175. Gell-Mann, M. & Brueckner, K. A. Correlation energy of an electron gas at high density. *Phys. Rev.* **106**, 364. doi:[10.1103/PhysRev.106.364](https://doi.org/10.1103/PhysRev.106.364) (1957) (p. 20, 49–50).
176. Dobson, J. F. Quasi-local-density approximation for a van der Waals energy functional. *pre-print*. arXiv cond-mat/0311371. doi:[10.48550/arXiv.cond-mat/0311371](https://doi.org/10.48550/arXiv.cond-mat/0311371) (2003) (p. 20, 50).
177. Dobson, J. F. & Gould, T. Calculation of dispersion energies. *J. Phys.: Condens. Matter* **24**, 073201. doi:[10.1088/0953-8984/24/7/073201](https://doi.org/10.1088/0953-8984/24/7/073201) (2012) (p. 20, 50).
178. Ren, X., Rinke, P., Joas, C. & Scheffler, M. Random-phase approximation and its applications in computational chemistry and materials science. *J. Mater. Sci.* **47**, 7447–7471. doi:[10.1007/s10853-012-6570-4](https://doi.org/10.1007/s10853-012-6570-4) (2012) (p. 20, 50).
179. Eshuis, H., Bates, J. E. & Furche, F. Electron correlation methods based on the random phase approximation. *Theor. Chem. Acc.* **131**, 1–18. doi:[10.1007/s00214-011-1084-8](https://doi.org/10.1007/s00214-011-1084-8) (2012) (p. 20, 50).
180. Goerigk, L. & Grimme, S. Double-hybrid density functionals. *WIREs: Comput. Mol. Sci.* **4**, 576–600. doi:[10.1002/wcms.1193](https://doi.org/10.1002/wcms.1193) (2014) (p. 20–21).
181. Tkatchenko, A., Ambrosetti, A. & DiStasio Jr, R. A. Interatomic methods for the dispersion energy derived from the adiabatic connection fluctuation-dissipation theorem. *J. Chem. Phys.* **138**, 074106. doi:[10.1063/1.4789814](https://doi.org/10.1063/1.4789814) (2013) (p. 21, 49, 90).
182. Grimme, S. & Neese, F. Double-hybrid density functional theory for excited electronic states of molecules. *J. Chem. Phys.* **127**, 154116. doi:[10.1063/1.2772854](https://doi.org/10.1063/1.2772854) (2007) (p. 21).
183. Becke, A. D. A remarkably simple dispersion damping scheme and the DH24 double hybrid density functional. *J. Chem. Phys.* **160**, 204118. doi:[10.1063/5.0207682](https://doi.org/10.1063/5.0207682) (2024) (p. 21, 129, 136, 144).
184. Møller, C. & Plesset, M. S. Note on an approximation treatment for many-electron systems. *Phys. Rev.* **46**, 618. doi:[10.1103/PhysRev.46.618](https://doi.org/10.1103/PhysRev.46.618) (1934) (p. 21).
185. Head-Gordon, M., Pople, J. A. & Frisch, M. J. MP2 energy evaluation by direct methods. *Chem. Phys. Lett.* **153**, 503–506. doi:[10.1016/0009-2614\(88\)85250-3](https://doi.org/10.1016/0009-2614(88)85250-3) (1988) (p. 21).
186. Cremer, D. Møller–Plesset perturbation theory: from small molecule methods to methods for thousands of atoms. *WIREs: Comput. Mol. Sci.* **1**, 509–530. doi:[10.1002/wcms.58](https://doi.org/10.1002/wcms.58) (2011) (p. 21).
187. Čížek, J. On the correlation problem in atomic and molecular systems. Calculation of wavefunction components in Ursell-type expansion using quantum-field theoretical methods. *J. Chem. Phys.* **45**, 4256–4266. doi:[10.1063/1.1727484](https://doi.org/10.1063/1.1727484) (1966) (p. 21).

188. Raghavachari, K., Trucks, G. W., Pople, J. A. & Head-Gordon, M. A fifth-order perturbation comparison of electron correlation theories. *Chem. Phys. Lett.* **157**, 479–483. doi:[10.1016/S0009-2614\(89\)87395-6](https://doi.org/10.1016/S0009-2614(89)87395-6) (1989) (p. 21, 23).
189. Karton, A., Rabinovich, E., Martin, J. M. & Ruscic, B. W4 theory for computational thermochemistry: In pursuit of confident sub-kJ/mol predictions. *J. Chem. Phys.* **125**, 144108. doi:[10.1063/1.2348881](https://doi.org/10.1063/1.2348881) (2006) (p. 21).
190. Anderson, J. B. A random-walk simulation of the Schrödinger equation: H_3^+ . *J. Chem. Phys.* **63**, 1499–1503. doi:[10.1063/1.431514](https://doi.org/10.1063/1.431514) (1975) (p. 21, 23).
191. Ceperley, D. & Alder, B. Quantum Monte Carlo. *Science* **231**, 555–560. doi:[10.1126/science.231.4738.555](https://doi.org/10.1126/science.231.4738.555) (1986) (p. 21, 23).
192. Surján, P. R. *The Brillouin Theorem in Second Quantized Approach to Quantum Chemistry: An Elementary Introduction* 87–92 (Springer, 1989). ISBN: 978-3-642-74755-7. doi:[10.1007/978-3-642-74755-7_11](https://doi.org/10.1007/978-3-642-74755-7_11) (p. 22).
193. Annarelli, A., Alfè, D. & Zen, A. A brief introduction to the diffusion Monte Carlo method and the fixed-node approximation. *J. Chem. Phys.* **161**. doi:[10.1063/5.0232424](https://doi.org/10.1063/5.0232424) (2024) (p. 23).
194. Parker, W. D., Wilkins, J. W. & Hennig, R. G. Accuracy of quantum Monte Carlo methods for point defects in solids. *Phys. Status Solidi B* **248**, 267–274. doi:[10.1002/pssb.201046149](https://doi.org/10.1002/pssb.201046149) (2011) (p. 23).
195. Shulenburger, L. & Mattsson, T. R. Quantum Monte Carlo applied to solids. *Phys. Rev. B: Condens. Matter* **88**, 245117. doi:[10.1103/PhysRevB.88.245117](https://doi.org/10.1103/PhysRevB.88.245117) (2013) (p. 23).
196. Della Pia, F., Zen, A., Alfè, D. & Michaelides, A. DMC-ICE13: Ambient and high pressure polymorphs of ice from diffusion Monte Carlo and density functional theory. *J. Chem. Phys.* **157**. doi:[10.1063/5.0102645](https://doi.org/10.1063/5.0102645) (2022) (p. 23, 141).
197. Huang, B., von Lilienfeld, O. A., Krogel, J. T. & Benali, A. Toward DMC accuracy across chemical space with scalable Δ -QML. *J. Chem. Theory Comput.* **19**, 1711–1721. doi:[10.1021/acs.jctc.2c01058](https://doi.org/10.1021/acs.jctc.2c01058) (2023) (p. 23).
198. Kodrycka, M. & Patkowski, K. Platinum, gold, and silver standards of intermolecular interaction energy calculations. *J. Chem. Phys.* **151**, 070901. doi:[10.1063/1.5116151](https://doi.org/10.1063/1.5116151) (2019) (p. 24, 115).
199. Burns, L. A., Marshall, M. S. & Sherrill, C. D. Appointing silver and bronze standards for noncovalent interactions: A comparison of spin-component-scaled (SCS), explicitly correlated (F12), and specialized wavefunction approaches. *J. Chem. Phys.* **141**, 234111. doi:[10.1063/1.4903765](https://doi.org/10.1063/1.4903765) (2014) (p. 24, 115).
200. Hattig, C., Klopper, W., Kohn, A. & Tew, D. P. Explicitly correlated electrons in molecules. *Chem. Rev.* **112**, 4–74. doi:[10.1021/cr200168z](https://doi.org/10.1021/cr200168z) (2012) (p. 24).
201. Kong, L., Bischoff, F. A. & Valeev, E. F. Explicitly correlated R12/F12 methods for electronic structure. *Chem. Rev.* **112**, 75–107. doi:[10.1021/cr200204r](https://doi.org/10.1021/cr200204r) (2012) (p. 24).

202. Helgaker, T., Klopper, W., Koch, H. & Noga, J. Basis-set convergence of correlated calculations on water. *J. Chem. Phys.* **106**, 9639–9646. doi:[10.1063/1.473863](https://doi.org/10.1063/1.473863) (1997) (p. 24, 35).
203. Halkier, A., Helgaker, T., Jørgensen, P., Klopper, W., Koch, H., Olsen, J. & Wilson, A. K. Basis-set convergence in correlated calculations on Ne, N₂, and H₂O. *Chem. Phys. Lett.* **286**, 243–252. doi:[10.1016/S0009-2614\(98\)00111-0](https://doi.org/10.1016/S0009-2614(98)00111-0) (1998) (p. 24, 35).
204. Řezáč, J. & Hobza, P. Describing Noncovalent Interactions beyond the Common Approximations: How Accurate Is the “Gold Standard,” CCSD(T) at the Complete Basis Set Limit? *J. Chem. Theory Comput.* **9**, 2151–2155. doi:[10.1021/ct400057w](https://doi.org/10.1021/ct400057w) (2013) (p. 24, 115).
205. Řezáč, J., Dubeccký, M., Jurečka, P. & Hobza, P. Extensions and applications of the A24 data set of accurate interaction energies. *Phys. Chem. Chem. Phys.* **17**, 19268–19277. doi:[10.1039/C5CP03151F](https://doi.org/10.1039/C5CP03151F) (2015) (p. 24).
206. Heßelmann, A. Improved supermolecular second order Møller–Plesset intermolecular interaction energies using time-dependent density functional response theory. *J. Chem. Phys.* **128**, 144112. doi:[10.1063/1.2905808](https://doi.org/10.1063/1.2905808) (2008) (p. 24).
207. Pitonak, M. & Heßelmann, A. Accurate intermolecular interaction energies from a combination of MP2 and TDDFT response theory. *J. Chem. Theory Comput.* **6**, 168–178. doi:[10.1021/ct9005882](https://doi.org/10.1021/ct9005882) (2010) (p. 24).
208. Al-Hamdani, Y. S., Nagy, P. R., Zen, A., Barton, D., Kállay, M., Brandenburg, J. G. & Tkatchenko, A. Interactions between large molecules pose a puzzle for reference quantum mechanical methods. *Nat. Commun.* **12**, 3927. doi:[10.1038/s41467-021-24119-3](https://doi.org/10.1038/s41467-021-24119-3) (2021) (p. 24).
209. Gray, M. & Herbert, J. M. Assessing the domain-based local pair natural orbital (DLPNO) approximation for non-covalent interactions in sizable supramolecular complexes. *J. Chem. Phys.* **161**. doi:[10.1063/5.0206533](https://doi.org/10.1063/5.0206533) (2024) (p. 24).
210. Bravais, A. Mémoire sur les polyèdres de forme symétrique. *J. Pure Appl. Math.*, 141–180. ISSN: 00217874. <http://eudml.org/doc/235690> (1849) (p. 25).
211. Ashcroft, N. W. & Mermin, N. D. *Solid state physics* ISBN: 0030839939 (Saunders College Publishing, 1976) (p. 26).
212. Bloch, F. Über die quantenmechanik der elektronen in kristallgittern. *Z. Angew. Phys.* **52**, 555–600. doi:[10.1007/BF01339455](https://doi.org/10.1007/BF01339455) (1929) (p. 26).
213. Marsman, M. *Basics: DFT, plane waves, PAW method, electronic minimization* VASP Workshop at NERSC, Berkeley, California. Nov. 2016. <https://www.nersc.gov/assets/Uploads/VASP-lecture-Basics.pdf> (p. 27, 30).

214. Gauss, C. F. (*Unpublished Manuscript*) *Theoria interpolationis methodo nova tractata [Theory regarding a new method of interpolation]* in *Carl Friedrich Gauss, Werke* **3** (Königlichen Gesellschaft der Wissenschaften zu Göttingen, 1866), 265–303 (p. 27).
215. Heideman, M., Johnson, D. & Burrus, C. Gauss and the history of the fast Fourier transform. *IEEE ASSP Mag.* **1**, 14–21. doi:[10.1109/MASSP.1984.1162257](https://doi.org/10.1109/MASSP.1984.1162257) (1984) (p. 27).
216. Cooley, J. W. & Tukey, J. W. An algorithm for the machine calculation of complex Fourier series. *Math. Comput.* **19**, 297–301. doi:[10.1090/S0025-5718-1965-0178586-1](https://doi.org/10.1090/S0025-5718-1965-0178586-1) (1965) (p. 27).
217. Brillouin, L. Les électrons libres dans les métaux et le rôle des réflexions de Bragg. *J. Phys. Radium* **1**, 377–400. doi:[10.1051/JPHYSRAD:01930001011037700](https://doi.org/10.1051/JPHYSRAD:01930001011037700) (1930) (p. 27).
218. Monkhorst, H. J. & Pack, J. D. Special points for Brillouin-zone integrations. *Phys. Rev. B* **13**, 5188. doi:[10.1103/PhysRevB.13.5188](https://doi.org/10.1103/PhysRevB.13.5188) (1976) (p. 28).
219. Sachs, E. S., Hinze, J. & Sabelli, N. H. Frozen core approximation, a pseudopotential method tested on six states of NaH. *J. Chem. Phys.* **62**, 3393–3398. doi:[10.1063/1.430993](https://doi.org/10.1063/1.430993) (1975) (p. 28).
220. Schwerdtfeger, P. The pseudopotential approximation in electronic structure theory. *ChemPhysChem* **12**, 3143–3155. doi:[10.1002/cphc.201100387](https://doi.org/10.1002/cphc.201100387) (2011) (p. 28).
221. Hamann, D., Schlüter, M. & Chiang, C. Norm-conserving pseudopotentials. *Phys. Rev. Lett.* **43**, 1494. doi:[10.1103/PhysRevLett.43.1494](https://doi.org/10.1103/PhysRevLett.43.1494) (1979) (p. 29).
222. Troullier, N. & Martins, J. L. Efficient pseudopotentials for plane-wave calculations. *Phys. Rev. B* **43**, 1993. doi:[10.1103/PhysRevB.43.1993](https://doi.org/10.1103/PhysRevB.43.1993) (1991) (p. 29, 73).
223. Troullier, N. & Martins, J. L. Efficient pseudopotentials for plane-wave calculations. II. Operators for fast iterative diagonalization. *Phys. Rev. B* **43**, 8861. doi:[10.1103/PhysRevB.43.8861](https://doi.org/10.1103/PhysRevB.43.8861) (1991) (p. 29, 73).
224. Vanderbilt, D. Soft self-consistent pseudopotentials in a generalized eigenvalue formalism. *Phys. Rev. B* **41**, 7892. doi:[10.1103/PhysRevB.41.7892](https://doi.org/10.1103/PhysRevB.41.7892) (1990) (p. 29).
225. Blöchl, P. E. Projector augmented-wave method. *Phys. Rev. B* **50**, 17953. doi:[10.1103/PhysRevB.50.17953](https://doi.org/10.1103/PhysRevB.50.17953) (1994) (p. 30, 69, 71, 82, 85).
226. Kresse, G. & Joubert, D. From ultrasoft pseudopotentials to the projector augmented-wave method. *Phys. Rev. B* **59**, 1758. doi:[10.1103/PhysRevB.59.1758](https://doi.org/10.1103/PhysRevB.59.1758) (1999) (p. 30, 69, 71, 82, 85).
227. Slater, J. C. An augmented plane wave method for the periodic potential problem. *Phys. Rev.* **92**, 603. doi:[10.1103/PhysRev.92.603](https://doi.org/10.1103/PhysRev.92.603) (1953) (p. 30).

228. Andersen, O. K. Linear methods in band theory. *Phys. Rev. B* **12**, 3060. doi:[10.1103/PhysRevB.12.3060](https://doi.org/10.1103/PhysRevB.12.3060) (1975) (p. 30).
229. Rostgaard, C. The projector augmented-wave method. *pre-print*. arXiv 0910.1921. doi:[10.48550/arXiv.0910.1921](https://doi.org/10.48550/arXiv.0910.1921) (2009) (p. 30).
230. Zwanziger, J. Computation of NMR observables: Consequences of projector-augmented wave sphere overlap. *Solid State Nucl. Magn. Reson.* **80**, 14–18. doi:[10.1016/j.ssnmr.2016.10.005](https://doi.org/10.1016/j.ssnmr.2016.10.005) (2016) (p. 31).
231. Torrent, M. & Jollet, F. *First tutorial on the projector augmented-wave (PAW) method* version 2025-05-30. <https://docs.abinit.org/tutorial/paw1/>. 2018. <https://docs.abinit.org/tutorial/paw1/> (p. 31).
232. Dal Corso, A. *atomic* version v6.1. Packaged with Quantum ESPRESSO: <https://gitlab.com/QEF/q-e/-/tree/develop/atomic>. May 2004. <https://gitlab.com/QEF/q-e/-/tree/develop/atomic> (p. 31).
233. Dal Corso, A. Pseudopotentials periodic table: From H to Pu. *Comput. Mater. Sci.* **95**, 337–350. doi:[10.1016/j.commatsci.2014.07.043](https://doi.org/10.1016/j.commatsci.2014.07.043) (2014) (p. 31).
234. Gonze, X., Beuken, J.-M., Caracas, R., Detraux, F., Fuchs, M., Rignanese, G.-M., Sindic, L., Verstraete, M., Zerah, G., Jollet, F., *et al.* First-principles computation of material properties: the ABINIT software project. *Comput. Mater. Sci.* **25**, 478–492. doi:[S0927-0256\(02\)00325-7](https://doi.org/10.1016/S0927-0256(02)00325-7) (2002) (p. 32).
235. Gonze, X. A brief introduction to the ABINIT software package. *Z. Kristallogr. - Cryst. Mater.* **220**, 558–562. doi:[10.1524/zkri.220.5.558.65066](https://doi.org/10.1524/zkri.220.5.558.65066) (2005) (p. 32).
236. Torrent, M., Jollet, F., Bottin, F., Zérah, G. & Gonze, X. Implementation of the projector augmented-wave method in the ABINIT code: Application to the study of iron under pressure. *Comput. Mater. Sci.* **42**, 337–351. doi:[10.1016/j.commatsci.2007.07.020](https://doi.org/10.1016/j.commatsci.2007.07.020) (2008) (p. 32).
237. Gonze, X., Amadon, B., Anglade, P.-M., Beuken, J.-M., Bottin, F., Boulanger, P., Bruneval, F., Caliste, D., Caracas, R., Côté, M., *et al.* ABINIT: First-principles approach to material and nanosystem properties. *Comput. Phys. Commun.* **180**, 2582–2615. doi:[10.1016/j.cpc.2009.07.007](https://doi.org/10.1016/j.cpc.2009.07.007) (2009) (p. 32).
238. Gonze, X., Jollet, F., Araujo, F. A., Adams, D., Amadon, B., Applencourt, T., Audouze, C., Beuken, J.-M., Bieder, J., Bokhanchuk, A., *et al.* Recent developments in the ABINIT software package. *Comput. Phys. Commun.* **205**, 106–131. doi:[10.1016/j.cpc.2016.04.003](https://doi.org/10.1016/j.cpc.2016.04.003) (2016) (p. 32).
239. Gonze, X., Amadon, B., Antonius, G., Arnardi, F., Baguet, L., Beuken, J.-M., Bieder, J., Bottin, F., Bouchet, J., Bousquet, E., *et al.* The ABINIT project: Impact, environment and recent developments. *Comput. Phys. Commun.* **248**, 107042. doi:[10.1016/j.cpc.2019.107042](https://doi.org/10.1016/j.cpc.2019.107042) (2020) (p. 32).
240. Lion, K. *FHI-aims Webinar: An Introduction to the FHI-aims Software Package* MA1P e.V., Online Webinar. Apr. 2025. <https://www.youtube.com/watch?v=YiHpu81C9x4> (p. 33).

241. Boys, S. F. & Bernardi, F. The calculation of small molecular interactions by the differences of separate total energies. Some procedures with reduced errors. *Mol. Phys.* **19**, 553–566. doi:[10.1080/00268977000101561](https://doi.org/10.1080/00268977000101561) (1970) (p. 33, 101, 117).
242. Simon, S., Duran, M. & Dannenberg, J. How does basis set superposition error change the potential surfaces for hydrogen-bonded dimers? *J. Chem. Phys.* **105**, 11024–11031. doi:[10.1063/1.472902](https://doi.org/10.1063/1.472902) (1996) (p. 33).
243. Bryenton, K. R. & Johnson, E. R. *XDM Tutorial for FHI-aims* version 2025-06-07. https://fhi-aims-club.gitlab.io/tutorials/xdm-tutorial/3_Fitting-XDM/. 2024. https://fhi-aims-club.gitlab.io/tutorials/xdm-tutorial/3%5C_Fitting-XDM/ (p. 34, 142).
244. Bryenton, K. R. & Johnson, E. R. The exchange-correlation dipole moment dispersion method. *Submitted To: Phys. Chem. Chem. Phys.* (Chapter 6 in this thesis). doi:[10.48550/arXiv.2506.02352](https://arxiv.org/abs/2506.02352) (2025) (p. 34, 128).
245. Slater, J. C. Atomic shielding constants. *Phys. Rev.* **36**, 57. doi:[10.1103/PhysRev.36.57](https://doi.org/10.1103/PhysRev.36.57) (1930) (p. 34).
246. Hehre, W. J., Stewart, R. F. & Pople, J. A. Self-consistent molecular-orbital methods. I. Use of Gaussian expansions of Slater-type atomic orbitals. *J. Chem. Phys.* **51**, 2657–2664. doi:[10.1063/1.1672392](https://doi.org/10.1063/1.1672392) (1969) (p. 35).
247. Hariharan, P. C. & Pople, J. A. The influence of polarization functions on molecular orbital hydrogenation energies. *Theor. Chim. Acta* **28**, 213–222. doi:[10.1007/BF00533485](https://doi.org/10.1007/BF00533485) (1973) (p. 35).
248. Dunning Jr, T. H. Gaussian basis sets for use in correlated molecular calculations. I. The atoms boron through neon and hydrogen. *J. Chem. Phys.* **90**, 1007–1023. doi:[10.1063/1.456153](https://doi.org/10.1063/1.456153) (1989) (p. 35, 117).
249. Clark, T., Chandrasekhar, J., Spitznagel, G. W. & Schleyer, P. V. R. Efficient diffuse function-augmented basis sets for anion calculations. III. The 3-21+ G basis set for first-row elements, Li–F. *J. Comput. Chem.* **4**, 294–301. doi:[10.1002/jcc.540040303](https://doi.org/10.1002/jcc.540040303) (1983) (p. 35).
250. Klüppelberg, D. A. *Calculation of stress tensor within the ab-initio full-potential linearized augmented plane wave method* Diplomarbeit in Physik (RWTH Aachen University, Peter Grünberg Institute, 2012). https://www.fz-juelich.de/SharedDocs/Downloads/PGI/PGI-1/EN/Klueppelberg_dipl_pdf (p. 36).
251. Feynman, R. P. Forces in molecules. *Phys. Rev.* **56**, 340. doi:[10.1103/PhysRev.56.340](https://doi.org/10.1103/PhysRev.56.340) (1939) (p. 36, 59).
252. Hellmann, H. *Einführung in die Quantenchemie [In English: Introduction to quantum chemistry]* doi:[10.1002/ange.19410541109](https://doi.org/10.1002/ange.19410541109) (Leipzig und Wien: Franz Deuticke, 1937) (p. 36, 59).

253. Griffiths, D. J. & Schroeter, D. F. *Introduction to quantum mechanics* 3rd ed. ISBN: 9781316995433. doi:[10.1017/9781316995433](https://doi.org/10.1017/9781316995433) (Cambridge University Press, 2018) (p. 36, 59).
254. Hirschfelder, J. O. & Eliason, M. A. Electrostatic Hellmann—Feynman theorem applied to the long-range interaction of two hydrogen atoms. *J. Chem. Phys.* **47**, 1164–1169. doi:[10.1063/1.1712002](https://doi.org/10.1063/1.1712002) (1967) (p. 36).
255. Steiner, E. Electrostatic Hellmann-Feynman theorem applied to long-range interatomic forces. The hydrogen molecule. *J. Chem. Phys.* **59**, 2427–2429. doi:[10.1063/1.1680353](https://doi.org/10.1063/1.1680353) (1973) (p. 36).
256. Cauchy, A. L. *Recherches sur l'équilibre et le mouvement intérieur des corps solides ou fluides. élastiques ou non élastiques* 9–13. doi:[10.1017/CBO9780511702518.038](https://doi.org/10.1017/CBO9780511702518.038) (Bull. Soc. Philomat, Paris, 1823) (p. 36, 38).
257. Cauchy, A. L. De la pression dans les fluides. *Exerc. Math.* **2**, 23–24 (1827) (p. 36, 38).
258. Cauchy, A. L. De la pression ou tension dans un corps solide. *Exerc. Math.* **2**, 42–56 (1827) (p. 36, 38).
259. Cauchy, A. L. Sur la condensation et la dilatation des corps solides. *Exerc. Math.* **2**, 60–69 (1827) (p. 36, 38).
260. Cauchy, A. L. Sur les relations qui existent, dans l'état d'équilibre d'un corps solide ou fluide, entre les pressions ou tensions et les forces accélératrices. *Exerc. Math.* **2**, 108–111 (1827) (p. 36, 38).
261. Martin, R. M. *Electronic Structure: Basic Theory and Practical Methods* doi:[10.1017/CBO9780511805769](https://doi.org/10.1017/CBO9780511805769) (Cambridge University Press, 2004) (p. 36, 38–39).
262. Truesdell, C. & Noll, W. *The non-linear field theories of mechanics* in *The non-linear field theories of mechanics* 1–579 (Springer, 2004). doi:[10.1007/978-3-662-10388-3](https://doi.org/10.1007/978-3-662-10388-3) (p. 36, 38).
263. Green, G. On the laws of the reflexion and refraction of light at the common surface of two noncrystallized media. *Trans. Cambridge Philos. Soc.* **7**, 1–24. doi:[10.1017/CBO9781107325074.009](https://doi.org/10.1017/CBO9781107325074.009) (1838) (p. 36, 38).
264. Green, G. On the propagation of light in crystallized media. *Trans. Cambridge Philos. Soc.* **7**, 121–140. doi:[10.1017/CBO9781107325074.012](https://doi.org/10.1017/CBO9781107325074.012) (1838) (p. 36, 38).
265. Green, G. Supplement to a memoir on the reflexion and refraction of light. *Trans. Cambridge Philos. Soc.* **7**, 113–120. doi:[10.1017/CBO9781107325074.011](https://doi.org/10.1017/CBO9781107325074.011) (1838) (p. 36, 38).
266. Green, G. *Mathematical Papers of the Late George Green* Edited by N. M. Ferrers. doi:[10.1017/CBO9781107325074](https://doi.org/10.1017/CBO9781107325074) (Courier Corporation, 2013) (p. 36, 38).

267. Nielsen, O. & Martin, R. M. First-principles calculation of stress. *Phys. Rev. Lett.* **50**, 697. doi:[10.1103/PhysRevLett.50.697](https://doi.org/10.1103/PhysRevLett.50.697) (1983) (p. 36, 38).
268. Starkschall, G. & Gordon, R. G. Calculation of Coefficients in the Power Series Expansion of the Long-Range Dispersion Force between Atoms. *J. Chem. Phys.* **56**, 2801–2806. doi:[10.1063/1.1677610](https://doi.org/10.1063/1.1677610) (1972) (p. 41).
269. Thakkar, A. J., Hettema, H. & Wormer, P. E. S. Ab initio dispersion coefficients for interactions involving rare-gas atoms. *J. Chem. Phys.* **97**, 3252–3257. doi:[10.1063/1.463012](https://doi.org/10.1063/1.463012) (1992) (p. 41).
270. Tang, K. & Toennies, J. P. An improved simple model for the van der Waals potential based on universal damping functions for the dispersion coefficients. *J. Chem. Phys.* **80**, 3726–3741. doi:[10.1063/1.447150](https://doi.org/10.1063/1.447150) (1984) (p. 41).
271. Chai, J.-D. & Head-Gordon, M. Systematic optimization of long-range corrected hybrid density functionals. *J. Chem. Phys.* **128**, 084106. doi:[10.1063/1.2834918](https://doi.org/10.1063/1.2834918) (2008) (p. 41, 76–77).
272. Koide, A. A new expansion for dispersion forces and its application. *J. Phys. B: At. Mol. Phys.* **9**, 3173. doi:[10.1088/0022-3700/9/18/009](https://doi.org/10.1088/0022-3700/9/18/009) (1976) (p. 42, 77).
273. Kaplan, I. G. *Intermolecular interactions: physical picture, computational methods and model potentials* ISBN: 0470863323 (John Wiley & Sons, 2006) (p. 42).
274. Casimir, H. B. G. & Polder, D. The influence of retardation on the London-van der Waals forces. *Phys. Rev.* **73**, 360. doi:[10.1103/PhysRev.73.360](https://doi.org/10.1103/PhysRev.73.360) (1948) (p. 42, 48, 92).
275. Lein, M., Dobson, J. F. & Gross, E. K. U. Toward the description of van der Waals interactions within density functional theory. *J. Comput. Chem.* **20**, 12–22. doi:[10.1002/\(SICI\)1096-987X\(19990115\)20:1<12::AID-JCC4>3.0.CO;2-U](https://doi.org/10.1002/(SICI)1096-987X(19990115)20:1<12::AID-JCC4>3.0.CO;2-U) (1999) (p. 42).
276. Axilrod, B. & Teller, E. Interaction of the van der Waals type between three atoms. *J. Chem. Phys.* **11**, 299–300. doi:[10.1063/1.1723844](https://doi.org/10.1063/1.1723844) (1943) (p. 43, 56, 81, 89, 93, 152).
277. Muto, Y. Force between nonpolar molecules. *J. Phys. Math. Soc. Japan* **17**, 629. doi:[10.11429/subutsukaishi1927.17.10-11-12_629](https://doi.org/10.11429/subutsukaishi1927.17.10-11-12_629) (1943) (p. 43, 56, 81, 89, 152).
278. Goerigk, L. & Grimme, S. A thorough benchmark of density functional methods for general main group thermochemistry, kinetics, and noncovalent interactions. *Phys. Chem. Chem. Phys.* **13**, 6670–6688. doi:[10.1039/C0CP02984J](https://doi.org/10.1039/C0CP02984J) (2011) (p. 44, 68, 78).

279. Goerigk, L., Hansen, A., Bauer, C. A., Ehrlich, S., Najibi, A. & Grimme, S. *GMTKN55 - A database for general main group thermochemistry, kinetics, and non-covalent interactions* version 2025-05-22. <https://www.chemie.uni-bonn.de/grimme/de/software/gmtkn/gmtkn55>. Dec. 2019. <https://www.chemie.uni-bonn.de/grimme/de/software/gmtkn/gmtkn55> (p. 44, 238–239, 241).
280. Goerigk, L., Hansen, A., Bauer, C., Ehrlich, S., Najibi, A. & Grimme, S. A look at the density functional theory zoo with the advanced GMTKN55 database for general main group thermochemistry, kinetics and noncovalent interactions. *Phys. Chem. Chem. Phys.* **19**, 32184–32215. doi:[10.1039/C7CP04913G](https://doi.org/10.1039/C7CP04913G) (2017) (p. 44, 129, 139, 142, 147–149, 152, 233, 238–241).
281. Santra, G., Sylvetsky, N. & Martin, J. M. Minimally empirical double-hybrid functionals trained against the GMTKN55 database: revDSD-PBEP86-D4, revDOD-PBE-D4, and DOD-SCAN-D4. *J. Phys. Chem. A* **123**, 5129–5143. doi:[10.1021/acs.jpca.9b03157](https://doi.org/10.1021/acs.jpca.9b03157) (2019) (p. 44, 148, 152).
282. Ghosh, D. C. & Islam, N. Semiempirical evaluation of the global hardness of the atoms of 103 elements of the periodic table using the most probable radii as their size descriptors. *Int. J. Quantum Chem.* **110**, 1206–1213. doi:[10.1002/qua.22202](https://doi.org/10.1002/qua.22202) (2010) (p. 44).
283. Bade, W. L. Drude-model calculation of dispersion forces. I. General theory. *J. Chem. Phys.* **27**, 1280–1284. doi:[10.1063/1.1743991](https://doi.org/10.1063/1.1743991) (1957) (p. 45, 48).
284. Bade, W. & Kirkwood, J. G. Drude-model calculation of dispersion forces. II. The linear lattice. *J. Chem. Phys.* **27**, 1284–1288. doi:[10.1063/1.1743992](https://doi.org/10.1063/1.1743992) (1957) (p. 45, 48).
285. Rezáć, J., Riley, K. E. & Hobza, P. S66: A well-balanced database of benchmark interaction energies relevant to biomolecular structures. *J. Chem. Theory Comput.* **7**, 2427–2438. doi:[10.1021/ct2002946](https://doi.org/10.1021/ct2002946) (2011) (p. 45, 50, 115).
286. Rezáć, J., Riley, K. E. & Hobza, P. Erratum to "S66: A well-balanced database of benchmark interaction energies relevant to biomolecular structures". *J. Chem. Theory Comput.* **10**, 1359–1360. doi:[10.1021/ct5000692](https://doi.org/10.1021/ct5000692) (2014) (p. 45, 50).
287. Brauer, B., Kesharwani, M. K., Kozuch, S. & Martin, J. M. The S66 \times 8 benchmark for noncovalent interactions revisited: Explicitly correlated ab initio methods and density functional theory. *Phys. Chem. Chem. Phys.* **18**, 20905–20925. doi:[10.1039/C6CP00688D](https://doi.org/10.1039/C6CP00688D) (2016) (p. 45, 50, 109).
288. Chu, X. & Dalgarno, A. Linear response time-dependent density functional theory for van der Waals coefficients. *J. Chem. Phys.* **121**, 4083–4088. doi:[10.1063/1.1779576](https://doi.org/10.1063/1.1779576) (2004) (p. 46, 110).
289. Mitroy, J. a., Safranova, M. S. & Clark, C. W. Theory and applications of atomic and ionic polarizabilities. *J. Phys. B: At. Mol. Opt. Phys.* **43**, 202001. doi:[10.1088/0953-4075/43/20/202001](https://doi.org/10.1088/0953-4075/43/20/202001) (2010) (p. 46).

290. Dzuba, V., Kozlov, A. & Flambaum, V. Scalar static polarizabilities of lanthanides and actinides. *Phys. Rev. A* **89**, 042507. doi:[10.1103/PhysRevA.89.042507](https://doi.org/10.1103/PhysRevA.89.042507) (2014) (p. 46).
291. Mavroyannis, C. & Stephen, M. J. Dispersion forces. *Mol. Phys.* **5**, 629–638. doi:[10.1080/00268976200100721](https://doi.org/10.1080/00268976200100721) (1962) (p. 46).
292. Tang, K. T. Dynamic polarizabilities and van der Waals coefficients. *Phys. Rev.* **177**, 108. doi:[10.1103/PhysRev.177.108](https://doi.org/10.1103/PhysRev.177.108) (1969) (p. 46).
293. Stone, A. J. *The Theory of Intermolecular Forces* 2nd ed. ISBN: 9780199672394. doi:[10.1093/acprof:oso/9780199672394.001.0001](https://doi.org/10.1093/acprof:oso/9780199672394.001.0001) (Oxford University Press, 2013) (p. 46–47).
294. Claudot, J., Kim, W. J., Dixit, A., Kim, H., Gould, T., Rocca, D. & Lebègue, S. Benchmarking several van der Waals dispersion approaches for the description of intermolecular interactions. *J. Chem. Phys.* **148**, 064112. doi:[10.1063/1.5018818](https://doi.org/10.1063/1.5018818) (2018) (p. 46, 50–51).
295. Reilly, A. M. & Tkatchenko, A. Understanding the role of vibrations, exact exchange, and many-body van der Waals interactions in the cohesive properties of molecular crystals. *J. Chem. Phys.* **139**, 024705. doi:[10.1063/1.4812819](https://doi.org/10.1063/1.4812819) (2013) (p. 46, 50, 71, 79–80, 89–90, 140).
296. Bucko, T., Lebegue, S., Hafner, J. & Angyan, J. G. Improved density dependent correction for the description of London dispersion forces. *J. Chem. Theory Comput.* **9**, 4293–4299. doi:[10.1021/ct400694h](https://doi.org/10.1021/ct400694h) (2013) (p. 46, 83, 108).
297. Padé, H. *On the approximate representation of a function by rational fractions* in *Scientific annals of the école Normale Supérieure* **9** (1892), 3–93. doi:[10.24033/asens.378](https://doi.org/10.24033/asens.378) (p. 47).
298. Baker Jr, G. A. *The theory and application of the Padé approximant method* tech. rep. (Los Alamos Scientific Lab., Univ. of California, N. Mex., 1964). doi:[10.2172/4585866](https://doi.org/10.2172/4585866) (p. 47).
299. Tang, K. T. & Karplus, M. Padé-approximant calculation of the nonretarded van der Waals coefficients for two and three helium atoms. *Phys. Rev.* **171**, 70. doi:[10.1103/PhysRev.171.70](https://doi.org/10.1103/PhysRev.171.70) (1968) (p. 47).
300. Bell, W. W. *Special functions for scientists and engineers* ISBN: 0486317560 (Courier Corporation, 2004) (p. 47).
301. Glaisher, J. W. L. XXXII. On a class of definite integrals. *London, Edinburgh, and Dublin Philos. Mag. and J. Sci.* **42**, 294–302. doi:[10.1080/14786447108640568](https://doi.org/10.1080/14786447108640568) (1871) (p. 47).
302. Gauss, C. F. *Methodus nova integralium valores per approximationem inventi* doi:[10.1017/CBO9781139058247.008](https://doi.org/10.1017/CBO9781139058247.008) (apvd Henricvm Dieterich, 1815) (p. 48).
303. Lucas, A. Collective contributions to the long-range dipolar interaction in rare-gas crystals. *Physica* **35**, 353–368. doi:[10.1016/0031-8914\(67\)90184-X](https://doi.org/10.1016/0031-8914(67)90184-X) (1967) (p. 48).

304. Donchev, A. G. Many-body effects of dispersion interaction. *J. Chem. Phys.* **125**, 074713. doi:[10.1063/1.2337283](https://doi.org/10.1063/1.2337283) (2006) (p. 48).
305. Cao, J. & Berne, B. J. Many-body dispersion forces of polarizable clusters and liquids. *J. Chem. Phys.* **97**, 8628–8636. doi:[10.1063/1.463381](https://doi.org/10.1063/1.463381) (1992) (p. 48).
306. Cole, M. W., Velegol, D., Kim, H.-Y. & Lucas, A. A. Nanoscale van der Waals interactions. *Mol. Simul.* **35**, 849–866. doi:[10.1080/08927020902929794](https://doi.org/10.1080/08927020902929794) (2009) (p. 48).
307. Berthoumieux, H. & Maggs, A. C. Collective dispersion forces in the fluid state. *Europhys. Lett.* **91**, 56006. doi:[10.1209/0295-5075/91/56006](https://doi.org/10.1209/0295-5075/91/56006) (2010) (p. 48).
308. Massa, D., Ambrosetti, A. & Silvestrelli, P. L. Many-body van der Waals interactions beyond the dipole approximation. *J. Chem. Phys.* **154**, 224115. doi:[10.1063/5.0051604](https://doi.org/10.1063/5.0051604) (2021) (p. 49).
309. Poier, P. P., Adjoua, O., Lagardère, L. & Piquemal, J.-P. Generalized many-body dispersion correction through random-phase approximation for chemically accurate density functional theory. *J. Phys. Chem. Lett.* **14**, 1609–1617. doi:[10.1021/acs.jpclett.2c03722](https://doi.org/10.1021/acs.jpclett.2c03722) (2023) (p. 49).
310. Langreth, D. C. & Perdew, J. P. The exchange-correlation energy of a metallic surface. *Solid State Commun.* **17**, 1425–1429. doi:[10.1016/0038-1098\(75\)90618-3](https://doi.org/10.1016/0038-1098(75)90618-3) (1975) (p. 49).
311. Langreth, D. C. & Perdew, J. P. Exchange-correlation energy of a metallic surface: Wave-vector analysis. *Phys. Rev. B* **15**, 2884. doi:[10.1103/PhysRevB.15.2884](https://doi.org/10.1103/PhysRevB.15.2884) (1977) (p. 49).
312. Gunnarsson, O. & Lundqvist, B. I. Exchange and correlation in atoms, molecules, and solids by the spin-density-functional formalism. *Phys. Rev. B* **13**, 4274. doi:[10.1103/PhysRevB.13.4274](https://doi.org/10.1103/PhysRevB.13.4274) (1976) (p. 49, 63).
313. Gunnarsson, O. & Lundqvist, B. Erratum: Exchange and correlation in atoms, molecules, and solids by the spin-density-functional formalism. *Phys. Rev. B* **15**, 6006. doi:[10.1103/PhysRevB.15.6006.3](https://doi.org/10.1103/PhysRevB.15.6006.3) (1977) (p. 49).
314. Jurečka, P., Šponer, J., Černý, J. & Hobza, P. Benchmark database of accurate (MP2 and CCSD (T) complete basis set limit) interaction energies of small model complexes, DNA base pairs, and amino acid pairs. *Phys. Chem. Chem. Phys.* **8**, 1985–1993. doi:[10.1039/B600027D](https://doi.org/10.1039/B600027D) (2006) (p. 50, 115).
315. Bryenton, K. R. & Johnson, E. R. Many-body dispersion in model systems and the sensitivity of self-consistent screening. *J. Chem. Phys.* **158**. (Chapter 4 in this thesis), 204110. doi:[10.1063/5.0142465](https://doi.org/10.1063/5.0142465) (2023) (p. 51, 88, 123, 141, 238–241, 245).
316. Vydrov, O. A. & Van Voorhis, T. Dispersion interactions from a local polarizability model. *Phys. Rev. A: At. Mol. Opt. Phys.* **81**, 062708. doi:[10.1103/PhysRevA.81.062708](https://doi.org/10.1103/PhysRevA.81.062708) (2010) (p. 51, 108).

317. Gutle, C., Savin, A., Krieger, J. B. & Chen, J. Correlation energy contributions from low-lying states to density functionals based on an electron gas with a gap. *Int. J. Quantum Chem.* **75**, 885–888. doi:[10.1002/\(SICI\)1097-461X\(1999\)75:4/5<885::AID-QUA53>3.0.CO;2-F](https://doi.org/10.1002/(SICI)1097-461X(1999)75:4/5<885::AID-QUA53>3.0.CO;2-F) (1999) (p. 51).
318. Von Weizsäcker, C. F. Zur theorie der kernmassen. *Z. Phys.* **96**, 431–458. doi:[10.1007/BF01337700](https://doi.org/10.1007/BF01337700) (1935) (p. 51, 131).
319. Becke, A. D. & Edgecombe, K. E. A simple measure of electron localization in atomic and molecular systems. *J. Chem. Phys.* **92**, 5397–5403. doi:[10.1063/1.458517](https://doi.org/10.1063/1.458517) (1990) (p. 52).
320. Kümmel, S. & Perdew, J. P. Two avenues to self-interaction correction within Kohn—Sham theory: unitary invariance is the shortcut. *Mol. Phys.* **101**, 1363–1368. doi:[10.1080/0026897031000094506](https://doi.org/10.1080/0026897031000094506) (2003) (p. 52).
321. Sun, J., Xiao, B., Fang, Y., Haunschild, R., Hao, P., Ruzsinszky, A., Csonka, G. I., Scuseria, G. E. & Perdew, J. P. Density functionals that recognize covalent, metallic, and weak bonds. *Phys. Rev. Lett.* **111**, 106401. doi:[10.1103/PhysRevLett.111.106401](https://doi.org/10.1103/PhysRevLett.111.106401) (2013) (p. 52).
322. Sun, J., Ruzsinszky, A. & Perdew, J. P. Strongly constrained and appropriately normed semilocal density functional. *Phys. Rev. Lett.* **115**, 036402. doi:[10.1103/PhysRevLett.115.036402](https://doi.org/10.1103/PhysRevLett.115.036402) (2015) (p. 52, 62, 72–73, 75, 78).
323. Kannemann, F. O. & Becke, A. D. van der Waals interactions in density-functional theory: intermolecular complexes. *J. Chem. Theory Comput.* **6**, 1081–1088. doi:[10.1021/ct900699r](https://doi.org/10.1021/ct900699r) (2010) (p. 53, 59, 71, 79–80, 138).
324. Rumble, J. R. *CRC Handbook of Chemistry and Physics* ISBN: 9780367712600 (CRC press, 2021) (p. 55, 215).
325. Otero-de-la-Roza, A., DiLabio, G. A. & Johnson, E. R. Exchange–correlation effects for noncovalent interactions in density functional theory. *J. Chem. Theory Comput.* **12**, 3160–3175. doi:[10.1021/acs.jctc.6b00298](https://doi.org/10.1021/acs.jctc.6b00298) (2016) (p. 56).
326. Johnson, E. R. & Becke, A. D. A post-Hartree-Fock model of intermolecular interactions. *J. Chem. Phys.* **123**, 024101. doi:[10.1063/1.1949201](https://doi.org/10.1063/1.1949201) (2005) (p. 56, 110, 138).
327. Johnson, E. R. & Becke, A. D. Van der Waals interactions from the exchange hole dipole moment: application to bio-organic benchmark systems. *Chem. Phys. Lett.* **432**, 600–603. doi:[10.1016/j.cplett.2006.10.094](https://doi.org/10.1016/j.cplett.2006.10.094) (2006) (p. 56).
328. Becke, A. D. & Johnson, E. R. A density-functional model of the dispersion interaction. *J. Chem. Phys.* **123**, 154101. doi:[10.1063/1.2065267](https://doi.org/10.1063/1.2065267) (2005) (p. 57, 79).
329. Burden, R. L. & Faires, J. D. *Numerical analysis* 9th ed. ISBN: 0538733519 (Boston, MA: Brooks/Cole, Cengage Learning, 2010) (p. 58).

330. Becke, A. D. & Johnson, E. R. A unified density-functional treatment of dynamical, nondynamical and dispersion correlations. *J. Chem. Phys.* **127**, 124108. doi:[10.1063/1.2768530](https://doi.org/10.1063/1.2768530) (2007) (p. 59, 71).
331. Buijse, M. & Baerends, E. An approximate exchange-correlation hole density as a functional of the natural orbitals. *Mol. Phys.* **100**, 401–421. doi:[10.1080/00268970110070243](https://doi.org/10.1080/00268970110070243) (2002) (p. 59, 63, 129–130).
332. van Noorden, R., Maher, B. & Nuzzo, R. The Top 100 Papers. *Nature* **514**, 550–553. doi:[10.1038/514550a](https://doi.org/10.1038/514550a) (2014) (p. 60).
333. Ziegler, T., Rauk, A. & Baerends, E. J. Calculation of multiplet energies by the Hartree-Fock-Slater method. *Theor. Chim. Acta* **43**, 261–271. doi:[10.1007/BF00551551](https://doi.org/10.1007/BF00551551) (1977) (p. 60).
334. Cohen, A. J., Mori-Sánchez, P. & Yang, W. Fractional spins and static correlation error in density functional theory. *J. Chem. Phys.* **129**, 121104. doi:[10.1063/1.2987202](https://doi.org/10.1063/1.2987202) (2008) (p. 60).
335. Cohen, A. J., Mori-Sánchez, P. & Yang, W. Challenges for density functional theory. *Chem. Rev.* **112**, 289–320. doi:[10.1021/cr200107z](https://doi.org/10.1021/cr200107z) (2011) (p. 60).
336. Ess, D. H., Johnson, E. R., Hu, X. & Yang, W. Singlet-triplet energy gaps for diradicals from fractional-spin density-functional theory. *J. Phys. Chem. A* **115**, 76–83. doi:[10.1021/jp109280y](https://doi.org/10.1021/jp109280y) (2011) (p. 60).
337. Hollett, J. W. & Gill, P. M. W. The two faces of static correlation. *J. Chem. Phys.* **134**, 114111. doi:[10.1063/1.3570574](https://doi.org/10.1063/1.3570574) (2011) (p. 60).
338. Fogueri, U. R., Kozuch, S., Karton, A. & Martin, J. M. L. A simple DFT-based diagnostic for nondynamical correlation. *Theor. Chem. Acc.* **132**, 1291. doi:[10.1007/s00214-012-1291-y](https://doi.org/10.1007/s00214-012-1291-y) (2013) (p. 60).
339. Grimme, S. & Waletzke, M. A combination of Kohn–Sham density functional theory and multi-reference configuration interaction methods. *J. Chem. Phys.* **111**, 5645. doi:[10.1063/1.479866](https://doi.org/10.1063/1.479866) (1999) (p. 60).
340. Filatov, M., Huix-Rotllant, M. & Burghardt, I. Ensemble density functional theory method correctly describes bond dissociation, excited state electron transfer, and double excitations. *J. Chem. Phys.* **142**, 184104. doi:[10.1063/1.4919773](https://doi.org/10.1063/1.4919773) (2015) (p. 60).
341. Filatov, M. Spin-restricted Ensemble-referenced Kohn–Sham method: Basic principles and application to strongly correlated ground and excited states of molecules. *WIREs Comput. Mol. Sci.* **5**, 146–167. doi:[10.1002/wcms.1209](https://doi.org/10.1002/wcms.1209) (2015) (p. 60).
342. Filatov, M. *Ensemble DFT Approach to Excited States of Strongly Correlated Molecular Systems in Density-Functional Methods for Excited States* (eds Ferré, N., Filatov, M. & Huix-Rotllant, M.) 97–124 (Springer International Publishing, Cham, 2016). doi:[10.1007/128_2015_630](https://doi.org/10.1007/128_2015_630) (p. 60).

343. Gould, T. & Pittalis, S. Hartree and exchange in ensemble density functional theory: Avoiding the nonuniqueness disaster. *Phys. Rev. Lett.* **119**, 243001. doi:[10.1103/PhysRevLett.119.243001](https://doi.org/10.1103/PhysRevLett.119.243001) (2017) (p. 60).
344. Gould, T., Stefanucci, G. & Pittalis, S. Ensemble density functional theory: Insight from the fluctuation-dissipation theorem. *Phys. Rev. Lett.* **125**, 233001. doi:[10.1103/PhysRevLett.125.233001](https://doi.org/10.1103/PhysRevLett.125.233001) (2020) (p. 60).
345. Gould, T., Kronik, L. & Pittalis, S. Double excitations in molecules from ensemble density functionals: Theory and approximations. *Phys. Rev. A* **104**, 022803. doi:[/10.1103/PhysRevA.104.022803](https://doi.org/10.1103/PhysRevA.104.022803) (2021) (p. 60).
346. Gräfenstein, J. & Cremer, D. Can density functional theory describe multi-reference systems? Investigation of carbenes and organic biradicals. *Phys. Chem. Chem. Phys.* **2**, 2091–2103. doi:[10.1039/A909905K](https://doi.org/10.1039/A909905K) (2000) (p. 60).
347. Slipchenko, L. V. & Krylov, A. I. Singlet-triplet gaps in diradicals by the spin-flip approach: A benchmark study. *J. Chem. Phys.* **117**, 4694. doi:[10.1063/1.1498819](https://doi.org/10.1063/1.1498819) (2002) (p. 60).
348. Peng, D., Hu, X., Devarajan, D., Ess, D. H., Johnson, E. R. & Yang, W. Variational Fractional-Spin Density-Functional Theory for Diradicals. *J. Chem. Phys.* **137**, 114112. doi:[10.1063/1.4749242](https://doi.org/10.1063/1.4749242) (2012) (p. 60).
349. Becke, A. D. Density functionals for static, dynamical, and strong correlation. *J. Chem. Phys.* **138**, 074109. doi:[10.1063/1.4790598](https://doi.org/10.1063/1.4790598) (2013) (p. 60).
350. Kong, J. & Proynov, E. Density functional model for nondynamic and strong correlation. *J. Chem. Theory Comput.* **12**, 133–143. doi:[10.1021/acs.jctc.5b00801](https://doi.org/10.1021/acs.jctc.5b00801) (2016) (p. 60).
351. Laqua, H., Kussmann, J. & Ochsenfeld, C. Density functional theory model for multi-reference systems based on the exact-exchange hole normalization. *J. Chem. Phys.* **148**, 121101. doi:[10.1063/1.5025334](https://doi.org/10.1063/1.5025334) (2018) (p. 60).
352. Wodyński, A., Arbuznikov, A. V. & Kaupp, M. Local hybrid functionals augmented by a strong-correlation model. *J. Chem. Phys.* **155**, 144101. doi:[10.1063/5.0058917](https://doi.org/10.1063/5.0058917) (2021) (p. 60).
353. Filatov, M. & Shaik, S. A Spin-restricted ensemble-referenced Kohn–Sham method and its application to diradicaloid situations. *Chem. Phys. Lett.* **304**, 429–437. doi:[10.1016/S0009-2614\(99\)00336-X](https://doi.org/10.1016/S0009-2614(99)00336-X) (1999) (p. 60).
354. Chermette, H., Ciofini, I., Mariotti, F. & Daul, C. Correct dissociation behavior of radical ions such as H_2^+ in density functional calculations. *J. Chem. Phys.* **114**, 1447–1453. doi:[10.1063/1.1332989](https://doi.org/10.1063/1.1332989) (2001) (p. 61–62, 66).
355. Gräfenstein, J., Kraka, E. & Cremer, D. The impact of the self-interaction error on the density functional theory description of dissociating radical cations: Ionic and covalent dissociation limits. *J. Chem. Phys.* **120**, 524–539. doi:[10.1063/1.1630017](https://doi.org/10.1063/1.1630017) (2004) (p. 61–62, 66).

356. Ruzsinszky, A., Perdew, J. P. & Csonka, G. I. Binding energy curves from nonempirical density functionals. I. Covalent bonds in closed-shell and radical molecules. *J. Phys. Chem. A* **109**, 11006–11014. doi:[10.1021/jp0534479](https://doi.org/10.1021/jp0534479) (2005) (p. 61, 66).
357. Janesko, B. G., Proynov, E., Kong, J., Scalmani, G. & Frisch, M. J. Practical density functionals beyond the overdelocalization–underbinding zero-sum game. *J. Phys. Chem. Lett.* **8**, 4314–4318. doi:[10.1021/acs.jpclett.7b02023](https://doi.org/10.1021/acs.jpclett.7b02023) (2017) (p. 61–62, 66).
358. Ruiz, E., Salahub, D. R. & Vela, A. Charge-transfer complexes: Stringent tests for widely used density functionals. *J. Phys. Chem.* **100**, 12265–12276. doi:[10.1021/jp9533077](https://doi.org/10.1021/jp9533077) (1996) (p. 61).
359. Sini, G., Sears, J. S. & Brèdas, J.-L. Evaluating the performance of DFT functionals in assessing the interaction energy and ground-state charge transfer of donor/acceptor complexes: tetrathiafulvalene-tetracyanoquinodimethane (TTF-TCNQ) as a model case. *J. Chem. Theory Comput.* **7**, 602–609. doi:[10.1021/ct1005517](https://doi.org/10.1021/ct1005517) (2011) (p. 61).
360. Steinmann, S. N., Piemontesi, C., Delachat, A. & Corminboeuf, C. Why are the interaction energies of charge-transfer complexes challenging for DFT?. *J. Chem. Theory Comput.* **8**, 1629–1640. doi:[10.1021/ct200930x](https://doi.org/10.1021/ct200930x) (2012) (p. 61).
361. Becke, A. D., Dale, S. G. & Johnson, E. R. Correct charge transfer in CT complexes from the Becke'05 density functional. *J. Chem. Phys.* **148**, 211101. doi:[10.1063/1.5039742](https://doi.org/10.1063/1.5039742) (2018) (p. 61).
362. Lynch, B. J. & Truhlar, D. G. How well can hybrid density functional methods predict transition state geometries and barrier heights? *J. Phys. Chem. A* **105**, 2936–2941. doi:[10.1021/jp004262z](https://doi.org/10.1021/jp004262z) (2001) (p. 61).
363. Csonka, G. I. & Johnson, B. G. Inclusion of exact exchange for self-interaction corrected H3 density functional potential energy surface. *Theor. Chem. Acc.* **99**, 158–165. doi:[10.1007/s002140050318](https://doi.org/10.1007/s002140050318) (1998) (p. 61).
364. Patchkovskii, S. & Ziegler, T. Improving “difficult” reaction barriers with self-interaction corrected density functional theory. *J. Chem. Phys.* **116**, 7806–7813. doi:[10.1063/1.1468640](https://doi.org/10.1063/1.1468640) (2002) (p. 61).
365. Dickson, R. M. & Becke, A. D. Reaction barrier heights from an exact-exchange-based density-functional correlation model. *J. Chem. Phys.* **123**, 111101. doi:[10.1063/1.2035587](https://doi.org/10.1063/1.2035587) (2005) (p. 61).
366. Lingwood, M., Hammond, J. R., Hrovat, D. A., Mayer, J. M. & Borden, W. T. MPW1K performs much better than B3LYP in DFT calculations on reactions that proceed by proton-coupled electron transfer (PCET). *J. Chem. Theory Comput.* **2**, 740–745. doi:[10.1021/ct050282z](https://doi.org/10.1021/ct050282z) (2006) (p. 61).
367. Janesko, B. G. & Scuseria, G. E. Hartree–Fock orbitals significantly improve the reaction barrier heights predicted by semilocal density functionals. *J. Chem. Phys.* **128**. doi:[10.1063/1.2940738](https://doi.org/10.1063/1.2940738) (2008) (p. 61).

368. Sham, L. & Schlüter, M. Density-functional theory of the band gap. *Phys. Rev. B* **32**, 3883. doi:[10.1103/PhysRevB.32.3883](https://doi.org/10.1103/PhysRevB.32.3883) (1985) (p. 61).
369. Schlüter, M. & Sham, L. *Density-functional theory of the band gap* in *Adv. Quantum Chem.* 97–112 (Elsevier, 1990). doi:[10.1016/S0065-3276\(08\)60593-6](https://doi.org/10.1016/S0065-3276(08)60593-6) (p. 61).
370. Perdew, J. P. Density functional theory and the band gap problem. *Int. J. Quantum Chem.* **28**, 497–523. doi:[10.1002/qua.560280846](https://doi.org/10.1002/qua.560280846) (1985) (p. 61).
371. Cohen, A. J., Mori-Sánchez, P. & Yang, W. Fractional charge perspective on the band gap in density-functional theory. *Phys. Rev. B* **77**, 115123. doi:[10.1103/PhysRevB.77.115123](https://doi.org/10.1103/PhysRevB.77.115123) (2008) (p. 61).
372. Mori-Sánchez, P., Cohen, A. J. & Yang, W. Localization and delocalization errors in density functional theory and implications for band-gap prediction. *Phys. Rev. Lett.* **100**, 146401. doi:[10.1103/PhysRevLett.100.146401](https://doi.org/10.1103/PhysRevLett.100.146401) (2008) (p. 61).
373. Crowley, J. M., Tahir-Kheli, J. & Goddard III, W. A. Resolution of the band gap prediction problem for materials design. *J. Phys. Chem. Lett.* **7**, 1198–1203. doi:[10.1021/acs.jpclett.5b02870](https://doi.org/10.1021/acs.jpclett.5b02870) (2016) (p. 61).
374. Perdew, J. P., Yang, W., Burke, K., Yang, Z., Gross, E. K., Scheffler, M., Scuseria, G. E., Henderson, T. M., Zhang, I. Y., Ruzsinszky, A., *et al.* Understanding band gaps of solids in generalized Kohn–Sham theory. *Proc. Nat. Acad. Sci.* **114**, 2801–2806. doi:[10.1073/pnas.1621352114](https://doi.org/10.1073/pnas.1621352114) (2017) (p. 61).
375. McDowell, S. A., Amos, R. D. & Handy, N. C. Molecular polarisabilities—a comparison of density functional theory with standard ab initio methods. *Chem. Phys. Lett.* **235**, 1–4. doi:[10.1016/0009-2614\(95\)00076-G](https://doi.org/10.1016/0009-2614(95)00076-G) (1995) (p. 61).
376. Champagne, B., Perpète, E. A., Van Gisbergen, S. J., Baerends, E.-J., Snijders, J. G., Soubra-Ghaoui, C., Robins, K. A. & Kirtman, B. Assessment of conventional density functional schemes for computing the polarizabilities and hyperpolarizabilities of conjugated oligomers: An ab initio investigation of polyacetylene chains. *J. Chem. Phys.* **109**, 10489–10498. doi:[10.1063/1.477731](https://doi.org/10.1063/1.477731) (1998) (p. 61).
377. Mori-Sánchez, P., Wu, Q. & Yang, W. Accurate polymer polarizabilities with exact exchange density-functional theory. *J. Chem. Phys.* **119**, 11001–11004. doi:[10.1063/1.1630011](https://doi.org/10.1063/1.1630011) (2003) (p. 61).
378. Jacquemin, D., Perpète, E. A., Scalmani, G., Frisch, M. J., Kobayashi, R. & Adamo, C. Assessment of the efficiency of long-range corrected functionals for some properties of large compounds. *J. Chem. Phys.* **126**, 144105. doi:[10.1063/1.2715573](https://doi.org/10.1063/1.2715573) (2007) (p. 61).
379. Sancho-García, J., Pérez-Jiménez, Á. J. & Moscardó, F. Description of C(sp²)-C(sp²) Rotation in Butadiene by Density Functionals. *J. Phys. Chem. A* **105**, 11541–11548. doi:[10.1021/jp0120615](https://doi.org/10.1021/jp0120615) (2001) (p. 61).

380. Beran, G. J., Sugden, I. J., Greenwell, C., Bowskill, D., Pantelides, C. C. & Adjiman, C. S. How many more polymorphs of ROY remain undiscovered? *Chem. Sci.* **13**, 1288–1297. doi:[10.1039/D1SC06074K](https://doi.org/10.1039/D1SC06074K) (2022) (p. 61).
381. Woodcock, H. L., Schaefer, H. F. & Schreiner, P. R. Problematic energy differences between cumulenes and poly-ynes: Does this point to a systematic improvement of density functional theory? *J. Phys. Chem. A* **106**, 11923–11931. doi:[10.1021/jp0212895](https://doi.org/10.1021/jp0212895) (2002) (p. 61).
382. Cai, Z.-L., Sendt, K. & Reimers, J. R. Failure of density-functional theory and time-dependent density-functional theory for large extended π systems. *J. Chem. Phys.* **117**, 5543–5549. doi:[10.1063/1.1501131](https://doi.org/10.1063/1.1501131) (2002) (p. 61).
383. Johnson, E. R., Clarkin, O. J. & DiLabio, G. A. Density functional theory based model calculations for accurate bond dissociation enthalpies. 3. A single approach for XH, XX, and XY (X, Y = C, N, O, S, halogen) bonds. *J. Phys. Chem. A* **107**, 9953–9963. doi:[10.1021/jp035315q](https://doi.org/10.1021/jp035315q) (2003) (p. 61).
384. Jacquemin, D., Femenias, A., Chermette, H., Ciofini, I., Adamo, C., André, J.-M. & Perpète, E. A. Assessment of several hybrid DFT functionals for the evaluation of bond length alternation of increasingly long oligomers. *J. Phys. Chem. A* **110**, 5952–5959. doi:[10.1021/jp060541w](https://doi.org/10.1021/jp060541w) (2006) (p. 61).
385. Heaton-Burgess, T. & Yang, W. Structural manifestation of the delocalization error of density functional approximations: C₄N+ 2 rings and C₂₀ bowl, cage, and ring isomers. *J. Chem. Phys.* **132**, 234113. doi:[10.1063/1.3445266](https://doi.org/10.1063/1.3445266) (2010) (p. 61).
386. White, M. A., Kahwaji, S., Freitas, V. L., Siewert, R., Weatherby, J. A., Ribeiro da Silva, M. D., Verevkin, S. P., Johnson, E. R. & Zwanziger, J. W. The Relative Thermodynamic stability of diamond and graphite. *Angew. Chem. Int. Ed.* **60**, 1546–1549. doi:[10.1002/anie.202009897](https://doi.org/10.1002/anie.202009897) (2021) (p. 61).
387. Nam, S., Cho, E., Sim, E. & Burke, K. Explaining and fixing DFT failures for torsional barriers. *J. Phys. Chem. Lett.* **12**, 2796–2804. doi:[10.1021/acs.jpclett.1c00426](https://doi.org/10.1021/acs.jpclett.1c00426) (2021) (p. 61).
388. Greenwell, C. & Beran, G. J. Inaccurate conformational energies still hinder crystal structure prediction in flexible organic molecules. *Cryst. Growth Des.* **20**, 4875–4881. doi:[10.1021/acs.cgd.0c00676](https://doi.org/10.1021/acs.cgd.0c00676) (2020) (p. 61).
389. Otero-de-la-Roza, A., Johnson, E. R. & DiLabio, G. A. Halogen bonding from dispersion-corrected density-functional theory: the role of delocalization error. *J. Chem. Theory Comput.* **10**, 5436–5447. doi:[10.1021/ct500899h](https://doi.org/10.1021/ct500899h) (2014) (p. 61).
390. Kim, Y., Song, S., Sim, E. & Burke, K. Halogen and chalcogen binding dominated by density-driven errors. *J. Phys. Chem. Lett.* **10**, 295–301. doi:[10.1021/acs.jpclett.8b03745](https://doi.org/10.1021/acs.jpclett.8b03745) (2019) (p. 61).

391. Mehta, N., Fellowes, T., White, J. M. & Goerigk, L. CHAL336 benchmark set: How well do quantum-chemical methods describe chalcogen-bonding interactions? *J. Chem. Theory Comput.* **17**, 2783–2806. doi:[10.1021/acs.jctc.1c00006](https://doi.org/10.1021/acs.jctc.1c00006) (2021) (p. 61).
392. LeBlanc, L. M., Dale, S. G., Taylor, C. R., Becke, A. D., Day, G. M. & Johnson, E. R. Pervasive Delocalisation Error Causes Spurious Proton Transfer in Organic Acid–Base Co-Crystals. *Angew. Chem. Int. Ed.* **57**, 14906–14910. doi:[10.1002/anie.201809381](https://doi.org/10.1002/anie.201809381) (2018) (p. 61).
393. Perdew, J. P. & Zunger, A. Self-interaction correction to density-functional approximations for many-electron systems. *Phys. Rev. B* **23**, 5048–5079. doi:[10.1103/PhysRevB.23.5048](https://doi.org/10.1103/PhysRevB.23.5048) (1981) (p. 61–62, 69).
394. Perdew, J. P., Parr, R. G., Levy, M. & Balduz Jr, J. L. Density-functional theory for fractional particle number: derivative discontinuities of the energy. *Phys. Rev. Lett.* **49**, 1691. doi:[10.1103/PhysRevLett.49.1691](https://doi.org/10.1103/PhysRevLett.49.1691) (1982) (p. 61).
395. Mori-Sánchez, P., Cohen, A. J. & Yang, W. Many-electron self-interaction error in approximate density functionals. *J. Chem. Phys.* **125**, 201102. doi:[10.1063/1.2403848](https://doi.org/10.1063/1.2403848) (2006) (p. 61).
396. Ruzsinszky, A., Perdew, J. P., Csonka, G. I., Vydrov, O. A. & Scuseria, G. E. Spurious fractional charge on dissociated atoms: Pervasive and resilient self-interaction error of common density functionals. *J. Chem. Phys.* **125**. doi:[10.1063/1.2387954](https://doi.org/10.1063/1.2387954) (2006) (p. 61).
397. Cohen, A. J., Mori-Sánchez, P. & Yang, W. Insights into current limitations of density functional theory. *Science* **321**, 792. doi:[10.1126/science.1158722](https://doi.org/10.1126/science.1158722) (2008) (p. 61).
398. Zhang, Y. & Yang, W. *Perspective on “Density-functional theory for fractional particle number: derivative discontinuities of the energy”* in *Theor. Chem. Acc.* 346–348 (Springer, Berlin, Heidelberg, 2000). doi:[10.1007/s002149900021](https://doi.org/10.1007/s002149900021) (p. 61).
399. Henderson, T. M., Janesko, B. G. & Scuseria, G. E. Range separation and local hybridization in density functional theory. *J. Phys. Chem. A* **112**, 12530–12542. doi:[10.1021/jp806573k](https://doi.org/10.1021/jp806573k) (2008) (p. 61).
400. Perdew, J. P., Ruzsinszky, A., Constantin, L. A., Sun, J. & Csonka, G. I. Some fundamental issues in ground-state density functional theory: A guide for the perplexed. *J. Chem. Theory Comput.* **5**, 902–908. doi:[10.1021/ct800531s](https://doi.org/10.1021/ct800531s) (2009) (p. 61).
401. Ruzsinszky, A. & Perdew, J. P. Twelve outstanding problems in ground-state density functional theory: A bouquet of puzzles. *Comput. Theor. Chem.* **963**, 2–6. doi:[10.1016/j.comptc.2010.09.002](https://doi.org/10.1016/j.comptc.2010.09.002) (2011) (p. 61).
402. Cohen, A. J., Mori-Sánchez, P. & Yang, W. Challenges for density functional theory. *Chem. Rev.* **112**, 289–320. doi:[10.1021/cr200107z](https://doi.org/10.1021/cr200107z) (2012) (p. 61).

403. Becke, A. D. Fifty years of density-functional theory in chemical physics. *J. Chem. Phys.* **140**, 18A301. doi:[10.1063/1.4869598](https://doi.org/10.1063/1.4869598) (2014) (p. 61).
404. Janesko, B. G. Replacing hybrid density functional theory: Motivation and recent advances. *Chem. Soc. Rev.* **50**, 8470–8495. doi:[10.1039/D0CS01074J](https://doi.org/10.1039/D0CS01074J) (2021) (p. 61).
405. Zhao, Y. & Truhlar, D. G. A new local density functional for main-group thermochemistry, transition metal bonding, thermochemical kinetics, and non-covalent interactions. *J. Chem. Phys.* **125**, 194101. doi:[10.1063/1.2370993](https://doi.org/10.1063/1.2370993) (2006) (p. 62, 74, 78).
406. Polo, V., Gräfenstein, J., Kraka, E. & Cremer, D. Influence of the self-interaction error on the structure of the DFT exchange hole. *Chem. Phys. Lett.* **352**, 469–478. doi:[10.1016/S0009-2614\(01\)01478-6](https://doi.org/10.1016/S0009-2614(01)01478-6) (2002) (p. 63).
407. Slater, J. C. *The Self-Consistent Field for Molecular and Solids, Quantum Theory of Molecular and Solids, Vol. 4* ISBN: 9780070580381 (McGraw-Hill, New York, 1974) (p. 63).
408. Perdew, J. P., Chevary, J. A., Vosko, S. H., Jackson, K. A., Pederson, M. R., Singh, D. J. & Fiolhais, C. Atoms, molecules, solids, and surfaces: Applications of the generalized gradient approximation for exchange and correlation. *Phys. Rev. B* **46**, 6671. doi:[10.1103/PhysRevB.46.6671](https://doi.org/10.1103/PhysRevB.46.6671) (1992) (p. 63, 69–71).
409. Becke, A. D. Hartree-Fock exchange energy of an inhomogeneous electron gas. *Int. J. Quantum Chem.* **23**, 1915–1922. doi:[10.1002/qua.560230605](https://doi.org/10.1002/qua.560230605) (1983) (p. 65).
410. Dyson, F. *et al.* A meeting with Enrico Fermi. *Nature* **427**, 297–297. doi:[10.1038/427297a](https://doi.org/10.1038/427297a) (2004) (p. 67).
411. Pernal, K., Podeszwa, R., Patkowski, K. & Szalewicz, K. Dispersionless density functional theory. *Phys. Rev. Lett.* **103**, 263201. doi:[10.1103/PhysRevLett.103.263201](https://doi.org/10.1103/PhysRevLett.103.263201) (2009) (p. 68).
412. Pérez-Jordá, J. & Becke, A. D. A density-functional study of van der Waals forces: rare gas diatomics. *Chem. Phys. Lett.* **233**, 134–137. doi:[10.1016/0009-2614\(94\)01402-H](https://doi.org/10.1016/0009-2614(94)01402-H) (1995) (p. 68).
413. Johnson, E. R., Wolkow, R. A. & DiLabio, G. A. Application of 25 density functionals to dispersion-bound homomolecular dimers. *Chem. Phys. Lett.* **394**, 334–338. doi:[10.1016/j.cplett.2004.07.029](https://doi.org/10.1016/j.cplett.2004.07.029) (2004) (p. 68, 72).
414. Kannemann, F. O. & Becke, A. D. Van der Waals interactions in density-functional theory: Rare-gas diatomics. *J. Chem. Theory Comput.* **5**, 719–727. doi:[10.1021/ct800522r](https://doi.org/10.1021/ct800522r) (2009) (p. 68, 116, 121).
415. Gillan, M. J. Many-body exchange-overlap interactions in rare gases and water. *J. Chem. Phys.* **141**, 224106. doi:[10.1063/1.4903240](https://doi.org/10.1063/1.4903240) (2014) (p. 68).

416. Perdew, J. P., Ruzsinszky, A., Csonka, G. I., Vydrov, O. A., Scuseria, G. E., Constantin, L. A., Zhou, X. & Burke, K. Restoring the density-gradient expansion for exchange in solids and surfaces. *Phys. Rev. Lett.* **100**, 136406. doi:[10.1103/PhysRevLett.100.136406](https://doi.org/10.1103/PhysRevLett.100.136406) (2008) (p. 69–71).
417. Zhang, Y. & Yang, W. Comment on “Generalized gradient approximation made simple”. *Phys. Rev. Lett.* **80**, 890–890. doi:[10.1103/PhysRevLett.80.890](https://doi.org/10.1103/PhysRevLett.80.890) (1998) (p. 69–70).
418. Spanu, L., Sorella, S. & Galli, G. Nature and strength of interlayer binding in graphite. *Phys. Rev. Lett.* **103**, 196401. doi:[10.1103/PhysRevLett.103.196401](https://doi.org/10.1103/PhysRevLett.103.196401) (2009) (p. 69, 73).
419. Goerigk, L. Treating London-dispersion effects with the latest Minnesota density functionals: Problems and possible solutions. *J. Phys. Chem. Lett.* **6**, 3891–3896. doi:[10.1021/acs.jpclett.5b01591](https://doi.org/10.1021/acs.jpclett.5b01591) (2015) (p. 68, 78).
420. Gillan, M. J., Alfè, D. & Michaelides, A. Perspective: How good is DFT for water? *J. Chem. Phys.* **144**, 130901. doi:[10.1063/1.4944633](https://doi.org/10.1063/1.4944633) (2016) (p. 69).
421. Austin, A., Petersson, G. A., Frisch, M. J., Dobek, F. J., Scalmani, G. & Throssell, K. A density functional with spherical atom dispersion terms. *J. Chem. Theory Comput.* **8**, 4989–5007. doi:[10.1021/ct300778e](https://doi.org/10.1021/ct300778e) (2012) (p. 71).
422. Johnson, E. R., Becke, A. D., Sherrill, C. D. & DiLabio, G. A. Oscillations in meta-generalized-gradient approximation potential energy surfaces for dispersion-bound complexes. *J. Chem. Phys.* **131**, 034111. doi:[10.1063/1.3177061](https://doi.org/10.1063/1.3177061) (2009) (p. 72, 74).
423. Wheeler, S. E. & Houk, K. N. Integration grid errors for meta-GGA-predicted reaction energies: Origin of grid errors for the M06 suite of functionals. *J. Chem. Theory Comput.* **6**, 395–404. doi:[10.1021/ct900639j](https://doi.org/10.1021/ct900639j) (2010) (p. 72).
424. Dasgupta, S. & Herbert, J. M. Standard grids for high-precision integration of modern density functionals: SG-2 and SG-3. *J. Comp. Chem.* **38**, 869–882. doi:[10.1002/jcc.24761](https://doi.org/10.1002/jcc.24761) (2017) (p. 72).
425. Morgante, P. & Peverati, R. The devil in the details: A tutorial review on some undervalued aspects of density functional theory calculations. *Int. J. Quantum Chem.* **120**, e26332. doi:[10.1002/qua.26332](https://doi.org/10.1002/qua.26332) (2020) (p. 72).
426. Mardirossian, N. & Head-Gordon, M. How accurate are the Minnesota density functionals for noncovalent interactions, isomerization energies, thermochemistry, and barrier heights involving molecules composed of main-group elements? *J. Chem. Theory Comput.* **12**, 4303–4325. doi:[10.1021/acs.jctc.6b00637](https://doi.org/10.1021/acs.jctc.6b00637) (2016) (p. 72).
427. Jiménez-Hoyos, C. A., Janesko, B. G. & Scuseria, G. E. Evaluation of range-separated hybrid density functionals for the prediction of vibrational frequencies, infrared intensities, and Raman activities. *Phys. Chem. Chem. Phys.* **10**, 6621–6629. doi:[10.1039/B810877C](https://doi.org/10.1039/B810877C) (2008) (p. 72).

428. Csonka, G. I., French, A. D., Johnson, G. P. & Stortz, C. A. Evaluation of density functionals and basis sets for carbohydrates. *J. Chem. Theory Comput.* **5**, 679–692. doi:[10.1021/ct8004479](https://doi.org/10.1021/ct8004479) (2009) (p. 72).
429. Gould, T., Johnson, E. R. & Tawfik, S. A. Are dispersion corrections accurate outside equilibrium? A case study on benzene. *Beilstein J. Org. Chem.* **14**, 1181–1191. doi:[10.3762/bjoc.14.99](https://doi.org/10.3762/bjoc.14.99) (2018) (p. 72, 74).
430. Furness, J. W., Kaplan, A. D., Ning, J., Perdew, J. P. & Sun, J. Accurate and numerically efficient r^2 SCAN meta-generalized gradient approximation. *J. Phys. Chem. Lett.* **11**, 8208–8215. doi:[10.1021/acs.jpclett.0c02405](https://doi.org/10.1021/acs.jpclett.0c02405) (2020) (p. 73, 75).
431. Voorhis, T. V. & Scuseria, G. E. A novel form for the exchange-correlation energy functional. *J. Chem. Phys.* **109**, 400–410. doi:[10.1063/1.476577](https://doi.org/10.1063/1.476577) (1998) (p. 74).
432. Tao, J., Perdew, J. P., Staroverov, V. N. & Scuseria, G. E. Climbing the density functional ladder: Nonempirical meta-generalized gradient approximation designed for molecules and solids. *Phys. Rev. Lett.* **91**, 146401. doi:[10.1103/PhysRevLett.91.146401](https://doi.org/10.1103/PhysRevLett.91.146401) (2003) (p. 74).
433. Tang, K. & Toennies, J. The van der Waals potentials between all the rare gas atoms from He to Rn. *J. Chem. Phys.* **118**, 4976–4983. doi:[10.1063/1.1543944](https://doi.org/10.1063/1.1543944) (2003) (p. 75, 104, 106).
434. Becke, A. D. & Dickson, R. M. Numerical-solution of Schrödinger's equation in polyatomic-molecules. *J. Chem. Phys.* **92**, 3610. doi:[10.1063/1.457869](https://doi.org/10.1063/1.457869) (1990) (p. 75, 224).
435. Becke, A. D. A multicenter numerical integration scheme for polyatomic molecules. *J. Chem. Phys.* **88**, 2547–2553. doi:[10.1063/1.454033](https://doi.org/10.1063/1.454033) (1988) (p. 74).
436. Ehlert, S., Huniar, U., Ning, J., Furness, J. W., Sun, J., Kaplan, A. D., Perdew, J. P. & Brandenburg, J. G. r^2 SCAN-D4: Dispersion corrected meta-generalized gradient approximation for general chemical applications. *J. Chem. Phys.* **154**, 061101. doi:[10.1063/5.0041008](https://doi.org/10.1063/5.0041008) (2021) (p. 74).
437. Zhao, Y. & Truhlar, D. G. The M06 suite of density functionals for main group thermochemistry, thermochemical kinetics, noncovalent interactions, excited states, and transition elements: two new functionals and systematic testing of four M06-class functionals and 12 other functionals. *Theor. Chem. Acc.* **120**, 215–241. doi:[10.1007/s00214-007-0310-x](https://doi.org/10.1007/s00214-007-0310-x) (2008) (p. 74).
438. Vanommeslaeghe, K., Hatcher, E., Acharya, C., Kundu, S., Zhong, S., Shim, J., Darian, E., Guvench, O., Lopes, P., Vorobyov, I., *et al.* CHARMM general force field: A force field for drug-like molecules compatible with the CHARMM all-atom additive biological force fields. *J. Comput. Chem.* **31**, 671–690. doi:[10.1002/jcc.21367](https://doi.org/10.1002/jcc.21367) (2010) (p. 79–80).

439. Wang, J., Wolf, R. M., Caldwell, J. W., Kollman, P. A. & Case, D. A. Development and testing of a general amber force field. *J. Comput. Chem.* **25**, 1157–1174. doi:[10.1002/jcc.20035](https://doi.org/10.1002/jcc.20035) (2004) (p. 79–80).
440. Jorgensen, W. L. & Tirado-Rives, J. Potential energy functions for atomic-level simulations of water and organic and biomolecular systems. *Proc. Natl. Acad. Sci.* **102**, 6665–6670. doi:[10.1073/pnas.0408037102](https://doi.org/10.1073/pnas.0408037102) (2005) (p. 79–80).
441. Lennard-Jones, J. E. Cohesion. *Proc. Phys. Sci.* **43**, 461–482. doi:[10.1088/0959-5309/43/5/301](https://doi.org/10.1088/0959-5309/43/5/301) (1931) (p. 79).
442. Wu, X., Vargas, M. C., Nayak, S., Lotrich, V. & Scoles, G. Towards extending the applicability of density functional theory to weakly bound systems. *J. Chem. Phys.* **115**, 8748–8757. doi:[10.1080/00268970412331333474](https://doi.org/10.1080/00268970412331333474) (2001) (p. 79).
443. Sato, T., Tsuneda, T. & Hirao, K. Van der Waals interactions studied by density functional theory. *Mol. Phys.* **103**, 1151–1164. doi:[10.1080/00268970412331333474](https://doi.org/10.1080/00268970412331333474) (2005) (p. 79).
444. Otero-de-la-Roza, A. & Johnson, E. R. Predicting energetics of supramolecular systems using the XDM dispersion model. *J. Chem. Theory Comput.* **11**, 4033–4040. doi:[10.1021/acs.jctc.5b00044](https://doi.org/10.1021/acs.jctc.5b00044) (2015) (p. 79).
445. Mohebifar, M., Johnson, E. R. & Rowley, C. N. Evaluating force-field London dispersion coefficients using the exchange-hole dipole moment model. *J. Chem. Theory Comput.* **13**, 6146–6157. doi:[10.1021/acs.jctc.7b00522](https://doi.org/10.1021/acs.jctc.7b00522) (2017) (p. 80).
446. Walters, E. T., Mohebifar, M., Johnson, E. R. & Rowley, C. N. Evaluating the London dispersion coefficients of protein force fields using the exchange-hole dipole moment model. *J. Phys. Chem. B* **122**, 6690–6701. doi:[10.1021/acs.jpcb.8b02814](https://doi.org/10.1021/acs.jpcb.8b02814) (2018) (p. 80).
447. Mohebifar, M. & Rowley, C. N. An efficient and accurate model for water with an improved non-bonded potential. *J. Chem. Phys.* **153**, 134105. doi:[10.1063/5.0014469](https://doi.org/10.1063/5.0014469) (2020) (p. 80).
448. Alkan, M., Xu, P. & Gordon, M. S. Many-body dispersion in molecular clusters. *J. Phys. Chem. A* **123**, 8406–8416. doi:[10.1021/acs.jpca.9b05977](https://doi.org/10.1021/acs.jpca.9b05977) (2019) (p. 81).
449. Von Lilienfeld, O. A. & Tkatchenko, A. Two-and three-body interatomic dispersion energy contributions to binding in molecules and solids. *J. Chem. Phys.* **132**, 234109. doi:[10.1063/1.3432765](https://doi.org/10.1063/1.3432765) (2010) (p. 81).
450. Johnson, E. R. Dependence of dispersion coefficients on atomic environment. *J. Chem. Phys.* **135**, 234109. doi:[10.1063/1.3670015](https://doi.org/10.1063/1.3670015) (2011) (p. 81, 89).
451. Wyckoff, R. W. G. & Wyckoff, R. W. G. *Crystal structures* ISBN: 0470968605 (Interscience publishers New York, 1963) (p. 81–82, 84–85).

452. Ruiz, V. G., Liu, W., Zojer, E., Scheffler, M. & Tkatchenko, A. Density-functional theory with screened van der Waals interactions for the modeling of hybrid inorganic-organic systems. *Phys. Rev. Lett.* **108**, 146103. doi:[10.1103/PhysRevLett.108.146103](https://doi.org/10.1103/PhysRevLett.108.146103) (2012) (p. 81–82).
453. Marzari, N., Vanderbilt, D., De Vita, A. & Payne, M. C. Thermal contraction and disordering of the Al (110) surface. *Phys. Rev. Lett.* **82**, 3296. doi:[10.1103/PhysRevLett.82.3296](https://doi.org/10.1103/PhysRevLett.82.3296) (1999) (p. 82, 85).
454. Otero-de-la-Roza, A. & Johnson, E. R. Application of XDM to ionic solids: The importance of dispersion for bulk moduli and crystal geometries. *J. Chem. Phys.* **153**, 054121. doi:[10.1063/5.0015133](https://doi.org/10.1063/5.0015133) (2020) (p. 82, 84).
455. Cutini, M., Maschio, L. & Ugliengo, P. Exfoliation energy of layered materials by DFT-D: Beware of dispersion! *J. Chem. Theory Comput.* **16**, 5244–5252. doi:[10.1021/acs.jctc.0c00149](https://doi.org/10.1021/acs.jctc.0c00149) (2020) (p. 82).
456. Bultinck, P., Van Alsenoy, C., Ayers, P. W. & Carbó-Dorca, R. Critical analysis and extension of the Hirshfeld atoms in molecules. *J. Chem. Phys.* **126**, 144111. doi:[10.1021/ct4000923](https://doi.org/10.1021/ct4000923) (2007) (p. 83).
457. Verstraelen, T., Ayers, P. W., Van Speybroeck, V. & Waroquier, M. Hirshfeld-E partitioning: AIM charges with an improved trade-off between robustness and accurate electrostatics. *J. Chem. Theory Comput.* **9**, 2221–2225. doi:[10.1021/ct4000923](https://doi.org/10.1021/ct4000923) (2013) (p. 83).
458. Steinmann, S. N. & Corminboeuf, C. Comprehensive benchmarking of a density-dependent dispersion correction. *J. Chem. Theory Comput.* **7**, 3567–3577. doi:[10.1021/ct200602x](https://doi.org/10.1021/ct200602x) (2011) (p. 83).
459. Körzdörfer, T., Sears, J. S., Sutton, C. & Brédas, J.-L. Long-range corrected hybrid functionals for π -conjugated systems: Dependence of the range-separation parameter on conjugation length. *J. Chem. Phys.* **135**, 204107. doi:[10.1063/1.3663856](https://doi.org/10.1063/1.3663856) (2011) (p. 87).
460. Kronik, L., Stein, T., Refaelly-Abramson, S. & Baer, R. Excitation gaps of finite-sized systems from optimally tuned range-separated hybrid functionals. *J. Chem. Theory Comput.* **8**, 1515–1531. doi:[10.1021/ct2009363](https://doi.org/10.1021/ct2009363) (2012) (p. 87).
461. Garrett, K., Sosa Vazquez, X. A., Egri, S. B., Wilmer, J., Johnson, L. E., Robinson, B. H. & Isborn, C. M. Optimum exchange for calculation of excitation energies and hyperpolarizabilities of organic electro-optic chromophores. *J. Chem. Theory Comput.* **10**, 3821–3831. doi:[10.1021/ct500528z](https://doi.org/10.1021/ct500528z) (2014) (p. 87).
462. Coleman, S. *Lectures of Sidney Coleman on Quantum Field Theory* (eds Chen, B. G.-g., Derbes, D., Griffiths, D., Hill, B., Sohn, R. & Ting, Y.-S.) Foreword by David Kaiser. ISBN: 978-9814635509. doi:[10.1142/9371](https://doi.org/10.1142/9371) (World Scientific, 2019) (p. 88).

463. Reilly, A. M. & Tkatchenko, A. van der Waals dispersion interactions in molecular materials: beyond pairwise additivity. *Chem. Sci.* **6**, 3289–3301. doi:[10.1039/C5SC00410A](https://doi.org/10.1039/C5SC00410A) (2015) (p. 89).
464. Ouyang, W., Azuri, I., Mandelli, D., Tkatchenko, A., Kronik, L., Urbakh, M. & Hod, O. Mechanical and tribological properties of layered materials under high pressure: Assessing the importance of many-body dispersion effects. *J. Chem. Theory Comput.* **16**, 666–676. doi:[10.1021/acs.jctc.9b00908](https://doi.org/10.1021/acs.jctc.9b00908) (2019) (p. 89).
465. Maass, F., Ajdari, M., Kabeer, F. C., Vogtland, M., Tkatchenko, A. & Tegeder, P. Nonadditivity of the adsorption energies of linear acenes on Au (111): molecular anisotropy and many-body effects. *J. Phys. Chem. Lett.* **10**, 1000–1004. doi:[10.1021/acs.jpcllett.9b00265](https://doi.org/10.1021/acs.jpcllett.9b00265) (2019) (p. 89).
466. Stöhr, M. & Tkatchenko, A. Quantum mechanics of proteins in explicit water: The role of plasmon-like solute-solvent interactions. *Sci. Adv.* **5**, eaax0024. doi:[10.1126/sciadv.aax0024](https://doi.org/10.1126/sciadv.aax0024) (2019) (p. 89).
467. Schubert, F., Rossi, M., Baldauf, C., Pagel, K., Warnke, S., von Helden, G., Filsinger, F., Kupser, P., Meijer, G., Salwiczek, M., *et al.* Exploring the conformational preferences of 20-residue peptides in isolation: Ac-Ala₁₉-Lys + H⁺ vs. Ac-Lys-Ala₁₉ + H⁺ and the current reach of DFT. *Phys. Chem. Chem. Phys.* **17**, 7373–7385. doi:[10.1039/C4CP05541A](https://doi.org/10.1039/C4CP05541A) (2015) (p. 89).
468. Gobre, V. V. & Tkatchenko, A. Scaling laws for van der Waals interactions in nanostructured materials. *Nat. Commun.* **4**, 1–6. doi:[10.1038/ncomms3341](https://doi.org/10.1038/ncomms3341) (2013) (p. 89).
469. Reilly, A. M. & Tkatchenko, A. Role of dispersion interactions in the polymorphism and entropic stabilization of the aspirin crystal. *Phys. Rev. Lett.* **113**, 055701. doi:[10.1103/PhysRevLett.113.055701](https://doi.org/10.1103/PhysRevLett.113.055701) (2014) (p. 89).
470. DiStasio Jr, R. A., von Lilienfeld, O. A. & Tkatchenko, A. Collective many-body van der Waals interactions in molecular systems. *Proc. Nat. Acad. Sci.* **109**, 14791–14795. doi:[10.1073/pnas.1208121109](https://doi.org/10.1073/pnas.1208121109) (2012) (p. 90, 113).
471. Hermann, J., DiStasio Jr, R. A. & Tkatchenko, A. First-principles models for van der Waals interactions in molecules and materials: Concepts, theory, and applications. *Chem. Rev.* **117**, 4714–4758. doi:[10.1021/acs.chemrev.6b00446](https://doi.org/10.1021/acs.chemrev.6b00446) (2017) (p. 90).
472. Ambrosetti, A., Ferri, N., DiStasio Jr, R. A. & Tkatchenko, A. Wavelike charge density fluctuations and van der Waals interactions at the nanoscale. *Science* **351**, 1171–1176. doi:[10.1126/science.aae0509](https://doi.org/10.1126/science.aae0509) (2016) (p. 90, 93).
473. Messiah, A. *Quantum mechanics—two volumes bound as one* ISBN: 0486409244 (Dover Publications New York, 2000) (p. 92).
474. Born, M. & Oppenheimer, R. Zur quantentheorie der moleküle. *Ann. Phys.* **389**, 457–484. doi:[10.1002/andp.19273892002](https://doi.org/10.1002/andp.19273892002) (1927) (p. 93, 215).

475. Stewart, J., Clegg, D. K. & Watson, S. *Calculus: early transcendentals* 971–981. ISBN: 1337613924 (Cengage Learning, 2020) (p. 97).
476. Kannemann, F. O. *Development and benchmarking of a semilocal density-functional approximation including dispersion* PhD thesis (Department of Chemistry, Dalhousie University, Halifax, Nova Scotia, Canada, 2013). <http://hdl.handle.net/10222/21434> (p. 101).
477. Applequist, J., Carl, J. R. & Fung, K.-K. Atom dipole interaction model for molecular polarizability. Application to polyatomic molecules and determination of atom polarizabilities. *J. Am. Chem. Soc.* **94**, 2952–2960. doi:[10.1021/ja00764a010](https://doi.org/10.1021/ja00764a010) (1972) (p. 105).
478. Gráfová, L., Pitonak, M., Rezac, J. & Hobza, P. Comparative study of selected wave function and density functional methods for noncovalent interaction energy calculations using the extended S22 data set. *J. Chem. Theory Comput.* **6**, 2365–2376. doi:[10.1021/ct1002253](https://doi.org/10.1021/ct1002253) (2010) (p. 107–109, 115).
479. Björkman, T. Testing several recent van der Waals density functionals for layered structures. *J. Chem. Phys.* **141**, 074708. doi:[10.1063/1.4893329](https://doi.org/10.1063/1.4893329) (2014) (p. 107–109, 126, 141).
480. Gobre, V. V. *Efficient modelling of linear electronic polarization in materials using atomic response functions* PhD thesis (Technische Universitaet Berlin, Straße des 17. Juni 135, 10623 Berlin, Germany, 2016). doi:[10.14279/depositonce-5503](https://doi.org/10.14279/depositonce-5503) (p. 107, 110).
481. Bučko, T., Lebègue, S., Ángyán, J. G. & Hafner, J. Extending the applicability of the Tkatchenko-Scheffler dispersion correction via iterative Hirshfeld partitioning. *J. Chem. Phys.* **141**, 034114. doi:[10.1063/1.4890003](https://doi.org/10.1063/1.4890003) (2014) (p. 108).
482. Burden, R. L. & Faires, J. D. *The nature of the physical world* ISBN: 978-1-998902-08-8. <https://lccn.loc.gov/29015261> (New York, The Macmillan company; Cambridge, Eng., The University press, 1928) (p. 114).
483. Nickerson, C. J., Bryenton, K. R., Price, A. J. & Johnson, E. R. Comparison of density-functional theory dispersion corrections for the DES15K database. *J. Phys. Chem. A* **127**. (Chapter 5 in this thesis), 8712–8722. doi:[10.1021/acs.jpca.3c04332](https://doi.org/10.1021/acs.jpca.3c04332) (2023) (p. 114, 116).
484. Donchev, A. G., Taube, A. G., Decolvenaere, E., Hargus, C., McGibbon, R. T., Law, K.-H., Gregersen, B. A., Li, J.-L., Palmo, K., Siva, K., et al. Quantum chemical benchmark databases of gold-standard dimer interaction energies. *Sci. Data* **8**, 55. doi:[10.1038/s41597-021-00833-x](https://doi.org/10.1038/s41597-021-00833-x) (2021) (p. 115–116, 126).
485. Boese, A. D. Basis set limit coupled-cluster studies of hydrogen-bonded systems. *Mol. Phys.* **113**, 1618–1629. doi:[10.1080/00268976.2014.1001806](https://doi.org/10.1080/00268976.2014.1001806) (2015) (p. 115).

486. Al-Hamdani, Y. S., Nagy, P. R., Zen, A., Barton, D., Kállay, M., Brandenburg, J. G. & Tkatchenko, A. Interactions between large molecules pose a puzzle for reference quantum mechanical methods. *Nat. Comm.* **12**, 3927. doi:[10.1038/s41467-021-24119-3](https://doi.org/10.1038/s41467-021-24119-3) (2021) (p. 115, 126).
487. Rezác, J., Riley, K. E. & Hobza, P. Extensions of the S66 data set: more accurate interaction energies and angular-displaced nonequilibrium geometries. *J. Chem. Theory Comput.* **7**, 3466–3470. doi:[10.1021/ct200523a](https://doi.org/10.1021/ct200523a) (2011) (p. 115).
488. Faver, J. C., Benson, M. L., He, X., Roberts, B. P., Wang, B., Marshall, M. S., Kennedy, M. R., Sherrill, C. D. & Merz Jr, K. M. Formal estimation of errors in computed absolute interaction energies of protein-ligand complexes. *J. Chem. Theory Comput.* **7**, 790–797. doi:[10.1021/ct100563b](https://doi.org/10.1021/ct100563b) (2011) (p. 115).
489. Rezac, J., Huang, Y., Hobza, P. & Beran, G. J. Benchmark calculations of three-body intermolecular interactions and the performance of low-cost electronic structure methods. *J. Chem. Theory Comput.* **11**, 3065–3079. doi:[10.1021/acs.jctc.5b00281](https://doi.org/10.1021/acs.jctc.5b00281) (2015) (p. 115).
490. Kozuch, S. & Martin, J. M. Halogen bonds: Benchmarks and theoretical analysis. *J. Chem. Theory Comput.* **9**, 1918–1931. doi:[10.1021/ct301064t](https://doi.org/10.1021/ct301064t) (2013) (p. 115).
491. Rezac, J., Riley, K. E. & Hobza, P. Benchmark calculations of noncovalent interactions of halogenated molecules. *J. Chem. Theory Comput.* **8**, 4285–4292. doi:[10.1021/ct300647k](https://doi.org/10.1021/ct300647k) (2012) (p. 115).
492. Gillan, M. J., Alfe, D. & Michaelides, A. Perspective: How good is DFT for water? *J. Chem. Phys.* **144**, 130901. doi:[10.1063/1.4944633](https://doi.org/10.1063/1.4944633) (2016) (p. 115).
493. Perdew, J. P., Ernzerhof, M. & Burke, K. Rationale for mixing exact exchange with density functional approximations. *J. Chem. Phys.* **105**, 9982–9985. doi:[10.1063/1.472933](https://doi.org/10.1063/1.472933) (1996) (p. 116).
494. Ihrig, A. C., Wieferink, J., Zhang, I. Y., Ropo, M., Ren, X., Rinke, P., Scheffler, M. & Blum, V. Accurate localized resolution of identity approach for linear-scaling hybrid density functionals and for many-body perturbation theory. *New J. Phys.* **17**, 093020. doi:[10.1088/1367-2630/17/9/093020](https://doi.org/10.1088/1367-2630/17/9/093020) (2015) (p. 116, 141, 231).
495. Havu, V., Blum, V., Havu, P. & Scheffler, M. Efficient O (N) integration for all-electron electronic structure calculation using numeric basis functions. *J. Chem. Phys.* **228**, 8367–8379. doi:doi.org/10.1016/j.jcp.2009.08.008 (2009) (p. 116, 141, 231).
496. Yu, V. W.-z., Corsetti, F., García, A., Huhn, W. P., Jacquelin, M., Jia, W., Lange, B., Lin, L., Lu, J., Mi, W., *et al.* ELSI: A unified software interface for Kohn-Sham electronic structure solvers. *Comput. Phys. Commun.* **222**, 267–285. doi:[10.1016/j.cpc.2017.09.007](https://doi.org/10.1016/j.cpc.2017.09.007) (2018) (p. 116, 141, 231).

497. Ren, X., Rinke, P., Blum, V., Wieferink, J., Tkatchenko, A., Sanfilippo, A., Reuter, K. & Scheffler, M. Resolution-of-identity approach to Hartree–Fock, hybrid density functionals, RPA, MP2 and GW with numeric atom-centered orbital basis functions. *New J. Phys.* **14**, 053020. doi:[10.1088/1367-2630/14/5/053020](https://doi.org/10.1088/1367-2630/14/5/053020) (2012) (p. 116, 141, 231).
498. Grimme, S. *DFT-D3 version 3.1, revision 1* version 2023-06-10. 2015. https://www.chemie.uni-bonn.de/grimme/de/software/dft-d3/get_dft-d3 (p. 117).
499. Caldeweyher, E., Ehlert, S. & Grimme, S. *DFT-D4 version 3.6.0* version 2023-08-14. 2023. <https://github.com/dftd4/dftd4> (p. 117).
500. Kendall, R. A., Dunning Jr, T. H. & Harrison, R. J. Electron affinities of the first-row atoms revisited. Systematic basis sets and wave functions. *J. Chem. Phys.* **96**, 6796–6806. doi:[10.1063/1.462569](https://doi.org/10.1063/1.462569) (1992) (p. 117).
501. Schuchardt, K. L., Didier, B. T., Elsethagen, T., Sun, L., Gurumoorthi, V., Chase, J., Li, J. & Windus, T. L. Basis set exchange: a community database for computational sciences. *J. Chem. Inf. Model.* **47**, 1045–1052. doi:[10.1021/ci600510j](https://doi.org/10.1021/ci600510j) (2007) (p. 117).
502. Prascher, B. P., Woon, D. E., Peterson, K. A., Dunning, T. H. & Wilson, A. K. Gaussian basis sets for use in correlated molecular calculations. VII. Valence, core-valence, and scalar relativistic basis sets for Li, Be, Na, and Mg. *Theor. Chem. Acc.* **128**, 69–82. doi:[10.1007/s00214-010-0764-0](https://doi.org/10.1007/s00214-010-0764-0) (2011) (p. 117).
503. Martin, J. M. Ab initio total atomization energies of small molecules—towards the basis set limit. *Chem. Phys. Lett.* **259**, 669–678. doi:[10.1016/0009-2614\(96\)00898-6](https://doi.org/10.1016/0009-2614(96)00898-6) (1996) (p. 117).
504. Otero-de-la-Roza, A. & Johnson, E. R. Analysis of density-functional errors for noncovalent interactions between charged molecules. *J. Phys. Chem. A* **124**, 353–361. doi:[10.1021/acs.jpca.9b10257](https://doi.org/10.1021/acs.jpca.9b10257) (2019) (p. 120).
505. Burns, L. A., Faver, J. C., Zheng, Z., Marshall, M. S., Smith, D. G., Vanommeslaeghe, K., MacKerell, A. D., Merz, K. M. & Sherrill, C. D. The BioFragment Database (BFD_b): An open-data platform for computational chemistry analysis of noncovalent interactions. *J. Chem. Phys.* **147**. doi:[10.1063/1.5001028](https://doi.org/10.1063/1.5001028) (2017) (p. 120).
506. Quiñonero, D., Garau, C., Frontera, A., Ballester, P., Costa, A. & Deyà, P. M. Structure and binding energy of anion- π and cation- π complexes: a comparison of MP2, RI-MP2, DFT, and DF-DFT methods. *J. Phys. Chem. A* **109**, 4632–4637. doi:[10.1021/jp044616c](https://doi.org/10.1021/jp044616c) (2005) (p. 123).
507. Ferretti, A., d'Ischia, M. & Prampolini, G. Benchmarking cation-π interactions: Assessment of density functional theory and Möller–Plesset second-order perturbation theory calculations with optimized basis sets (MP2^{mod}) for complexes of benzene, phenol, and catechol with Na⁺, K⁺, Rb⁺, and Cs⁺. *J. Phys. Chem. A* **124**, 3445–3459. doi:[10.1021/acs.jpca.0c02090](https://doi.org/10.1021/acs.jpca.0c02090) (2020) (p. 123).

508. Spicher, S., Caldeweyher, E., Hansen, A. & Grimme, S. Benchmarking London dispersion corrected density functional theory for noncovalent ion–π interactions. *Phys. Chem. Chem. Phys.* **23**, 11635–11648. doi:[10.1039/D1CP01333E](https://doi.org/10.1039/D1CP01333E) (2021) (p. 123).
509. Mahadevi, A. S. & Sastry, G. N. Cation- π interaction: Its role and relevance in chemistry, biology, and material science. *Chem. Rev.* **113**, 2100–2138. doi:[10.1021/cr300222d](https://doi.org/10.1021/cr300222d) (2013) (p. 123).
510. Rehak, F. R., Piccini, G., Alessio, M. & Sauer, J. Including dispersion in density functional theory for adsorption on flat oxide surfaces, in metal–organic frameworks and in acidic zeolites. *Phys. Chem. Chem. Phys.* **22**, 7577–7585. doi:[10.1039/D0CP00394H](https://doi.org/10.1039/D0CP00394H) (2020) (p. 126).
511. Sheldon, C., Paier, J. & Sauer, J. Adsorption of CH₄ on the Pt (111) surface: Random phase approximation compared to density functional theory. *J. Chem. Phys.* **155**, 174702. doi:[10.1063/5.0071995](https://doi.org/10.1063/5.0071995) (2021) (p. 126).
512. Okamoto, Y. Density functional theory calculations of alkali metal (Li, Na, and K) graphite intercalation compounds. *J. Phys. Chem. C* **118**, 16–19. doi:[10.1021/jp4063753](https://doi.org/10.1021/jp4063753) (2014) (p. 127).
513. Pande, V. & Viswanathan, V. Robust high-fidelity DFT study of the lithium-graphite phase diagram. *Phys. Rev. Mater.* **2**, 125401. doi:[10.1103/PhysRevMaterials.2.125401](https://doi.org/10.1103/PhysRevMaterials.2.125401) (2018) (p. 127).
514. Huang, J.-X., Csányi, G., Zhao, J.-B., Cheng, J. & Deringer, V. L. First-principles study of alkali-metal intercalation in disordered carbon anode materials. *J. Mater. Chem. A* **7**, 19070–19080. doi:[10.1039/C9TA05453G](https://doi.org/10.1039/C9TA05453G) (2019) (p. 127).
515. Panosetti, C., Anniés, S. B., Grosu, C., Seidlmaier, S. & Scheurer, C. DFTB modeling of lithium-intercalated graphite with machine-learned repulsive potential. *J. Phys. Chem. A* **125**, 691–699. doi:[10.1021/acs.jpca.0c09388](https://doi.org/10.1021/acs.jpca.0c09388) (2021) (p. 127).
516. Holland, J., Bhandari, A., Kramer, D., Milman, V., Hanke, F. & Skylaris, C.-K. Ab initio study of lithium intercalation into a graphite nanoparticle. *Mater. Adv.* **3**, 8469–8484. doi:[10.1039/D2MA00857B](https://doi.org/10.1039/D2MA00857B) (2022) (p. 127).
517. Dirac, P. A. M. The evolution of the physicist’s picture of nature. *Scientific American* **208**, 45–53. doi:[10.1038/scientificamerican0563-45](https://doi.org/10.1038/scientificamerican0563-45) (1963) (p. 128).
518. Dalgarno, A. & Davison, W. *The calculation of van der Waals interactions* in *Advances in atomic and molecular physics* 1–32 (Elsevier, 1966). doi:[10.1016/S0065-2199\(08\)60216-X](https://doi.org/10.1016/S0065-2199(08)60216-X) (p. 129).
519. Ángyán, J. G. On the exchange-hole model of London dispersion forces. *J. Chem. Phys.* **127**, 024108. doi:[10.1063/1.2749512](https://doi.org/10.1063/1.2749512) (2007) (p. 129).

520. Ayers, P. W. A perspective on the link between the exchange (-correlation) hole and dispersion forces. *J. Math. Chem.* **46**, 86–96. doi:[10.1007/s10910-008-9451-y](https://doi.org/10.1007/s10910-008-9451-y) (2009) (p. 129).
521. Heßelmann, A. Derivation of the dispersion energy as an explicit density- and exchange-hole functional. *J. Chem. Phys.* **130**, 084104. doi:[10.1063/1.3077939](https://doi.org/10.1063/1.3077939) (2009) (p. 129).
522. Becke, A. D. Thermochemical tests of a kinetic-energy dependent exchange-correlation approximation. *Int. J. Quantum Chem.* **52**, 625–632. doi:[10.1002/qua.560520855](https://doi.org/10.1002/qua.560520855) (1994) (p. 129–131, 223).
523. Löwdin, P.-O. Twenty-five years of Sanibel symposia: A brief historic and scientific survey. *Int. J. Quantum Chem.* **28**, 19–37. doi:[10.1002/qua.560280805](https://doi.org/10.1002/qua.560280805) (1985) (p. 130, 153).
524. Neumann, R., Nobes, R. H. & Handy, N. C. Exchange functionals and potentials. *Mol. Phys.* **87**, 1–36. doi:[10.1080/00268979600100011](https://doi.org/10.1080/00268979600100011) (1996) (p. 130).
525. Spackman, M. A. Time-dependent Hartree–Fock second-order molecular properties with a moderately sized basis set. II. Dispersion coefficients. *J. Chem. Phys.* **94**, 1295–1305. doi:[10.1063/1.460039](https://doi.org/10.1063/1.460039) (1991) (p. 138).
526. Kumar, A., Meath, W. J., Bündgen, P. & Thakkar, A. J. Reliable anisotropic dipole properties, and dispersion energy coefficients, for O₂ evaluated using constrained dipole oscillator strength techniques. *J. Chem. Phys.* **105**, 4927–4937. doi:[10.1063/1.472344](https://doi.org/10.1063/1.472344) (1996) (p. 138).
527. Kumar, A. & Meath, W. J. Dipole oscillator strength properties and dispersion energies for acetylene and benzene. *Mol. Phys.* **75**, 311–324. doi:[10.1080/00268970210162682](https://doi.org/10.1080/00268970210162682) (1992) (p. 138).
528. Kumar, A. Reliable isotropic dipole properties and dispersion energy coefficients for CCl₄. *J. Mol. Struct. THEOCHEM* **591**, 91–99. doi:[10.1016/S0166-1280\(02\)00213-0](https://doi.org/10.1016/S0166-1280(02)00213-0) (2002) (p. 138).
529. Kumar, A., Kumar, M. & Meath, W. J. Dipole oscillator strength properties and dispersion energies for SiH₄. *Chem. Phys.* **286**, 227–236. doi:[10.1016/S0301-0104\(02\)00926-6](https://doi.org/10.1016/S0301-0104(02)00926-6) (2003) (p. 138).
530. Kumar, A., Kumar, M. & Meath, W. J. Dipole oscillator strengths, dipole properties and dispersion energies for SiF₄. *Mol. Phys.* **101**, 1535–1543. doi:[10.1080/0026897031000092986](https://doi.org/10.1080/0026897031000092986) (2003) (p. 138).
531. Otero-de-la-Roza, A. *refdata* version 2025-02-04. Sept. 2015. <https://github.com/aoterodelaroza/refdata> (p. 138, 140–141).
532. Johnson, E. R. *gmtkn55-fhiaims* version 2024-12-23. Dec. 2024. <https://github.com/erin-r-johnson/gmtkn55-fhiaims> (p. 139).
533. Wittmann, L., Neugebauer, H., Grimme, S. & Bursch, M. Dispersion-corrected r2SCAN based double-hybrid functionals. *J. Chem. Phys.* **159**, 224103. doi:[10.1063/5.0174988](https://doi.org/10.1063/5.0174988) (2023) (p. 139, 225).

534. Dolgonos, G. A., Hoja, J. & Boese, A. D. Revised values for the X23 benchmark set of molecular crystals. *Phys. Chem. Chem. Phys.* **21**, 24333–24344. doi:[10.1039/C9CP04488D](https://doi.org/10.1039/C9CP04488D) (2019) (p. 140).
535. Otero-de-la-Roza, A., LeBlanc, L. M. & Johnson, E. R. Dispersion XDM with hybrid functionals: Delocalization error and halogen bonding in molecular crystals. *J. Chem. Theory Comput.* **15**, 4933–4944. doi:[10.1021/acs.jctc.9b00550](https://doi.org/10.1021/acs.jctc.9b00550) (2019) (p. 141).
536. Dean, J. A. *Lange's Handbook of Chemistry* 15e. ISBN: 978-0070163843 (McGraw-Hill, 1999) (p. 141).
537. Brandenburg, J. G., Maas, T. & Grimme, S. Benchmarking DFT and semiempirical methods on structures and lattice energies for ten ice polymorphs. *J. Chem. Phys.* **142**, 124104. doi:[10.1063/1.4916070](https://doi.org/10.1063/1.4916070) (2015) (p. 141).
538. Zagorac, D., Müller, H., Ruehl, S., Zagorac, J. & Rehme, S. Recent developments in the Inorganic Crystal Structure Database: Theoretical crystal structure data and related features. *J. Appl. Crystallogr.* **52**, 918–925. doi:[10.1107/S160057671900997X](https://doi.org/10.1107/S160057671900997X) (2019) (p. 141).
539. Levchenko, S. V., Ren, X., Wieferink, J., Johann, R., Rinke, P., Blum, V. & Scheffler, M. Hybrid functionals for large periodic systems in an all-electron, numeric atom-centered basis framework. *Comput. Phys. Commun.* **192**, 60–69. doi:[10.1016/j.cpc.2015.02.021](https://doi.org/10.1016/j.cpc.2015.02.021) (2015) (p. 141, 231).
540. Beck, A. D. Density-functional thermochemistry. III. The role of exact exchange. *J. Chem. Phys.* **98**, 5648–5652. doi:[10.1063/1.464913](https://doi.org/10.1063/1.464913) (1993) (p. 142).
541. Stephens, P. J., Devlin, F. J., Chabalowski, C. F. & Frisch, M. J. Ab initio calculation of vibrational absorption and circular dichroism spectra using density functional force fields. *J. Phys. Chem.* **98**, 11623–11627. doi:[10.1021/j100096a001](https://doi.org/10.1021/j100096a001) (1994) (p. 142).
542. Vosko, S. H., Wilk, L. & Nusair, M. Accurate spin-dependent electron liquid correlation energies for local spin density calculations: a critical analysis. *Can. J. Phys.* **58**, 1200–1211. doi:[10.1139/p80-159](https://doi.org/10.1139/p80-159) (1980) (p. 142).
543. Pople, J. A., Head-Gordon, M., Fox, D. J., Raghavachari, K. & Curtiss, L. A. Gaussian-1 theory: A general procedure for prediction of molecular energies. *J. Chem. Phys.* **90**, 5622–5629. doi:[10.1063/1.456415](https://doi.org/10.1063/1.456415) (1989) (p. 142).
544. Curtiss, L. A., Jones, C., Trucks, G. W., Raghavachari, K. & Pople, J. A. Gaussian-1 theory of molecular energies for second-row compounds. *J. Chem. Phys.* **93**, 2537–2545. doi:[10.1063/1.458892](https://doi.org/10.1063/1.458892) (1990) (p. 142).
545. Hoja, J. & Tkatchenko, A. First-principles stability ranking of molecular crystal polymorphs with the DFT+ MBD approach. *Faraday Discuss.* **211**, 253–274. doi:[10.1039/C8FD00066B](https://doi.org/10.1039/C8FD00066B) (2018) (p. 143).
546. Ratcliffe, S. *Oxford essential quotations* doi:[10.1093/acref/9780191866692.001.0001](https://doi.org/10.1093/acref/9780191866692.001.0001) (Oxford university press, Oxford, 2014) (p. 154).

547. Lehtola, S., Steigemann, C., Oliveira, M. J. & Marques, M. A. Recent developments in libxc—A comprehensive library of functionals for density functional theory. *SoftwareX* **7**, 1–5. doi:[10.1016/j.softx.2017.11.002](https://doi.org/10.1016/j.softx.2017.11.002) (2018) (p. 161).
548. Bryenton, K. R. *Darboux-Crum Transformations, Supersymmetric Quantum Mechanics, and the Eigenvalue Problem* Bachelor’s Thesis (University of Prince Edward Island, 2016). doi:[10.13140/RG.2.2.23129.98408](https://doi.org/10.13140/RG.2.2.23129.98408) (p. 213).
549. Bryenton, K. R. & Saad, N. Exactly solvable Schrödinger eigenvalue problems for new anharmonic potentials with variable bumps and depths. *Eur. Phys. J. Plus* **135**, 1–20. doi:[10.1140/epjp/s13360-020-00378-9](https://doi.org/10.1140/epjp/s13360-020-00378-9) (2020) (p. 213).
550. Moshinsky, M. & Kittel, C. How good is the Born-Oppenheimer approximation? *Proc. Natl. Acad. Sci.* **60**, 1110. doi:[10.1073/pnas.60.4.1110](https://doi.org/10.1073/pnas.60.4.1110) (1968) (p. 216).
551. Butler, L. J. Chemical reaction dynamics beyond the Born-Oppenheimer approximation. *Annu. Rev. Phys. Chem.* **49**, 125–171. doi:[10.1146/annurev.physchem.49.1.125](https://doi.org/10.1146/annurev.physchem.49.1.125) (1998) (p. 216).
552. Kolesov, G., Kaxiras, E. & Manousakis, E. Density functional theory beyond the Born-Oppenheimer approximation: Accurate treatment of the ionic zero-point motion. *Phys. Rev. B* **98**, 195112. doi:[10.1103/PhysRevB.98.195112](https://doi.org/10.1103/PhysRevB.98.195112) (2018) (p. 216).
553. Heßelmann, A. Geometry optimisations with a nonlocal density-functional theory method based on a double Hirshfeld partitioning. *J. Chem. Phys.* **149**, 044103. doi:[10.1063/1.5032175](https://doi.org/10.1063/1.5032175) (2018) (p. 221).

APPENDIX A

CHAPTER 1 SUPPLEMENT

In Chapter 1 we discussed how, using 2nd-order perturbation theory, it is possible to derive the interaction energy of London dispersion forces for two atoms with internuclear separation R , and show this energy is proportional to $R^{-6} + \mathcal{O}(R^{-8})$. The multipole expansion of this dispersion energy has the form

$$E_{\text{disp}} = -\frac{C_6}{R^6} - \frac{C_8}{R^8} - \frac{C_{10}}{R^{10}} - \dots \quad (\text{A.0.1})$$

where the C_6 term accounts for dipole-dipole interactions, the C_8 coefficient accounts for dipole-quadrupole interactions, and the C_{10} coefficient accounts for quadrupole-quadrupole and dipole-octupole interactions.

To supplement Section 1.2, Appendix A.1 will give a detailed derivation of an interacting hydrogen dimer from a perturbation theory perspective [66–69]. This section will explicitly derive the approximate interaction Hamiltonian given by Eq. (1.2.3), demonstrate why the first-order energy of Eq. (1.2.3) is zero, and derive Eq. (1.2.5). Appendix A.2 will detail how to arrive at Eq. (1.2.6) following the closure approximation, and will show how to use Eq. (1.2.6) together with Eq. (1.2.5) to obtain a highly-accurate approximation for the C_6 coefficient of hydrogen. Appendix A.3 will derive the asymptotic interaction between oscillating dipoles using methods similar to that shown in Refs. [68, 69].

A.1 THE DISPERSION INTERACTION FOR THE HYDROGEN DIMER

Consider two interacting hydrogen atoms with an internuclear separation $R \gg a_0$, where a_0 is the Bohr radius. Let (x_1, y_1, z_1) and (x_2, y_2, z_2) represent the coordinates of electrons 1 and 2 with respect to nuclei A and B respectively. The Hamiltonian for the H_2 dimer is

$$\hat{H} = \hat{h}_A + \hat{h}_B + \hat{H}_I, \quad (\text{A.1.1})$$

where $\hat{h}_A + \hat{h}_B$ represent the single-particle Hamiltonian for particles A and B respectively, and

$$\hat{H}_I = \frac{e^2}{4\pi\epsilon_0} \left[-\frac{1}{r_{1B}} - \frac{1}{r_{2A}} + \frac{1}{r_{12}} + \frac{1}{R} \right] \quad (\text{A.1.2})$$

captures the interacting terms of the Hamiltonian. The goal shall be to derive the dispersion energy expression for this system both numerically and in terms of the polarizability of the hydrogen atom. For the problem at hand, it is convenient to define position vectors

$$\begin{aligned} \mathbf{r}_{1A} &= x_1 \hat{\mathbf{i}} + y_1 \hat{\mathbf{j}} + z_1 \hat{\mathbf{k}}, & \mathbf{r}_{2A} &= x_2 \hat{\mathbf{i}} + y_2 \hat{\mathbf{j}} + (z_2 + R) \hat{\mathbf{k}}, \\ \mathbf{r}_{2B} &= x_2 \hat{\mathbf{i}} + y_2 \hat{\mathbf{j}} + z_2 \hat{\mathbf{k}}, & \mathbf{r}_{1B} &= x_1 \hat{\mathbf{i}} + y_1 \hat{\mathbf{j}} + (z_1 - R) \hat{\mathbf{k}}, \end{aligned} \quad (\text{A.1.3})$$

where $r = |\mathbf{r}|$. The $1/r_{12}$ term is troublesome for numeric integration, so we will eliminate it. Using the definitions from Eq. (A.1.3), this interaction Hamiltonian may instead be written as

$$\begin{aligned} \hat{H}_I &= \frac{e^2}{4\pi\epsilon_0 R} \left[-\frac{R}{\sqrt{x_1^2 + y_1^2 + (z_1 - R)^2}} - \frac{R}{\sqrt{x_2^2 + y_2^2 + (z_2 + R)^2}} \right. \\ &\quad \left. + \frac{R}{\sqrt{(x_2 - x_1)^2 + (y_2 - y_1)^2 + (z_2 - z_1 + R)^2}} + 1 \right] \end{aligned} \quad (\text{A.1.4})$$

and we may then write these rational terms in the form $(1 + x)^{-n}$. Let

$$(1 + X_1)^{-1/2} = \frac{R}{\sqrt{x_1^2 + y_1^2 + (z_1 - R)^2}}, \quad (\text{A.1.5})$$

$$(1 + X_2)^{-1/2} = \frac{R}{\sqrt{x_2^2 + y_2^2 + (z_2 + R)^2}}, \quad (\text{A.1.6})$$

$$(1 + X_3)^{-1/2} = \frac{R}{\sqrt{(x_2 - x_1)^2 + (y_2 - y_1)^2 + (z_2 - z_1 + R)^2}}, \quad (\text{A.1.7})$$

then X_1 , X_2 , and X_3 may be written in terms of r_{1A} and r_{2B} where applicable:

$$X_1 = \frac{r_{1A}^2 - 2z_1R}{R^2}, \quad (\text{A.1.8})$$

$$X_2 = \frac{r_{2B}^2 + 2z_2R}{R^2}, \quad (\text{A.1.9})$$

$$X_3 = \frac{r_{1A}^2 + r_{2B}^2 + 2R(z_2 - z_1) - 2(x_1x_2 + y_1y_2 + z_1z_2)}{R^2}. \quad (\text{A.1.10})$$

After substituting Eqs. (A.1.5) to (A.1.10) into Eq. (A.1.4), the binomial series expansion

$$(1 + x)^{-n} = 1 - nx + \frac{n(n+1)}{2!}x^2 - \dots, \quad x < 1, \quad (\text{A.1.11})$$

may be used to write an approximate expression for our interacting Hamiltonian,

$$\begin{aligned} \hat{H}_I &= \frac{e^2}{4\pi\epsilon_0 R} \left(-[1 + X_1]^{-1/2} - [1 + X_2]^{-1/2} + [1 + X_3]^{-1/2} + 1 \right) \\ &\approx \frac{e^2}{4\pi\epsilon_0 R} \left(-\left[1 - \frac{1}{2}X_1 + \frac{3}{8}X_1^2 \right] - \left[1 - \frac{1}{2}X_2 + \frac{3}{8}X_2^2 \right] + \left[1 - \frac{1}{2}X_3 + \frac{3}{8}X_3^2 \right] + 1 \right) \\ &= \frac{e^2}{4\pi\epsilon_0 R} \left(-\left[1 - \frac{1}{2}\frac{r_{1A}^2 - 2z_1R}{R^2} + \frac{3}{8}\left(\frac{r_{1A}^2 - 2z_1R}{R^2}\right)^2 \right] \right. \\ &\quad - \left[1 - \frac{1}{2}\frac{r_{2B}^2 + 2z_2R}{R^2} + \frac{3}{8}\left(\frac{r_{2B}^2 + 2z_2R}{R^2}\right)^2 \right] \\ &\quad + \left[1 - \frac{1}{2}\frac{r_{1A}^2 + r_{2B}^2 + 2R(z_2 - z_1) - 2(x_1x_2 + y_1y_2 + z_1z_2)}{R^2} \right. \\ &\quad \left. \left. + \frac{3}{8}\left(\frac{r_{1A}^2 + r_{2B}^2 + 2R(z_2 - z_1) - 2(x_1x_2 + y_1y_2 + z_1z_2)}{R^2}\right)^2 \right] + 1 \right), \quad (\text{A.1.12}) \end{aligned}$$

where we have only taken the first three terms from the expansion in Eq. (A.1.11). Grouping these terms by powers of R^{-n} yields the approximate interaction Hamiltonian for two interacting electric dipoles,

$$\hat{H}_I = \frac{e^2}{4\pi\epsilon_0 R} \left[\frac{1}{R^2} (x_1x_2 + y_1y_2 + z_1z_2) + \frac{3 \cdot 4R^2}{8R^4} (-2z_1z_2) + \dots \right]$$

$$\begin{aligned}
 &= \frac{e^2}{4\pi\epsilon_0 R^3} \left[(x_1 x_2 + y_1 y_2 + z_1 z_2) + \frac{3}{2} (-2z_1 z_2) + \dots \right] \\
 &= \frac{e^2}{4\pi\epsilon_0 R^3} [(x_1 x_2 + y_1 y_2 - 2z_1 z_2) + \dots],
 \end{aligned} \tag{A.1.13}$$

where the R^{-4} and R^{-5} terms from Eq. (A.1.12) were omitted. Eq. (A.1.13) corresponds to Eq. (1.2.3), and thus completes its derivation.

To calculate the interaction energy we need to consider the ground state wavefunction where $\psi = 1s_A(1) \cdot 1s_B(2) = |1, 1\rangle$ is written in terms of the hydrogen 1s orbitals. Upon applying first-order perturbation theory to the interaction Hamiltonian from Eq. (A.1.13), it is shown that the first-order energy is

$$\begin{aligned}
 E' &= \langle \psi | \hat{H}_I | \psi \rangle \\
 &\approx \left\langle 1, 1 \left| \frac{e^2}{4\pi\epsilon_0 R^3} (x_1 x_2 + y_1 y_2 - 2z_1 z_2) \right| 1, 1 \right\rangle \\
 &= \frac{e^2}{4\pi\epsilon_0 R^3} (\langle 1|x_1|1\rangle \langle 1|x_2|1\rangle + \langle 1|y_1|1\rangle \langle 1|y_2|1\rangle - 2 \langle 1|z_1|1\rangle \langle 1|z_2|1\rangle) \\
 &= 0,
 \end{aligned} \tag{A.1.14}$$

because the integrands are odd functions. Thus, this problem requires second-order perturbation theory where the ground state energy is expressed as

$$E'' = \sum_{m,n \neq 1} \frac{\left| \langle 1, 1 | \hat{H}_I | m, n \rangle \right|^2}{E_{1,1}^{H_2} - E_{m,n}^{H_2}}, \tag{A.1.15}$$

where the zeroth-order energy for the hydrogen dimer is

$$E_{m,n}^{H_2} = -\frac{1}{2} \left[\frac{1}{m^2} + \frac{1}{n^2} \right] \tag{A.1.16}$$

in Hartree atomic units. Thus, the second-order energy can be expressed as

$$\begin{aligned}
 E'' &= \sum_{m,n \neq 1} \frac{\left| \langle 1, 1 | \hat{H}_I | m, n \rangle \right|^2}{(-\frac{1}{2} [\frac{1}{1^2} + \frac{1}{1^2}]) - (-\frac{1}{2} [\frac{1}{m^2} + \frac{1}{n^2}])} \\
 &= - \sum_{m,n \neq 1} \frac{2m^2 n^2}{2m^2 n^2 - m^2 - n^2} \left| \left\langle 1, 1 \left| \frac{e^2}{4\pi\epsilon_0 R^3} (x_1 x_2 + y_1 y_2 - 2z_1 z_2) \right| m, n \right\rangle \right|^2,
 \end{aligned} \tag{A.1.17}$$

and thus completes the derivation of Eq. (1.2.5).

A.2 APPROXIMATE HYDROGEN-DIMER INTERACTION ENERGY

The closure (or Unsöld) approximation [77] applied to Eq. (A.1.15) obtains an approximate second-order energy of the form

$$\begin{aligned} E'' &= \sum_{m,n \neq 1} \frac{\left| \langle 1, 1 | \hat{H}_I | m, n \rangle \right|^2}{E_{1,1}^{\text{H}_2} - E_{m,n}^{\text{H}_2}} \\ &\approx -\frac{1}{\Delta E_A + \Delta E_B} \sum_{m,n \neq 1} \left| \langle 1, 1 | \hat{H}_I | n, m \rangle \right|^2 \\ &= -\frac{1}{\Delta E_A + \Delta E_B} \sum_{m,n \neq 1} \langle 1, 1 | \hat{H}_I | m, n \rangle \langle m, n | \hat{H}_I | 1, 1 \rangle \\ &= -\frac{1}{\Delta E_A + \Delta E_B} \langle 1, 1 | \hat{H}_I^2 | 1, 1 \rangle. \end{aligned} \quad (\text{A.2.1})$$

Here, ΔE is the mean excitation energy for either particle. Substituting in Eq. (A.1.13) into Eq. (A.2.1) gives a second-order correction of the form

$$\begin{aligned} E'' &\approx \frac{-1}{\Delta E_A + \Delta E_B} \left\langle 1, 1 \left| \left[\frac{e^2}{4\pi\epsilon_0 R^3} (x_1 x_2 + y_1 y_2 - 2z_1 z_2) \right]^2 \right| 1, 1 \right\rangle \\ &= \frac{-e^4}{(4\pi\epsilon_0)^2 R^6} \frac{\langle 1, 1 | x_1^2 x_2^2 + y_1^2 y_2^2 + 4z_1^2 z_2^2 + 2x_1 x_2 y_1 y_2 - 4x_1 x_2 z_1 z_2 - 4y_1 y_2 z_1 z_2 | 1, 1 \rangle}{\Delta E_A + \Delta E_B} \\ &= -\frac{2}{3} \frac{e^4}{(4\pi\epsilon_0)^2 R^6} \frac{\langle 1 | r^2 | 1 \rangle^2}{\Delta E_A + \Delta E_B}, \end{aligned} \quad (\text{A.2.2})$$

where the odd terms have vanished, the index on r was dropped as the particles are symmetric, and we have employed the fact that $\langle 1 | x^2 | 1 \rangle = \langle 1 | y^2 | 1 \rangle = \langle 1 | z^2 | 1 \rangle = \langle 1 | r^2 | 1 \rangle / 3$. Using the hydrogen 1s orbital, $\psi_{1s} = e^{-r/a_0} / \sqrt{\pi a_0^3}$, the expectation value of Eq. (A.2.2) may now be computed:

$$\begin{aligned} \langle 1 | r_1^2 | 1 \rangle &= \left\langle \frac{e^{-r/a_0}}{\sqrt{\pi a_0^3}} \left| r^2 \right| \frac{e^{-r/a_0}}{\sqrt{\pi a_0^3}} \right\rangle \\ &= \frac{1}{\pi a_0^3} \int_{r=0}^{\infty} \int_{\theta=0}^{\pi} \int_{\phi=0}^{2\pi} e^{-2r/a_0} r^4 \sin(\theta) dr d\theta d\phi \end{aligned}$$

$$= 3a_0^2. \quad (\text{A.2.3})$$

To further simplify Eq. (A.2.2), consider that the upper bound of $E_{1,1}^{\text{H}_2} - E_{m,n}^{\text{H}_2}$ is $-3/4$ when $m = n = 2$, and monotonically decreases to -1 for increasing values of m or n . Thus, we may approximate our mean excitation energies to be the hydrogen ionization energy, $\Delta E_A = \Delta E_B \approx I \approx 0.5$ a.u., and our ground-state's second-order energy becomes

$$E'' \approx -6/R^6 \quad (\text{A.2.4})$$

in Hartree atomic units, where $e = 4\pi\epsilon_0 = a_0 = 1$ a.u.

A.3 INTERACTION BETWEEN TWO OSCILLATING DIPOLES

Consider that two oppositely charged particles in a dipole, interacting with each other according to a harmonic oscillator potential,

$$V(\mathbf{r}) = \frac{k_s \mathbf{r} \cdot \mathbf{r}}{2} = \frac{1}{2} k_s (x^2 + y^2 + z^2), \quad (\text{A.3.1})$$

where $\mathbf{r} = (x, y, z)$ is the radial distance from the positive charge to the negative charge in Cartesian coordinates, and k_s is the spring constant. Let two identical dipoles be separated by a distance R . Via Eq. (A.1.13), the potential energy may be written as

$$V = \frac{1}{2} k_s (x_1^2 + y_1^2 + z_1^2) + \frac{1}{2} k_s (x_2^2 + y_2^2 + z_2^2) + \frac{e^2}{R^3} (x_1 x_2 + y_1 y_2 - 2z_1 z_2) \quad (\text{A.3.2})$$

where e is the charge on each end of the dipoles, and higher order terms in the expansion of Eq. (A.1.13) are ignored. To solve the Schrödinger equation for this potential, the following substitutions are made for convenience

$$X_{\pm} = (x_1 \pm x_2) / \sqrt{2}, \quad (\text{A.3.3})$$

$$Y_{\pm} = (y_1 \pm y_2) / \sqrt{2}, \quad (\text{A.3.4})$$

$$Z_{\pm} = (z_1 \pm z_2) / \sqrt{2}. \quad (\text{A.3.5})$$

Substituting Eqs. (A.3.3) to (A.3.5) into Eq. (A.3.2) permits the Schrödinger equation to be separable into six equations

$$-\frac{\hbar^2}{2m}\partial_{X_\pm}^2\psi_{X_\pm} + \frac{1}{2}\left(k_s \pm \frac{e^2}{R^3}\right)X_\pm^2\psi_{X_\pm} = E_{X_\pm}\psi_{X_\pm}, \quad (\text{A.3.6})$$

$$-\frac{\hbar^2}{2m}\partial_{Y_\pm}^2\psi_{Y_\pm} + \frac{1}{2}\left(k_s \pm \frac{e^2}{R^3}\right)Y_\pm^2\psi_{Y_\pm} = E_{Y_\pm}\psi_{Y_\pm}, \quad (\text{A.3.7})$$

$$-\frac{\hbar^2}{2m}\partial_{Z_\pm}^2\psi_{Z_\pm} + \frac{1}{2}\left(k_s \mp \frac{2e^2}{R^3}\right)Z_\pm^2\psi_{Z_\pm} = E_{Z_\pm}\psi_{Z_\pm}, \quad (\text{A.3.8})$$

where $\partial_\alpha \equiv \partial/\partial\alpha$. These separated equations fall under the more general harmonic form $V(x) = (ax + b)^2$ which has been solved in previous works [548, 549]. With substitutions of $a = \sqrt{(k_s \pm \frac{e^2}{R^3})/m}$ and $b = 0$, the energy eigenvalues of Eqs. (A.3.6) and (A.3.7) are given by

$$E_n = \frac{\hbar}{2}(2n+1)\sqrt{\left(k_s \pm \frac{e^2}{R^3}\right)/m}, \quad n \in \mathbb{N}. \quad (\text{A.3.9})$$

Similarly, with $a = \sqrt{(k_s \mp \frac{2e^2}{R^3})/m}$ and $b = 0$, the energy eigenvalues of Eq. (A.3.8) are given by

$$E_n = \frac{\hbar}{2}(2n+1)\sqrt{\left(k_s \mp \frac{2e^2}{R^3}\right)/m}, \quad n \in \mathbb{N}. \quad (\text{A.3.10})$$

By taking $n = 0$, we see the lowest energy of the system of two interacting dipoles is

$$E = \frac{\hbar}{2}\sqrt{\frac{k_s}{m}}\left[2\left(\sqrt{1 + \frac{e^2}{k_s R^3}} + \sqrt{1 - \frac{e^2}{k_s R^3}}\right) + \sqrt{1 + \frac{2e^2}{k_s R^3}} + \sqrt{1 - \frac{2e^2}{k_s R^3}}\right], \quad (\text{A.3.11})$$

which may be expanded using the binomial series expansion, $\sqrt{1+x} = 1 + \frac{1}{2}x - \frac{1}{8}x^2 + \dots$, when $e^2/(k_s R^3) \ll 1$. Employing this expansion up to second order yields a ground-state energy of

$$E = 3h\nu_0 - \frac{3}{4}h\nu_0\frac{e^4}{k_s^2 R^6}, \quad (\text{A.3.12})$$

where $\nu_0 = \sqrt{k_s/m}/(2\pi)$ is the natural frequency of the oscillators and the linear terms from the binomial expansion have cancelled. It can be seen from this equation that as R decreases, so too does the energy, showing that this is an attractive force.

We now want to write this energy in terms of the dipole polarizability, α . Polarizability is defined via $\mathbf{m} = \alpha \mathbf{E}$ where $\mathbf{m} = e\mathbf{r}$ is the induced dipole moment with respect to an electric field \mathbf{E} . The net force on the oscillator will be an attractive force from the electric field, and a repulsive force from Hooke's law. Thus

$$\mathbf{F} = e\mathbf{E} - k\mathbf{r} = e\mathbf{E} - \frac{k_s}{e}\mathbf{m}. \quad (\text{A.3.13})$$

We assume the oscillators are at equilibrium so $\mathbf{F} = 0$. Then, Eq. (A.3.13) may be rearranged to derive a polarizability of $\alpha = e^2/k$. Because we have assumed a system of two identical dipoles, the polarizabilities of these dipoles will be the same (i.e. $\alpha_A = \alpha_B$). Finally, the energy of interaction between these two oscillators in their ground states may be expressed in terms of the polarizability α as

$$E = -\frac{3}{4} \frac{h\nu_0\alpha}{R^6}, \quad (\text{A.3.14})$$

which largely resembles the London dispersion formula from Eq. (1.2.10).

APPENDIX B

CHAPTER 2 SUPPLEMENT

B.1 COMMON UNIT CONVERSION FACTORS

Table B.1: Conversion factors between common energy units used in electronic structure theory to six significant figures. Units include: Hartree (Ha.), electronvolt (eV), kilocalorie per mole (kcal/mol), kilojoule per mole (kJ/mol), and wavenumber (cm^{-1}). To convert from a row unit to a column unit, multiply by the corresponding table entry. For commonly used units of length, note that $1 \text{ \AA} = 10^{-10} \text{ m} \approx 1.88973 \text{ bohr}$. Values were obtained from Ref. [324].

	Ha.	eV	kcal/mol	kJ/mol	cm^{-1}
Ha.	1	27.2114	627.510	2625.50	219475
eV	3.67493×10^{-2}	1	23.0605	96.4853	8065.54
kcal/mol	1.59360×10^{-3}	4.33641×10^{-3}	1	4.18400	349.755
kJ/mol	3.80880×10^{-4}	1.03643×10^{-3}	2.39006×10^{-1}	1	83.5935
cm^{-1}	4.55634×10^{-6}	1.23984×10^{-4}	2.85914×10^{-3}	1.19627×10^{-3}	1

B.2 THE BORN–OPPENHEIMER APPROXIMATION

At no point has the kinetic energy of the nuclei been considered throughout this work. This is because we have made the Born–Oppenheimer approximation, where all nuclei are assumed to be effectively stationary compared to the electrons, thus having zero kinetic energy [474]. This approximation recognizes that the mass of even the lightest nuclei is three orders of magnitude larger than the mass of the electron. If the nucleus and electron have similar momentum, then the electron should be able to adiabatically react to any changing nuclear positions. For the hydrogen atom, the

fractional energy correction is estimated to be on the order of 0.01%. For a proton in a hydrogen bond between two nitrogen atoms, the fractional energy correction is still only on the order of 2% [550].

However, this stationary-nuclei approximation will break down whenever electrons are unable to adiabatically adapt to changing nuclear positions, such as in relativistic conditions or during proton-transfer transition states [551]. In recent years, some researchers have presented methods to carry out DFT calculations without relying on the BO approximation [552]. However, these issues are not present for the systems considered within this thesis, thus the approximation remains valid and shall be utilized throughout.

B.3 IMPROVING DFT DISPERSION FORCES & STRESSES

B.3.1 ASSESSMENT OF STRESS ERRORS WITH FHI-AIMS

In Section 2.5.3, we indicated that the current implementation of forces and stresses in XDM is insufficient. This was then shown explicitly in Chapter 3, where we optimized the geometry of some selected materials with cubic unit cells (CO_2 , Diamond, Si, Cu, Ni, GaAs, MgO, NaCl) with the planewave code, Quantum ESPRESSO (QE) [111]. First, we performed a variable-cell relaxation on the materials where we assumed constant dispersion coefficients. Then, the lattice constants (a_{latt} in Å) were manually adjusted to scan over a range of geometries about equilibrium. Later, we reran the same systems in FHI-aims [120], which uses numerical atom-centred orbitals. The purpose of this was twofold: (i) to compare TS and XDM results on the same structures and (ii) to test if the same issues we saw in the planewave code (QE) are also present in a numerical atom-centred basis code (FHI-aims).

From Table B.2, we confirm our previous conjecture that similar errors seen in XDM geometry optimizations would be present with TS, although to a lesser degree. For XDM, we believe that the errors were reduced with FHI-aims compared to QE due to the quick decay of the basis functions. However, the issues were still present. In Table B.3, we see that TS vastly overestimates the C_6 coefficients compared to XDM, which is the cause of TS's systematic overbinding problem. XDM's $C_{6,ij}$ is dependent on both volume and moment integrals, while TS's $C_{6,ij}$ is dependent only on the volume integrals. Volume integrals tend to be less sensitive to geometry changes than

Table B.2: A comparison of the lattice-constant (a_{latt} in Å) errors and corresponding energy errors (ΔE in eV) for selected materials with cubic unit cells, as computed by TS and XDM using FHI-aims (FHI) [120], and XDM in Quantum ESPRESSO (QE) [111]. $a_{\text{latt}}^{\text{min}}$ is the minimum-energy lattice constant obtained via a manual scan. $a_{\text{latt}}^{\text{rel}}$ is the lattice constant obtained by a variable-cell relaxation assuming constant dispersion coefficients. ΔE is the corresponding energy error of the variable-cell relaxation. The FHI-aims calculations used numerical atom-centred orbital basis sets with `light` settings, the PBE functional [149, 150], with the same \mathbf{k} -point meshes used in the Quantum ESPRESSO calculations as discussed in Chapter 3, with one exception: XDM FHI-aims relaxation of NaCl was computed using a primitive lattice with a $9 \times 9 \times 9$ \mathbf{k} -point grid.

Material	TS (FHI)			XDM (FHI)			XDM (QE)		
	$a_{\text{latt}}^{\text{min}}$	$a_{\text{latt}}^{\text{rel}}$	ΔE	$a_{\text{latt}}^{\text{min}}$	$a_{\text{latt}}^{\text{rel}}$	ΔE	$a_{\text{latt}}^{\text{min}}$	$a_{\text{latt}}^{\text{rel}}$	ΔE
CO ₂	5.93	5.93	<.001	5.93	5.93	<.001	5.69	5.66	0.001
Diamond	3.57	3.56	0.008	3.57	3.56	0.002	3.57	3.56	0.009
Si	5.49	5.46	0.007	5.49	5.44	0.011	5.46	5.42	0.020
GaAs	5.71	5.73	0.004	5.71	5.67	0.023	5.71	5.66	0.036
Ni	3.41	3.41	<.001	3.48	3.45	0.016	3.51	3.47	0.034
Cu	3.54	3.54	<.001	3.61	3.56	0.021	3.62	3.58	0.026
NaCl	5.40	5.40	<.001	5.56	5.55	0.007	5.52	5.44	0.040
MgO	4.22	4.20	0.005	4.26	4.22	0.012	4.23	4.19	0.036

moment integrals [80, 98], explaining why TS’s errors in C_6 are lower than those of XDM. For XDM, the C_6 coefficients were smaller in QE than they were in FHI-aims. This is perhaps because the multipole moment integrals capture the core regions in FHI-aims, which are missing in QE due to the use of pseudopotentials. This is consistent with the fact that the observed differences in C_6 are larger for atoms with large cores (e.g. Ni, Cu) compared to atoms with small cores (e.g. C, O).

Table B.3: A comparison of selected cubic solids' heteroatomic C_6 coefficient sensitivity to cell compression for TS and XDM using FHI-aims (FHI) and Quantum ESPRESSO (QE). The C_6 column gives the dispersion coefficient at the energy-minimum geometry given in Table B.2 for the respective atoms (and material) given in the left-most column. The $|\Delta C_6|$ column computes the magnitude of the difference of C_6 between 5% compressed and 5% expanded geometries. Calculations were performed as for Table B.2, and all values are in atomic units.

Bond (Material)	TS (FHI)		XDM (FHI)		XDM (QE)	
	C_6	$ \Delta C_6 $	C_6	$ \Delta C_6 $	C_6	$ \Delta C_6 $
C-O (CO_2)	19.80	1.2	15.63	2.0	15.10	.17
C-C (Diamond)	38.55	.96	15.42	3.8	14.16	3.6
Si-Si (Si)	271.9	6.9	129.1	27.	99.50	24.
Ga-As (GaAs)	302.1	6.9	184.7	34.	156.5	31.
Ni-Ni (Ni)	361.7	14.	136.3	26.	112.2	24.
Cu-Cu (Cu)	295.2	2.5	144.9	30.	105.7	19.
Na-Cl (NaCl)	220.3	7.4	87.38	12.	75.53	9.5
Mg-O (MgO)	67.01	.50	25.82	5.8	26.60	5.4

B.3.2 IMPROVED XDM FORCES AND STRESSES

This section develops rigorous formulae for XDM forces and stresses that explicitly account for the variation in dispersion coefficients with atom positions and cell dimensions. We start from

$$E^{\text{XDM}} = -\frac{1}{2} \sum_{\mathbf{L}} \sum_{i \neq j'} \sum_{n=6,8,10} \frac{C_{n,ij}^{\text{XDM}}}{R_{ij}^n + R_{\text{vdw},ij}^n} \quad (\text{B.3.1})$$

and we wish to derive the force expression. We do this by taking the derivative with respect to interatomic distance. The α^{th} component (where α is one of x , y , or z) to the force on atom k is given by

$$F_{k,\alpha}^{\text{XDM}} = -\frac{\partial E^{\text{XDM}}}{\partial x_{k,\alpha}}, \quad (\text{B.3.2})$$

where $x_{k,\alpha}$ is the α^{th} component of the atomic position of atom k . The first step will be to take the derivative of the Becke–Johnson damping function. For simplicity, we will consider the derivative of the denominator above:

$$\frac{\partial}{\partial x_{k,\alpha}} \left[\frac{f_n^{\text{BJ}}}{R_{ij}^n} \right] = \frac{\partial}{\partial x_{k,\alpha}} \left[\frac{1}{R_{ij}^n + R_{\text{vdw},ij}^n} \right] \quad (\text{B.3.3})$$

$$= -\frac{n R_{ij}^{n-1}}{(R_{ij}^n + R_{\text{vdw},ij}^n)^2} \frac{\partial R_{ij}}{\partial x_{k,\alpha}} - \frac{n R_{\text{vdw},ij}^{n-1}}{(R_{ij}^n + R_{\text{vdw},ij}^n)^2} \frac{\partial R_{\text{vdw},ij}}{\partial x_{k,\alpha}} \quad (\text{B.3.4})$$

$$= -\frac{n \left(R_{ij}^{n-1} \frac{\partial R_{ij}}{\partial x_{k,\alpha}} + R_{\text{vdw},ij}^{n-1} \frac{\partial R_{\text{vdw},ij}}{\partial x_{k,\alpha}} \right)}{(R_{ij}^n + R_{\text{vdw},ij}^n)^2}. \quad (\text{B.3.5})$$

The derivatives of the interatomic distance, $R_{ij} = |\mathbf{x}_i - \mathbf{x}_j + \mathbf{R}_a|$, are given by

$$\frac{\partial R_{ij}}{\partial x_{i,\alpha}} = \frac{(\mathbf{x}_i - \mathbf{x}_j + \mathbf{R}_a)_{\alpha}}{R_{ij}}, \quad (\text{B.3.6})$$

$$\frac{\partial R_{ij}}{\partial x_{j,\alpha}} = -\frac{(\mathbf{x}_i - \mathbf{x}_j + \mathbf{R}_a)_{\alpha}}{R_{ij}}, \quad (\text{B.3.7})$$

where $(\dots)_{\alpha}$ indicates the α^{th} component and \mathbf{R}_a is the lattice vector. We note that for interatomic distance derivatives

$$\frac{\partial R_{ij}}{\partial x_{i,\alpha}} = -\frac{\partial R_{ij}}{\partial x_{j,\alpha}}. \quad (\text{B.3.8})$$

Now we take the derivative of the van der Waal's radius,

$$\begin{aligned}\frac{\partial R_{\text{vdw},ij}}{\partial x_{k,\alpha}} &= \frac{\partial (a_1 R_{c,ij} + a_2)}{\partial x_{k,\alpha}} \\ &= a_1 \frac{\partial R_{c,ij}}{\partial x_{k,\alpha}},\end{aligned}\quad (\text{B.3.9})$$

where a_1 and a_2 are XDM's empirical damping parameters. The derivative of the critical damping radius, $R_{c,ij}$, is

$$\frac{\partial R_{c,ij}}{\partial x_{k,\alpha}} = \frac{\partial}{\partial x_{k,\alpha}} \left[\frac{1}{3} \left(\left(\frac{C_{8,ij}^{\text{XDM}}}{C_{6,ij}^{\text{XDM}}} \right)^{1/2} + \left(\frac{C_{10,ij}^{\text{XDM}}}{C_{6,ij}^{\text{XDM}}} \right)^{1/4} + \left(\frac{C_{10,ij}^{\text{XDM}}}{C_{8,ij}^{\text{XDM}}} \right)^{1/2} \right) \right] \quad (\text{B.3.10})$$

$$\begin{aligned}&= \frac{1}{6} \left[\frac{C_{6,ij}(C_{8,ij})' - (C_{6,ij})' C_{8,ij}}{C_{6,ij}^{3/2} C_{8,ij}^{1/2}} + \frac{C_{6,ij}(C_{10,ij})' - (C_{6,ij})' C_{10,ij}}{2C_{6,ij}^{5/4} C_{10,ij}^{3/4}} \right. \\ &\quad \left. + \frac{C_{8,ij}(C_{10,ij})' - (C_{8,ij})' C_{10,ij}}{C_{8,ij}^{3/2} C_{10,ij}^{1/2}} \right],\end{aligned}\quad (\text{B.3.11})$$

where the XDM superscripts on the dispersion coefficients are implied, and the primed notation indicates a partial derivative with respect to $x_{k,\alpha}$.

We now take the derivatives of the $C_{n,ij}^{\text{XDM}}$ dispersion coefficients. We recall their forms as given in Section 2.5.3 as

$$C_{6,ij}^{\text{XDM}} = \frac{\alpha_i \alpha_j \langle M_1^2 \rangle_i \langle M_1^2 \rangle_j}{\alpha_i \langle M_1^2 \rangle_j + \alpha_j \langle M_1^2 \rangle_i}, \quad (\text{B.3.12})$$

$$C_{8,ij}^{\text{XDM}} = \frac{3 \alpha_i \alpha_j \left(\langle M_1^2 \rangle_i \langle M_2^2 \rangle_j + \langle M_2^2 \rangle_i \langle M_1^2 \rangle_j \right)}{2 \left(\alpha_i \langle M_1^2 \rangle_j + \alpha_j \langle M_1^2 \rangle_i \right)}, \quad (\text{B.3.13})$$

$$C_{10,ij}^{\text{XDM}} = 2 \frac{\alpha_i \alpha_j \left(\langle M_1^2 \rangle_i \langle M_3^2 \rangle_j + \langle M_3^2 \rangle_i \langle M_1^2 \rangle_j \right)}{\alpha_i \langle M_1^2 \rangle_j + \alpha_j \langle M_1^2 \rangle_i} + \frac{21}{5} \frac{\alpha_i \alpha_j \langle M_2^2 \rangle_i \langle M_2^2 \rangle_j}{\alpha_i \langle M_1^2 \rangle_j + \alpha_j \langle M_1^2 \rangle_i}. \quad (\text{B.3.14})$$

Here, the polarizabilities, α_i , and multipole moment integrals, $\langle M_m^2 \rangle_\ell$, are both dependent on the atomic positions. The derivatives follow:

$$\frac{\partial C_{6,ij}^{\text{XDM}}}{\partial x_{k,\alpha}} = \frac{\alpha_i^2 \langle M_1^2 \rangle_j^2 \left[\alpha_j \langle M_1^2 \rangle'_i + \alpha'_j \langle M_1^2 \rangle_i \right] + \alpha_j^2 \langle M_1^2 \rangle_i^2 \left[\alpha_i \langle M_1^2 \rangle'_j + \alpha'_i \langle M_1^2 \rangle_j \right]}{\left(\alpha_i \langle M_1^2 \rangle_j + \alpha_j \langle M_1^2 \rangle_i \right)^2}, \quad (\text{B.3.15})$$

$$\begin{aligned} \frac{\partial C_{8,ij}^{\text{XDM}}}{\partial x_{k,\alpha}} = & \frac{3}{2} \frac{\alpha_i \alpha_j \left[\langle M_1^2 \rangle_i \langle M_2^2 \rangle'_j + \langle M_1^2 \rangle'_i \langle M_2^2 \rangle_j + \langle M_1^2 \rangle_j \langle M_2^2 \rangle'_i + \langle M_1^2 \rangle'_j \langle M_2^2 \rangle_i \right]}{\alpha_i \langle M_1^2 \rangle_j + \alpha_j \langle M_1^2 \rangle_i} \\ & + \frac{3}{2} \frac{(\alpha_i \alpha'_j + \alpha'_i \alpha_j) \left[\langle M_1^2 \rangle_i \langle M_2^2 \rangle_j + \langle M_1^2 \rangle_j \langle M_2^2 \rangle_i \right]}{\alpha_i \langle M_1^2 \rangle_j + \alpha_j \langle M_1^2 \rangle_i} \\ & - \frac{3}{2} \frac{\alpha_i \alpha_j \left[\langle M_1^2 \rangle_i \langle M_2^2 \rangle_j + \langle M_1^2 \rangle_j \langle M_2^2 \rangle_i \right] \left[\alpha_i \langle M_1^2 \rangle'_j + \alpha'_i \langle M_1^2 \rangle_j + \alpha_j \langle M_1^2 \rangle'_i + \alpha'_j \langle M_1^2 \rangle_i \right]}{\left(\alpha_i \langle M_1^2 \rangle_j + \alpha_j \langle M_1^2 \rangle_i \right)^2}, \end{aligned} \quad (\text{B.3.16})$$

$$\begin{aligned} \frac{\partial C_{10,ij}^{\text{XDM}}}{\partial x_{k,\alpha}} = & 2 \frac{\alpha_i \alpha_j \left[\langle M_1^2 \rangle_i \langle M_3^2 \rangle'_j + \langle M_1^2 \rangle'_i \langle M_3^2 \rangle_j + \langle M_1^2 \rangle_j \langle M_3^2 \rangle'_i + \langle M_1^2 \rangle'_j \langle M_3^2 \rangle_i \right]}{\alpha_i \langle M_1^2 \rangle_j + \alpha_j \langle M_1^2 \rangle_i} \\ & + 2 \frac{(\alpha_i \alpha'_j + \alpha'_i \alpha_j) \left[\langle M_1^2 \rangle_i \langle M_3^2 \rangle_j + \langle M_1^2 \rangle_j \langle M_3^2 \rangle_i \right]}{\alpha_i \langle M_1^2 \rangle_j + \alpha_j \langle M_1^2 \rangle_i} \\ & - 2 \frac{\alpha_i \alpha_j \left[\langle M_1^2 \rangle_i \langle M_3^2 \rangle_j + \langle M_1^2 \rangle_j \langle M_3^2 \rangle_i \right] \left[\alpha_i \langle M_1^2 \rangle'_j + \alpha'_i \langle M_1^2 \rangle_j + \alpha_j \langle M_1^2 \rangle'_i + \alpha'_j \langle M_1^2 \rangle_i \right]}{\left(\alpha_i \langle M_1^2 \rangle_j + \alpha_j \langle M_1^2 \rangle_i \right)^2} \\ & + \frac{21}{5} \frac{\alpha_i \alpha_j \left[\langle M_2^2 \rangle_i \langle M_2^2 \rangle'_j + \langle M_2^2 \rangle'_i \langle M_2^2 \rangle_j \right]}{\alpha_i \langle M_1^2 \rangle_j + \alpha_j \langle M_1^2 \rangle_i} \\ & - \frac{21}{5} \frac{\langle M_2^2 \rangle_i \langle M_2^2 \rangle_j \left[\alpha_i^2 \left(\alpha_j \langle M_1^2 \rangle'_j - \alpha'_j \langle M_1^2 \rangle_j \right) + \alpha_j^2 \left(\alpha_i \langle M_1^2 \rangle'_i - \alpha'_i \langle M_1^2 \rangle_i \right) \right]}{\left(\alpha_i \langle M_1^2 \rangle_j + \alpha_j \langle M_1^2 \rangle_i \right)^2}. \end{aligned} \quad (\text{B.3.17})$$

The derivative of the general multipole moment is

$$\frac{\partial \langle M_\ell^2 \rangle_i}{\partial x_{k,\alpha}} = \sum_\sigma \int \frac{\partial \omega_i}{\partial x_{k,\alpha}} \rho_\sigma(\mathbf{r}) [r^\ell - (r - d_{X\sigma})^\ell]^2 d\mathbf{r}, \quad (\text{B.3.18})$$

where the derivatives of the Hirshfeld weights, ω_i , are already known [553]. The derivatives of the polarizability and volume elements are given by

$$\begin{aligned} \frac{\partial \alpha_i}{\partial x_{k,\alpha}} &= \frac{\partial}{\partial x_{k,\alpha}} \left[\frac{v_i}{v_i^{\text{free}}} \alpha_i^{\text{free}} \right] \\ &= \frac{\alpha_i^{\text{free}}}{v_i^{\text{free}}} \frac{\partial v_i}{\partial x_{k,\alpha}}, \end{aligned} \quad (\text{B.3.19})$$

and

$$\begin{aligned} v_i &= \int \rho(r) |\mathbf{r} - \mathbf{x}_i|^3 w_i(\mathbf{r}) d\mathbf{r} \\ &= \sum_j w_{\text{int}}^j \rho(r_j) |\mathbf{r} - \mathbf{x}_i|^3 w_i(\mathbf{r}_j), \end{aligned} \quad (\text{B.3.20})$$

which we express as a sum over integration weights, w_{int}^j . Then taking the derivative yields

$$\frac{\partial v_i}{\partial x_{k,\alpha}} = \sum_j w_{\text{int}}^j \rho(\mathbf{r}_j) \frac{\partial (|\mathbf{r}_j - \mathbf{x}_i|^3 w_i(\mathbf{r}_j))}{\partial x_{k,\alpha}}. \quad (\text{B.3.21})$$

The derivative of $|\mathbf{r}_j - \mathbf{x}_i|^3 w_i(\mathbf{r}_j)$ may be expanded as a product rule,

$$\frac{\partial (|\mathbf{r}_j - \mathbf{x}_i|^3 w_i(\mathbf{r}_j))}{\partial x_{k,\alpha}} = \frac{\partial (|\mathbf{r}_j - \mathbf{x}_i|^3)}{\partial x_{k,\alpha}} w_i(\mathbf{r}_j) + |\mathbf{r}_j - \mathbf{x}_i|^3 \frac{\partial w_i(\mathbf{r}_j)}{\partial x_{k,\alpha}}. \quad (\text{B.3.22})$$

The second term is the derivative of the Hirshfeld weight, as in Eq. (B.3.18), and the derivative in the first term is given by

$$\begin{aligned} \frac{\partial (|\mathbf{r}_j - \mathbf{x}_i|^3)}{\partial x_{k,\alpha}} &= 3 |\mathbf{r}_j - \mathbf{x}_i|^2 \frac{\partial \sqrt{(r_{j,\alpha} - x_{i,\alpha})^2 + (r_{j,\beta} - x_{i,\beta})^2 + (r_{j,\gamma} - x_{i,\gamma})^2}}{\partial x_{k,\alpha}} \\ &= 3 |\mathbf{r}_j - \mathbf{x}_i|^2 \cdot \frac{1}{2} \frac{-2(r_{j,\alpha} - x_{i,\alpha})}{|\mathbf{r}_j - \mathbf{x}_i|} \\ &= -3 |\mathbf{r}_j - \mathbf{x}_i| (r_{j,\alpha} - x_{i,\alpha}). \end{aligned} \quad (\text{B.3.23})$$

APPENDIX C

CHAPTER 6 SUPPLEMENT

C.1 XCDM’S USE OF THE FIRST SCALAR MOMENT

The BR correlation hole used in this work comes from the spherically symmetric B88 real-space correlation model [135], but using the BR exchange functional to determine the correlation lengths [522]. This spherical symmetry means that the BR correlation hole will not have a dipole moment. However, the real correlation hole is not spherically symmetric in general, similar to how the BR exchange hole is not symmetric, but its spherical average is used to compute exchange energies.

While the spherically symmetric hole is centred about the reference electron at some distance r from the nearest nucleus, one can envision a shifted hole centred at $r - (d_X + d_C)$ that is not spherically symmetric due to polarization effects, but would give the same spherical average. The magnitude of d_X is determined from the BR exchange-hole dipole moment. However, for the correlation hole, we use its radial size (the first scalar moment) as a proxy for the extent of polarisation, d_C .

Here, we assess whether the use of the first scalar moment,

$$d_X(\mathbf{r}) \approx \int h_X(\mathbf{r}, s) s d\mathbf{s}, \quad (\text{C.1.1})$$

is a good approximation for the BR exchange hole, where we can compare with the result $d_X(\mathbf{r}) = b$ used in XDM. For the BR model, the spherically averaged hole, expressed as a positive quantity, is [16]

$$h_{X\sigma}(\mathbf{r}, s) = \frac{a}{16\pi bs} \left[(a|b - s| + 1) e^{-a|b-s|} \right]$$

$$-(a|b+s|+1) e^{-a|b+s|} \Big]. \quad (\text{C.1.2})$$

The first scalar moment can be shown to be

$$\begin{aligned} \mu_X &= \int h_X(\mathbf{r}, s) s d\mathbf{s} = \frac{4 + a^2 b^2 - (4 + ab) e^{-ab}}{a^2 b} \\ &= \frac{b}{x^2} [4 + x^2 - (4 + x) e^{-x}] \end{aligned} \quad (\text{C.1.3})$$

which simplifies to $\mu_X = b = d_X$ in the limit $a \rightarrow \infty$. A comparison of μ and b is shown in Figure C.1 for the He atom using an variational, exponential wavefunction, as well as for He, H₂, and N₂ using both LDA and HF electron densities obtained from the NUMOL program [434]. The results confirm that the approximation of $d_X = \mu_X$ is exact for the BR exchange hole in the density tails far from atoms, although $\mu_X > d_X$ in bonding regions.

C.2 XCDM DIMENSIONAL ANALYSIS

We consider the units of $c_{\sigma\sigma}$ and $c_{\sigma\sigma'}$. From Eq. (2.5.72), it is clear that a has units of 1/length and b units of length and so x is dimensionless, consistent with Eqs. (6.2.19) and (6.2.20). Then, $U_X = 1/b[1 - \exp(-x) - 0.5x \exp(-x)]$ has units of 1/length. The correlation length z , by definition, has units of length [135]; thus c is dimensionless. For $g_{\sigma\sigma'}$, we consider Eq. (2.5.71), which states $d_{XC} = \frac{g_{\sigma\sigma'} z^5}{1+z} \rho - \mathbf{r}$. Since d_{XC} has units of length and from $\frac{g_{\sigma\sigma'} \times \text{length}^5}{\text{length}} \times \frac{1}{\text{length}^3}$ it follows that $g_{\sigma\sigma'}$ is dimensionless. Similarly for $g_{\sigma\sigma}$, we first examine D_σ , the difference in kinetic energy densities, where $\tau = \frac{(\nabla\rho)^2}{\rho} = \frac{(1/\text{length}^4)^2}{1/\text{length}^3} = 1/\text{length}^5$ (dropping $\hbar/2m$ in atomic units). Thus, from Eq. (2.5.70), $\frac{g_{\sigma\sigma} z^7}{1+z} D = \frac{g_{\sigma\sigma} \times \text{length}^7}{\text{length}} \times \frac{1}{\text{length}^5}$ and therefore $g_{\sigma\sigma}$ is also dimensionless.

C.3 DAMPING FUNCTION PARAMETERIZATION

Tabulated values of the optimal a_1 , a_2 (Å), and z_{damp} for XDM and XCDM, along with the associated mean absolute error (MAE) and mean absolute percent error (MAPE), are provided in Table C.2. The functionals considered are B86bPBE, B86bPBE0, B86bPBE50, PBE, PBE0, PBE50, B3LYP, BHLYP, HSE06 [168] ($\omega = 0.11$ bohr⁻¹), LC- ω PBE ($\omega = 0.2$ bohr⁻¹), and LC- ω PBEh ($\omega = 0.4$ bohr⁻¹ & 20% HF), while the basis sets are `light`, `lightdense`, `lightdenser`, `intermediate`,

and `tight`. We note that the XDM(BJ) damping parameters are very slightly different from those reported in Ref. [119] due to some code modifications; the current values are recommended for FHI-aims version 240314 and later. Additional fits using the `tier2_aug2` basis were also performed for B86bPBE, PBE, LC- ω PBE ($\omega = 0.2 \text{ bohr}^{-1}$), and LC- ω PBEh ($\omega = 0.4 \text{ bohr}^{-1}$ & 20% HF).

Unfortunately, SCF convergence could not be achieved for some systems using LC- ω PBE and LC- ω PBEh with FHI-aims, particularly within the GMTKN55 subsets of C60ISO, MCONF, PCONF, and UPU23. We note, however, that addressing SCF convergence issues with range-separated functionals is an active area of development within the FHI-aims community. Thus, to be able to report range-separated hybrid results, some additional calculations were performed using the Gaussian16 program [126]. In these calculations, damping parameters for XDM(BJ), XDM(Z), XCDM(BJ), and XCDM(Z) were optimised for use with the PBE0 and LC- ω PBE ($\omega = 0.4 \text{ bohr}^{-1}$) functionals in combination with the aug-cc-pVTZ basis set. The XDM(BJ), XDM(Z), XCDM(BJ), and XCDM(Z) dispersion corrections were applied *ad hoc* using the postg code [124].

C.4 ANALYSIS OF WTMAD CONTRIBUTIONS

A recent work proposed the WTMAD-3 weighting scheme which attenuates the weights for a subset to be no more than 1% of the total reactions considered [533]. Some GMTKN55 subsets have dozens of reaction energies, while others contain only a handful. Because the more commonly used WTMAD-2 weights by the number of systems equally across all subsets, it introduces a bias toward subsets with larger numbers of reactions. To address this, the WTMAD-3 attenuates the weights for a subset to be no more than 1% of the total reactions out of the subset; for the full set of 55 subsets, this limits each subset's weight to 15 systems. The WTMAD-3 is calculated via

$$\text{WTMAD-3} = \sum_{i=1}^{N_{\text{bench}}} \frac{N_i^{\text{damp}}}{N_{\text{total}}} \cdot \frac{\overline{|\Delta E|}_{\text{total}}}{\overline{|\Delta E|}_i} \cdot \text{MAD}_i, \quad (\text{C.4.1})$$

where $N_i^{\text{damp}} = \max(0.01 \times N_{\text{total}}, N_i)$. When calculating the per-category values for GMTKN55's WTMAD-2 and WTMAD-3, a fixed value of $\overline{|\Delta E|}_{\text{total}} = 56.84 \text{ kcal/mol}$ is used across all categories, while N_{total} is rescaled per category.

WTMAD-1.5 is also introduced, which attempts to address the same issues as WTMAD-3, but by fully removing the dependence on the number of subsets. This

results in a combination of WTMAD-1 and WTMAD-2 methods, and is calculated as

$$\text{WTMAD-1.5} = \frac{1}{N_{\text{bench}}} \sum_{i=1}^{N_{\text{bench}}} \frac{\overline{|\Delta E|}_{\text{total}}}{\overline{|\Delta E|}_i} \cdot \text{MAD}_i. \quad (\text{C.4.2})$$

To determine the contributions of each subset to the overall WTMAD values, we first calculated the mean MAD for each GMTKN55 subset by averaging the MAD values across our 36 combinations of functionals and dispersion corrections. The results, collected in Table C.4, show that none of these four treatments fairly weighted all subsets across the entire GMTKN55. We determined that the dynamic weights—ratios of N_i/N_{total} to account for the number of reactions, and $\text{MAD}_i/\overline{|\Delta E|}_i$ to account for error relative to average reference energy—resulted in numerous systems being over- or under-represented in the WTMAD error. For WTMAD-2 specifically, the largest disparity observed was for PBE-D3(BJ), where BH76 contributed to 14.26% of the WTMAD-2, while DIPCS10 contributed only 0.02%—a 713-fold difference in scale. Although dynamic weights allow for easy expansion and transferability to other benchmarks, we could not find a dynamic weighting scheme that fairly represented all systems within GMTKN55.

Our analysis of the disparities in WTMAD-2 led to the formulation of WTMAD-4, defined as

$$\text{WTMAD-4} = \frac{1}{N_{\text{bench}}} \sum_{i=1}^{N_{\text{bench}}} w_i^{\text{WTMAD-4}} \cdot \text{MAD}_i. \quad (\text{C.4.3})$$

This weighting scheme is identical to WTMAD-1 in its construction, but the weights are chosen such that each benchmark contributes roughly evenly (between 1.1% and 3.5%) to the overall WTMAD-4. We then examined the subsets within each of the five categories to determine if their weights should be adjusted based on three criteria: (i) qualitatively based on how representative they are of their category, (ii) the fraction of reactions they represent within the category, and (iii) the quality of the reference

data compared to others in the same category. The final weights are given by

$$w_i = \left\{ \begin{array}{ll} 50 & \text{ACONF, RG18} \\ 25 & \text{ADIM6, Amino20x4, BUT14DIOL,} \\ & \text{HEAVY28, ICONF, MCONF, S66} \\ 10 & \text{BHRROT27, HAL59, IL16, PCONF21,} \\ & \text{PNICO23, RSE43, S22, SCONF, UPU23} \\ 5 & \text{AHB21, CARBHB12, CDIE20,} \\ & \text{CHB6, ISO34, PArel, TAUT15} \\ 2.5 & \text{AL2X6, BH76, BH76RC, BHPERI,} \\ & \text{BSR36, FH51, G21EA, HEAVYSB11,} \\ & \text{IDISP, INV24, ISOL24, NBPRC,} \\ & \text{PA26, YBDE18} \\ 1 & \text{ALK8, ALKBDE10, BHDIV10, DARC,} \\ & \text{DIPCS10, G21IP, G2RC, PX13,} \\ & \text{RC21, W4-11, WATER27, WCPT18} \\ 0.5 & \text{C60ISO, DC13, MB16-43, SIE4x4} \end{array} \right. \quad (\text{C.4.4})$$

As an example, BH76 contains 40% of the reactions in the “Barrier” category, while having reference data of approximately equivalent quality to the other subsets in this category. Thus, its weight was increased from the 0.2 bin to 0.5. At our discretion, the following benchmarks were given increased weight: MB16-43, W4-11, RSE43, BH76; while the following were given decreased weight: AL2X6, C60ISO, G21IP. Table C.4 shows the percent contributions to the total weighted MAD under the various WTMAD schemes for each subset in GMTKN55. The percentage change of the “Basic+Small” and “Barriers” categories between WTMAD-2 and WTMAD-4 is notable. However, we consider this shift in weight towards thermochemistry desirable and representative for general chemistry applications.

C.5 TABULATED DATA

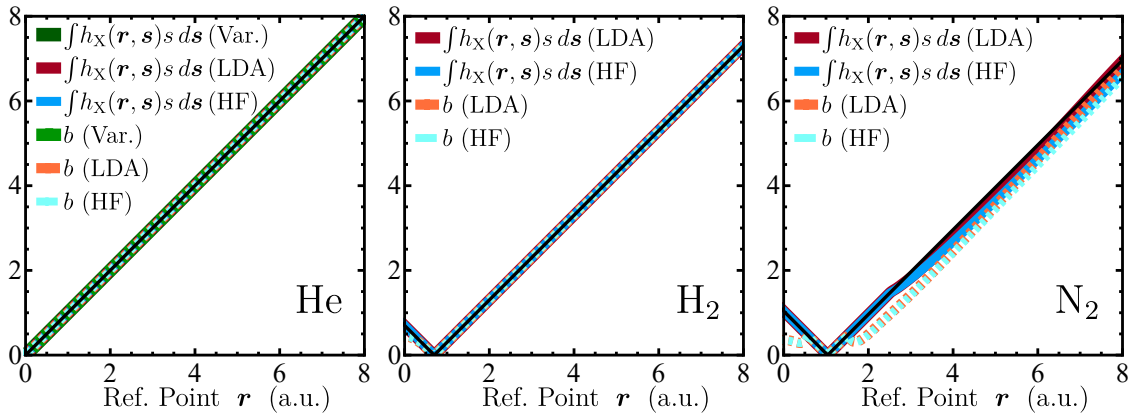


Figure C.1: Plots comparing the computed BR exchange-hole dipole moment (b), with the first scalar moment ($\int h_X(\mathbf{r}, \mathbf{s}) s d\mathbf{s}$) of the BR exchange hole for He, H₂, and N₂. The nuclei in H₂ and N₂ are placed at $z = \pm 0.7$ and $z = \pm 1.04$ (in a.u.) respectively, and exchange-hole contributions are shown for the nucleus at the positive position as the reference point \mathbf{r} is varied along the z -axis. Calculations were performed either with a variational, exponential density, or with HF or LDA densities from NUMOL. The black line shows the $r_i - d_X \geq 0$ limit, which is enforced for all quantities.

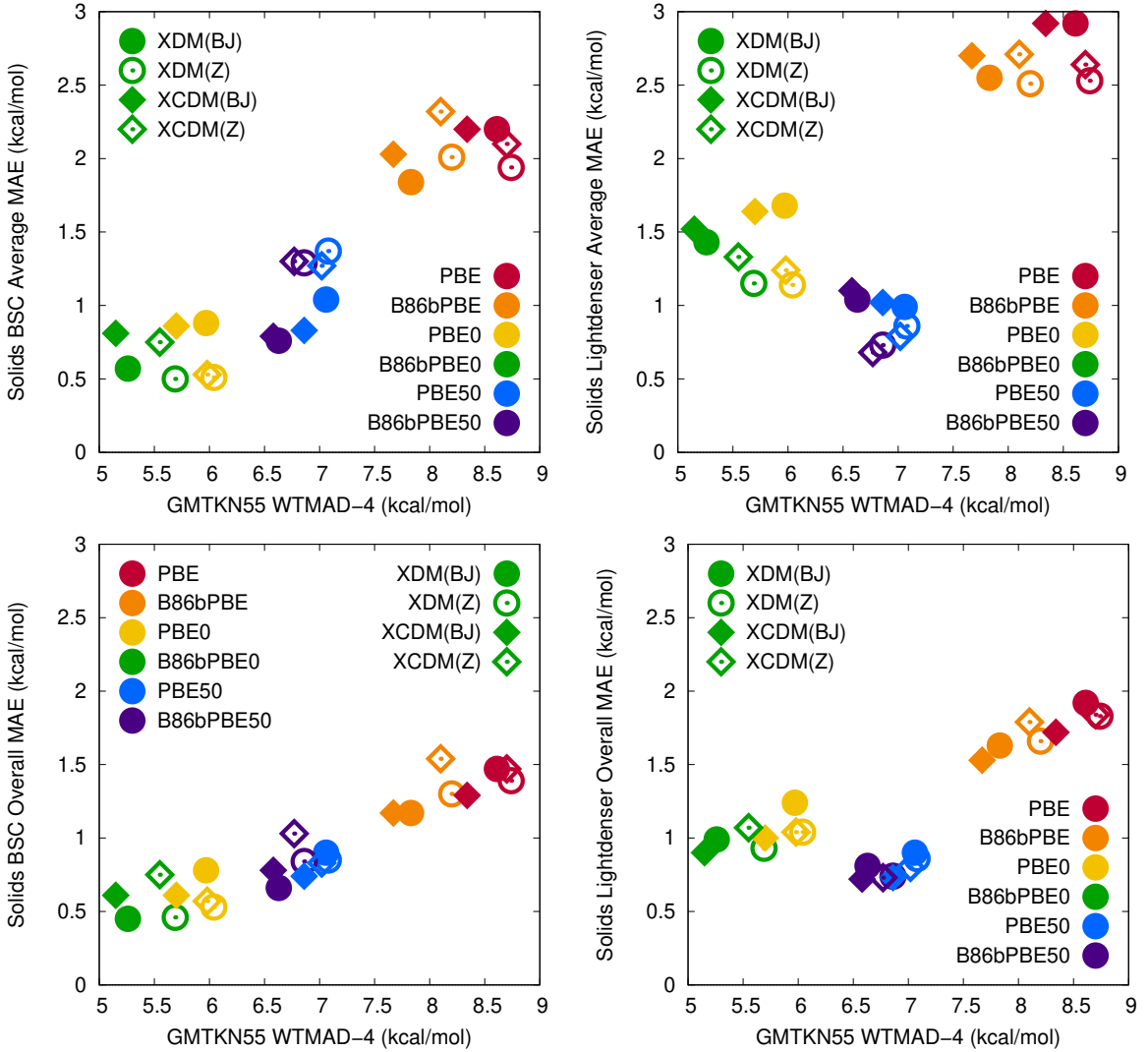


Figure C.2: Scatter plots show the GMTKN55 WTMAD-4 values (in kcal/mol) on the x -axis, and both the averaged and overall mean absolute errors (MAEs) for the basis-set-corrected and `lightdenser` solid-state data on the y -axis. XDM is indicated by circles and XCDM by diamonds; solid and hollow shapes denote BJ- and Z-Damping respectively. The average MAE was computed as the average of the four benchmark MAEs, while the overall MAE was computed as the mean of all individual reaction errors across all four benchmarks.

Table C.1: The mean absolute percent error (MAPE) and mean percent error (MPE) for the MolC6 benchmark of homomolecular C_6 coefficients are shown for each normalization function considered for XCDM. All data was calculated with FHI-aims [120] using both the `lightdenser` and `tight` basis sets for the B86bPBE and PBE functionals, as well as their associated 25% and 50% hybrid counterparts. Also shown is an XCDM parameterization based on the rounded mean of all three normalization functions, F_1 , F_2 , F_3 , as well as XDM data for comparison.

$F_1(x)$	<code>lightdenser</code>		<code>tight</code>	
Functional	MAPE	MPE	MAPE	MPE
PBE	8.6	5.5	8.4	3.3
B86bPBE	8.5	4.9	8.5	2.7
PBE0	8.7	5.8	8.5	1.1
B86bPBE0	8.6	5.3	8.6	0.6
PBE50	8.8	6.0	8.9	-0.9
B86bPBE50	8.7	5.8	9.0	-1.2
$F_2(x)$	<code>lightdenser</code>		<code>tight</code>	
Functional	MAPE	MPE	MAPE	MPE
PBE	9.4	6.9	8.6	4.6
B86bPBE	9.1	6.3	8.6	4.0
PBE0	9.5	7.1	8.3	2.3
B86bPBE0	9.3	6.7	8.4	1.9
PBE50	9.8	7.4	8.5	0.4
B86bPBE50	9.6	7.1	8.6	0.1
$F_3(x)$	<code>lightdenser</code>		<code>tight</code>	
Functional	MAPE	MPE	MAPE	MPE
PBE	20.8	19.8	18.8	17.0
B86bPBE	20.2	19.1	18.2	16.4
PBE0	21.0	20.0	16.7	14.6
B86bPBE0	20.6	19.5	16.3	14.1
PBE50	21.3	20.3	14.8	12.5
B86bPBE50	21.0	20.0	14.6	12.2
Mean: 0.02 & 0.6	<code>lightdenser</code>		<code>tight</code>	
Functional	MAPE	MPE	MAPE	MPE
PBE	11.9	10.3	10.4	8.0
B86bPBE	11.4	9.7	10.0	7.3
PBE0	12.1	10.6	9.0	5.7
B86bPBE0	11.8	10.2	8.8	5.2
PBE50	12.4	10.9	8.4	3.6
B86bPBE50	12.2	10.6	8.4	3.4
XDM	<code>lightdenser</code>		<code>tight</code>	
Functional	MAPE	MPE	MAPE	MPE
PBE	15.1	-12.2	18.1	-16.1
B86bPBE	15.5	-12.6	18.4	-16.4
PBE0	14.7	-12.0	19.4	-17.9
B86bPBE0	14.9	-12.2	19.6	-18.1
PBE50	15.6	-12.4	16.6	-14.0
B86bPBE50	16.0	-12.9	17.0	-14.5

Table C.2: Optimal XDM and XCDM BJ-damping (a_1 and a_2) and Z-Damping (z_{damp}) parameters for selected functionals calculated using version 250425 of FHI-aims [119, 120, 162, 494–497, 539], commit b38a7049. The mean absolute errors (MAE, in kcal/mol) and mean absolute percent errors (MAPE) for the KB49 fit set are also shown. The values of ω used for HSE and LC- ω PBEh were 0.11 and 0.20 bohr⁻¹ respectively. If the a_1 BJ-damping parameter was negative, it was set to zero and a_2 was optimized under that constraint.

Functional	XDM(BJ)				XDM(Z)			XCDM(BJ)				XCDM(Z)		
	a_1	$a_2(\text{ang})$	MAE	MAPE	z_{damp}	MAE	MAPE	a_1	$a_2(\text{ang})$	MAE	MAPE	z_{damp}	MAE	MAPE
								light						
B86bPBE	0.5772	1.9027	0.49	13.6	113812	0.56	15.6	0.6299	2.0037	0.46	12.7	128057	0.52	14.6
PBE	0.2086	3.3113	0.62	17.6	195103	0.70	20.1	0.3375	3.1266	0.57	16.0	211728	0.67	19.3
B86bPBE0	0.2330	3.0772	0.30	8.6	146570	0.37	9.8	0.2232	3.3246	0.30	9.1	164382	0.34	9.3
PBE0	0.0000	4.0356	0.40	10.9	227147	0.48	13.0	0.0000	4.2125	0.38	10.5	247457	0.46	12.5
B3LYP	0.4922	1.9577	0.27	7.0	76047	0.41	10.1	0.2129	3.0078	0.25	7.5	88511	0.34	8.6
B86bPBE-50x	0.0000	4.0471	0.26	7.9	233058	0.35	10.0	0.0000	4.2466	0.29	9.3	256780	0.34	9.9
PBE-50x	0.0000	4.2524	0.33	8.9	326565	0.42	11.5	0.0000	4.4442	0.33	9.1	352651	0.42	11.4
BHLYP	0.0000	3.8449	0.33	8.8	163245	0.47	12.8	0.0000	4.0297	0.31	8.7	181833	0.45	12.4
HSE	0.0000	4.0661	0.46	12.0	239528	0.54	14.2	0.0000	4.2409	0.43	11.4	259900	0.52	13.7
LC- ω PBEh-00x	0.3117	2.7533	0.35	9.3	128736	0.38	10.6	0.3797	2.7680	0.34	9.1	145050	0.37	10.1
LC- ω PBEh-20x	0.2084	3.2019	0.26	7.2	162118	0.30	8.3	0.2953	3.1529	0.28	8.5	181335	0.30	8.5
lightdense														
B86bPBE	0.6893	1.5815	0.53	14.9	118327	0.60	16.9	0.7800	1.5878	0.50	14.0	132553	0.56	15.9
PBE	0.3280	2.9685	0.66	18.8	203179	0.74	21.2	0.4874	2.7116	0.61	17.3	219712	0.71	20.4
B86bPBE0	0.4611	2.4173	0.35	10.0	155058	0.41	11.3	0.5597	2.3821	0.35	10.4	172992	0.39	10.8
PBE0	0.1817	3.5163	0.45	12.5	241315	0.53	14.3	0.3072	3.3530	0.43	11.9	261696	0.51	13.9
B3LYP	0.5777	1.7232	0.31	8.2	79788	0.44	11.0	0.3681	2.5860	0.29	8.7	92375	0.38	9.9
B86bPBE-50x	0.0521	3.9424	0.30	8.7	252984	0.37	10.3	0.1073	3.9862	0.32	9.9	277103	0.36	10.2
PBE-50x	0.0000	4.3141	0.37	9.9	357356	0.45	12.2	0.0000	4.5037	0.36	9.9	383792	0.45	12.1
BHLYP	0.0000	3.8868	0.35	9.7	175059	0.47	12.6	0.0000	4.0711	0.32	9.3	194020	0.45	12.3
HSE	0.1617	3.6063	0.51	13.5	253830	0.58	15.4	0.2966	3.4101	0.48	12.8	274207	0.56	14.9
LC- ω PBEh-00x	0.4124	2.4657	0.39	10.3	136727	0.42	11.7	0.5021	2.4300	0.38	10.4	153271	0.40	11.2
LC- ω PBEh-20x	0.3815	2.6951	0.30	8.1	174490	0.34	9.2	0.4983	2.5822	0.31	9.3	194077	0.32	9.1
lightdense														
B86bPBE	0.6881	1.5789	0.53	14.9	116996	0.60	17.0	0.7731	1.6013	0.50	14.1	131105	0.56	15.9
PBE	0.3275	2.9627	0.66	18.9	200770	0.74	21.2	0.4832	2.7163	0.61	17.3	217181	0.71	20.4
B86bPBE0	0.4545	2.4309	0.35	9.9	153336	0.41	11.3	0.5445	2.4188	0.34	10.4	171142	0.39	10.9
PBE0	0.1775	3.5217	0.45	12.4	238489	0.53	14.3	0.2973	3.3737	0.42	11.8	258739	0.51	13.9
B3LYP	0.5816	1.7060	0.32	8.2	78928	0.44	11.1	0.3692	2.5767	0.29	8.6	91407	0.38	9.9
B86bPBE-50x	0.0330	3.9929	0.30	8.7	250118	0.37	10.3	0.0692	4.0891	0.32	9.8	274099	0.36	10.2
PBE-50x	0.0000	4.3052	0.37	9.9	353058	0.45	12.2	0.0000	4.4945	0.36	9.9	379358	0.45	12.1
BHLYP	0.0000	3.8799	0.36	9.7	173138	0.47	12.6	0.0000	4.0636	0.32	9.2	191978	0.45	12.3
HSE	0.1579	3.6101	0.51	13.5	250809	0.58	15.4	0.2876	3.4284	0.48	12.8	271056	0.56	14.9
LC- ω PBEh-00x	0.4044	2.4840	0.39	10.4	135037	0.43	11.8	0.4896	2.4599	0.38	10.4	151439	0.40	11.3
LC- ω PBEh-20x	0.3699	2.7245	0.30	8.1	172337	0.34	9.2	0.4816	2.6247	0.31	9.2	191773	0.32	9.1
intermediate														
B86bPBE	0.5550	1.9356	0.44	11.9	111561	0.50	13.5	0.5064	2.3267	0.42	11.6	125779	0.46	12.7
PBE	0.2856	3.0526	0.56	15.7	190929	0.64	18.1	0.3345	3.1085	0.53	14.4	207676	0.61	17.3
B86bPBE0	0.1564	3.2861	0.29	8.3	143700	0.34	8.9	0.0000	3.9540	0.31	9.5	161864	0.33	9.1
PBE0	0.0243	3.9447	0.38	10.2	222695	0.45	11.8	0.0000	4.1994	0.38	10.1	243612	0.43	11.5
B3LYP	0.4120	2.1684	0.26	6.3	74190	0.37	8.5	0.0757	3.3789	0.26	8.0	86675	0.33	8.0
B86bPBE-50x	0.0000	4.0234	0.28	8.7	230518	0.33	9.9	0.0000	4.2346	0.31	10.3	255698	0.33	10.0
PBE-50x	0.0000	4.2363	0.32	9.1	323677	0.41	11.4	0.0000	4.4376	0.34	9.8	351727	0.40	11.3
BHLYP	0.0000	3.8224	0.31	8.4	161458	0.45	12.1	0.0000	4.0148	0.32	9.1	180866	0.43	12.0
HSE	0.0321	3.9537	0.43	11.2	235387	0.51	12.9	0.0087	4.2039	0.42	11.0	256348	0.49	12.6
LC- ω PBEh-00x	0.3083	2.7542	0.32	7.9	126720	0.33	8.6	0.2000	3.2992	0.34	8.8	143146	0.32	8.6
LC- ω PBEh-20x	0.0570	3.6558	0.25	7.2	159185	0.28	7.7	0.0000	4.0230	0.29	8.8	178851	0.29	8.2
tight														
B86bPBE	0.9004	0.7808	0.39	11.0	96089	0.43	12.1	1.0379	0.6748	0.36	10.4	109207	0.38	11.0
PBE	0.5124	2.2588	0.49	14.0	162373	0.56	16.3	0.7306	1.8435	0.45	12.6	177910	0.53	15.3
B86bPBE0	0.7284	1.3781	0.32	8.4	108291	0.38	9.1	0.9321	1.0594	0.30	8.3	123250	0.34	8.4
PBE0	0.4713	2.3855	0.40	10.3	162110	0.48	12.0	0.6999	1.9465	0.36	9.3	179250	0.45	11.3
B3LYP	0.6791	1.2394	0.27	6.4	59992	0.40	8.9	0.6271	1.6680	0.24	7.3	70838	0.31	6.8
B86bPBE-50x	0.5908	1.9047	0.36	8.3	131706	0.43	9.4	0.8237	1.4876	0.33	8.2	149034	0.40	8.8
PBE-50x	0.4233	2.5711	0.41	9.5	173943	0.50	11.1	0.6592	2.1147	0.37	8.7	192993	0.47	10.6
BHLYP	0.2877	2.7329	0.35	8.2	106257	0.51	11.5	0.2889	2.9460	0.29	7.1	121070	0.46	10.6
HSE	0.4523	2.4809	0.45	11.2	173227	0.52	12.9	0.6873	2.0193	0.41	10.1	190628	0.49	12.2
LC- ω PBEh-00x	0.7358	1.3088	0.26	6.9	106223	0.28	7.6	0.8467	1.2583	0.27	7.6	120890	0.25	6.9
LC- ω PBEh-20x	0.6823	1.5353	0.24	5.9	118151	0.30	6.9	0.8475	1.3178	0.26	7.1	134162	0.27	6.5
tier2_aug2														
B86bPBE	0.8663	0.8411	0.38	10.7	95323	0.42	11.8	0.9772	0.8049	0.37	10.6	108366	0.37	10.6
PBE	0.4734	2.3536	0.48	13.7	160030	0.54	15.8	0.6706	1.9851	0.44	12.4	175488	0.51	14.9
LC- ω PBEh-00x	0.7387	1.2975	0.26	6.8	104587	0.27	7.4	0.8070	1.3745	0.28	7.8	119121	0.25	6.7
LC- ω PBEh-20x	0.7161	1.4251	0.25	6.1	116762	0.29	6.9	0.8718	1.2417	0.26	7.3	132649	0.26	6.4

Table C.3: Optimal XDM and XCDM BJ- (a_1 and a_2) and Z- (z_{damp}) damping parameters for selected functionals, calculated using Gaussian 16 [126], and postg release: XCDM(Z) [124]. The mean absolute errors (MAE, in kcal/-mol) and mean absolute percent errors (MAPE) for the KB49 fit set are also shown. LC- ω PBE used $\omega = 0.4 \text{ bohr}^{-1}$. For XCDM(BJ)'s fit to LC- ω PBE, the optimal a_2 damping coefficient was negative, so it was set to zero and a_1 was optimized under that constraint.

Functional	XDM(BJ)				XDM(Z)			XCDM(BJ)				XCDM(Z)		
	a_1	$a_2(\text{ang})$	MAE	MAPE	z_{damp}	MAE	MAPE	a_1	$a_2(\text{ang})$	MAE	MAPE	z_{damp}	MAE	MAPE
aug-cc-pvtz														
PBE0	0.4186	2.6791	—	10.4	189594	0.47	12.0	0.7051	2.0701	0.38	10.1	206696	0.44	11.4
LC- ω PBE	1.0149	0.6755	—	7.3	138857	0.19	6.2	1.3618	0.0000	0.28	9.7	156059	0.21	6.9

Table C.4: Percent contributions to the total weighted MAD using all the WTMAD schemes for each GMTKN55 subset. The number of systems in each subset, N_{syst} , and WTMAD-4 weights, w_i , are also indicated. The level of theory and mean reference energy for each benchmark can be obtained from Ref. [280]. The percent contributions were calculated by dividing each term in the WTMAD summations by their respective total values. The MAD values for each subset were taken as the mean of all 36 combinations of nine functionals (PBE, B86bPBE, PBE0, B86bPBE0, B3LYP, PBE50, B86bPBE50, BHLYP, LC- ω PBE) and four dispersion corrections (XDM(BJ), XDM(Z), XCDDM(BJ), XCDDM(Z)) studied in the Chapter 6.

Subset	N_{syst}	w_i	WTMAD-1	WTMAD-2	WTMAD-3	WTMAD-1.5	WTMAD-4
Basic + Small							
AL2X6	6	2.50	0.80	0.16	0.39	0.69	1.19
ALK8	8	1.00	3.30	0.51	0.93	1.64	1.98
ALKBDE10	10	1.00	0.35	0.42	0.61	1.08	2.08
BH76RC	30	2.50	1.26	2.16	2.08	1.84	1.89
DC13	13	0.50	4.35	1.26	1.40	2.47	1.30
DIPCS10	10	1.00	0.20	0.04	0.05	0.09	1.18
FH51	51	2.50	1.37	2.75	2.64	1.38	2.05
G21EA	25	2.50	1.57	1.43	1.37	1.46	2.36
G21IP	36	1.00	0.18	0.31	0.30	0.22	1.09
G2RC	25	1.00	2.71	1.61	1.55	1.65	1.62
HEAVYSB11	11	2.50	1.38	0.32	0.42	0.74	2.07
NBPRC	12	2.50	1.28	0.68	0.81	1.44	1.92
PA26	26	2.50	0.13	0.21	0.20	0.21	1.90
RC21	21	1.00	2.15	1.54	1.48	1.88	1.29
SIE4x4	16	0.50	5.97	3.46	3.32	5.52	1.79
TAUT15	15	5.00	4.88	2.93	2.82	4.99	1.46
W4-11	140	1.00	0.46	2.58	2.48	0.47	2.78
YBDE18	18	2.50	1.70	0.76	0.73	1.07	2.54
Total:			34.0	23.1	23.6	28.8	32.5
Iso + Large							
BSR36	36	2.50	1.32	3.58	3.44	2.54	1.98
C60ISO	9	0.50	0.40	0.44	0.71	1.26	1.19
CDIE20	20	5.00	4.94	2.97	2.85	3.80	1.48
DARC	14	1.00	2.66	1.40	1.44	2.55	1.59
ISO34	34	5.00	0.71	2.03	1.95	1.52	2.13
ISOL24	24	2.50	1.75	2.34	2.25	2.49	2.62
MB16-43	43	0.50	0.96	1.22	1.17	0.72	2.88
PArel	20	5.00	5.95	3.14	3.01	4.01	1.78
RSE43	43	10.00	0.58	4.03	3.87	2.39	3.49
Total:			19.3	21.2	20.7	21.3	19.1
Barriers							
BH76	76	2.50	1.92	9.58	9.20	3.22	2.88
BHDIV10	10	1.00	1.82	0.49	0.71	1.25	1.09
BHPERI	26	2.50	1.44	2.19	2.11	2.15	2.16
BHROT27	27	10.00	2.45	1.29	1.24	1.22	1.47
INV24	24	2.50	0.85	0.78	0.75	0.83	1.27
PX13	13	1.00	2.45	1.16	1.29	2.29	1.47
WCPT18	18	1.00	1.90	1.20	1.15	1.70	1.14
Total:			12.8	16.7	16.4	12.7	11.5
Intermolecular NCI							
ADIM6	6	25.00	0.85	0.19	0.45	0.79	1.28
AHB21	21	5.00	0.53	0.60	0.58	0.73	1.58
CARBHB12	12	5.00	4.81	1.17	1.41	2.49	1.44
CHB6	6	5.00	0.66	0.18	0.43	0.76	1.97
HAL59	59	10.00	3.27	5.13	4.93	2.22	1.96
HEAVY28	28	25.00	1.71	4.70	4.52	4.29	2.56
IL16	16	10.00	0.03	0.05	0.05	0.08	1.69
PNICO23	23	10.00	2.55	1.68	1.61	1.86	1.53
RG18	18	50.00	0.57	2.17	2.09	3.09	1.72
S22	22	10.00	2.04	0.75	0.72	0.87	1.23
S66	66	25.00	1.56	2.30	2.21	0.89	2.34
WATER27	27	1.00	0.24	0.97	0.93	0.92	1.43
Total:			18.8	19.9	19.9	19.0	20.7
Intramolecular NCI							
ACONF	15	50.00	0.43	0.43	0.41	0.73	1.28
Amino20x4	80	25.00	1.29	5.17	4.96	1.65	1.93
BUT14DIOL	64	25.00	1.32	3.69	3.54	1.47	1.98
ICONF	17	25.00	1.62	1.03	0.98	1.54	2.42
IDISP	6	2.50	1.37	0.71	1.70	3.01	2.06
MCONF	51	25.00	1.21	1.51	1.45	0.76	1.81
PCONF21	18	10.00	3.28	4.45	4.27	6.31	1.97
SCONF	17	10.00	1.95	0.88	0.84	1.32	1.17
UPU23	23	10.00	2.59	1.27	1.22	1.41	1.55
Total:			15.0	19.1	19.4	18.2	16.2

Table C.5: Mean absolute deviation (MAD) values (kcal/mol) for each benchmark in GMTKN55 for the XDM(BJ) dispersion correction for selected functionals. All results were calculated in FHI-aims [120] as described in the computational methods in the Chapter 6, except LC- ω PBE ($\omega = 0.4$ bohr $^{-1}$) which was calculated using Gaussian 16 [126], and postg release: XCDM(Z) [124].

Subset	PBE	B86bPBE	PBE0	B86bPBE0	B3LYP	PBE50	B86bPBE50	BHLYP	LC- ω PBE
AL2X6	1.65	2.19	1.33	0.91	3.41	2.26	1.84	1.49	1.04
ALK8	13.60	6.67	15.56	9.43	10.24	17.55	12.97	32.02	3.42
ALKBDE10	6.02	5.81	5.01	5.33	4.12	12.50	12.88	12.73	5.48
BH76RC	4.18	3.70	2.16	1.95	2.00	2.79	2.81	3.59	2.37
DC13	9.38	8.84	8.60	7.94	10.03	11.94	11.28	9.14	11.40
DIPCS10	4.40	3.94	3.19	3.24	4.87	4.66	4.83	7.20	3.26
FH51	3.12	3.10	2.66	2.42	2.42	4.25	4.03	1.84	3.56
G21EA	3.26	3.33	2.59	2.62	2.57	4.68	4.68	5.03	2.86
G21IP	3.79	3.91	3.63	3.76	3.92	4.35	4.40	4.41	4.59
G2RC	6.72	6.15	6.66	5.97	2.72	8.65	8.12	4.23	5.97
HEAVYSB11	3.55	3.19	1.23	1.58	3.12	2.59	3.02	5.77	4.47
NBPRC	2.28	2.08	2.79	2.28	2.28	4.00	3.63	2.54	3.28
PA26	1.85	2.46	2.15	2.80	2.19	3.36	3.70	2.70	2.81
RC21	6.55	5.95	5.28	4.74	2.48	5.49	5.09	2.26	4.75
SIE4x4	23.46	23.40	14.20	14.10	17.91	5.41	5.31	7.28	9.59
TAUT15	1.76	1.73	1.10	1.05	1.09	0.82	0.75	0.55	0.94
W4-11	15.46	13.11	3.49	3.88	3.28	14.63	16.07	19.82	4.20
YBDE18	5.12	5.15	1.18	1.67	4.85	3.82	4.01	6.10	2.51
BSR36	3.49	3.46	3.38	3.18	3.18	3.31	3.12	4.14	1.83
C60ISO	11.12	10.89	2.26	2.25	2.58	11.27	11.40	11.44	16.78
CDIE20	1.69	1.65	1.25	1.21	0.97	0.94	0.91	0.63	0.90
DARC	3.88	4.35	3.28	2.55	7.34	9.69	9.15	3.20	10.10
ISO34	1.57	1.52	1.43	1.30	1.62	1.98	1.86	1.24	1.90
ISOL24	4.75	4.76	2.21	1.99	5.16	3.95	3.76	3.39	5.90
MB16-43	24.70	21.81	15.52	13.67	25.30	18.95	18.06	26.25	22.39
PArel	1.81	1.76	1.18	1.07	1.10	1.46	1.37	1.25	1.00
RSE43	2.99	2.80	1.47	1.34	1.72	0.46	0.43	0.49	0.58
BH76	9.24	8.81	4.24	3.92	5.18	1.82	1.81	2.15	1.62
BHDIV10	8.61	8.11	4.65	4.27	3.27	1.74	1.63	2.91	1.57
BHPERI	5.86	5.82	2.76	2.63	1.19	1.86	1.83	4.73	2.50
BHROT27	0.44	0.41	0.55	0.52	0.39	0.75	0.73	0.55	0.58
INV24	2.42	2.32	1.07	1.02	0.91	2.36	2.39	2.42	2.20
PX13	11.68	10.85	6.23	5.53	4.32	1.56	1.25	2.59	4.87
WCPT18	9.01	8.34	4.17	3.62	2.37	2.27	2.19	3.66	2.53
ADIM6	0.09	0.09	0.19	0.18	0.10	0.34	0.33	0.04	0.14
AHB21	1.21	0.84	1.40	1.12	0.61	1.85	1.69	1.21	0.65
CARBHB12	1.69	1.57	1.28	1.18	0.84	1.07	0.99	0.52	0.55
CHB6	0.58	0.44	1.34	1.15	1.50	2.17	2.03	2.62	1.51
HAL59	1.21	0.99	0.67	0.56	0.57	0.41	0.37	0.32	0.58
HEAVY28	0.50	0.25	0.36	0.21	0.18	0.28	0.21	0.26	0.32
IL16	0.65	0.35	0.49	0.34	0.40	0.50	0.44	0.68	1.34
PNICO23	1.01	0.78	0.73	0.59	0.23	0.61	0.52	0.21	0.30
RG18	0.24	0.10	0.11	0.05	0.15	0.04	0.05	0.06	0.13
S22	0.52	0.39	0.48	0.38	0.29	0.57	0.49	0.46	0.34
S66	0.39	0.31	0.36	0.29	0.27	0.41	0.37	0.35	0.21
WATER27	7.61	7.09	5.25	4.51	6.09	3.90	3.19	3.74	1.64
ACONF	0.08	0.12	0.10	0.04	0.17	0.14	0.06	0.13	0.09
Amino20x4	0.32	0.33	0.26	0.25	0.21	0.32	0.31	0.29	0.31
BUT14DIOL	0.43	0.56	0.23	0.30	0.52	0.11	0.14	0.17	0.09
ICONF	0.36	0.34	0.29	0.27	0.31	0.42	0.41	0.45	0.34
IDISP	3.45	3.03	2.13	1.69	3.52	3.12	2.95	4.08	3.91
MCONF	0.49	0.41	0.26	0.22	0.19	0.12	0.15	0.19	0.33
PCONF21	1.50	0.97	1.09	0.73	0.45	0.78	0.56	0.44	0.47
SCONF	0.64	0.98	0.21	0.38	0.47	0.17	0.13	0.51	0.32
UPU23	0.60	0.44	0.56	0.50	0.45	0.64	0.61	0.73	0.70
WTMAD-1	5.76	5.23	4.01	3.54	3.65	4.05	3.72	3.82	3.45
WTMAD-2	10.40	9.38	6.55	5.78	6.27	6.06	5.67	5.72	5.48
WTMAD-3	5.59	4.95	3.68	3.17	3.40	3.46	3.18	3.17	3.21
WTMAD-1.5	10.79	9.54	7.18	6.16	6.70	6.96	6.39	6.51	6.35
WTMAD-4	8.99	8.13	6.06	5.34	6.12	6.92	6.50	7.06	5.98

Table C.6: Mean absolute deviation (MAD) values (kcal/mol) for each benchmark in GMTKN55 for the XDM(Z) dispersion correction for selected functionals. All results were calculated in FHI-aims [120] as described in the computational methods in the Chapter 6, except LC- ω PBE ($\omega = 0.4$ bohr $^{-1}$) which was calculated using Gaussian 16 [126], and postg release: XCDM(Z) [124].

Subset	PBE	B86bPBE	PBE0	B86bPBE0	B3LYP	PBE50	B86bPBE50	BHLYP	LC- ω PBE
AL2X6	1.61	1.49	1.21	1.21	2.88	1.89	1.86	2.76	1.85
ALK8	3.13	2.86	3.27	3.04	1.89	3.92	3.75	3.87	2.67
ALKBDE10	6.05	5.87	5.07	5.36	4.17	12.60	12.94	13.02	5.50
BH76RC	4.21	3.77	2.20	1.97	1.92	2.83	2.85	3.60	2.39
DC13	8.57	8.27	8.63	8.01	9.20	12.20	11.68	9.74	12.03
DIPCS10	4.57	4.01	3.29	3.33	4.75	4.71	4.86	7.37	3.19
FH51	3.06	2.97	2.84	2.61	2.12	4.51	4.32	2.09	3.73
G21EA	3.20	3.36	2.64	2.64	2.54	4.74	4.71	5.38	2.86
G21IP	3.81	3.93	3.66	3.78	3.92	4.36	4.42	4.47	4.59
G2RC	6.66	6.09	6.63	6.02	2.58	8.66	8.29	4.46	6.09
HEAVYSB11	3.30	2.91	0.99	1.14	2.70	2.57	2.76	6.30	3.46
NBPRC	2.27	1.94	3.02	2.62	2.28	4.30	4.02	2.88	3.64
PA26	2.07	2.54	2.57	3.15	2.68	3.73	4.09	3.46	2.90
RC21	6.86	6.23	5.65	5.11	2.81	5.85	5.47	2.28	4.98
SIE4x4	23.56	23.42	14.30	14.17	18.00	5.51	5.40	7.44	9.60
TAUT15	1.81	1.78	1.12	1.10	1.19	0.77	0.71	0.56	0.97
W4-11	15.51	13.11	3.46	3.77	3.34	14.55	15.97	19.78	4.20
YBDE18	5.20	5.09	1.17	1.36	4.48	3.66	3.85	6.05	2.48
BSR36	3.14	2.26	3.09	2.44	2.34	3.09	2.68	4.27	0.73
C60ISO	10.85	10.90	2.30	2.29	2.48	11.63	11.65	12.19	16.56
CDIE20	1.65	1.55	1.21	1.13	0.86	0.90	0.86	0.60	0.89
DARC	3.23	3.30	4.08	3.61	5.93	10.46	10.07	2.26	11.09
ISO34	1.53	1.44	1.45	1.31	1.49	2.01	1.90	1.16	1.91
ISOL24	4.42	4.25	2.14	1.99	4.46	4.34	4.23	2.97	6.37
MB16-43	23.10	21.78	15.03	14.00	26.18	20.74	20.33	38.12	20.39
PArel	1.84	1.76	1.20	1.11	1.04	1.50	1.43	1.23	1.04
RSE43	2.86	2.62	1.34	1.17	1.44	0.40	0.39	0.45	0.57
BH76	9.32	9.01	4.33	4.07	5.40	1.83	1.79	2.12	1.62
BHDIV10	8.62	8.25	4.65	4.34	3.19	1.79	1.73	2.97	1.75
BHPERI	6.03	5.96	2.96	2.81	1.19	1.93	1.91	4.60	2.41
BHROT27	0.45	0.43	0.56	0.54	0.42	0.75	0.74	0.57	0.58
INV24	2.43	2.27	1.08	1.02	0.90	2.38	2.41	2.43	2.21
PX13	11.96	11.18	6.51	5.88	4.83	1.78	1.51	2.16	5.09
WCPT18	9.21	8.56	4.38	3.86	2.69	2.49	2.43	3.37	2.66
ADIM6	0.10	0.20	0.02	0.09	0.33	0.15	0.10	0.17	0.09
AHB21	1.27	1.16	1.45	1.32	0.90	1.89	1.79	1.24	0.72
CARBHB12	1.76	1.60	1.36	1.24	0.91	1.15	1.07	0.57	0.58
CHB6	0.65	0.60	1.43	1.38	1.70	2.24	2.19	2.54	1.81
HAL59	1.44	1.47	0.88	0.90	1.01	0.57	0.59	0.53	0.56
HEAVY28	0.71	0.76	0.55	0.59	0.57	0.43	0.46	0.35	0.33
IL16	0.97	1.14	0.66	0.76	0.58	0.53	0.53	0.60	0.56
PNICO23	1.05	0.96	0.75	0.69	0.37	0.62	0.58	0.44	0.28
RG18	0.30	0.14	0.17	0.09	0.19	0.12	0.09	0.19	0.13
S22	0.57	0.40	0.57	0.44	0.46	0.66	0.59	0.66	0.26
S66	0.41	0.31	0.40	0.33	0.44	0.47	0.41	0.51	0.17
WATER27	9.52	8.13	7.26	6.12	8.06	5.95	5.10	6.70	2.27
ACONF	0.06	0.11	0.06	0.04	0.12	0.10	0.05	0.11	0.10
Amino20x4	0.33	0.33	0.28	0.27	0.22	0.33	0.32	0.26	0.33
BUT14DIOL	0.52	0.53	0.32	0.33	0.52	0.20	0.20	0.30	0.10
ICONF	0.34	0.31	0.30	0.28	0.32	0.45	0.44	0.52	0.37
IDISP	3.17	2.78	1.91	1.51	3.38	3.19	3.07	4.18	3.97
MCONF	0.47	0.43	0.25	0.24	0.19	0.15	0.22	0.13	0.41
PCONF21	1.40	1.05	0.97	0.72	0.50	0.67	0.52	0.30	0.47
SCONF	0.87	1.00	0.43	0.52	0.62	0.14	0.18	0.21	0.34
UPU23	0.55	0.47	0.56	0.54	0.52	0.65	0.65	0.72	0.83
WTMAD-1	5.70	5.36	3.95	3.68	3.76	3.93	3.77	3.51	3.51
WTMAD-2	10.78	10.00	6.96	6.43	6.88	6.44	6.20	6.09	5.51
WTMAD-3	5.73	5.25	3.83	3.49	3.66	3.60	3.41	3.26	3.25
WTMAD-1.5	10.96	10.06	7.34	6.69	7.13	7.08	6.71	6.51	6.43
WTMAD-4	9.10	8.52	6.12	5.73	6.44	6.95	6.74	7.16	5.92

Table C.7: Mean absolute deviation (MAD) values (kcal/mol) for each benchmark in GMTKN55 for the XCDM(BJ) dispersion correction for selected functionals. All results were calculated in FHI-aims [120] as described in the computational methods in the Chapter 6, except LC- ω PBE ($\omega = 0.4$ bohr $^{-1}$) which was calculated using Gaussian 16 [126], and postg release: XCDM(Z) [124].

Subset	PBE	B86bPBE	PBE0	B86bPBE0	B3LYP	PBE50	B86bPBE50	BHLYP	LC- ω PBE
AL2X6	1.79	2.24	1.05	0.79	3.26	1.71	1.32	1.70	0.85
ALK8	8.40	5.55	9.03	6.04	12.09	10.09	7.87	28.48	2.15
ALKBDE10	5.99	5.78	5.08	5.41	4.15	12.63	13.02	12.90	5.49
BH76RC	4.16	3.68	2.15	1.93	2.00	2.79	2.81	3.59	2.36
DC13	9.15	8.79	8.49	7.84	10.09	11.78	11.10	9.17	11.32
DIPCS10	4.47	4.00	3.23	3.30	4.81	4.68	4.85	7.24	3.16
FH51	3.11	3.13	2.63	2.36	2.54	4.23	3.98	1.83	3.49
G21EA	3.21	3.33	2.63	2.64	2.60	4.72	4.71	5.13	2.87
G21IP	3.79	3.92	3.64	3.77	3.92	4.35	4.41	4.43	4.59
G2RC	6.62	6.06	6.52	5.84	2.62	8.50	7.99	4.08	5.89
HEAVYSB11	3.46	3.10	1.46	1.95	3.17	3.00	3.45	6.06	4.82
NBPRC	2.30	2.17	2.70	2.14	2.32	3.90	3.49	2.67	3.10
PA26	1.91	2.47	2.27	2.91	2.07	3.46	3.81	2.79	2.92
RC21	6.53	5.83	5.25	4.64	2.33	5.45	5.01	2.26	4.68
SIE4x4	23.46	23.36	14.20	14.09	17.82	5.41	5.30	7.26	9.60
TAUT15	1.77	1.73	1.11	1.05	1.07	0.81	0.75	0.55	0.94
W4-11	15.39	12.93	3.46	3.98	3.20	14.73	16.21	20.02	4.26
YBDE18	5.19	5.23	1.29	1.91	5.10	3.81	4.01	6.40	2.48
BSR36	3.48	3.12	3.44	3.13	2.55	3.43	3.23	4.23	1.80
C60ISO	11.05	10.90	2.26	2.26	2.71	11.42	11.54	11.48	16.88
CDIE20	1.71	1.68	1.27	1.25	1.02	0.96	0.95	0.65	0.92
DARC	3.86	4.40	3.21	2.40	7.74	9.60	8.99	3.43	9.96
ISO34	1.59	1.55	1.46	1.32	1.69	1.99	1.87	1.28	1.92
ISOL24	4.66	4.68	2.17	1.95	5.02	4.00	3.79	3.31	5.97
MB16-43	24.25	22.13	15.04	13.76	24.97	18.82	18.47	29.01	23.51
PArel	1.81	1.74	1.18	1.07	1.11	1.46	1.37	1.25	1.00
RSE43	3.00	2.82	1.47	1.35	1.75	0.46	0.43	0.50	0.58
BH76	9.17	8.71	4.17	3.83	5.03	1.83	1.82	2.17	1.60
BHDIV10	8.57	8.06	4.59	4.20	3.13	1.71	1.60	2.99	1.55
BHPERI	5.75	5.57	2.63	2.39	1.11	1.81	1.78	5.02	2.66
BHROT27	0.44	0.41	0.56	0.52	0.37	0.75	0.72	0.55	0.58
INV24	2.45	2.38	1.07	1.03	0.93	2.36	2.39	2.40	2.24
PX13	11.64	10.72	6.19	5.45	4.03	1.54	1.22	2.67	4.82
WCPT18	8.95	8.19	4.11	3.50	2.09	2.23	2.12	3.79	2.45
ADIM6	0.16	0.26	0.28	0.36	0.10	0.44	0.49	0.09	0.39
AHB21	1.07	0.75	1.24	0.96	0.43	1.70	1.53	1.04	0.64
CARBHB12	1.66	1.49	1.25	1.12	0.69	1.04	0.94	0.47	0.50
CHB6	0.54	0.46	1.12	0.94	1.11	1.95	1.78	2.35	1.37
HAL59	1.10	0.92	0.58	0.50	0.52	0.36	0.35	0.24	0.69
HEAVY28	0.34	0.19	0.20	0.15	0.15	0.15	0.16	0.19	0.47
IL16	0.48	0.33	0.36	0.35	0.55	0.44	0.48	0.94	1.59
PNICO23	0.92	0.71	0.63	0.53	0.18	0.52	0.47	0.22	0.37
RG18	0.22	0.09	0.09	0.05	0.15	0.05	0.07	0.04	0.16
S22	0.48	0.33	0.46	0.34	0.24	0.56	0.47	0.42	0.33
S66	0.37	0.30	0.36	0.30	0.21	0.42	0.38	0.32	0.26
WATER27	7.22	5.80	4.89	3.67	3.85	3.59	2.64	2.84	1.20
ACONF	0.11	0.09	0.15	0.04	0.08	0.19	0.12	0.21	0.03
Amino20x4	0.32	0.32	0.26	0.25	0.20	0.32	0.30	0.30	0.28
BUT14DIOL	0.43	0.53	0.22	0.29	0.43	0.11	0.12	0.13	0.09
ICONF	0.37	0.34	0.30	0.28	0.30	0.41	0.41	0.46	0.34
IDISP	3.31	2.99	2.09	1.56	3.12	3.44	3.18	4.00	4.06
MCONF	0.47	0.40	0.25	0.22	0.24	0.12	0.19	0.16	0.37
PCONF21	1.39	0.90	1.00	0.67	0.45	0.72	0.51	0.43	0.42
SCONF	0.67	0.93	0.21	0.38	0.28	0.16	0.12	0.58	0.36
UPU23	0.50	0.40	0.51	0.46	0.49	0.60	0.58	0.71	0.66
WTMAD-1	5.55	5.12	3.80	3.42	3.52	3.86	3.62	3.76	3.51
WTMAD-2	10.06	9.10	6.23	5.59	5.95	5.86	5.60	5.60	5.67
WTMAD-3	5.40	4.81	3.50	3.07	3.24	3.34	3.13	3.12	3.30
WTMAD-1.5	10.41	9.30	6.81	5.97	6.39	6.71	6.29	6.40	6.55
WTMAD-4	8.71	7.97	5.79	5.23	5.82	6.74	6.48	7.08	6.20

Table C.8: Mean absolute deviation (MAD) values (kcal/mol) for each benchmark in GMTKN55 for the XCDM(Z) dispersion correction for selected functionals. All results were calculated in FHI-aims [120] as described in the computational methods in the Chapter 6, except LC- ω PBE ($\omega = 0.4$ bohr $^{-1}$) which was calculated using Gaussian 16 [126], and postg release: XCDM(Z) [124].

Subset	PBE	B86bPBE	PBE0	B86bPBE0	B3LYP	PBE50	B86bPBE50	BHLYP	LC- ω PBE
AL2X6	1.66	1.57	1.17	1.14	3.26	1.77	1.68	2.91	1.73
ALK8	3.03	2.69	3.15	2.80	2.32	3.79	3.56	3.93	2.49
ALKBDE10	6.04	5.85	5.08	5.38	4.20	12.62	12.97	13.06	5.50
BH76RC	4.20	3.75	2.19	1.96	1.92	2.82	2.84	3.60	2.38
DC13	8.57	8.38	8.57	7.83	9.63	12.06	11.47	9.98	11.83
DIPCS10	4.57	4.02	3.29	3.33	4.75	4.71	4.86	7.38	3.18
FH51	3.06	2.99	2.80	2.54	2.22	4.47	4.26	2.05	3.66
G21EA	3.20	3.36	2.64	2.64	2.54	4.74	4.71	5.39	2.86
G21IP	3.81	3.93	3.66	3.78	3.92	4.36	4.42	4.47	4.59
G2RC	6.63	6.02	6.58	5.95	2.54	8.61	8.23	4.40	6.03
HEAVYSB11	3.25	2.85	1.00	1.19	2.86	2.65	2.87	6.38	3.58
NBPRC	2.28	2.02	2.95	2.51	2.45	4.22	3.90	2.98	3.53
PA26	2.07	2.52	2.55	3.13	2.64	3.72	4.07	3.44	2.88
RC21	6.79	6.09	5.57	4.97	2.61	5.77	5.35	2.27	4.87
SIE4x4	23.55	23.40	14.29	14.15	17.97	5.50	5.39	7.42	9.59
TAUT15	1.80	1.77	1.12	1.09	1.17	0.77	0.71	0.55	0.97
W4-11	15.47	13.02	3.45	3.84	3.30	14.61	16.07	19.90	4.21
YBDE18	5.23	5.15	1.21	1.53	4.83	3.68	3.87	6.27	2.47
BSR36	3.23	2.44	3.20	2.62	2.61	3.21	2.85	4.46	0.89
C60ISO	10.82	10.85	2.31	2.30	2.45	11.67	11.69	12.24	16.61
CDIE20	1.66	1.58	1.22	1.16	0.91	0.92	0.88	0.62	0.89
DARC	3.35	3.62	3.86	3.21	6.70	10.24	9.74	2.63	10.77
ISO34	1.54	1.48	1.46	1.32	1.57	2.01	1.90	1.19	1.91
ISOL24	4.46	4.36	2.15	1.96	4.59	4.30	4.16	3.04	6.30
MB16-43	23.03	21.60	14.90	13.88	28.42	20.66	20.21	39.37	20.65
PArel	1.83	1.75	1.19	1.10	1.05	1.49	1.41	1.23	1.03
RSE43	2.87	2.64	1.35	1.20	1.49	0.41	0.39	0.45	0.58
BH76	9.30	8.94	4.30	4.01	5.28	1.83	1.79	2.13	1.61
BHDIV10	8.59	8.17	4.61	4.27	3.11	1.77	1.70	3.05	1.71
BHPERI	5.91	5.72	2.82	2.58	1.06	1.87	1.83	4.84	2.53
BHROT27	0.45	0.43	0.56	0.54	0.41	0.75	0.74	0.56	0.58
INV24	2.45	2.30	1.08	1.02	0.93	2.38	2.40	2.42	2.21
PX13	11.91	11.08	6.46	5.79	4.64	1.75	1.46	2.25	5.02
WCPT18	9.16	8.46	4.33	3.76	2.51	2.44	2.36	3.47	2.60
ADIM6	0.15	0.27	0.05	0.15	0.42	0.13	0.09	0.22	0.12
AHB21	1.22	1.07	1.40	1.24	0.73	1.84	1.72	1.16	0.68
CARBHB12	1.74	1.56	1.34	1.20	0.85	1.13	1.03	0.53	0.54
CHB6	0.64	0.51	1.37	1.27	1.49	2.18	2.10	2.43	1.73
HAL59	1.42	1.41	0.85	0.85	0.94	0.55	0.56	0.49	0.55
HEAVY28	0.69	0.73	0.53	0.56	0.54	0.40	0.43	0.32	0.31
IL16	0.90	0.99	0.59	0.62	0.41	0.49	0.47	0.70	0.64
PNICO23	1.02	0.90	0.71	0.64	0.29	0.60	0.55	0.43	0.27
RG18	0.29	0.13	0.17	0.09	0.17	0.12	0.09	0.18	0.14
S22	0.56	0.36	0.55	0.41	0.40	0.65	0.58	0.63	0.27
S66	0.40	0.29	0.39	0.31	0.40	0.46	0.40	0.49	0.17
WATER27	9.28	7.64	7.00	5.67	7.24	5.69	4.72	6.24	1.89
ACONF	0.07	0.09	0.09	0.02	0.07	0.13	0.08	0.15	0.05
Amino20x4	0.33	0.32	0.27	0.27	0.21	0.33	0.32	0.26	0.33
BUT14DIOL	0.50	0.51	0.30	0.30	0.49	0.18	0.17	0.27	0.08
ICONF	0.35	0.32	0.31	0.28	0.32	0.45	0.45	0.52	0.37
IDISP	3.22	2.86	2.00	1.67	3.63	3.34	3.25	4.34	4.15
MCONF	0.47	0.42	0.25	0.25	0.21	0.16	0.23	0.13	0.41
PCONF21	1.39	1.02	0.97	0.71	0.50	0.66	0.51	0.28	0.46
SCONF	0.84	0.94	0.39	0.46	0.53	0.12	0.14	0.26	0.28
UPU23	0.50	0.46	0.54	0.53	0.53	0.63	0.64	0.71	0.81
WTMAD-1	5.67	5.31	3.91	3.61	3.74	3.89	3.71	3.54	3.46
WTMAD-2	10.70	9.87	6.88	6.29	6.76	6.37	6.11	6.08	5.44
WTMAD-3	5.69	5.19	3.79	3.41	3.60	3.56	3.36	3.27	3.20
WTMAD-1.5	10.90	9.96	7.27	6.56	7.07	7.01	6.62	6.56	6.35
WTMAD-4	9.05	8.42	6.06	5.60	6.37	6.90	6.66	7.25	5.85

Table C.9: Mean absolute deviation (MAD) values (kcal/mol) for each benchmark in GMTKN55 for D3(BJ)^{a,d}, TS, MBD@rsSCS^b, and MBD-NL^c dispersion corrections paired with the PBE and PBE0 functionals. All results were calculated in FHI-aims [120] as described in the computational methods in the Chapter 6, except for D3(BJ), where data computed with ORCA was obtained from Ref. [280].

Subset	D3(BJ) ^{a,d}		TS		MBD@rsSCS ^b		MBD-NL ^c	
	PBE	PBE0	PBE	PBE0	PBE	PBE0	PBE	PBE0
AL2X6	1.63	1.48	1.93	1.52	1.71	1.34	2.22	1.80
ALK8	4.14	4.61	11.56	10.01	15.15	13.75	6.64	6.36
ALKBDE10	6.30	5.66	5.95	5.18	6.07	5.06	6.07	5.05
BH76RC	4.18	2.46	4.11	2.12	4.13	2.16	3.80	2.04
DC13	8.63	8.01	9.04	8.42	8.57	8.88	8.62	9.19
DIPCS10	4.50	2.99	4.59	3.28	4.51	3.24	4.61	3.30
FH51	3.17	2.77	3.08	2.64	3.04	2.82	3.07	3.01
G21EA	3.43	2.62	3.20	2.64	3.22	2.63	3.19	2.63
G21IP	3.85	3.68	3.82	3.67	3.80	3.65	3.74	3.60
G2RC	6.92	6.75	6.39	6.32	6.74	6.63	6.85	6.73
HEAVYSB11	3.55	1.37	3.34	2.22	3.39	2.14	2.99	1.22
NBPRC	2.41	3.18	2.41	2.61	2.36	2.94	2.62	3.22
PA26	2.19	2.88	2.02	2.46	2.05	2.51	2.27	2.82
RC21	6.85	5.50	6.47	5.09	6.90	5.54	7.10	5.78
SIE4x4	23.72	14.39	23.50	14.23	23.53	14.25	23.57	14.28
TAUT15	1.84	1.13	1.71	1.05	1.81	1.12	1.85	1.14
W4-11	15.68	3.70	15.03	3.46	15.39	3.49	15.47	3.52
YBDE18	4.93	0.98	5.34	1.67	5.06	1.16	4.91	0.98
BSR36	3.17	3.25	4.00	4.25	2.56	2.95	2.52	2.83
C60ISO	10.72	2.35	10.73	2.44	10.65	2.40	10.44	2.47
CDIE20	1.65	1.24	1.81	1.38	1.64	1.21	1.63	1.20
DARC	3.31	3.76	3.92	2.57	2.92	4.11	2.51	4.99
ISO34	1.49	1.42	1.56	1.45	1.50	1.44	1.50	1.47
ISOL24	4.39	2.11	4.72	2.22	3.99	2.27	3.74	2.34
MB16-43	24.26	15.86	22.50	14.60	24.33	15.41	23.99	14.86
PArel	1.81	1.21	1.84	1.17	1.82	1.19	1.83	1.20
RSE43	2.94	1.45	2.93	1.44	2.89	1.39	2.71	1.23
BH76	9.62	5.00	9.09	4.07	9.25	4.22	8.57	3.66
BHDIV10	8.87	4.81	8.19	4.21	8.71	4.66	8.79	4.72
BHPERI	6.69	3.27	5.43	2.15	6.31	3.00	6.58	3.28
BHROT27	0.47	0.58	0.38	0.50	0.49	0.59	0.50	0.60
INV24	2.07	1.17	2.50	1.20	2.43	1.07	2.40	1.09
PX13	12.02	6.55	11.59	6.12	11.74	6.24	11.98	6.47
WCPT18	9.34	4.33	8.78	3.92	9.11	4.21	9.19	4.28
ADIM6	0.21	0.06	1.30	1.01	0.45	0.22	0.41	0.21
AHB21	1.15	1.24	0.93	1.03	1.10	1.21	0.91	1.07
CARBHB12	1.91	1.44	1.67	1.23	1.73	1.28	1.82	1.37
CHB6	0.93	1.37	1.60	2.18	1.92	2.54	1.59	2.30
HAL59	1.18	0.61	0.92	0.59	1.01	0.61	1.06	0.63
HEAVY28	0.42	0.31	0.24	0.21	0.21	0.20	0.25	0.18
IL16	0.59	0.34	0.34	0.43	0.69	0.35	0.92	0.67
PNICO23	1.32	0.94	0.87	0.54	0.93	0.61	1.03	0.68
RG18	0.26	0.11	0.23	0.11	0.19	0.12	0.20	0.12
S22	0.48	0.48	0.35	0.38	0.52	0.56	0.64	0.65
S66	0.40	0.36	0.52	0.46	0.41	0.40	0.46	0.45
WATER27	8.92	5.92	8.07	5.42	8.93	6.20	8.82	6.19
ACONF	0.07	0.06	0.14	0.08	0.09	0.03	0.11	0.03
Amino20x4	0.34	0.28	0.39	0.38	0.34	0.29	0.36	0.30
BUT14DIOL	0.46	0.22	0.49	0.24	0.43	0.21	0.46	0.23
ICONF	0.32	0.28	0.47	0.41	0.39	0.33	0.38	0.33
IDISP	2.76	1.54	3.55	2.56	2.57	1.74	2.45	1.53
MCONF	0.49	0.27	0.44	0.30	0.53	0.30	0.58	0.39
PCONF21	1.25	0.90	1.12	0.92	1.45	1.12	1.55	1.22
SCONF	0.80	0.27	0.62	0.32	0.83	0.32	0.95	0.42
UPU23	0.53	0.54	0.56	0.53	0.52	0.55	0.69	0.69
WTMAD-1	5.67	3.87	5.77	4.02	5.75	4.03	5.75	4.06
WTMAD-2	10.41 ^d	6.60 ^d	10.07	6.53	9.96	6.45	10.05	6.53
WTMAD-3	5.54	3.63	5.39	3.60	5.37	3.64	5.44	3.70
WTMAD-1.5	10.64	6.97	10.67	7.19	10.46	7.12	10.52	7.18
WTMAD-4	8.94	5.87	9.37	6.43	9.04	6.12	9.04	6.16

^a D3(BJ) result obtained from Ref. [280], values recalculated using Tables S24 and S68 in their ESI.

^b MBD@rsSCS crashed for some systems due to a polarization catastrophe [315], so two reactions were substituted using MBD-NL results: 1 na8 → 4 na2 and 1 li5_ch → 1 li4_c + 1 li_h.

^c MBD-NL crashed for some systems due to a polarization catastrophe [315], so two reactions were substituted using MBD@rsSCS results: 1 f + 1 H2 → 1 RKT10 and 1 hf + 1 h → 1 RKT10.

^d When recalculating D3(BJ)'s WTMAD-2 we noticed a discrepancy between our calculated values for "Basic+Small" and "GMTKN55" categories compared to the values listed both in Ref. [280]'s ESI and the online GMTKN55 database [279].

Table C.10: The GMTKN55 WTMAD-2 values (kcal/mol), broken down by category, for each dispersion correction and functional tested in this study. All results were calculated in FHI-aims [120] as described in the computational methods in the Chapter 6, except for D3(BJ), where data computed with ORCA was obtained from Ref. [280].

Functional	DC	Basic + Small	Iso + Large	Barriers	Intermol NCI	Intramol NCI	All NCI	GMTKN55
PBE	D3(BJ) ^{a,d}	6.78 ^d	12.36	18.36	10.21	9.58	9.90	10.41 ^d
PBE	TS	6.68	13.13	17.08	8.61	9.87	9.23	10.07
PBE	MBDrssCS ^b	6.83	11.84	17.80	8.20	10.07	9.12	9.96
PBE	MBD-NL ^c	6.71	11.45	17.14	8.79	10.88	9.81	10.05
PBE	XDM(BJ)	6.80	12.85	17.54	9.94	9.91	9.92	10.40
PBE	XDM(Z)	6.66	12.26	17.78	12.07	10.20	11.16	10.78
PBE	XCDM(BJ)	6.71	12.84	17.41	8.77	9.63	9.19	10.06
PBE	XCDM(Z)	6.65	12.36	17.69	11.84	10.04	10.96	10.70
B86bPBE	XDM(BJ)	6.38	12.43	16.71	6.94	9.37	8.13	9.38
B86bPBE	XDM(Z)	6.31	11.17	17.10	10.82	9.41	10.13	10.00
B86bPBE	XCDM(BJ)	6.34	12.30	16.47	6.28	8.93	7.58	9.10
B86bPBE	XCDM(Z)	6.29	11.41	16.90	10.40	9.16	9.79	9.87
PBE0	D3(BJ) ^{a,d}	4.42 ^d	8.39	9.88	6.65	6.40	6.53	6.60 ^d
PBE0	TS	4.32	8.91	8.12	6.14	7.49	6.80	6.53
PBE0	MBDrssCS ^b	4.51	8.17	8.76	6.09	6.99	6.53	6.45
PBE0	MBD-NL ^c	4.47	8.00	8.26	6.30	7.75	7.01	6.53
PBE0	XDM(BJ)	4.43	8.43	8.66	6.77	6.79	6.78	6.55
PBE0	XDM(Z)	4.34	8.14	8.92	8.71	7.12	7.93	6.96
PBE0	XCDM(BJ)	4.32	8.48	8.52	5.61	6.59	6.09	6.23
PBE0	XCDM(Z)	4.32	8.21	8.81	8.42	7.02	7.74	6.88
B86bPBE0	XDM(BJ)	4.16	7.76	7.99	5.00	6.11	5.54	5.78
B86bPBE0	XDM(Z)	4.17	7.21	8.34	8.06	6.50	7.30	6.43
B86bPBE0	XCDM(BJ)	4.09	7.79	7.75	4.52	5.87	5.18	5.59
B86bPBE0	XCDM(Z)	4.13	7.32	8.15	7.66	6.29	6.99	6.29
B3LYP	XDM(BJ)	4.30	9.78	8.38	4.94	6.55	5.73	6.27
B3LYP	XDM(Z)	4.13	8.41	8.80	8.77	6.82	7.82	6.88
B3LYP	XCDM(BJ)	4.33	9.59	8.08	4.20	5.96	5.06	5.95
B3LYP	XCDM(Z)	4.17	8.89	8.54	8.09	6.61	7.37	6.76
PBE50	XDM(BJ)	5.59	8.65	4.95	5.44	6.03	5.73	6.06
PBE50	XDM(Z)	5.46	8.71	5.06	7.20	6.24	6.73	6.44
PBE50	XCDM(BJ)	5.46	8.76	4.94	4.72	5.91	5.30	5.86
PBE50	XCDM(Z)	5.44	8.76	5.02	6.94	6.18	6.57	6.37
B86bPBE50	XDM(BJ)	5.44	8.20	4.85	4.75	5.45	5.09	5.67
B86bPBE50	XDM(Z)	5.40	8.22	4.95	6.89	5.94	6.42	6.20
B86bPBE50	XCDM(BJ)	5.34	8.31	4.83	4.52	5.39	4.94	5.60
B86bPBE50	XCDM(Z)	5.37	8.27	4.90	6.56	5.85	6.21	6.11
BHLYP	XDM(BJ)	5.25	7.54	6.57	4.28	5.91	5.08	5.72
BHLYP	XDM(Z)	5.01	7.55	6.42	6.82	5.66	6.25	6.09
BHLYP	XCDM(BJ)	5.24	7.71	6.72	3.49	5.86	4.65	5.60
BHLYP	XCDM(Z)	5.03	7.78	6.54	6.48	5.63	6.07	6.08
LC- ω PBE	XDM(BJ)	4.35	8.24	5.11	5.07	5.68	5.37	5.48
LC- ω PBE	XDM(Z)	4.45	7.85	5.14	4.92	6.16	5.53	5.51
LC- ω PBE	XCDM(BJ)	4.30	8.28	5.13	6.33	5.38	5.86	5.67
LC- ω PBE	XCDM(Z)	4.40	7.90	5.14	4.78	5.96	5.36	5.44

^a D3(BJ) result obtained from Ref. [280], values recalculated using Tables S24 and S68 in their ESI.

^b MBD@rsSCS crashed for some systems due to a polarization catastrophe [315], so two reactions were substituted using MBD-NL results: 1 na8 \rightarrow 4 na2 and 1 li5_ch \rightarrow 1 li4_c + 1 li_h.

^c MBD-NL crashed for some systems due to a polarization catastrophe [315], so two reactions were substituted using MBD@rsSCS results: 1 f + 1 H2 \rightarrow 1 RKT10 and 1 hf + 1 h \rightarrow 1 RKT10.

^d When recalculating D3(BJ)'s WTMAD-2 we noticed a discrepancy between our calculated values for "Basic+Small" and "GMTKN55" categories compared to the values listed both in Ref. [280]'s ESI and the online GMTKN55 database [279].

Table C.11: The GMTKN55 WTMAD-4 values (kcal/mol), broken down by category, for each dispersion correction and functional tested in this study. All results were calculated in FHI-aims [120] as described in the computational methods in the Chapter 6, except for D3(BJ), where data computed with ORCA was obtained from Ref. [280].

Functional	DC	Basic + Small	Iso + Large	Barriers	Intermol NCI	Intramol NCI	All NCI	GMTKN55
PBE	D3(BJ) ^a	7.63	10.43	11.55	8.61	8.49	8.56	8.94
PBE	TS	7.90	10.86	10.71	9.75	9.26	9.54	9.37
PBE	MBD@rsSCS ^b	8.11	10.06	11.34	8.35	9.00	8.63	9.04
PBE	MBD-NL ^c	7.69	9.70	11.27	8.73	9.77	9.17	9.04
PBE	XDM(BJ)	8.02	10.85	11.08	7.93	8.88	8.34	8.99
PBE	XDM(Z)	7.44	10.31	11.25	9.49	9.00	9.28	9.10
PBE	XCDM(BJ)	7.73	10.82	11.01	7.19	8.79	7.88	8.71
PBE	XCDM(Z)	7.43	10.38	11.19	9.35	8.91	9.16	9.05
B86bPBE	XDM(BJ)	7.41	10.44	10.54	5.62	8.73	6.95	8.13
B86bPBE	XDM(Z)	7.06	9.54	10.77	8.59	8.60	8.60	8.52
B86bPBE	XCDM(BJ)	7.34	10.38	10.38	5.46	8.26	6.66	7.97
B86bPBE	XCDM(Z)	7.05	9.71	10.62	8.24	8.37	8.30	8.42
PBE0	D3(BJ) ^a	5.23	6.68	6.44	6.13	5.58	5.90	5.87
PBE0	TS	5.46	6.85	5.41	7.88	6.79	7.41	6.43
PBE0	MBD@rsSCS ^b	5.71	6.57	5.95	6.58	6.00	6.33	6.12
PBE0	MBD-NL ^c	5.34	6.46	5.93	6.92	6.65	6.81	6.16
PBE0	XDM(BJ)	5.55	6.68	5.83	6.44	6.09	6.29	6.06
PBE0	XDM(Z)	4.98	6.49	6.01	7.51	6.24	6.96	6.12
PBE0	XCDM(BJ)	5.20	6.68	5.74	5.75	6.17	5.93	5.79
PBE0	XCDM(Z)	4.95	6.52	5.93	7.26	6.32	6.85	6.06
B86bPBE0	XDM(BJ)	5.18	6.09	5.36	4.98	5.35	5.14	5.34
B86bPBE0	XDM(Z)	4.93	5.80	5.60	6.97	5.72	6.44	5.73
B86bPBE0	XCDM(BJ)	5.04	6.09	5.21	4.91	5.18	5.03	5.23
B86bPBE0	XCDM(Z)	4.89	5.84	5.46	6.62	5.50	6.14	5.60
B3LYP	XDM(BJ)	6.01	8.65	4.58	4.77	6.82	5.64	6.12
B3LYP	XDM(Z)	5.39	7.62	4.81	7.74	6.86	7.36	6.44
B3LYP	XCDM(BJ)	6.11	8.57	4.38	4.07	5.94	4.87	5.82
B3LYP	XCDM(Z)	5.56	8.08	4.65	7.15	6.61	6.92	6.37
PBE50	XDM(BJ)	8.33	7.71	4.02	6.49	6.11	6.33	6.92
PBE50	XDM(Z)	7.66	7.92	4.13	7.35	6.21	6.86	6.95
PBE50	XCDM(BJ)	7.90	7.77	3.99	6.14	6.32	6.22	6.74
PBE50	XCDM(Z)	7.63	7.93	4.10	7.07	6.34	6.76	6.90
B86bPBE50	XDM(BJ)	8.09	7.34	3.91	5.84	5.39	5.65	6.50
B86bPBE50	XDM(Z)	7.72	7.57	4.05	6.84	5.90	6.44	6.74
B86bPBE50	XCDM(BJ)	7.79	7.42	3.88	5.89	5.75	5.83	6.48
B86bPBE50	XCDM(Z)	7.66	7.56	3.99	6.50	6.02	6.29	6.66
BHLYP	XDM(BJ)	9.24	6.82	5.42	5.14	6.79	5.85	7.06
BHLYP	XDM(Z)	8.22	7.21	5.29	7.14	6.48	6.86	7.16
BHLYP	XCDM(BJ)	9.21	7.05	5.56	4.79	7.09	5.77	7.08
BHLYP	XCDM(Z)	8.30	7.43	5.41	7.02	6.72	6.89	7.25
LC- ω PBE	XDM(BJ)	5.78	8.20	4.36	5.36	6.24	5.74	5.98
LC- ω PBE	XDM(Z)	5.84	8.02	4.41	4.66	6.81	5.58	5.92
LC- ω PBE	XCDM(BJ)	5.70	8.29	4.41	6.64	5.90	6.33	6.20
LC- ω PBE	XCDM(Z)	5.78	8.04	4.43	4.65	6.50	5.44	5.85

^a D3(BJ) result obtained from Ref. [280], values recalculated using Tables S24 and S68 in their ESI.

^b MBD@rsSCS crashed for some systems due to a polarization catastrophe [315], so two reactions were substituted using MBD-NL results: 1 na8 -> 4 na2 and 1 li5_ch -> 1 li4_c + 1 li_h.

^c MBD-NL crashed for some systems due to a polarization catastrophe [315], so two reactions were substituted using MBD@rsSCS results: 1 f + 1 H2 -> 1 RKT10 and 1 hf + 1 h -> 1 RKT10.

Table C.12: WTMAD-1, 2, 3, 1.5, and 4 values (kcal/mol) for each functional and DC combination for the full GMTKN55 benchmark. All results were calculated in FHI-aims [120] as described in the computational methods in the Chapter 6, except for D3(BJ), where data computed with ORCA was obtained from Ref. [280].

	PBE	B86bPBE	PBE0	B86bPBE0	B3LYP	PBE50	B86bPBE50	BHLYP	LC- ω PBE
D3(BJ)^{a,d}									
WTMAD-1	5.67	-	3.87	-	-	-	-	-	-
WTMAD-2	10.41 ^d	-	6.60 ^d	-	-	-	-	-	-
WTMAD-3	5.54	-	3.63	-	-	-	-	-	-
WTMAD-1.5	10.64	-	6.97	-	-	-	-	-	-
WTMAD-4	8.94	-	5.87	-	-	-	-	-	-
TS									
WTMAD-1	5.77	-	4.02	-	-	-	-	-	-
WTMAD-2	10.07	-	6.53	-	-	-	-	-	-
WTMAD-3	5.39	-	3.60	-	-	-	-	-	-
WTMAD-1.5	10.67	-	7.19	-	-	-	-	-	-
WTMAD-4	9.03	-	6.37	-	-	-	-	-	-
MBDrsSCS^b									
WTMAD-1	5.75	-	4.03	-	-	-	-	-	-
WTMAD-2	9.96	-	6.45	-	-	-	-	-	-
WTMAD-3	5.37	-	3.64	-	-	-	-	-	-
WTMAD-1.5	10.46	-	7.12	-	-	-	-	-	-
WTMAD-4	8.68	-	6.05	-	-	-	-	-	-
MBD-NL^c									
WTMAD-1	5.75	-	4.06	-	-	-	-	-	-
WTMAD-2	10.05	-	6.53	-	-	-	-	-	-
WTMAD-3	5.44	-	3.70	-	-	-	-	-	-
WTMAD-1.5	10.52	-	7.18	-	-	-	-	-	-
WTMAD-4	8.73	-	6.14	-	-	-	-	-	-
XDM(BJ)									
WTMAD-1	5.76	5.23	4.01	3.54	3.65	4.05	3.72	3.82	3.45
WTMAD-2	10.40	9.38	6.55	5.78	6.27	6.06	5.67	5.72	5.48
WTMAD-3	5.59	4.95	3.68	3.17	3.40	3.46	3.18	3.17	3.21
WTMAD-1.5	10.79	9.54	7.18	6.16	6.70	6.96	6.39	6.51	6.35
WTMAD-4	8.61	7.83	5.97	5.26	6.09	7.06	6.63	7.15	6.16
XDM(Z)									
WTMAD-1	5.70	5.36	3.95	3.68	3.76	3.93	3.77	3.51	3.51
WTMAD-2	10.78	10.00	6.96	6.43	6.88	6.44	6.20	6.09	5.51
WTMAD-3	5.73	5.25	3.83	3.49	3.66	3.60	3.41	3.26	3.25
WTMAD-1.5	10.96	10.06	7.34	6.69	7.13	7.08	6.71	6.51	6.43
WTMAD-4	8.74	8.20	6.04	5.69	6.40	7.08	6.86	7.27	6.14
XCDM(BJ)									
WTMAD-1	5.55	5.12	3.80	3.42	3.52	3.86	3.62	3.76	3.51
WTMAD-2	10.06	9.10	6.23	5.59	5.95	5.86	5.60	5.60	5.67
WTMAD-3	5.40	4.81	3.50	3.07	3.24	3.34	3.13	3.12	3.30
WTMAD-1.5	10.41	9.30	6.81	5.97	6.39	6.71	6.29	6.40	6.55
WTMAD-4	8.34	7.67	5.70	5.15	5.79	6.86	6.58	7.16	6.36
XCDM(Z)									
WTMAD-1	5.67	5.31	3.91	3.61	3.74	3.89	3.71	3.54	3.46
WTMAD-2	10.70	9.87	6.88	6.29	6.76	6.37	6.11	6.08	5.44
WTMAD-3	5.69	5.19	3.79	3.41	3.60	3.56	3.36	3.27	3.20
WTMAD-1.5	10.90	9.96	7.27	6.56	7.07	7.01	6.62	6.56	6.35
WTMAD-4	8.70	8.10	5.98	5.55	6.34	7.02	6.77	7.36	6.06

^a D3(BJ) result obtained from Ref. [280], values recalculated using Tables S24 and S68 in their ESI.

^b MBD@rsSCS crashed for some systems due to a polarization catastrophe [315], so two reactions were substituted using MBD-NL results: 1 na8 -> 4 na2 and 1 li5_ch -> 1 li4_c + 1 li_h.

^c MBD-NL crashed for some systems due to a polarization catastrophe [315], so two reactions were substituted using MBD@rsSCS results: 1 f + 1 H2 -> 1 RKT10 and 1 hf + 1 h -> 1 RKT10.

^d When recalculating D3(BJ)'s WTMAD-2 we noticed a discrepancy between our calculated values for "Basic+Small" and "GMTKN55" categories compared to the values listed both in Ref. [280]'s ESI and the online GMTKN55 database [279].

Table C.13: Mean absolute errors (MAE) and mean errors (ME), in kcal/mol, for the X23 molecular crystal structure benchmark, calculated in FHI-aims [120] using selected functionals and basis sets. Results are shown for the XDM(BJ), XDM(Z), XCDM(BJ), and XCDM(Z) dispersion corrections. Full geometry optimizations were carried out with the `lightdenser` and `tight` basis sets. Single-point calculations were then performed at the GGA/`lightdenser` geometries. These were used to compute a basis set correction to approximate hybrid/`tight` results at the GGA/`lightdenser` geometry. Binding energies are positive, such that a positive mean error indicates overbinding.

Basis	Functional	XDM(BJ)		XDM(Z)	
		MAE	ME	MAE	ME
Full Optimization					
lightdenser	B86bPBE	0.849	-0.643	0.775	-0.025
lightdenser	B86bPBE0	0.825	-0.792	0.615	-0.001
lightdenser	B86bPBE50	0.938	-0.932	0.754	-0.039
lightdenser	PBE	1.151	-0.961	0.992	-0.347
lightdenser	PBE0	1.120	-1.090	0.780	-0.361
lightdenser	PBE50	1.098	-1.085	0.856	-0.346
tight	B86bPBE	0.695	-0.266	0.810	0.135
tight	PBE	1.127	-0.918	0.917	-0.319
Single-Point Calc. at GGA/ <code>lightdenser</code> Geometry					
lightdenser	B86bPBE0	0.668	-0.619	0.612	0.129
lightdenser	B86bPBE50	0.610	-0.535	0.704	0.287
lightdenser	PBE0	0.997	-0.977	0.744	-0.290
lightdenser	PBE50	0.870	-0.863	0.810	-0.186
tight	B86bPBE	0.702	-0.269	0.807	0.137
tight	PBE	1.129	-0.911	0.915	-0.319
Basis-Set Corr. at GGA/ <code>lightdenser</code> Geometry					
BSC	B86bPBE0	0.483	-0.245	0.607	0.290
BSC	B86bPBE50	0.507	-0.161	0.731	0.448
BSC	PBE0	0.999	-0.928	0.663	-0.261
BSC	PBE50	0.869	-0.813	0.751	-0.158
Basis	Functional	XCDM(BJ)		XCDM(Z)	
		MAE	ME	MAE	ME
Full Optimization					
lightdenser	B86bPBE	0.538	0.148	0.966	0.848
lightdenser	B86bPBE0	0.530	-0.071	0.860	0.765
lightdenser	B86bPBE50	0.651	-0.288	0.760	0.608
lightdenser	PBE	0.609	-0.111	0.916	0.397
lightdenser	PBE0	0.503	-0.333	0.702	0.322
lightdenser	PBE50	0.631	-0.451	0.756	0.250
tight	B86bPBE	0.640	0.426	1.213	1.061
tight	PBE	0.636	-0.056	0.984	0.477
Single-Point Calc. at GGA/ <code>lightdenser</code> Geometry					
lightdenser	B86bPBE0	0.512	0.091	0.949	0.886
lightdenser	B86bPBE50	0.623	0.088	0.983	0.921
lightdenser	PBE0	0.445	-0.229	0.711	0.388
lightdenser	PBE50	0.573	-0.239	0.718	0.403
tight	B86bPBE	0.628	0.403	1.199	1.051
tight	PBE	0.634	-0.061	0.981	0.471
Basis-Set Corr. at GGA/ <code>lightdenser</code> Geometry					
BSC	B86bPBE0	0.650	0.346	1.188	1.088
BSC	B86bPBE50	0.729	0.343	1.239	1.123
BSC	PBE0	0.531	-0.178	0.743	0.462
BSC	PBE50	0.595	-0.188	0.785	0.477

Table C.14: Mean absolute errors (MAE) and mean errors (ME), in kcal/mol, for the ICE13 ice polymorph benchmark, calculated in FHI-aims [120] using selected functionals and basis sets. Results are shown for the XDM(BJ), XDM(Z), XCDM(BJ), and XCDM(Z) dispersion corrections. Full geometry optimizations were carried out with the `lightdenser` and `tight` basis sets. Single-point calculations were then performed at the `lightdenser`/GGA geometries. These were used to compute a basis set correction to approximate `tight`/hybrid results at the `lightdenser`/GGA geometry. Binding energies are positive, such that a positive mean error indicates overbinding.

Basis	Functional	XDM(BJ)				XDM(Z)			
		Abs MAE	ME	MAE	Rel ME	Abs MAE	ME	MAE	Rel ME
Full Optimization									
lightdenser	B86bPBE	2.389	2.389	0.779	0.643	2.995	2.995	0.568	0.432
lightdenser	B86bPBE0	0.960	0.960	0.567	0.428	1.705	1.705	0.347	0.161
lightdenser	B86bPBE50	0.447	0.411	0.445	0.286	1.220	1.220	0.210	-0.012
lightdenser	PBE	2.560	2.560	1.024	0.891	3.274	3.274	0.781	0.648
lightdenser	PBE0	1.164	1.164	0.716	0.578	1.911	1.911	0.466	0.314
lightdenser	PBE50	0.681	0.681	0.477	0.327	1.367	1.367	0.281	0.079
tight	B86bPBE	1.559	1.559	0.523	0.384	1.888	1.888	0.410	0.241
tight	PBE	1.445	1.445	0.829	0.693	2.104	2.104	0.608	0.473
Single-Point Calculation at GGA/ <code>lightdenser</code> Geometry									
lightdenser	B86bPBE0	0.757	0.734	0.524	0.384	1.472	1.472	0.316	0.121
lightdenser	B86bPBE50	0.452	-0.418	0.341	0.151	0.379	0.379	0.171	-0.138
lightdenser	PBE0	0.946	0.928	0.672	0.534	1.667	1.667	0.434	0.272
lightdenser	PBE50	0.356	-0.182	0.371	0.191	0.491	0.491	0.187	-0.054
tight	B86bPBE	1.560	1.560	0.517	0.376	1.883	1.883	0.406	0.236
tight	PBE	1.440	1.440	0.824	0.689	2.097	2.097	0.605	0.469
Basis-Set Correction at GGA/ <code>lightdenser</code> Geometry									
BSC	B86bPBE0	0.296	-0.095	0.312	0.116	0.360	0.360	0.171	-0.075
BSC	B86bPBE50	1.247	-1.247	0.183	-0.117	0.733	-0.733	0.334	-0.334
BSC	PBE0	0.427	-0.192	0.480	0.332	0.500	0.490	0.293	0.093
BSC	PBE50	1.302	-1.302	0.213	-0.011	0.686	-0.686	0.240	-0.233
Basis	Functional	XCDM(BJ)				XCDM(Z)			
		Abs MAE	ME	MAE	Rel ME	Abs MAE	ME	MAE	Rel ME
Full Optimization									
lightdenser	B86bPBE	2.187	2.187	0.840	0.706	2.999	2.999	0.558	0.425
lightdenser	B86bPBE0	0.851	0.830	0.611	0.474	1.707	1.707	0.344	0.160
lightdenser	B86bPBE50	0.405	0.361	0.456	0.302	1.236	1.236	0.206	-0.014
lightdenser	PBE	2.549	2.549	1.027	0.895	3.314	3.314	0.768	0.638
lightdenser	PBE0	1.146	1.146	0.721	0.585	1.940	1.940	0.459	0.307
lightdenser	PBE50	0.658	0.657	0.479	0.330	1.399	1.399	0.274	0.072
tight	B86bPBE	1.289	1.289	0.601	0.464	1.876	1.876	0.401	0.233
tight	PBE	1.435	1.435	0.833	0.699	2.135	2.135	0.596	0.463
Single-Point Calculation at GGA/ <code>lightdenser</code> Geometry									
lightdenser	B86bPBE0	0.659	0.606	0.568	0.431	1.475	1.475	0.312	0.120
lightdenser	B86bPBE50	0.489	-0.466	0.354	0.171	0.397	0.397	0.169	-0.141
lightdenser	PBE0	0.928	0.909	0.678	0.541	1.697	1.697	0.428	0.266
lightdenser	PBE50	0.367	-0.208	0.374	0.197	0.523	0.523	0.184	-0.060
tight	B86bPBE	1.286	1.286	0.596	0.460	1.870	1.870	0.398	0.229
tight	PBE	1.430	1.430	0.829	0.696	2.128	2.128	0.593	0.459
Basis-Set Correction at GGA/ <code>lightdenser</code> Geometry									
BSC	B86bPBE0	0.395	-0.295	0.363	0.184	0.347	0.347	0.166	-0.076
BSC	B86bPBE50	1.367	-1.367	0.194	-0.075	0.732	-0.732	0.337	-0.337
BSC	PBE0	0.434	-0.209	0.486	0.342	0.517	0.512	0.287	0.088
BSC	PBE50	1.327	-1.327	0.219	-0.002	0.663	-0.663	0.245	-0.238

Table C.15: Mean absolute errors (MAE) and mean errors (ME), in kcal/mol, for the HalCrys4 halogen crystal benchmark, calculated in FHI-aims [120] using selected functionals and basis sets. Results are shown for the XDM(BJ), XDM(Z), XCDM(BJ), and XCDM(Z) dispersion corrections. Full geometry optimizations were carried out with the `lightdenser` and `tight` basis sets. Single-point calculations were then performed at the `lightdenser`/GGA geometries. These were used to compute a basis set correction to approximate `tight`/hybrid results at the `lightdenser`/GGA geometry. Binding energies are positive, such that a positive mean error indicates overbinding.

Basis	Functional	XDM(BJ)		XDM(Z)	
		MAE	ME	MAE	ME
Full Optimization					
lightdenser	B86bPBE	6.189	6.189	5.721	5.721
lightdenser	B86bPBE0	3.361	3.361	1.937	1.937
lightdenser	B86bPBE50	2.349	2.349	0.721	-0.461
lightdenser	PBE0	3.714	3.714	1.418	1.418
lightdenser	PBE	6.928	6.928	5.060	5.060
lightdenser	PBE50	1.707	1.707	0.917	-0.818
tight	B86bPBE	4.601	4.601	4.922	4.922
tight	PBE	5.383	5.383	4.112	4.112
Single-Point Calc. at GGA/ <code>lightdenser</code> Geometry					
lightdenser	B86bPBE0	2.693	2.693	1.284	1.161
lightdenser	B86bPBE50	1.449	0.382	2.673	-2.673
lightdenser	PBE0	3.040	3.040	0.786	0.691
lightdenser	PBE50	1.011	-0.341	2.908	-2.908
tight	B86bPBE	4.704	4.704	5.031	5.031
tight	PBE	5.494	5.494	4.185	4.185
Basis-Set Corr. at GGA/ <code>lightdenser</code> Geometry					
BSC	B86bPBE0	1.208	1.208	0.860	0.471
BSC	B86bPBE50	1.103	-1.103	3.363	-3.363
BSC	PBE0	1.606	1.606	0.567	-0.183
BSC	PBE50	1.775	-1.775	3.783	-3.783
Basis	Functional	XCDM(BJ)		XCDM(Z)	
		MAE	ME	MAE	ME
Full Optimization					
lightdenser	B86bPBE	7.217	7.217	6.325	6.325
lightdenser	B86bPBE0	4.074	4.074	2.421	2.421
lightdenser	B86bPBE50	2.884	2.884	0.518	-0.090
lightdenser	PBE0	4.184	4.184	1.845	1.845
lightdenser	PBE	7.494	7.494	5.566	5.566
lightdenser	PBE50	2.320	2.320	0.727	-0.471
tight	B86bPBE	5.580	5.580	5.774	5.774
tight	PBE	5.891	5.891	4.670	4.670
Single-Point Calc. at GGA/ <code>lightdenser</code> Geometry					
lightdenser	B86bPBE0	3.395	3.395	1.686	1.664
lightdenser	B86bPBE50	1.663	0.899	2.253	-2.253
lightdenser	PBE0	3.513	3.513	1.126	1.126
lightdenser	PBE50	1.329	0.331	2.545	-2.545
tight	B86bPBE	5.661	5.661	5.676	5.676
tight	PBE	5.974	5.974	4.729	4.729
Basis-Set Corr. at GGA/ <code>lightdenser</code> Geometry					
BSC	B86bPBE0	1.839	1.839	1.298	1.015
BSC	B86bPBE50	0.873	-0.657	2.902	-2.902
BSC	PBE0	1.992	1.992	0.587	0.289
BSC	PBE50	1.190	-1.190	3.382	-3.382

Table C.16: Mean absolute errors (MAE) and mean errors (ME), in meV/Å², for the LM26 layered materials benchmark and the LM11 subset, calculated in FHI-aims [120] using selected functionals and basis sets. Results are shown for the XDM(BJ), XDM(Z), XCDM(BJ), and XCDM(Z) dispersion corrections. In this case, a negative ME indicates overbinding.

Basis	Functional	XDM(BJ) [†]				XDM(Z)			
		LM26		LM11		LM26		LM11	
MAE	ME	MAE	ME	MAE	ME	MAE	ME	MAE	ME
lightdenser	B86bPBE	5.9	-5.9	4.5	-4.5	5.8	-5.5	4.2	-3.8
lightdenser	PBE	5.6	-5.5	4.2	-3.9	4.1	-3.2	3.2	-1.8
tight	B86bPBE	7.7	-7.7	6.0	-6.0	7.3	-7.1	5.3	-5.0
tight	PBE	6.8	-6.7	5.2	-4.8	5.4	-4.8	4.0	-3.0

Basis	Functional	XCDM(BJ)				XCDM(Z)			
		LM26		LM11		LM26		LM11	
MAE	ME	MAE	ME	MAE	ME	MAE	ME	MAE	ME
lightdenser	B86bPBE	16.1	-16.1	14.3	-14.3	13.0	-13.0	11.1	-11.1
lightdenser	PBE	15.0	-15.0	13.0	-13.0	9.6	-9.4	8.4	-7.9
tight	B86bPBE	16.9	-16.9	15.0	-15.0	15.5	-15.5	13.1	-13.1
tight	PBE	15.8	-15.8	13.6	-13.6	11.8	-11.7	9.9	-9.7

[†] We note a slight discrepancy of ca. 0.3 meV/Å² (\approx 0.1 kcal/mol/cell) between the LM11 and LM26 MAEs reported here and those in Ref. [315]. These differences were examined, and the cause was determined to be the change in XDM damping parameters between the two versions of the code: 221103 and 250425. For more details regarding this change, see Appendix C.3.

Table C.17: Mean absolute errors (MAE) and mean errors (ME), in kcal/-mol/cell, for the LM26 layered materials benchmark and the LM11 subset, calculated in FHI-aims [120] using selected functionals and basis sets. Results are shown for the XDM(BJ), XDM(Z), XCDM(BJ), and XCDM(Z) dispersion corrections. In this case, a negative ME indicates overbinding.

Basis	Functional	XDM(BJ)				XDM(Z)			
		LM26	LM11	MAE	ME	LM26	LM11	MAE	ME
lightdenser	B86bPBE	1.5	-1.5	1.1	-1.1	1.6	-1.5	1.1	-1.0
lightdenser	PBE	1.5	-1.5	1.1	-1.0	1.1	-0.9	0.7	-0.6
tight	B86bPBE	2.0	-2.0	1.5	-1.5	2.0	-1.9	1.4	-1.3
tight	PBE	1.8	-1.8	1.3	-1.3	1.4	-1.3	1.0	-0.9

Basis	Functional	XCDM(BJ)				XCDM(Z)			
		LM26	LM11	MAE	ME	LM26	LM11	MAE	ME
lightdenser	B86bPBE	4.0	-4.0	3.4	-3.4	3.4	-3.4	2.8	-2.8
lightdenser	PBE	3.8	-3.8	3.2	-3.2	2.5	-2.5	2.1	-2.0
tight	B86bPBE	4.2	-4.2	3.6	-3.6	4.0	-4.0	3.3	-3.3
tight	PBE	4.0	-4.0	3.3	-3.3	3.1	-3.1	2.5	-2.5